10/12/95

SANDIA REPORT

SAND95–0591 • UC–814
Unlimited Release
Printed September 1995

Yucca Mountain Site Characterization Project

Batch and Column Studies of Adsorption of Li, Ni and Br by a Reference Sand for Contaminant Transport Experiments

RECEIVED
OCT 23 1995
OSTI

M. D. Siegel, D. B. Ward, C. R. Bryan, C. Boyle

Prepared by
Sandia National Laboratories
Albuquerque, New Mexico 87185 and Livermore, California 94550
for the United States Department of Energy
under Contract DE-AC04-94AL85000

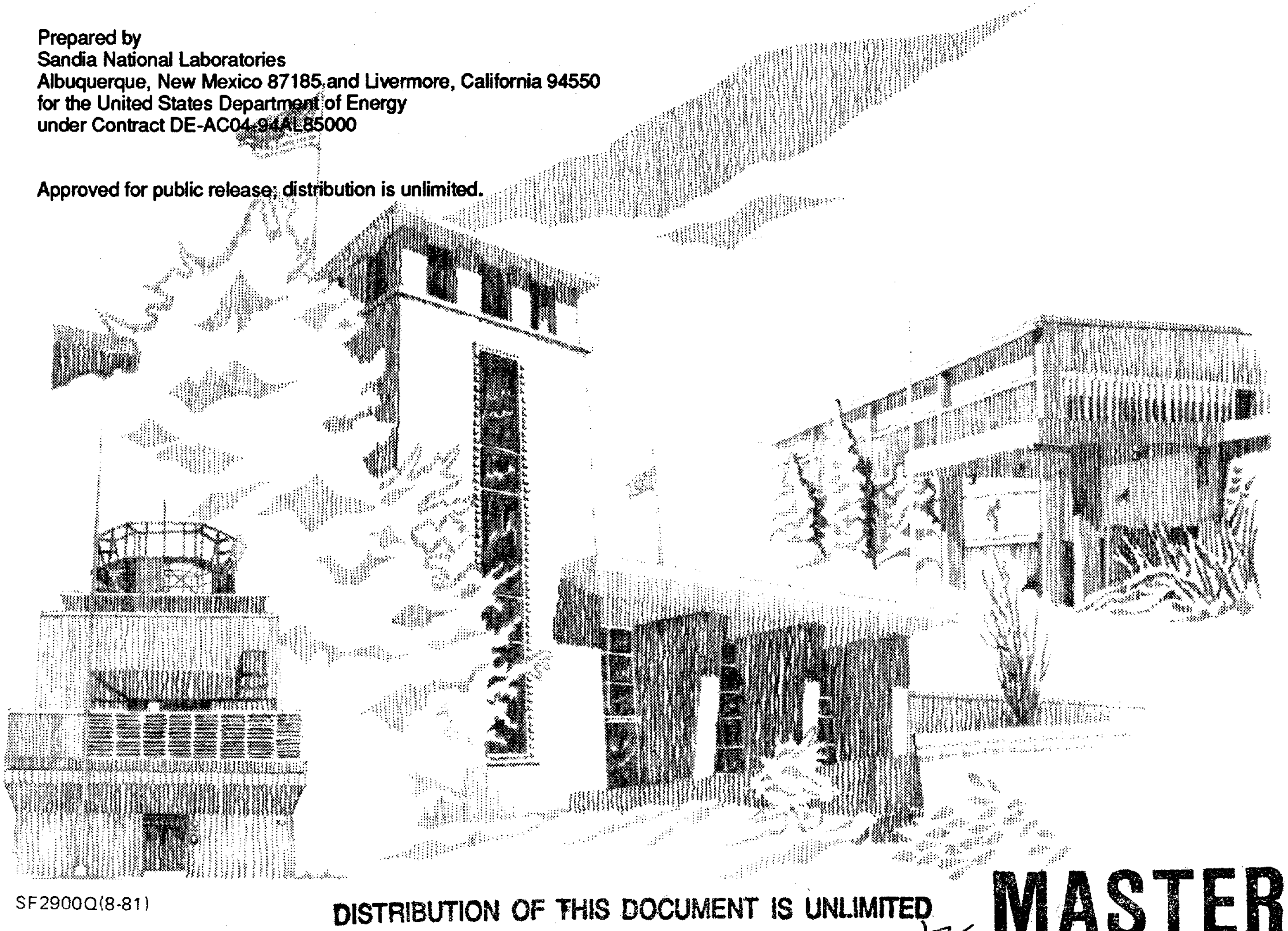

SF2900Q(8-81)

MASTER

"Prepared by Yucca Mountain Site Characterization Project (YMSCP) participants as part of the Civilian Radioactive Waste Management Program (CRWM). The YMSCP is managed by the Yucca Mountain Project Office of the U.S. Department of Energy, DOE Field Office, Nevada (DOE/NV). YMSCP work is sponsored by the Office of Geologic Repositories (OGR) of the DOE Office of Civilian Radioactive Waste Management (OCRWM)."

Issued by Sandia National Laboratories, operated for the United States Department of Energy by Sandia Corporation.

Available to DOE and DOE contractors from
Office of Scientific and Technical Information
PO Box 62
Oak Ridge, TN 37831

Prices available from (615) 576-8401, FTS 626-8401

Available to the public from
National Technical Information Service
US Department of Commerce
5285 Port Royal Rd
Springfield, VA 22161

NTIS price codes
Printed copy: A20
Microfiche copy: A01

SAND95-0591
Unlimited Release
Printed September 1995

Distribution
Category UC-814

Batch and Column Studies of Adsorption of Li, Ni and Br by a Reference Sand for Contaminant Transport Experiments

Final Characterization of Wedron 510 Sand for the Caisson Experiment

M. D. Siegel
Sandia National Laboratories
Albuquerque, NM 87185

D. B. Ward, C.R. Bryan, C. Boyle
University of New Mexico
Albuquerque, NM

Abstract

A processed quartz sand (Wedron 510), mined from the St. Peter sandstone, has been characterized by a variety of chemical and physical methods for use as a reference porous media in transport model validation experiments. Wedron 510 sand was used in an intermediate-scale experiment involving migration of Ni, Li and Br through a 6-m high x 3-m diameter caisson. Ni and Li adsorption/desorption and Li/Ni site-competition experiments yielded information on the importance of the trace mineral phases to adsorption of Li and Ni by the sand. The presence of an iron hydroxide coating similar to goethite on the sand grains is suggested by visual observation and leaching experiments. Kaolinite was identified by SEM and XRD as a significant trace mineral phase in the sand and occurs as small particles coating the sand grains. Quartz, the predominant constituent of the sand by weight, does not appear to contribute significantly to the adsorption properties of the sand. Qualitatively, the adsorption properties of the sand can be adequately modeled as a two-mineral system (goethite and kaolinite). The extent and rate of Ni adsorption by the sand are pH-dependent; Ni adsorption occurs primarily on the iron oxyhydroxide coatings on the sand, on sites where Li does not compete. Some of the Ni adsorbs to kaolinite, and competes with Li for adsorption sites on that

mineral. Li adsorbs irreversibly, suggesting that kaolinite is the only important phase in the sand with respect to Li adsorption.

Breakthrough curves (BTCs) for Ni and Li transport in bench-scale columns were consistent with the batch sorption data. The shapes of BTCs for two different Li concentrations were consistent with the non-linear sorption observed in the batch systems. Apparent retardation factors of both of the Li BTCs were consistent with the equilibrium batch K_ds, adsorption rate constants, and the pore water velocity of the columns. In contrast, it is difficult to compare Ni retardation factors obtained from column tests to those calculated from the results of batch tests because the pH of the Ni columns varied and the K_d and rate of Ni adsorption are strongly dependent on pH. Nevertheless, the calculated retardation factors of slow and fast flowing columns were within the bounds calculated from the ranges of the batch K_ds, adsorption rate constants, and pore water pH values.

The studies described in this report should provide a basis for understanding transport of Ni, Li and Br through porous media similar to the reference sand. Techniques were developed for obtaining parameter values for surface complexation and kinetic adsorption models for the sand and its mineral components. These constants can be used directly in coupled hydrogeochemical transport codes. The techniques should be useful for characterization of other natural materials and elements in high-level nuclear waste in support of coupled hydrogeochemical transport calculations for Yucca Mountain.

This work was supported by the Yucca Mountain Site Characterization Office under W.B.S. 1.2.5.4.6 and Contract DE-AC04-94AL85000.

Acknowledgments

The authors acknowledge the valuable assistance provided by several of their colleagues J. Kelly and C. Ashley (SNL) provided logistic support and valuable advice and assistance in the BET analyses and related calculations under the QA guidance of the authors. M. Crawford (British Geological Survey, Nottingham, U.K.) provided samples of Min-U-Sil 5 and results of his Ni adsorption experiments. E. Springer, (Los Alamos National Laboratory) was responsible for the fielding of the caisson experiment and coordinated the collection of water samples.

The reviews by P. Brady (SNL) and B. Thomson (University of New Mexico) provided useful suggestions that lead to revisions of this report. The work was carried out under QAGR 1.2.1.4.6, Rev 0, (current WBS 1.2.5.4.6). This report contains no qualified data; calculations were not carried out with qualified software and the work should not be used for licensing or design activities. This work was performed for the U.S. Department of Energy under Contract DE-AC04-76D00789 and Contract DE-AC04-94AL85000.

Table of Contents

Appendices

Executive Summary

A processed quartz sand (Wedron 510), mined from the St. Peter sandstone, has been characterized by several chemical and physical methods for use as a reference porous media in transport model validation experiments. An intermediate-scale experiment has been carried out by Sandia National Laboratories and Los Alamos National Laboratory for the Yucca Mountain Site Characterization Project to demonstrate a strategy to validate key geochemical and hydrological assumptions in performance assessment models. The experiment involved the detection and prediction of the migration of fluid and tracers through a 6-m high x 3-m diameter caisson filled with Wedron 510 sand. The role of Sandia National Laboratories in the Caisson Experiment was to study the characteristics of the sand that would control chemical interactions between the tracers, fluid and substrates. This report described the results of the following studies: 1) obtaining Li and Ni adsorption data for components of the raw sand, 2) studying reversibility of Ni and Li sorption by the sand, 3) studying the competition between Li and Ni for sorption sites on the sand and its components, 4) examining transport of Li and Ni in well-controlled bench-scale columns to provide an intermediate link between static batch sorption tests and the caisson transport experiment, and 5) obtaining data on breakthrough of a Ni pulse in the caisson.

Wedron 510 sand provides a relatively simple natural material to test alternative models for trace metal adsorption by mineral mixtures. The sand is more than 99% quartz in bulk mineralogy, yet its adsorption behavior is dominated by iron oxyhydroxide and kaolinite, two trace components. Fe-oxyhydroxide probably coats most (50 – 80%) of the available surface area in the raw sand; its presence is inferred from the quantity of Fe leached during an acid wash. Scanning electron microscopy shows that kaolinite platelets litter exposed sand grain surfaces.

Qualitatively, the adsorption properties of the sand can be adequately modeled as a two-mineral system (goethite and kaolinite). Ni adsorption occurs primarily on the iron oxyhydroxide, on sites where Li does not compete; some of the Ni adsorbs to kaolinite, and competes with Li for adsorption sites on that mineral. The presence of Li leads to diminished Ni adsorption by both the raw sand and pure kaolinite. Ni adsorption by goethite is insensitive to the presence of Li., suggesting that in the sand, iron oxyhydroxide could not be the site of the Li-Ni competition. The acid-washed sand adsorbs Ni in a manner similar to that of kaolinite. Acid stripping removes a substantial fraction of the kaolinite from the sand but may expose additional reactive surfaces by dissolving carbonate cement and iron oxyhydroxides. The presence of the cement is inferred from potentiometric titration of the raw sand and the amount of Ca and Mg that is leached by acid-stripping.

Two triple-layer surface-complexation models have been developed for simulating Ni adsorption onto goethite. The models were fit to Ni adsorption data in batch systems with approximately 5 and 50 m^2/l goethite under both CO_2-free and air-equilibrated conditions. The adsorption stoichiometry is modeled as a 1:1, $SONi^+$ inner-sphere complex. The simpler one-site model performs poorly at lower surface concentrations when optimized at the higher surface concentration. The two site model contains a small fraction of high-energy sites and fits data for both goethite concentrations well. A quantitative model of Ni adsorption onto kaolinite was also developed; attempts to develop a model for quartz were less successful. Thermodynamic speciation calculations were carried out with HYDRAQL 94 (Ward, 1995), a revised version of HYDRAQL (Papelis *et al.*, 1988) using an internally consistent set of formation constants for aqueous Ni species. The formation constants for Ni carbonato-complexes are two orders of magnitude lower than the values commonly used in the literature. The lower values are consistent with the results of Ni solubility measurements in batch systems with low concentrations of CO_2 and Ni adsorption experiments at high pH.

Batch studies revealed that adsorption of Li by sand was non-linear, relatively slow and predominantly irreversible. Similar studies of Ni sorption revealed that extents and rates of adsorption were pH dependent and partially irreversible. Many available transport models rely on simple geochemical assumptions such as linear reversible sorption. More sophisticated codes such as HYDRUS (Kool and van Genuchten, 1992), CXTFIT (Parker and van Genuchten, 1984) and LEHGC (Yeh, 1995) incorporate non-linear sorption, kinetics or surface complexation models, but none of these codes can model the full complexity of the adsorption behavior of these tracers on these substrates. It was shown, however, that the breakthrough curves for Ni and Li were consistent with the batch sorption data. Specifically, the differences between the shapes of the 1 and 17.4 ppm BTCs for Li were consistent with the non-linear sorption observed in the batch systems. Second, apparent retardation factors of both of the Li BTCs were consistent with the equilibrium batch K_d and adsorption rate constants and the pore water velocity of the columns. Third, although, both the K_d and rate of Ni sorption are strongly dependent on pH, and the pH of the Ni columns varied, the calculated retardation factor of slow and fast flowing columns were within the bounds predicted from the batch experiment data and the pore water velocity.

Previously (Kent *et al.*, 1988), it has been asserted that the Surface Complexation Modeling approach provides a useful framework to collect and evaluate adsorption data. The results of the present study provide support for that assertion. Although a unique quantitative adsorption model based on the properties of the component minerals of Wedron 510 sand has not yet been obtained, the adsorption properties of the sand can be qualitatively understood in terms of the properties of its components. Attempts to quantify the effects of solution parameters on adsorption revealed many trends that may have not been noticed. These trends include: effect of pH, P_{CO_2}, ionic strength and substrate surface area on adsorption, and the competition between Ni and Li for adsorption sites on the sand and on kaolinite.

The studies described in this report provide the basis for the development of models for the prediction of Ni, Li and Br transport through porous media similar to the reference sand. Techniques were developed for obtaining parameter values for surface complexation and kinetic adsorption models for the sand and its mineral components. These constants can be used directly in coupled hydrogeochemical transport codes for calculations of transport of these tracers through common aquifer materials. The techniques developed should be useful for characterization of other natural materials present at Yucca Mountain in support of coupled hydrogeochemical transport calculations in porous or equivalent porous media. Such models will be required for contaminant transport calculations for complex chemical systems in which a simple K_d model can not predict tracer retardation.

Batch and Column Studies of Adsorption of Li, Ni and Br by a Reference Sand for Contaminant Transport Experiments

1. Introduction

Integrated flow and transport experiments are being carried out to validate transport models used by the Yucca Mountain Site Characterization Project. Major issues that are being addressed include: (1) What geochemical characteristics of fractured and porous media will dominate chemical retardation of radionuclides? (2) What are the primary contributors to the uncertainty in the accurate detection of the tracers in field transport experiments? and (3) Which retardation models adequately describe tracer and radionuclide migration?

An intermediate-scale transport experiments was carried out at the Experimental Engineered Test Facility at Los Alamos National Laboratory during 1994. The experiment involved the detection and prediction of the migration of fluid and tracers (Li, Br, Ni) through a 6-m-high x 3-m-diameter caisson filled with Wedron 510 sand, a commercially available silica sand (Wedron Silica, Wedron, IL. 60557). The Caisson Experiment was designed to provide a relatively simple system for the formulation of a framework for data collection and model development for the validation of reactive transport models. The results of the transport experiments with these tracers and minerals has applications to other studies in the Yucca Mountain Site Characterization Project (YMSCP). Nickel is representative of radionuclides released from the structural components of the spent fuel rods in high-level waste and is considered an important waste element due its relatively low retardation in Yucca Mountain tuffs (Meijer, 1992). Lithium is a weakly sorbing tracer and forms few complexes in environmental systems. Bromine is a conservative tracer that can be used to measure the velocity of the pore water. The component minerals of the caisson sand (quartz, calcite and iron oxyhydroxides) are present in fractures in Yucca Mountain tuffs (Meijer, 1992).

An overview of the design of the caisson, characterization of the hydraulic properties of the porous media and a description of transport calculations used in the design is given in Siegel *et al.* (1992, 1993) and Springer *et al.* (1993). The role of Sandia National Laboratories in the Caisson Experiment was to study the characteristics of the sand that would control chemical interactions between the tracers, fluid and substrates. Siegel *et al.* (1995) provides a summary of the interim results of the detailed materials characterization phase of the caisson experiment as of January 1994. During this phase, characterization and modeling techniques were developed and preliminary data describing the interactions between each tracer and the sand, among the tracers, and among the tracers and the other solutes in the pore water of the sand were collected. Detailed descriptions of underlying theory, experimental procedures and experimental results are found in a set of appendices to that report. The work described in that report was carried out prior to the fielding of the transport experiments at the Experimental Engineered Test Facility at Los Alamos National Laboratory. This current report describes the final geochemical model for the Wedron 510 sand.

The characterization studies were designed to address several key geochemical issues that are important to contaminant transport. These include (1) the relationship between the adsorptive properties of a bulk rock to the surface properties of its mineralogical components and (2) the feasibility of predicting solute transport in laboratory-scale columns and field sites from a description of a hydrologic flow field and measurements of the geochemical properties of the solute and porous matrix obtained in batch adsorption studies. As the caisson experiment progressed, the general questions posed at the beginning of the study (Siegel *et al.*, 1992, 1993) were replaced by more specific ones. Table 1 illustrates how these early general questions, which were difficult to answer, led to more focused questions that could be answered by properly designed experiments.

Progress was made in answering the specific questions by: 1) obtaining Li and Ni adsorption data under atmospheric and CO_2-free conditions for components of the raw sand and acid-washed sand; 2) studying the reversibility and kinetics of Ni and Li adsorption by the raw sand and its components; 3) carrying out batch adsorption studies with solutions containing both Li and Ni to examine competition for sorption sites on the sand and its components; and 4) examining transport of Ni and Li in well-controlled bench-scale columns filled with the raw sand to provide an intermediate link between static batch sorption experiments and the caisson. The results are described in detail in Appendices A - E and are summarized below. A description of the results of the Ni transport experiment in the caisson is given in Appendix F.

Table 1. General and Specific Questions Addressed in Characterization Studies

General Questions	Specific Questions
What geochemical characteristics of the porous medium will dominate chemical retardation of the tracers?	Can we model adsorption properties of raw sand as a mixture of two components: goethite and kaolinite, and ignore the quartz?
What role do minor mineral phases play in the overall sorption behavior of the sand? Can geochemical transport properties (i.e. solute retardation factors) for porous media composed of mixtures be predicted from batch sorption studies of the constituent minerals?	Is goethite the only important adsorbent in the sand for Ni? Is goethite an important phase for Li adsorption? Do Li and Ni adsorb onto the same sites? Are carbonato complexes important for Ni sorption by sand or components? Are the formation constants for Ni carbonato-complexes reported in the literature reliable?
Which geochemical models adequately describe tracer migration? Can transport of Ni and Li in lab-scale columns be predicted from batch sorption studies?	Is a linear equilibrium adsorption model adequate for Li and Ni transport? Is Ni adsorption by the sand fast and reversible? Is Li adsorption by the sand fast and reversible?

2. Summary of Methods and Results

2.1. Equilibrium Ni and Li Adsorption by Wedron 510 Sand and Pure Mineral Components

2.1.1. Introduction

The sand used in the caisson experiment (Wedron 510 sand) contains several mineralogical components that are potentially important contributors to its aggregate surface chemistry and adsorption of Ni and Li. Specifically, quartz, Fe-oxyhydroxide, kaolinite, and Ca-Mg carbonate were identified by a variety of mineralogical, wet chemical and spectroscopic techniques. In a previous study (Siegel *et al.*, 1995), Ni adsorption measurements were reported for the raw sand under both CO_2-free conditions and conditions of partial equilibration with air, and for synthetic goethite and quartz (Min-U-Sil 5) under CO_2-free conditions. Based on the goethite data, we proposed a preliminary geochemical model in which pH-dependent Ni adsorption onto the raw sand was controlled by Fe-oxyhydroxides that effectively covered 50 – 80% of the surface of the sand (Siegel *et al.*, 1995). Li adsorption by the sand was independent of pH and could be described by a Freundlich isotherm.

The final geochemical model presented in this report is based on additional Ni and Li adsorption measurements made on Wedron sand, acid-washed sand and goethite under both CO_2-free and atmospheric conditions, and on kaolinite and Min-U-Sil 5 quartz under atmospheric conditions. These data, in combination with results from a study of competition between Ni and Li for adsorption sites, allow us to propose a more refined and realistic model for the surface chemistry of Wedron 510 sand, in which kaolinite as well as Fe-oxyhydroxides is important, with a negligible role played by quartz and Ca-Mg carbonate. The methods, results and calculations used to derive the model are summarized below; details of the supporting studies may be found in Appendices A and C to this report.

2.1.2. Methods

Batch adsorption experiments were conducted using “raw” (untreated) Wedron 510 sand, acid-washed Wedron 510 sand, Min-U-Sil 5 (a quartz reference material, U.S. Silica Corp., Berkeley Springs, West Virginia); kaolinite (kaolin powder #2242-01, U.S.P., J.T. Baker Co.), and goethite synthesized using the technique of Tripathi (1983). The acid-washed sand, Min-U-Sil 5 quartz, and kaolinite were prepared by the boiling-HCl method (Ward *et al.*, 1995a). An aliquot of Min-U-Sil 5 was obtained from Mark Crawford of the British Geological Survey. It had been treated by the ignition-$HClO_4$ method, in which the sample was ignited at 500 °C for 48 h prior to leaching in boiling $HClO_4$. The two cleaning methods were found to be equivalent for Min-U-Sil 5, with no detectable differences in surface chemistry. Details of all the preparation techniques can be found in Appendix A.

Surface areas of substrates were measured using the BET method (Brunauer, *et al.*, 1938) with either Kr or N_2 as the adsorbing gas at five values of P/P_0. Reproducibilities of the N_2 measurements on the single minerals were 1% or better, while on the sand, replicates varied by nearly 6%. Surface areas of raw sand, acid-washed sand, goethite, Min-U-Sil and kaolinite in batch adsorption experiments were approximately 78 m^2/l, 58 m^2/l, 5, 41, 47 and 55 m^2/l, 124 and 247 m^2/l and 124 m^2/l, respectively, as estimated from the BET measurements.

Potentiometric titrations to measure the zero-point of charge and protolysis constants of HCl-washed Wedron sand and Min-U-Sil quartz have been previously reported by Ward *et al.* (1995a). Potentiometric titrations of goethite are described in this report. The measurements generally followed the procedures described in Ward *et al.* (1995a), with modifications described in Appendix A. Titrations were performed from pH 10 down to 4 with HCl and then back to 10 with NaOH. Solid NaCl was then added to increase the ionic strength, and the titrations were repeated. Calculations of ionic strength and net added acid included the effects of all reagent additions; titration curves were adjusted to account for bubbles in the reagent tubing and refilling of syringes.

Ni and Li adsorption measurements under CO_2-free conditions were carried out in batch systems as described in our previous report (Siegel *et al.*, 1995.). The procedure for adsorption measurements under air-equilibrated conditions was modified to provide near-air-equilibrated ($P_{CO_2} = 10^{-3.5}$ atm) quantities of total dissolved CO_2 at high pH. Rather than rely on the slow uptake of CO_2 by the electrolyte, the present measurements were made by using both NaOH and $NaHCO_3$ to increase the pH of the systems. As discussed in Appendix A, Section A.2.3, the quantity of $NaHCO_3$ required to reach equilibrium with atmospheric P_{CO_2} was calculated from the target pH and equations for equilibrium carbonate speciation. Such systems are referred to in this report as "air-equilibrated". Batch systems prepared under the methods described in Siegel *et al.* (1995) are referred to as "partially-air equilibrated" in this report. Calculations described in Section A.2.3 show that in these earlier experiments, the dissolved carbonate species were in equilibrium with air below pH 7.5, but at higher pH values, total carbonate was below atmospheric equilibrium and maintained a constant value of about $10^{-3.7}$ M.

The Li batch adsorption experiments were conducted to characterize Li adsorption onto Wedron 510 sand at higher concentrations than those previously reported (Cheng *et al.* 1995). Experiments were carried out under CO_2-free or "air equilibrated" conditions, at initial Li concentrations of 100 µg/m*l* or 1000 µg/m*l* (0.014 M and 0.14 M), in the presence or absence of 100 ppb Ni, at solid:solution ratios of 1 g/m*l*. Batch adsorption studies were also carried out with 100 ppm Li with synthetic goethite (41 m^2/l) and kaolinite (124 m^2/l) in the presence of 100 ppb Ni.

The protocols used for pH measurements, measurement of Ni by graphite-furnace atomic absorption spectrophotometry, and measurement of Li concentrations by flame atomic absorption spectrophotometry are described in Ward *et al.* (1995a). In buffered systems (e.g., "air-equilibrated"), pH measurements were reproducible to better than ± 0.03 pH units; in unbuffered systems (e.g., nominally CO_2-free), the precision is best estimated from the scatter of the adsorption data in the figures in this report. Overall uncertainties in the Ni measurements were 2% for absolute concentrations and 1% for relative concentrations for measurements from the same experiment.

2.1.3. Results of surface characterization measurements

Surface Area. The Kr-BET measurements averaged 0.08 m^2/g for the raw sand and 0.06 m^2/g following acid-washing. Numerous aliquots of Min-U-Sil 5 were measured, with surface areas ranging from 4.05 to 5.81 m^2/g using N_2. The N_2-BET surface area of the kaolinite was determined to be 24.6 m^2/g. Measurements of surface area by N_2-BET on the goethite were 33.8, 39.9, and 45.4 m^2/g for the 3 batches of synthetic goethite used in the adsorption studies. For comparison, using goethite synthesized by the same method, Balistrieri and Murray (1979, 1981) have reported N_2-BET surface areas of 48.5 and 51.8 m^2/g, and van Geen *et al.* (1994) have reported a value of 45 m^2/g. A complete list of the surface area determinations and associated uncertainties is found in Appendix A, Table A.3.

Potentiometric Titrations of Goethite. Potentiometric titrations were performed on goethite batch #5, with results plotted as surface charge (C/m^2) vs. pH in Figure 1. The intersection of the curves for each ionic strength is the pH of zero proton condition (pH_{ZPC}) in this system where H^+ is the only potential-determining ion. The data define a $pH_{ZPC} = 8.9$, identical to that obtained by van Geen *et al.* (1994) but substantially higher than that reported by earlier workers (cf. Balistrieri and Murray, 1981). van Geen *et al.* suggest that earlier measurements were made in the presence of significant quantities of CO_2, which lowers the pH_{ZSE} (pH of zero salt effect) by introducing another potential-determining ion (CO_3^{2-}) (see Appendix A.3.2).

2.1.4. Results for Li adsorption

The results of the studies of adsorption of Li by Wedron 510 sand, goethite and kaolinite as a function of pH are shown in Figures C.1 - C.2 and C.4 - C.5 in Appendix C. At 100 μg/m*l* total Li, sorption by Wedron 510 sand (1 g/m*l*) shows a

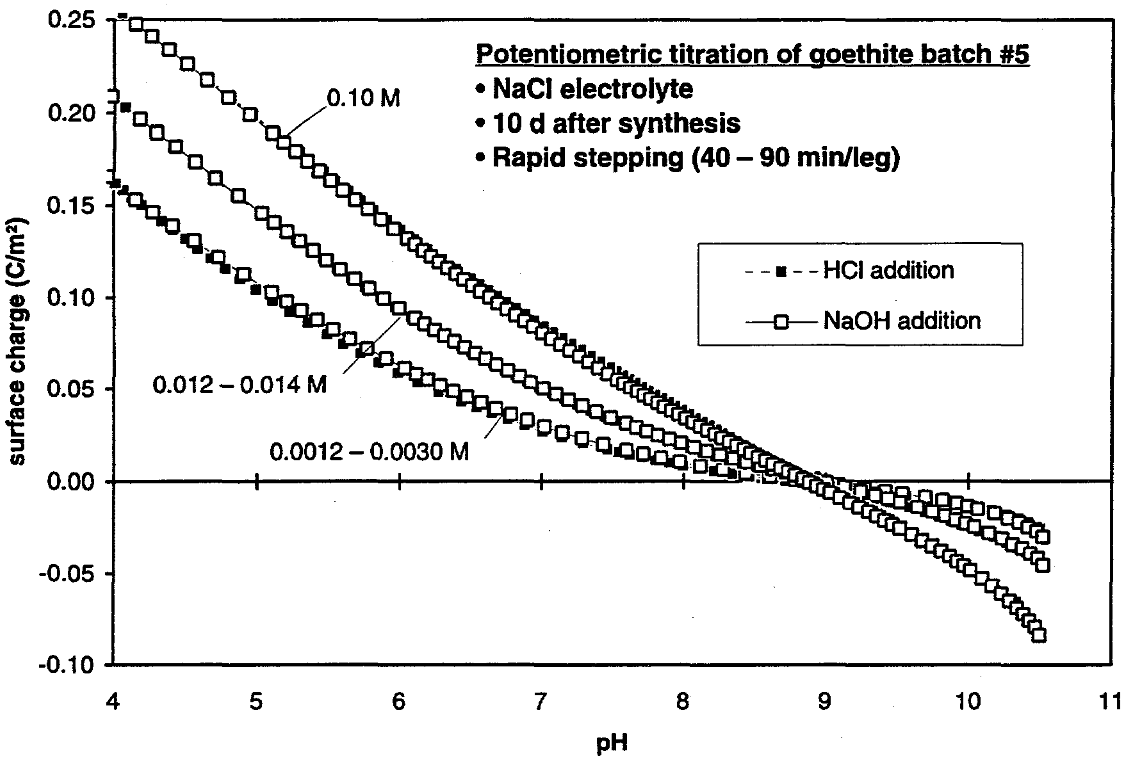

Figure 1. Potentiometric titration of goethite batch #5.

broad sorption peak between pH = 6.8 and 7.5. Maximum adsorption is ~3.5 % for the measurements under atmospheric conditions, and about 0.7% lower for the CO_2-free curve. Adsorption for the 1000 μg/m*l* Li adsorption experiment is about 1% over the pH range 4.5 - 10. The data for Wedron sand at near-neutral pH from this study and previous studies (Cheng *et al.*, 1995) are used to produce the isotherm plot shown in Figure 2 (Figure C.3 in Appendix C.) The data are best described by a Freundlich rather than a linear (K_d) or a Langmuir isotherm.

Adsorption of 100 ppm Li by 1.24 mg/m*l* goethite is constant at ~3% over the pH range 4 to 10, under the same conditions (goethite surface area of 41 m^2/l) (Figure C.4; Appendix C). In contrast, the adsorption curve for 5 mg/m*l* kaolinite, under atmospheric conditions(124 m^2/l surface area), broadly resembles that produced by Wedron 510 sand under similar conditions (Fig. C.1). The results are shown in Figure C.5; adsorption varies somewhat with pH, increasing from 1.5% to 3% from pH 4 to pH 7 and then leveling off or dropping slightly with further increases in pH.

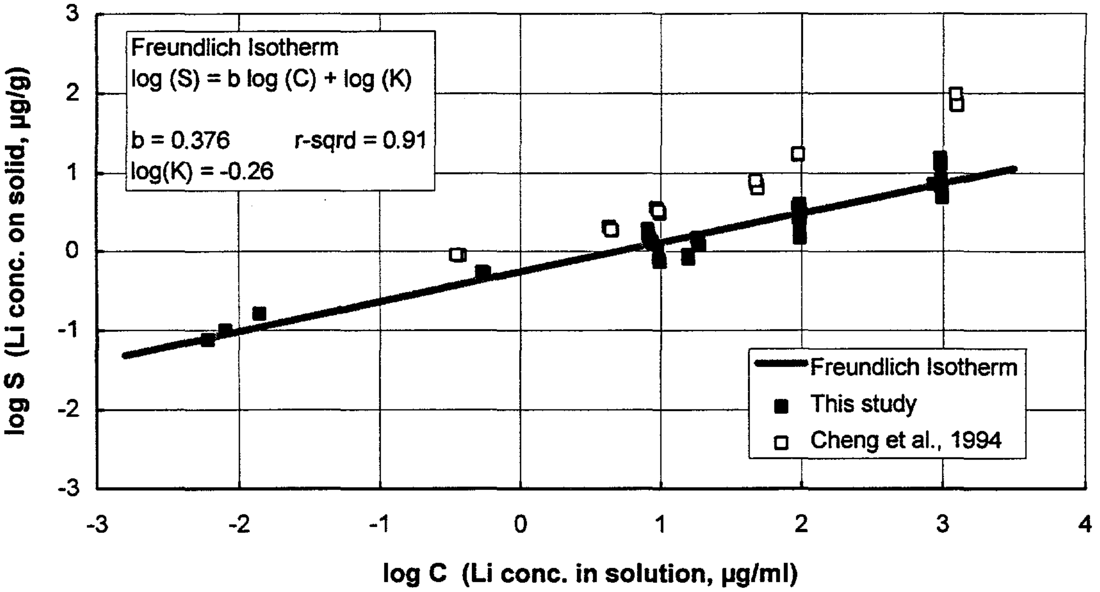

Figure 2. Li adsorption isotherm plot for Wedron 510 sand. Only data between pH 7 and 8 were included; solid:solution ratio is 1 g/m*l*)

2.1.5. Results for Ni adsorption

Ni adsorption onto goethite was measured in batch systems with 0.001 M NaCl background electrolyte containing 3.7–5.4 or 41–55 m^2/l goethite surface area under both "CO_2-free" and air-equilibrated protocols. These measurements for goethite batch #5 (5.4 and 55 m^2/l) are plotted in Figure 3. Adsorption at the higher surface concentrations is similar to that seen on Wedron sand in systems containing 78 m^2/l (Bryan *et al.*, 1995) and is consistent with the hypothesis that Fe-oxyhydroxide is the dominant adsorbent in the raw sand.

Washing the Wedron sand in boiling HCl should remove the iron oxyhydroxide coatings. Figure 4 shows that Ni adsorption onto acid-washed Wedron 510 sand parallels that of the raw sand but is displaced toward lower pH by just over one unit. The pH_{50} values, (pH at which 50% of the Ni is adsorbed) are 4.9 and 5.0, respectively, for CO_2-free and air-equilibrated systems. Unexpectedly, acid-washing has left behind a much more reactive surface with respect to Ni adsorption. This observation is consistent the potentiometric titration data for the acid-washed sand (Ward *et al.*, 1995), which implied that the effective surface area for the acid-washed sand in aqueous solution may be an order of magnitude greater than the 0.06 m^2/g measured by Kr-BET. The effect of CO_2 on the acid-washed sand is reversed from that on the raw sand, with pH_{50} shifted to higher pH by ~0.1 instead of lower pH by ~0.2. Adsorption on the acid-washed sand plateaus at 90 – 95%

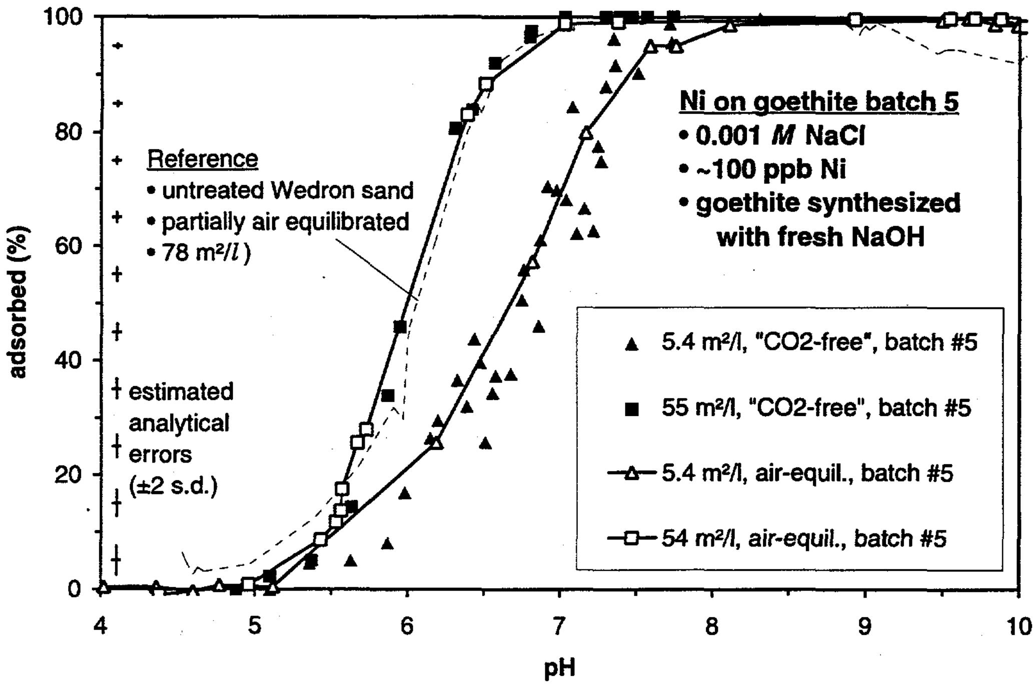

Figure 3 Ni adsorption onto goethite. The data show the influence of variations in surface area and P_{CO_2} (nominally CO_2-free, or equilibrated with air). A curve for Wedron 510 sand is shown for reference (Bryan, *et al.*, 1995).

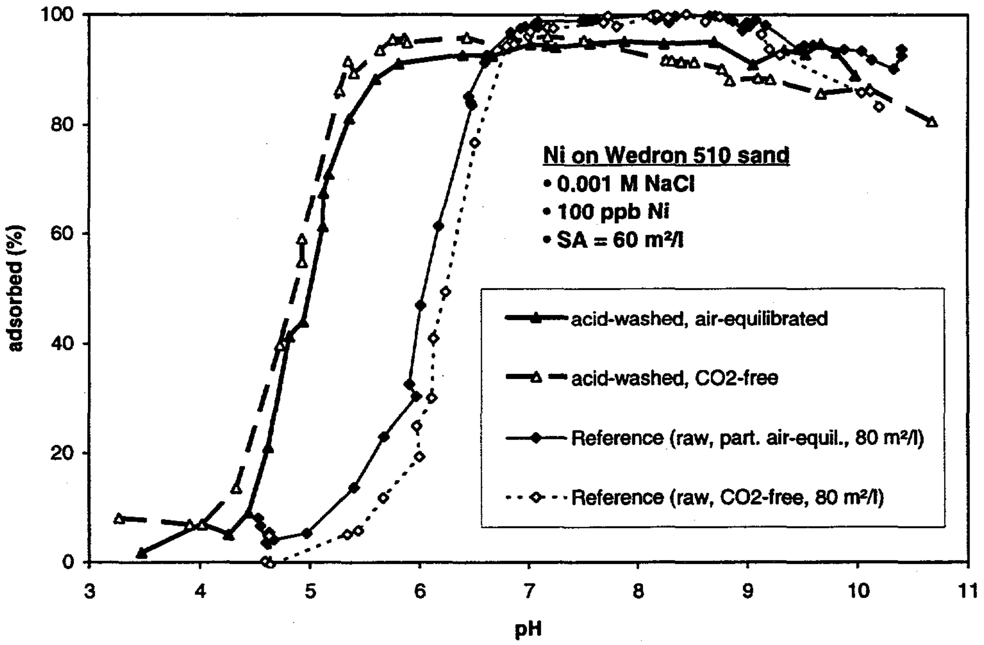

Figure 4. Ni adsorption onto acid-washed Wedron 510 sand along with reference curves for raw Wedron 510 sand, showing the influence of P_{CO_2}

and then declines gradually with increasing pH. The similar but less pronounced effect, seen above pH 9 for the raw sand, was due to colloids penetrating the 0.2 μm filters used to sample the suspensions; presumably the same phenomenon has occurred to a greater extent with the acid-washed sand.

Ni adsorption onto Min-U-Sil 5 quartz lacks any resemblance to either the raw or the acid-washed sand and is very dependent on ionic strength (Figure 5). As shown by the reference curve in the figure , sensitivity to ionic strength is not a characteristic of the raw sand (Bryan *et al.*, 1995). This, and the dramatic difference in shape of the adsorption curves between Min-U-Sil 5 quartz and Wedron 510 sand suggest that quartz surfaces play a negligible role in Ni adsorption onto the sand in both the raw and acid-washed states.

In contrast, Ni adsorption onto kaolinite (estimated surface area of 124 m^2/l from BET measurements), shows an adsorption edge at $pH_{50} = 4.2$ with a profile much like the sand curves (Figure 6). If we assume that adsorption of Ni by kaolinite involves formation of an $SO\text{-}Ni^+$ surface complex, then the amount of adsorption will be linearly related to both the kaolinite surface area and the pH of the solution. If kaolinite were the major adsorbent in the acid-washed sand, application of the law of mass action ($K= \{SO\text{-}Ni^+\}\{H^+\}/\{SOH\}\{Ni2^+\}$) suggests that in order to shift the adsorption edge to $pH_{50} = 5.0$, the concentration of kaolinite should be reduced by a factor of $10^{-(5.0-4.2)} = 0.16$, giving a surface area (19.8 m^2/l) that accounts for only about 34% of that exposed by the acid-washed sand. In this model, the remaining surface of the sand grains (presumably predominantly quartz surfaces) would not appreciably absorb Ni. As discussed in Appendix A.4.6, it is possible that the effective surface area of the kaolinite is greater than the BET-measured surface area. If this is true, then the unreactive surface area of the sand would be even greater.

2.2. Kinetics and Reversibility of Li Adsorption onto Wedron 510 Sand

2.2.1. Methods

Adsorption Kinetics. The adsorption kinetics experiments run on Wedron sand were done in batch mode in 50 m*l* polyallomar centrifuge tubes, using a solid:solution ratio of 1g/m*l*; (surface area of ~80 m^2/l.) The experiments were conducted under partially-equilibrated conditions with respect to atmospheric P_{CO_2}. Samples, containing sand and 0.001 M NaCl electrolyte, were pre-equilibrated on hematology mixers for 48 hours. After pre-equilibration, LiBr was pipetted into each tube, resulting in a final Li concentration of about 10 ppm and the tube were placed back on the mixer. Samples were run in triplicate; aliquots were taken from

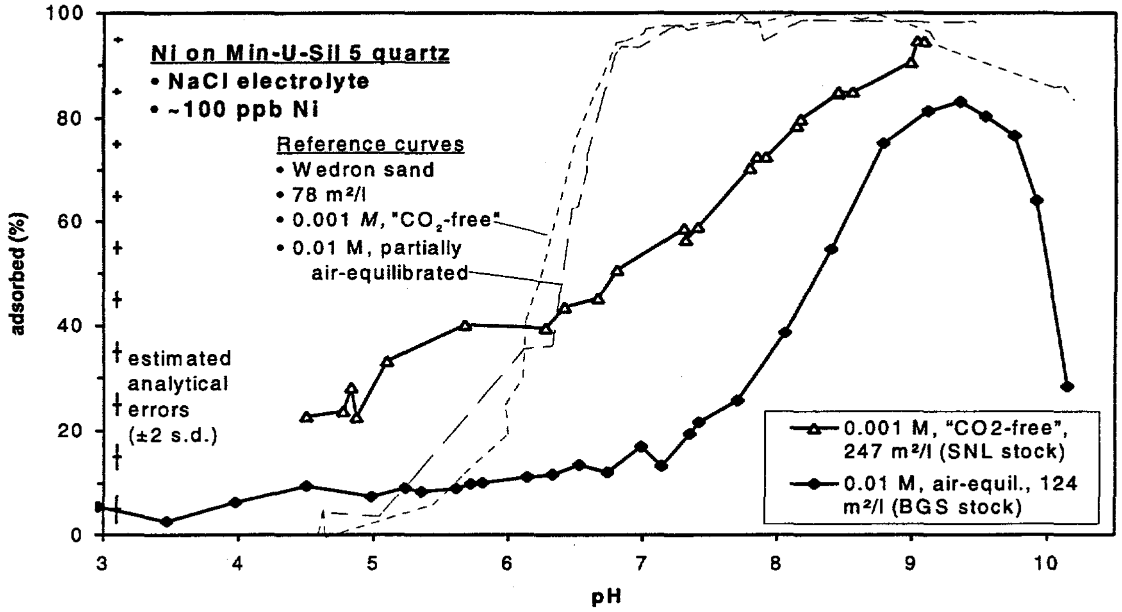

Figure 5. Ni adsorption onto Min-U-Sil 5 quartz. Curves for untreated Wedron sand at similar ionic strengths are included for reference.

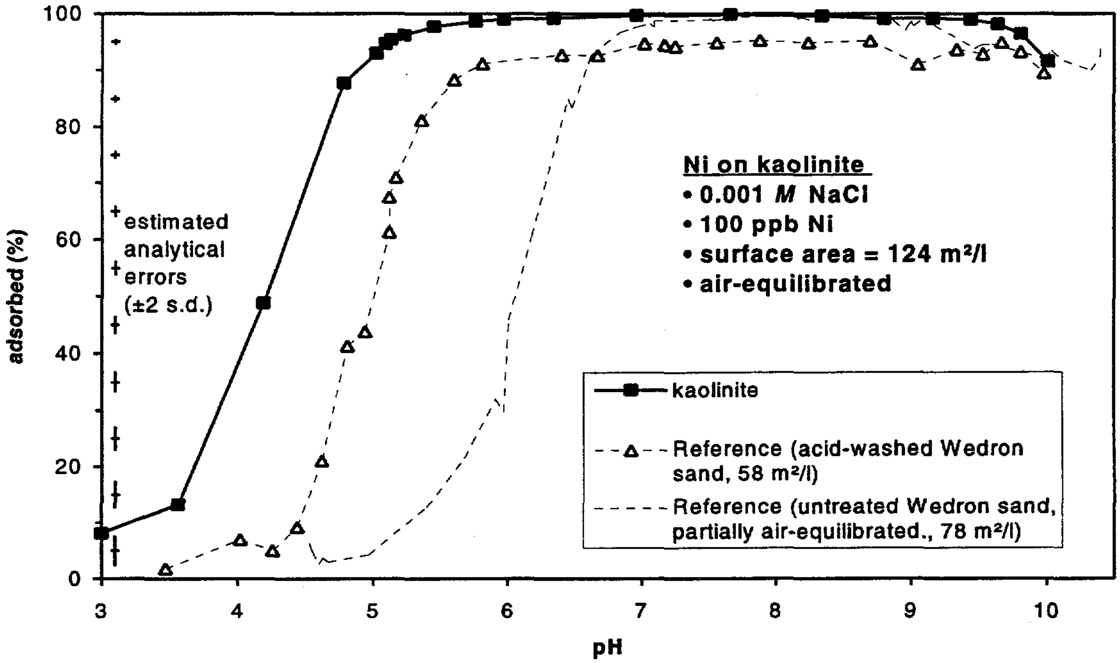

Figure 6. Ni adsorption onto kaolinite. Curves for both acid-washed and untreated Wedron 510 sand are included for reference.

each set at elapsed times of 0, 0.5, 1, 2, 4, 5, 7, 10, 15, 20, 30, 46, 60, 100, and 120 hours, using 10 ml disposable syringes and 0.2 μm membrane filters.

Reversibility (Desorption) Studies. Desorption of adsorbed Li from Wedron sand was examined in three sets of experiments. Two were carried out with sand that had been previously equilibrated in a batch system with 100 ppm Li; and a surface concentration of 80 m^2/l. The first experiment was run under partially air-equilibrated conditions, at three pH values (4, 7, 10). The second experiments was run under CO_2-free conditions, over a pH range of 4 - 10, in the presence of 100 ppb Ni. In a third experiment, sand was equilibrated with 20 ppm Li electrolyte at near neutral pH, rinsed three times with neutral unspiked electrolyte and then re-equilibrated with either fresh neutral electrolyte or fresh electrolyte with pH = 2. Details of the solid:solution separation procedures can be found in Appendix C.2.

2.2.2. Results

Adsorption Kinetics. The results of the 10 ppm Li adsorption kinetics study are shown in Figure 7. As discussed on Appendix C, the data were not modeled well by either the first or second-order rate equations, based on low r^2 values. Separate first-order rate equations for the time intervals from 0-10 hr. and 10-120 hr. described the data well:

$$\ln C = \ln C_o - k_a t \qquad (1)$$

where:
C = Concentration of Li in solution at time t (ppm).
C_o = Initial concentration of Li at time zero (ppm).
k_a = Apparent rate constant (hr^{-1})

The multiple slopes may indicate the presence of two different sites or mechanisms for sorption. Another explanation may be a change in physical properties of the sand due to abrasion caused by the mixing action.

The apparent rate constant for the interval 0-10 hr. agreed closely with a first-order apparent constant derived from previous 5 ppm Li kinetic sorption data (Cheng *et al.*, 1995; Figure C.6). This confirms that for Li sorption on Wedron sand, for sorption times up to 15 hr., the reaction can be modeled as first-order with an apparent rate constant in the range 0.0043 hr^{-1} to 0.0057 hr^{-1}.

Reversibility. The results from all three desorption studies indicate that Li does not desorb from Wedron sand under conditions of moderate pH. However, most or all of the Li can be stripped off by lowering the pH of the electrolyte to 2 or less. Details of the results are found in Appendix C. The data are consistent with the interpretation that Li is primarily adsorbing onto kaolinite in the sand;

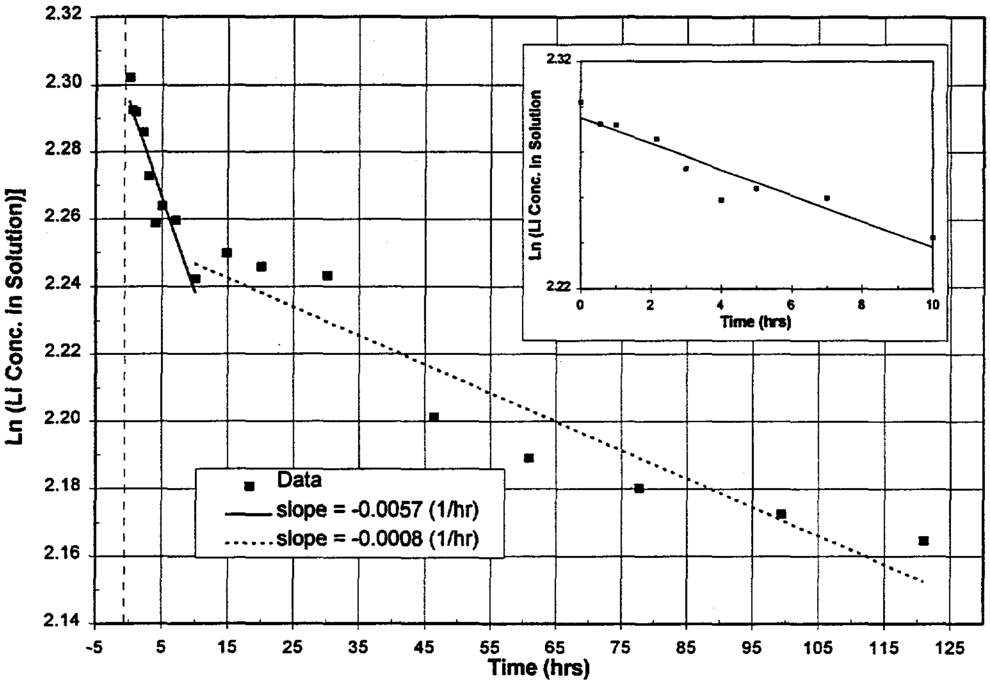

Figure 7. Results of kinetics experiments for 10 ppm Li adsorption by Wedron sand. Regression lines for first-order rate equations are shown for two separate time intervals; the time interval 0<t<10 hr. is shown inset.

irreversible adsorption of Li by kaolinite has been reported by Anderson *et al.* (1989), who postulated that Li is strongly bound into octahedral edge sites in kaolinite.

2.3. Kinetics and Reversibility of Ni Adsorption onto Wedron 510 Sand

Previous studies (Bryan *et al.*, 1995) determined that the kinetics of Ni adsorption onto Wedron 510 sand at pH ~7.6 are moderately fast, reaching equilibrium in 2 – 4 h. The studies summarized below provide information on adsorption and desorption rates of Ni on Wedron sand as a function of pH and are described in detail in Appendix B.

2.3.1. Methods

Adsorption Rate Experiments. Two experiments were run to examine the kinetics of Ni adsorption. The first was run in screw-cap polycarbonate centrifuge tubes containing 20 g Wedron 510 sand and 100 ppb Ni in 20 m*l* of 0.001 M NaCl at pH ~7.7. After pre-equilibration and addition of a spike, each tube was mixed by hand or on a hematology mixer for 1 minute to 24 hours. Samples of the electrolyte were extracted and acidified to 2% HNO_3 for later Ni analysis by GFAA. The pH of the remaining solutions, measured immediately after Ni aliquots were extracted, did not vary with equilibration time and were 7.70 ± 0.10.

The second adsorption experiment was run at pH 6.3, on the steep part of the Ni adsorption edge. A single large system was used; consisting of 80 m*l* electrolyte, 80 g sand, and 2.4 m*l* of 50 mmol HCl. After two days pre-equilibration, sparging with air to remove excess CO_2, and addition of tracer spike to produce a concentration of 100 ppb Ni, the system was agitated violently to mix the sand and electrolyte and returned to the mixer. Aliquots (1.5 m*l*) of the electrolyte were collected at timed intervals from 1 minute to 24 hours and acidified for later Ni analysis. The pH of the system was measured before the first sampling interval (1 minute), and after collection of the final (24 hr) sample.

Details of pre-equilibration, preparation of spikes, and solid/solution separation techniques for both studies are found in Appendix B, Section 2.3.1. Procedures for Ni analysis by GFAA for both adsorption studies and the desorption studies described below are described in Ward *et al.* (1995a). Note that in these experiments, as in the equilibrium adsorption experiments, the "total exchangeable Ni" is the sum of the added Ni and the Ni naturally present in the sand that can be desorbed at a given pH.

Desorption Rate Experiments. One batch desorption experiment was run using screw-cap polycarbonate centrifuge tubes containing 20 g sand and an initial electrolyte Ni concentration of 100 ppb in 20 m*l* 0.001 M NaCl. Samples were pre-equilibrated for two days at pH ~7.7, spiked, equilibrated for two days and then sampled to verify that Ni adsorption was ~100%. Acid (50 mmol HCl) was then added to each tube, in amounts varying from 210 to 1000 μl, to lower the pH and cause desorption. Each tube was then sampled after re-equilibration intervals ranging from ½ hour to 130 hours. Sampling was done as described above for the adsorption experiments.

The other desorption experiment was performed using an autotitrator (described in detail in Ward *et al.*, 1995b; Appendix E.6), with the standard reactor jar replaced by a 1 *l* polyethylene bottle immersed in a 25 °C constant-temperature water bath. A single large batch of sand suspended in 0.001 *M* NaCl was pre-equilibrated with the electrolyte, spiked with Ni, allowed to equilibrate for 2 h, and then an aliquot of acid was added to lower the pH after an equilibration interval. During equilibration, the autotitrator was used as a pH-stat to maintain constant pH as the carbonate in the sand dissolved. This equilibration and adjustment loop was repeated until pH 4 was reached. Samples were taken immediately before and after pH adjustment, and also after the initial ~2 h equilibration if the next pH adjustment was not going to take place immediately. Total available Ni was determined at the end of the experiment by acidifying the system to pH 3 and allowing it to equilibrate for several weeks, with occasional agitation before sampling it for Ni-GFAA analysis. Detailed descriptions of both experiments are found in Appendix B, Section 2.3.1.

2.3.2. Results

Adsorption Kinetics. The results of experiments to examine the kinetics of Ni adsorption are summarized in Figure 8. For the first experiments, measured pH values for the individual batch systems were 7.70 ± 0.10. Adsorption was extremely rapid; about 66% of the added Ni (75% of the total exchangeable Ni) was adsorbed within one minute, 90% was adsorbed within ½ hr, and equilibrium was reached after 2 – 4 hours. In the second set of experiments (set A), the pH increased from 6.30 initially to 6.43 after 24 hours; in the third (set B), the pH rose from 6.15 to 6.27 in 24 hours. Adsorption is considerably slower at pH 6.3 than at 7.7. There was no measurable adsorption for several minutes after addition of the spike, and only about 40 % of the total exchangeable Ni was adsorbed after 4 hours. Equilibrium (70% adsorbed) was not reached even after 24 hours. Even the small pH difference between the two replicates caused a significant difference in adsorption rate; adsorption was slower in the slightly more acidic set B. Previous studies (Bryan *et al.*, 1995) showed that at pH 7.7 and 6.3, 100 % and 70%, respectively, of the Ni is adsorbed at equilibrium.

First-order Ni adsorption rate constants were calculated for the three experiments using equation (1) above; regression lines for the equations are shown in the figure. Reasonable fits are evident for the low pH experiments; calculated rate constants for data sets A and B were 0.00066 min^{-1} and 0.00050 min^{-1}, respectively. Data for the higher pH experiment are modeled better as the sum of two separate first-order reactions: a very rapid reaction (1), occurring early in the experiment (<20 minutes), with a rate constant of 0.0455 min^{-1}, and a slower reaction (2), occurring throughout the experiment, with a rate constant of 0.0106 min^{-1} .

Reversibility (Desorption) Studies. The Ni batch desorption data are difficult to interpret and are not suitable for the derivation of desorption rate constants.. Results are shown in Figures B.4 and B.5, Appendix B and illustrate an adsorption/desorption hysteresis: desorption appears to be incomplete over the pH range 6 – 4. Although the amount of Ni desorbed per unit time increased with decreasing pH, equilibrium was reached more slowly than at higher pH. At pH > 6, equilibrium was re-established within several hours of pH adjustment. At lower pH, equilibrium was not reached by the end of the experiment (after 41 hours at pH 5.1). Finally, at pH 4, desorption is complete and the rate may have increased.

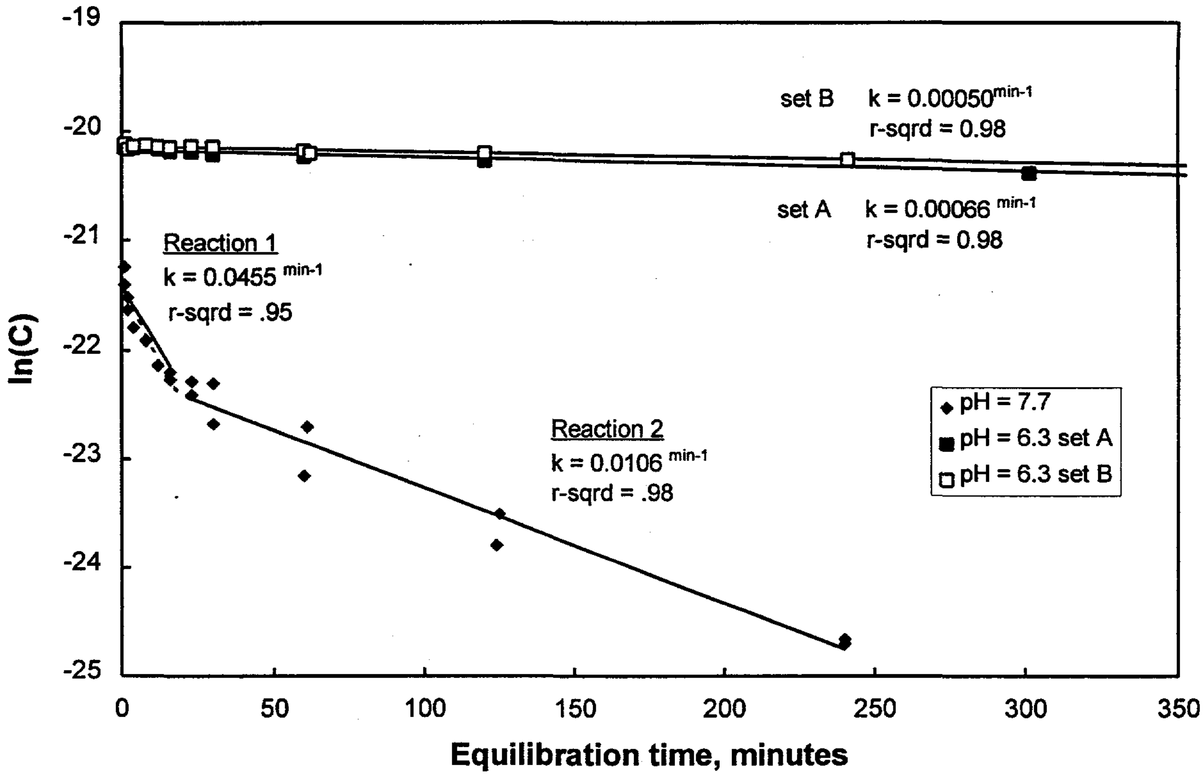

Figure 8. Calculated first-order rate constants for Ni adsorption data. Best-fit lines, determined by least squares regression, are shown. Data from experiment at pH = 7.7 are modeled as two first-order reactions.

The results might be qualitatively interpreted in terms of kinetic effects related to a range of surface-site energies. As pH was lowered from pH 8 in the autotitrator system, Ni desorbed rapidly from low-energy sites. By pH 6.5, desorption slowed because there was little Ni remaining on the rapidly exchangeable sites. Finally, the desorption rates are high at pH 4.1; the driving force for desorption may be large because the system is initially far from equilibrium as indicated in Figure B.5. More detailed discussions of the experimental results and interpretations are found in Appendix B.

2.4. Li-Ni site competition on Wedron 510 Sand

2.4.1. Methods

Li-Ni site competition on Wedron sand was evaluated at initial Li concentrations of 100 μg/m*l* and 1000 μg/m*l* (0.014 M and 0.14 M)., using initial Ni concentrations of 100 ng/m*l* ($1.7 \cdot 10^{-6}$ M). A second set of Ni-Li sorption competition studies with higher Li and Ni concentrations was carried out with Wedron sand under air-equilibrated conditions at near-neutral pH. Total Li concentrations were 0.1, 1 or 10 μg/m*l*; the total Ni content ranged from 80 - 5000 ng/m*l* ($1.36 \cdot 10^{-6}$ M to $8.5 \cdot 10^{-4}$ M). Finally, Li adsorption and Li/Ni site competition studies were conducted on goethite and kaolinite only under air equilibrated conditions ($P_{CO2} = 10^{-3.5}$), using Li and Ni initial concentrations of 100 μg/m*l* and 100 ng/m*l*, respectively.

2.4.2. Results

The measurements of Ni adsorption by Wedron sand (Ni concentration of 100 ng/m*l*) in the presence of a high concentration of Li (100 μg/m*l*) revealed competitive effects between the two cations. On the raw sand, Ni adsorption was slightly diminished in the presence of Li, with the adsorption edge shifting from $pH_{50} = 6.3$ to 6.5 (see Figure 9). The results of the study of the effect of elevated Ni concentrations on Li sorption by Wedron sand are summarized in Figure 10. Ni competition appears to limit Li adsorption only for the experiments carried out at 1 ppm total Li concentration. The results are discussed in more detail in Appendix A where it is proposed that Li adsorption may be occurring on sites with different energies. At intermediate Li concentrations (1 ppm), Ni and Li compete for the same favorable high-energy sites; at lower Li concentrations (0.1 ppb), both Li and Ni can be accommodated by the available high-energy sites, whereas at higher Li concentrations, Li is dominantly adsorbed by a lower energy site.

Ni adsorption by kaolinite is diminished by the presence of Li, producing a curve with shallower slope at low pH and then nearly leveling off between pH 5 and 6 before reaching complete adsorption near pH 7.5 (Figure 11). The order in which the tracer elements are added has a slight effect on the location of the adsorption curves; Ni adsorption appears to be slightly higher in those samples to which Ni was added first. This suggests that some of the Ni is adsorbing irreversibly. Alternatively, because kinetic studies show that Li adsorption is slow to reach equilibrium, perhaps Li/Ni exchange is also slow, and insufficient time was allowed for equilibrium to be reached.

In contrast, Li has no measurable effect on Ni adsorption onto goethite (Figure A.10, Appendix A). These results suggest that the decrease in Ni adsorption by raw sand in the presence of Li reflects the presence of a kaolinite component.

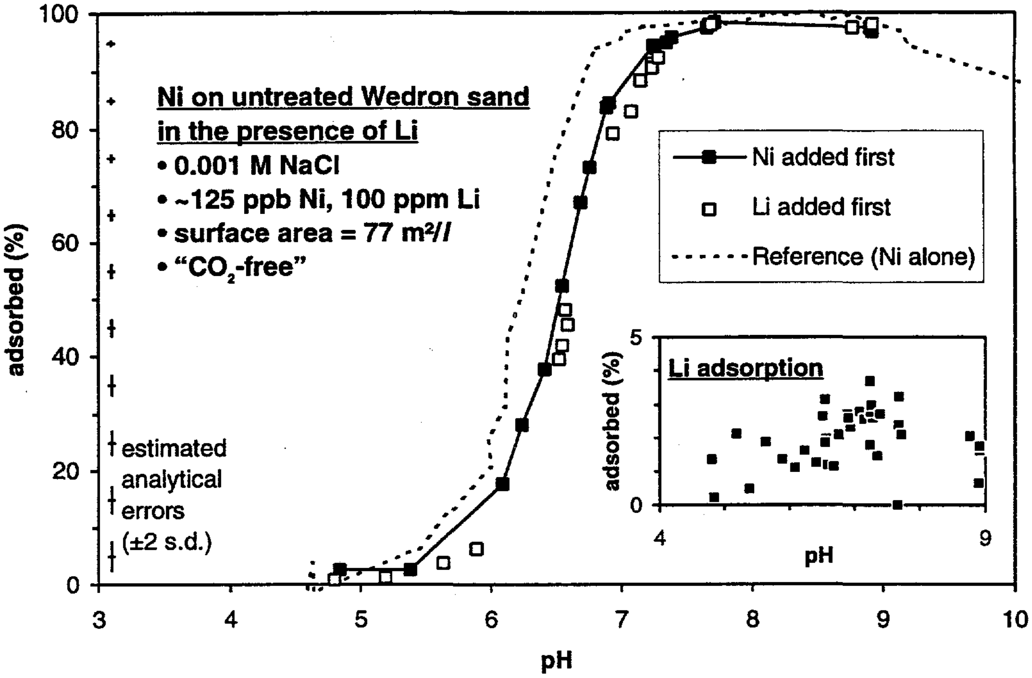

Figure 9. Ni adsorption onto Wedron sand in the presence of 100 ppm Li. Adsorption of Ni alone is shown for reference. Inset shows Li adsorption onto the sand in the same experiment.

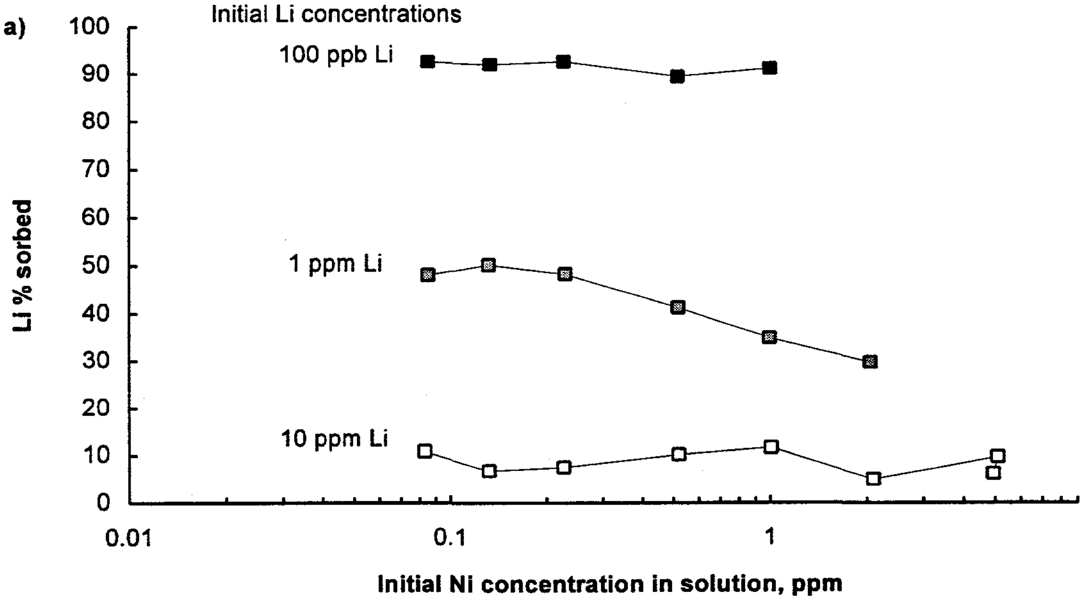

Figure 10. The effect of Ni concentration in solution on the adsorption of Li by Wedron 510 sand at pH ~7.7, under atmospheric conditions.

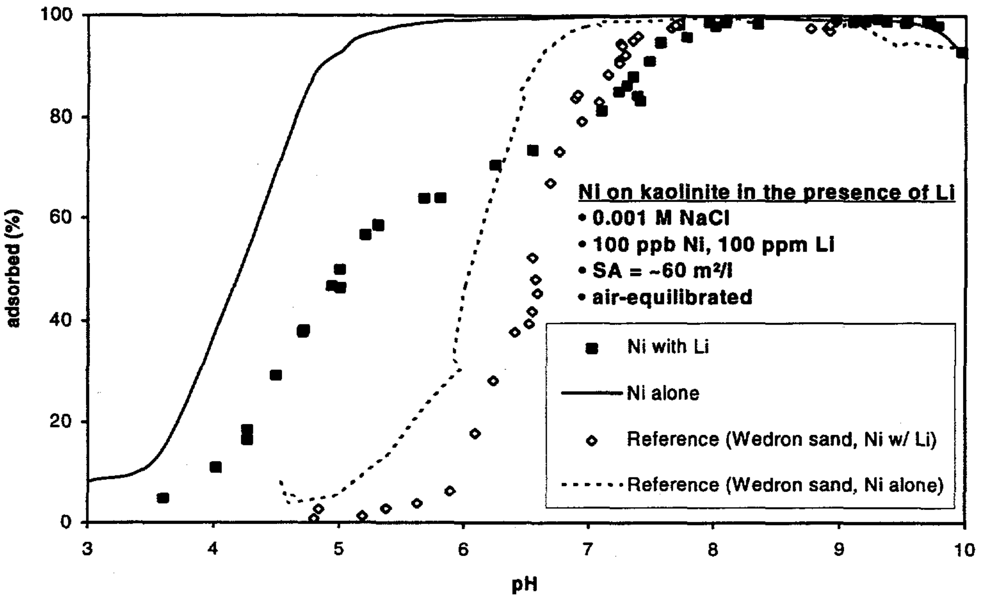

Figure 11. Ni adsorption onto kaolinite in the presence of Li compared to adsorption of Ni alone, with reference to Wedron 510 sand under similar P_{CO_2} conditions.

2.5 Transport of Li and Ni in Saturated Bench-Scale Sand Columns

2.5.1. Introduction

Bench-scale column experiments provide a link between batch adsorption studies and field tracer tests. A series of column experiments was carried out as part of this study to determine if transport of adsorbing tracers can be predicted from equilibrium and kinetic adsorption parameters measured in batch systems. Previously, breakthrough curves (BTC's) for Li and Br through saturated Wedron 510 sand were measured as part of the design and detailed characterization phases of the caisson experiment (Cheng *et al.*, 1995). In that study, the Br pulses showed a retardation factor slightly less than 1, and were satisfactorily modeled by the equilibrium linear-isotherm convective-dispersive model of the CXTFIT code (Parker and van Genuchten, 1984). The Li pulses were not adequately modeled by the equilibrium convective-dispersive model. A one-site kinetic adsorption model was calculated with CXTFIT using K_d (0.15 m*l*/g) and k (0.00012 min^{-1}) values similar to those measured in the laboratory batch experiments. This model gave a reasonable fit to the elution curve for the micro-layered sand column ($r^2 = 0.911$). A two-site kinetic model with simultaneous calculation of D (hydrodynamic dispersion coefficient), R (retardation factor), k (first order sorption rate constant) and F (fraction of sites assumed to be in equilibrium) improved the fit significantly to account for the sharper leading edge and the tail. However, the fitted values of R and k were not consistent with the batch experimental data.

The rate expression for the kinetics model in CXTFIT includes a K_d to establish the equilibrium concentration in the solid phase. Because Li batch adsorption data indicated that the Li K_d for the Wedron sand depends on concentration, it is possible that a transport model allowing for nonlinear sorption might model the Li effluent curves better. Batch experiments described in the previous section and in Appendix C, confirmed that a Freundlich isotherm was appropriate for Li adsorption. In this section and in Appendix D, attempts to model new column experiments at different initial Li concentrations with CXTFIT (Parker and van Genuchten, 1984) and HYDRUS, (Kool and van Genuchten, 1992), a transport code that includes non-linear adsorption, are described. In addition, the results of Ni transport experiments in saturated columns of Wedron sand are described in the subsequent section and in Appendix E.

2.5.2. Li transport experiments

The methods used follow those described in Cheng *et al.* (1995). A 5 cm diameter by 30.5 cm long Plexiglas column was filled with Wedron 510 sand and saturated with 0.001 M NaCl solution. The bulk density, ρ_b, and porosity, η, were 1.8 g/m*l* and 0.30, respectively; the pore water velocity was 0.071 cm/min. About 0.3 pore volumes of 1 ppm Li (as LiBr) tracer were pumped into the column and then the column was flushed with a total of ~6 pore volumes of the 0.001M NaCl solution. Column effluent samples were taken for 30 minutes at a time.

The observed breakthrough curves (BTC)'s for Br and Li are shown in Figure 12 and are similar to Br and Li BTC's derived from previous experiments (Cheng *et al.*, 1995). The Br BTC displays a retardation factor of ~1 with little or no adsorption while the Li BTC indicates some retardation and attenuation of the pulse with a noticeable tailing effect. The Br pulse was adequately modeled using the CXTFIT linear equilibrium model (Appendix D, Section D.3).

The shape of the Li BTC is consistent with the fact that Li adsorption is not described by a linear isotherm. As discussed in Appendix D, the BTC for a solute with non-linear sorption is often characterized by a steep leading edge and a long tail (self-sharpening BTC). The effect of different initial Li concentrations on the shape of the BTC is also noticeable. Higher concentrations of the solute in the input pulse give a BTC with a higher peak and a narrower pulse; at lower concentrations the pulse broadens as the tail becomes more pronounced and the relative peak concentration drops. A comparison of the 1 ppm Li BTC with a 17.4 ppm Li BTC

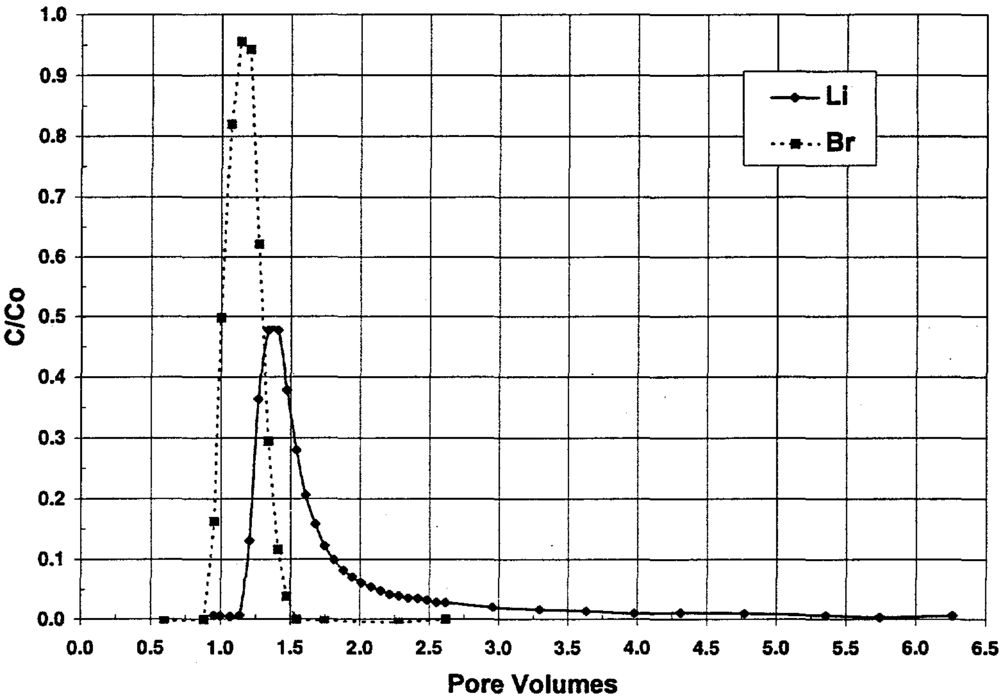

Figure 12. Experimental Li and Br breakthrough curves for a 0.3 pore volume pulse input of 1 ppm Li as LiBr.

from a previous experiment (Cheng *et al.*, Figure C.12, in Siegel *et al.*, 1995), shown in Figure 13, reveals such behavior.

The Freundlich isotherm model of HYDRUS and both the equilibrium and 1-site kinetic models of CXTFIT were used to calculate Li breakthrough curves. When parameter values obtained in the batch studies (cf. Table 2) were used as input to the calculations, none of the models provided an adequate fit to the observed BTC (cf. Figure 14).

Because the kinetic model more closely modeled the observed data, a series of fitted curves were generated using CXTFIT, with a two-site kinetic model. The pore water velocity was the only input value held constant and combinations of D, R, k, and F, were allowed to vary. The results are summarized in Table D.1 in Appendix D. The Li BTC (Li BTC #5) shown in Figure 15 was obtained by allowing only k and F, the fraction of equilibrium sorption sites) to vary. This BTC gave the best fit to the data while still producing parameters that were close to the batch values obtained in batch studies. The curve, however, did not account for the tailing of the Li pulse.

The CXTFIT equilibrium model was used to obtain an apparent retardation factor (R_{ap}) for the Li BTC by using the value of D from the Br BTC and allowing R

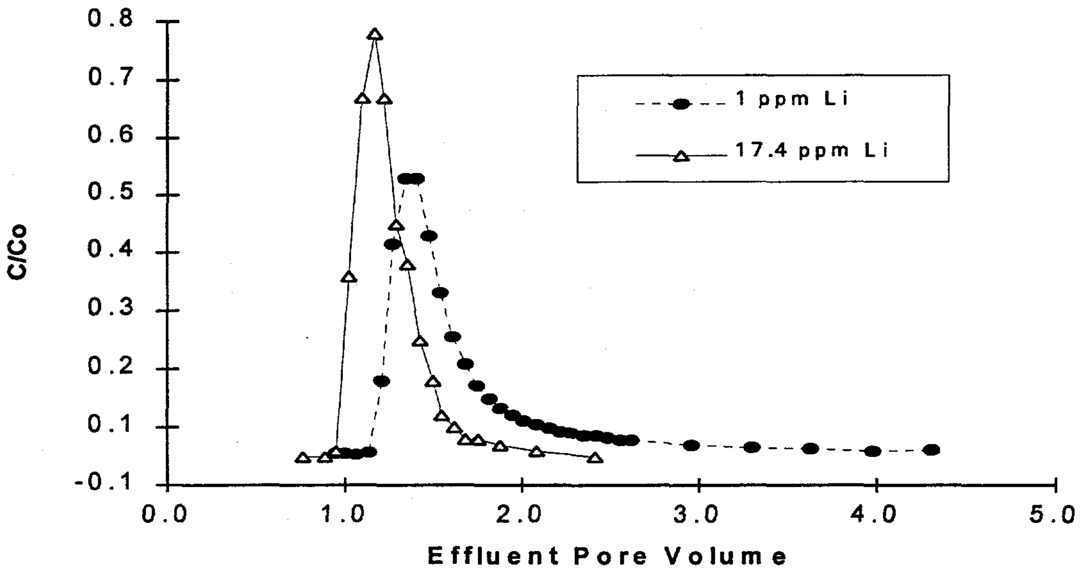

Figure 13. Li BTC's for input pulse concentrations of 1 ppm and 17.4 ppm in laboratory columns of saturated Wedron sand.

to vary. The resulting BTC (Li BTC#3 shown in Figure 15) was symmetrical and greatly overestimated the peak concentration and tracer mass.

Failure to obtain a good correlation between the simple models described above and the experimental data was not unexpected. CXTFIT models adsorption as linear and reversible, whereas the batch studies described in Section 2.2 and 2.3 above have shown that Li adsorption can be modeled by a Freundlich isotherm but is dominantly irreversible. The apparent retardation factor, obtained from the BTC above, however, can be shown to be consistent with the equilibrium and kinetic adsorption parameters obtained in batch studies described in Section 2.2 and 2.3. Kuhn and Peters (1981) developed a relationship between the apparent retardation factor and the number of theoretical mass transfer units along a column (n).

The number of mass transfer units is defined by

$$n = \frac{\rho_b K_d L}{\eta V_w} k$$

where:
V_w = average pore water velocity (cm/min)
R_{ap} = apparent retardation factor of the experimental BTC
R_{eq} = 1 + ($\rho_b K_d / \eta$), the equilibrium retardation factor
k = adsorption rate constant (min^{-1})

Table 2. Adsorption and transport parameters obtained from batch and column studies of Li and Ni

Parameter	Li (1 ppm)	Ni (~ 200 ppm)			
		Fast Column		*Slow Column*	
Batch Studies		pH=6.5	pH=7	pH=6.5	pH=7
R_{eq}	7	36	240	36	240
K_d (m*l*/ g)	1	7	48	7	48
k (min^{-1})	9.5x10^{-5}	6.6x10^{-4}	0.0106	6.6x10^{-4}	0.0106
Freundlich Isotherm					
K	0.55	na		na	
n	0.376	na		na	
Flow Parameters					
D (cm^2/min) from Br	0.005	na			
V_w (cm/min)	0.071	0.24		0.04	
Calculated Parameters					
Kuhn and Peters					
n (mass transfer units)	0.24	0.96	106	5	636
R_{ap}	1.24	6.6	237	25	240
CXTFIT					
D (cm^2/min)	na	0.0073		0.003	
R_{ap}	1.26	16.8		73	

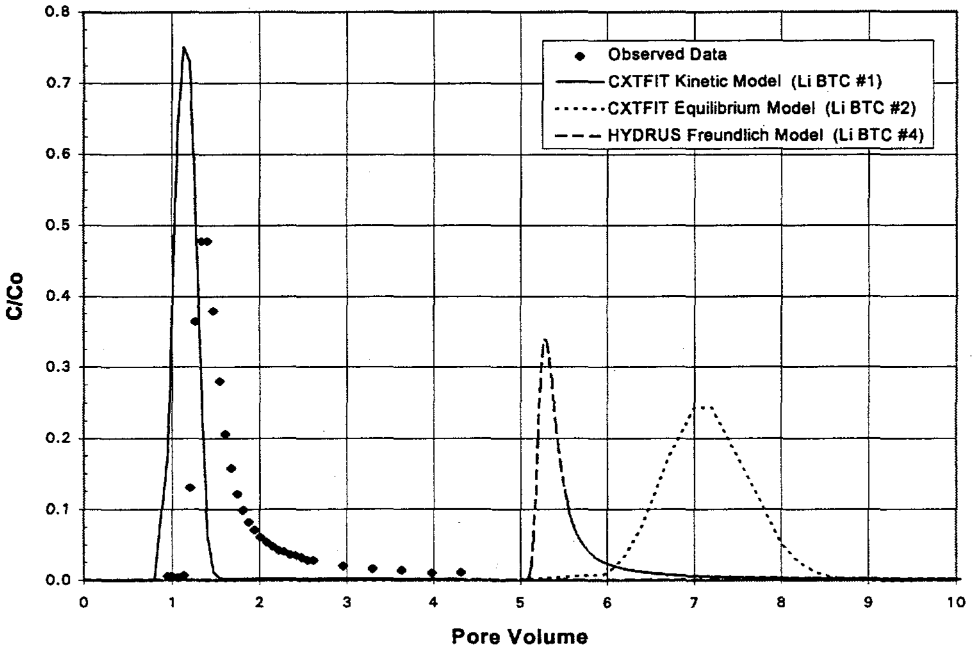

Figure 14. Predicted 1 ppm Li BTC's, using the CXTFIT equilibrium and kinetic models, and the HYDRUS Freundlich model. The constants K_d, k, K, n, obtained from laboratory studies (Table 2), and the value of D obtained from the Br BTC, were used as input for the models. $V_w = 0.071$ cm/min for all models.

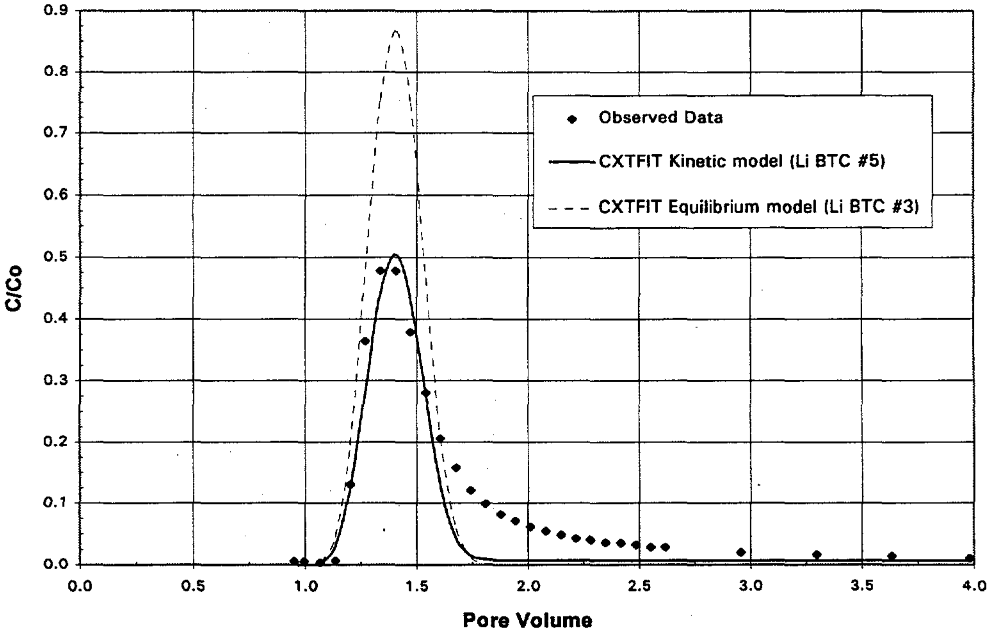

Figure 15. CXTFIT kinetic and equilibrium models fitted to the Li data. Li BTC #5 was calculated with F=0.04 and k=0.0003 min^{-1}; Li BTC #3 was obtained with R =1.28.

and all other variables are as defined previously.

As discussed in Appendix D, application of the analysis of Kuhn and Peters to the data obtained in this study predicts an R_{ap} of 1.24. This compares well to the apparent R values obtained from the CXTFIT kinetic models of 1.26, and to the R_{ap} of 1.28, obtained from the CXTFIT equilibrium model. The good agreement is similar to that obtained for the 17.4 ppm Li tracer pulse shown in Figure **13** as described in Cheng *et al.* (1995). The apparent R values determined from the CXTFIT equilibrium sorption model for the BTC ranged from 1.04 to 1.08 and the apparent R value determined from this analysis was 1.06.

Successful application of this analysis to two separate Li column experiments, suggests that apparent retardation factors for Li pulses can be predicted when adsorption in the column is rate limited and the equilibrium K_d can be calculated from the relevant sorption isotherm. In order to accurately simulate the *shape* of the Li BTC for transport in Wedron sand, however, a transport model which includes some irreversible sorption sites and allows reversible adsorption to be modeled by the Freundlich isotherm and first-order kinetics, would probably be more appropriate.

2.5.3. Ni Transport experiments

Two small (10 cm by 2.5 cm) bench-scale saturated column experiments were conducted using Ni tracer at two flow velocities. Both columns were filled with Wedron 510 sand through a series of screens which insured homogeneous sand distribution in the column. Electrolyte solution (0.001 M NaCl) containing the tracer was pumped through the columns from the bottom up. The effluent lines from the top of the columns were connected to automatic fraction collectors, holding 16 mm sample tubes, to collect the column effluent. The *faster* column experiment was run without provision for monitoring of the effluent pH; the effluent pH measurements were taken on samples which had been sitting in the fraction collector for a minimum of 4 hours. The effluent pH of the *slower* column was monitored using an in-line pH sensor and reference electrode from Microelectrodes Inc. and was recorded every 15 minutes. Table 3 summarizes the properties of the columns. Details of the column design and experimental procedures are described in Appendix E.

Fast Column Results. The Ni BTC from the fast column is shown in Figure 16. Breakthrough of the pulse at C/Co = 0.5 occurred at about 17 pore volumes. The high peak value (C/Co ~1.3) was notable, as well as the tailing of the pulse from the peak to a C/Co value of 1. Once the input pulse was stopped, the effluent Ni concentration dropped rapidly. Most of the measured effluent pH values were about 6.7 (cf. Figure E.2, Appendix E), however, it is likely that the pH was more alkaline

Table 3. Summary of Ni Transport Column Parameters.

	Fast Column	Slow Column
Pore Volume, pv, (m*l*)	16.6	16.9
Mass of sand in column (g)	82.16	82.32
Porosity, η	0.34	0.34
Bulk Density, ρ_b, (g/cm^3)	1.7	1.7
Pore Water Velocity, *v*, (cm/min)	0.24	0.04
Conc. of Ni Tracer (ppb)	182 initial pH=5.8	197.8 (Feed 1) initial pH=5.5 205.4 (Feed 2) initial pH=6.5 201.6 (average)
Amount of Tracer (in pv's)	49.4	78.0
Total Ni input (μg)	149.9	264.1
Total Ni eluted (μg)	112.0	71.8
Ni retained by sand (μg)	37.92	192
Total Ni leached by 2% HNO_3(μg)	2.15	92.1

(>7.2) immediately after elution and then decreased as CO_2 from the air diffused into the solutions (see Section E.2.).

The equilibrium model of CXTFIT was used to fit the Ni breakthrough curve. The input parameters R, D, and the size of pulse were allowed to vary, while the average pore water velocity was held constant. The retardation factor and dispersion calculated from the elution curve were 16.8 m*l*/g and 0.035 cm, respectively. It is obvious that while the model cannot describe the unusually high peak, it does model the leading and trailing edges of the BTC well. A Ni mass balance for the system indicates that ~25% of the total input Ni was retained on the sand. The K_d, calculated from the retardation factor equation for a linear isotherm, was 2.7 ml/g as described in Appendix E. This value is within the previously reported K_d range of 0.5 to 89 m*l*/g in the pH range 5.9 to 7.5 for Wedron sand and a 200 ppb Ni solution (Bryan *et al.*, 1995). In this pH range the Ni sorption edge is very steep, so a slight change in pH will result in a large change in K_d.

Slow Column Results. The BTC from the slow column is shown in Figure 17, along with influent and effluent pH measurements. The BTC from this column is significantly more retarded than the fast one, with Ni first appearing in the effluent after about 57 pore volumes had been eluted. The BTC appears to have two peaks, the first at about $C/C_0 = 0.3$, after which the Ni concentration climbs to a second peak of over $C/C_0 = 0.7$.

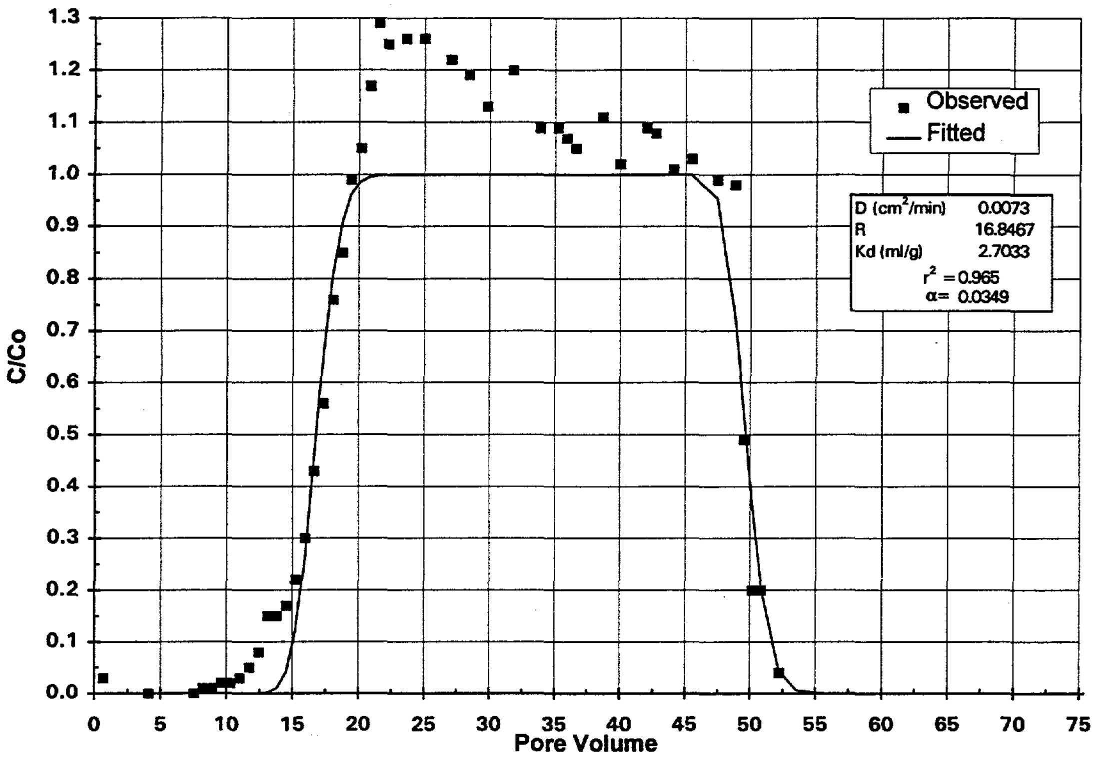

Figure 16. Ni BTC from the fast Ni column experiment. Input Ni pulse concentration of 182 ppb with average pore water velocity of 0.24 cm/min. Fitted Ni BTC using CXTFIT linear equilibrium model is also shown. Values for K_d and α were calculated from R and D, respectively.

The BTC was modeled with the equilibrium model of CXTFIT. The input parameters R and D were allowed to vary and the points which comprised the first peak were excluded. (Analysis with all the points showed that this had a negligible effect on the calculated retardation factor; see Section E.3 in Appendix E). Calculated values of D and R were 71.9 and 0.0043 cm^2/min, respectively. Mass balance calculations showed that about 73% of the total Ni in the input pulse was retained in the column.

Figure 17 shows that the pH of the column effluent changed continuously during the experiment and ranged from about 7.4 to 6.5. The effect of changing column pH on retardation of the Ni pulse is unclear. The K_d, calculated from the retardation factor obtained from the CXTFIT fit of the BTC, is 14.2 m*l*/g. This corresponds to a pH of about 6.6 according to a linear regression between K_d and pH as shown in Figure E.6 in Appendix E. This appears to be a reasonable value based on the range of pH conditions in the column. The same regression equation suggests that the K_d in the column could have ranged from 7 to 48 over the pH range 6.5 to 7.

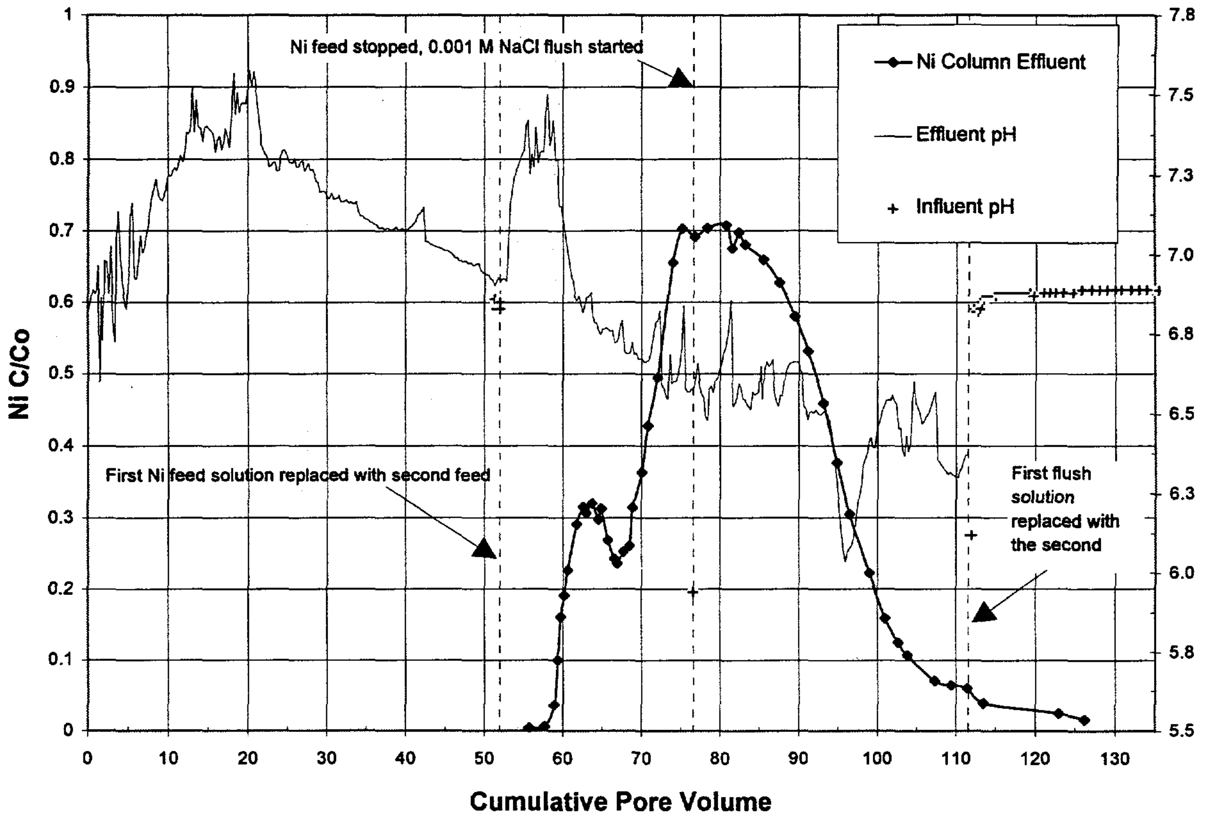

Figure 17. Ni BTC for the slow column experiment. Average input Ni concentration of 201 ppb and a average pore water velocity of 0.04 cm/min. Effluent pH was measured with in-line (closed to the atmosphere) microelectrodes and influent pH was measured by a glass combination electrode with the feed solution open to the atmosphere.

The analysis of Kuhn and Peters (1981) and Relyea (1982) can be applied to predict the apparent retardation, R_{ap}, of the Ni BTC's in a manner similar to that described for Li transport above. The results are summarized in Table 2 for pH's of 6.5 and 7. The apparent retardation factors calculated for the BTC by CXTFIT falls within the range predicted from the relationship between n, the number of mass transfer units and the apparent retardation factor R_{ap}. The analysis is also applied to the fast column experiments assuming that the pH ranged from 6.5 to 7 in that column. Again, the R_{ap} calculated from the BTC falls within the range of predicted retardation factors. A more detailed analysis is given in Appendix E, Section E.4.

2.6 Measurements of Ni Transport Through the Los Alamos Caisson

During FY94, staff from Sandia National Laboratories worked with staff from Los Alamos National Laboratory (LANL) to design and implement sampling and analysis procedures for the caisson experiment. Water samples are collected and analyses of Li and Br are made by LANL staff; Ni analyses are made by SNL staff using the procedures described in Siegel *et al.* (1995, Appendix E). A review of the history of the fielding of the caisson experiment and descriptions of pH measurement and water sampling techniques are found in Appendix F to this letter report.

Figure 18 shows the caisson geometry and indicates the locations of working solution samples. In addition to the 7 functioning samplers in the middle of the caisson, approximately 150 ceramic cup samplers in the bottom plate worked. The combined flow rate of these bottom samplers was far less than the influent flow rate, indicating that much of the effluent may have flowed through gaps and fractures in the bottom plate. In addition, it was observed that the water was not distributed uniformly over the top of the sand; a disproportionately large amount of fluid flowed from the center of the sprinkler system.

On June 1, 1994, a continuous pulse of 200 ppb Ni in a background electrolyte of Los Alamos tap water was added to the caisson influent. This influent concentration was maintained until July 22 (51 days), and then Ni-free tap water

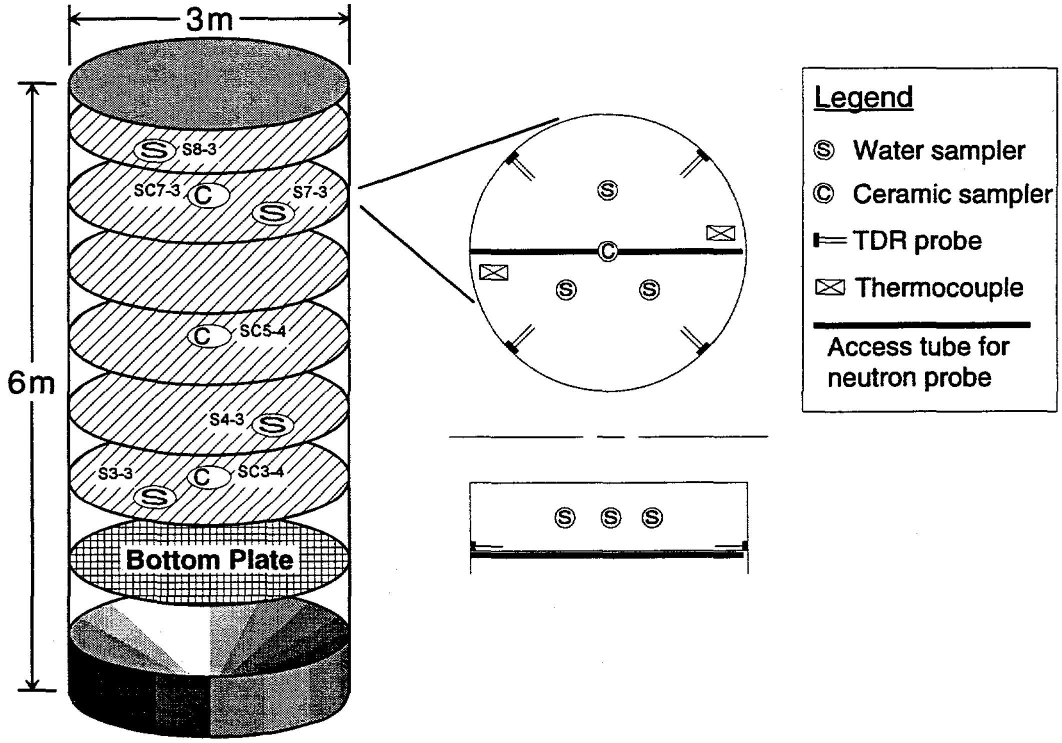

Figure 18. Caisson geometry and instrumentation. Original design specifications called for 4 samplers per level, but many failed; working samplers are indicated in the diagram.

was re-introduced. On August 2 (elapsed time, *t* = 62 days), a LiBr pulse was initiated; the concentration used was ~9 ppm Li (~100 ppm Br). The Li pulse ended August 4; flushing continued until August 18 (*t* = 78 days), at which time the experiment was terminated. An influent flow rate of approximately 1.8 gal/min was maintained over the course of the experiment. Water samples were collected daily from each working sampler in the 6 upper levels, from the influent, from individual bottom samplers and from a hose (composite sample) draining all of the bottom samplers. The samples represent instantaneous or 24-hour accumulations depending on the sampler flow rate.

Over the course of the Ni pulse, the pH was measured on 609 water samples. Most of these were taken from ceramic samplers on the bottom plate; others were composite samples from the open-ended drain hose. The pH of both types of samples, measured immediately after collection ranged from approximately 8.2 to 8.4. In-line pH measurements, taken twice daily from a free-flowing hollow fiber sampler (S8-3) near the top surface were more acidic but more scattered (approximately 6.6 - 8.5) as shown in Figure F.2, Appendix F. Interpretation of the pH values obtained in this manner is difficult; degassing of CO_2 occurs very rapidly from the water samples. The pH of samples collected during a test run prior to the Ni pulse rose from ~7 to ~8 within seconds of being exposed to ambient atmosphere (Table F.1, Appendix F). These measurements suggest that the *in-situ* pH may have been 7 or less. This is consistent with results from the caisson influent and local tap water, both of which were near pH = 7 prior to equilibrating with the atmosphere.

The results of Ni analyses for 384 water samples are summarized in Table F.2, in Appendix F. Ni breakthrough curves for 3 individual samplers, influent (surface water), and composite bottom water are shown in Figure 19. Additional profiles can be found in Appendix F. Ni breakthrough (the first appearance of elevated Ni in the collected samples) occurred at different times for each of the three water samplers. Ni was detected at SC3-4, along the central axis of the caisson after 4 days, and at bottom sampler C-26, 50 cm from the central axis, 4 days later. Breakthrough occurred at bottom sampler D-58, along the edge of the caisson, 8 days after that. These results suggest that flow was channeling through the center of the caisson. This suggestion is supported by the hydrological data. TDR (Time Domain Reflectometry) data collected during the last few weeks of the experiment indicate that the edges of the caisson were drying out (E. Springer, Los Alamos National Laboratory, pers. comm.). As discussed in detail in Appendix F, examination of other BTC's confirms that channeling is occurring; break-though is a function not only of depth, but also of location in the caisson.

Several of the Ni breakthrough curves have a steep leading edge, but flatten and level off well below the influent Ni concentration. Steady-state or near-steady-

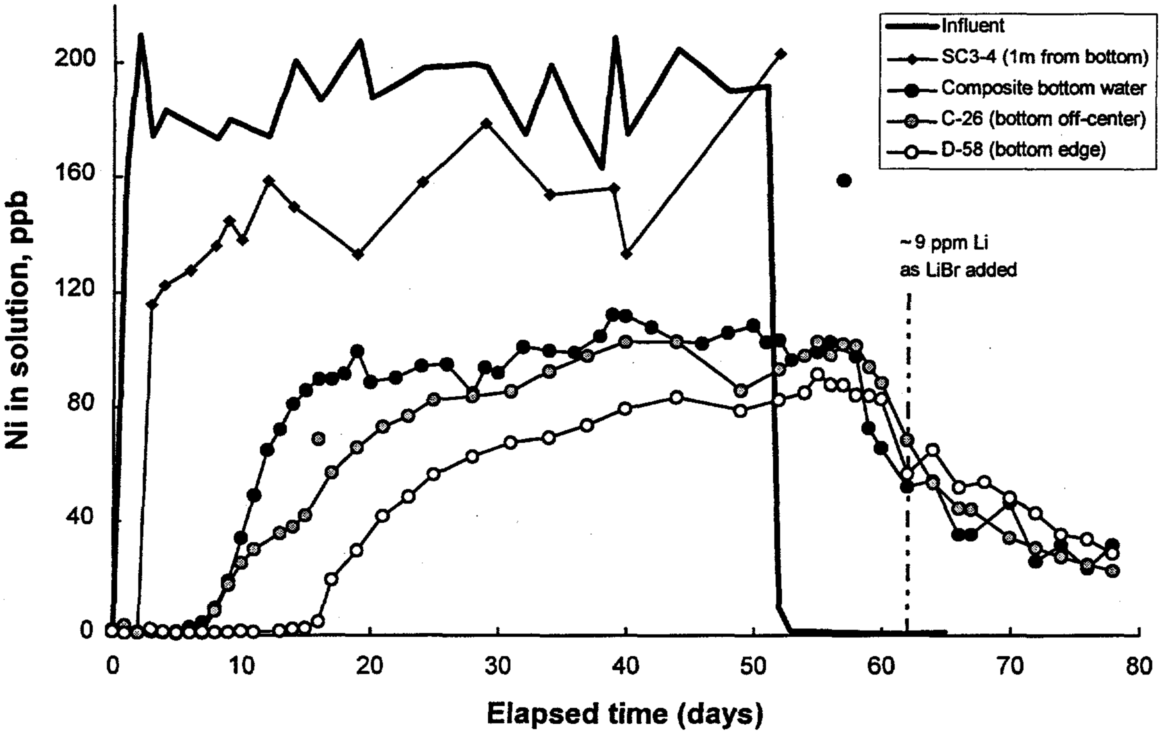

Figure 19. Breakthrough curves for several samplers in the caisson.

state conditions are reached, but, as Ni concentrations are well below influent concentrations, Ni adsorption sites in the sand have not been saturated. The observed BTCs may be caused by mixing between Ni-rich waters permeating outward from the more fluid-saturated central channel and the slower moving Ni-poor waters percolating downward from the top of the caisson. Alternatively, this pattern might be caused by adsorption kinetic effects. The adsorption kinetics studies described in Appendix B of this report suggest that Ni adsorption is occurring onto two different sites in the sand, with very different reaction rates and degrees of reversibility. The Ni concentration will only rise to that of the influent when all of the low-energy (slow adsorption rate) or irreversible sorption sites are filled. Saturation of these low-energy sites may not have occurred during the Ni pulse.

Ni breakthrough occurred more rapidly than predicted by laboratory batch adsorption experiments (Siegel *et al.*, 1995). Rather than taking months to break through, Ni showed up in the caisson effluent within days. Channeling through the center of the caisson may be responsible for this, allowing the Ni to bypass most of the sand, and effectively producing a smaller diameter column with a greatly increased flow rate. In addition, the rapidity of breakthrough might also indicate adsorption reaction rates are slower than expected from the pH measured from the bottom samplers. Batch Ni adsorption experiments described in Appendix B of this paper indicate that both the rate and the degree of Ni adsorption are very pH-sensitive and decrease markedly from pH 7 to pH 6.5. If the caisson pH is below 7, as suggested by the in-line pH electrodes, then the sorption equilibrium was probably not reached.

If Br acted as a conservative tracer in the caisson, then the flow rates during the second LiBr pulse within the caisson ranged from approximately 0.2 to 0.7 cm/min (cf. Table F.3, Appendix F). If it is assumed that the velocity of that LiBr pulse (introduced on day 62 of the experiment) represents the water velocity during the elution of the Ni pulse, then the apparent retardation factors measured for Ni at the working samplers in the caisson ranged from approximately 12 to 20 (cf. Table F.4).

3. Discussion

3.1. Thermodynamic Models for Ni Adsorption by Goethite, Quartz and Kaolinite

3.1.1 Triple-layer model for goethite

Adsorption onto goethite is a promising analog for Ni adsorption onto Wedron 510 sand, giving an adsorption edge which closely resembles that for the sand. Of the two other important components of the sand, kaolinite also has the potential to explain the observed patterns of Ni adsorption, whereas quartz is comparatively inert over the pH range of interest. A triple-layer model of surface complexation of Ni^{2+} onto goethite was developed in Siegel *et al.* (1995) based on a single set of Ni adsorption data at a presumed surface concentration of 6 m^2/l in 0.001 M NaCl partially equilibrated with air. Aqueous Ni-carbonato species thought to be favored at high pH were eliminated from consideration by setting $P_{CO_2} = 10^{-6}$ atm in the model, and the equilibrium constant for adsorption was adjusted to obtain a visual best-fit to the experimental data, giving $\log K_{fm}(SONi^+) = -1$.

In Appendix A, Section A.4, more rigorous and complete models for Ni adsorption by goethite, kaolinite and quartz are presented. An internally consistent set of equilibrium constants for plausible aqueous Ni species was developed. Formation constants (K_{fm}) for expected aqueous complexes in the system H_2O–Na^+–Cl^-–CO_3^{2-}–Ni^{2+} are presented in Table A.4, and corresponding free energies of formation (ΔG_f°) are presented in Table A.5. The constants proposed for $NiHCO_3^+$ and $NiCO_3^\circ$ are two orders magnitude lower than those used most commonly by other researchers. The latter were proposed by Mattigod and Sposito (1977) and were not based on experimental work with Ni-carbonato complexes, but instead were predicted with the electrostatic ion-pairing model of Kester and Pytkowicz (1973). The constants proposed here are based in part on Ni hydroxide solubility data and estimates of P_{CO_2} values for "CO_2-free" batch systems. As discussed in detail in Sections A.4.3.1 and A.4.4.2, measured Ni concentrations in saturated systems agree with those calculated values only if the values of the Ni-carbonato complexes suggested by Mattigod and Sposito (1977) are reduced by two orders of magnitude. As shown in Figures A.13 and A.14, use of the reduced constants in speciation calculations extends the predominance of Ni^{2+} to nearly pH 8.5, so that Ni-carbonato species are of little concern over the pH range of interest for adsorption (pH 5 – 8). These new values are considered provisional until they can be verified with experiments at higher values of P_{CO_2}. All Ni adsorption modeling performed in this study uses the reduced values of the Ni-carbonato complexation constants. Had the larger values of Mattigod and Sposito been used, calculated adsorption would have been substantially lower at high pH, inconsistent with experimental observations.

Thermodynamic calculations were carried out with HYDRAQL 94 (Ward, 1995), a revised version of HYDRAQL (Papelis *et al.*, 1988). The original program was modified by fixing an error in a subroutine used to calculate pH-adsorption edges, permitting overall charge-balance optimization, and including the Davies activity correction for aqueous species involved in surface reactions. The modified version is documented in Ward (1995). FITEQL 2.0 (Westall, 1982), a generalized least-squares non-linear regression program, was used to extract formation constants from the experimental data.

Two triple-layer surface-complexation models have been developed for simulating Ni adsorption onto goethite. The adsorption stoichiometry is presumed to be 1:1, forming an $SONi^+$ inner-sphere complex, as is typical for adsorption of divalent cations onto insoluble oxides (Dzombak and Morel, 1990). As discussed in Siegel *et al.* (1995), other stoichiometries were investigated but rejected because of poorer fits to the experimental data. A list of parameters for the triple-layer surface-complexation model (Davis *et al.*, 1978), their definitions and values, and their sources is presented in Table 4. FITEQL was used to extract optimum values of the inner-layer capacitance (C_1), and formation constants for electrolyte binding (K_{fm}(SO-Na) and K_{fm}(SOH_2-Cl)) from subsets of the potentiometric titration data on goethite #5 (Figure 1) as discussed in Section A.4.4.1. Formation constants for the protonated and deprotonated surface species ($K_{fm}(SOH_2^+)$ and $K_{fm}(SO^-)$) were taken from the work of van Geen *et al.* (1994). Methods used to obtain the constants are discussed in detail in Section A.4.4.1 of Appendix A.

The simpler of the two models is a single-site model similar to that proposed in Siegel *et al.* (1995). Using FITEQL, values for $K_{fm}(SONi^+)$ were extracted from the Ni-adsorption data from goethite batch #5. Only data lying within the region of the adsorption edge were considered (pH 4.8–7.4 for ~55 m^2/*l*, and pH 5.1–7.6 for 5.4 m^2/*l* systems), and log [H_2CO_3] was fixed at –4.97 for air-equilibrated systems and –6.25 or –5.32 for "CO_2-free" systems with ~55 m^2/*l* or 5.4 m^2/*l* goethite ($P_{CO_2} = 10^{-4.78}$ and $10^{-4.13}$), respectively. The adsorption edges calculated using the weighted average $K_{fm}(SONi^+)$ from the two optimizations at the two surface areas are displayed in Figure 20a. It can be seen that the single site model performs poorly at the lower surface concentration; its slope is too steep, passing to the low-pH side of all the data above 30% adsorbed at 5.4 m^2/*l* goethite concentration.

The decrease in slope of the adsorption edge with a decrease in surface concentration suggests that more than one adsorption site may be present on the goethite surface. The alternative is that a subset of the surface sites have a high affinity for the ion of interest. As the high-affinity sites become mostly occupied, further adsorption must occur at less favorable sites and thus requires a larger increase in pH to effect the same change in amount adsorbed. This decreases the slope in the pH-adsorption edge at higher pH. If the affinities of the two types of sites differ greatly, the adsorption "edge" will have a plateau where all of the high-affinity sites have been occupied but where the pH is too low for significant adsorption by the low-affinity sites.

HYDRAQL 94 was used to implement a two-site model, with goodness-of-fit determined by visual comparison of the model output with the experimental data. The model is similar to that used by Dzombak and Morel (1990) for hydrous ferric oxide, in which two surface components are required: type I (SO^IH) for the high-affinity sites and type II ($SO^{II}H$) for the total number of sites. The results of the two-site model with visually optimized parameters are summarized and illustrated in Figure **20**b. The model was optimized at $P_{CO_2} = 10^{-3.5}$ atm to produce essentially the same adsorption edge at ~55 m^2/*l* as was obtained from the single-site model while at the same time providing the best-looking fit to the 5.4 m^2/*l* data. Its superior fit at the lower surface area is readily apparent in comparison to the single-site model. The fraction of high-affinity (SO^IH) sites was ~0.04, about the same as the value of 0.025 accepted by Dzombak and Morel (1990) for hydrous ferric oxide after their comprehensive survey of the literature.

The performance of the two goethite models with respect to a decrease in P_{CO_2} is illustrated by the dotted lines in Figure 20b, obtained when P_{CO_2} was decreased to its apparent value appropriate for each surface concentration under nominally CO_2-free conditions. Both models predict decreased adsorption at decreased P_{CO_2}, with the two-site model being slightly more sensitive. The two models differ in their predictions at high pH, where Ni speciation is modeled to undergo a transition from

Table 4. Parameters and values for the triple-layer surface-complexation models of Ni adsorption onto goethite.

Parameter	Value	Source
Inner-layer capacitance (C_1)	1.20 F/m^2	This work.
Outer-layer capacitance (C_2)	0.20 F/m^2	Davis *et al.* (1978)
Site density	2.31 sites/nm^2	As advocated by Davis and Kent (1990).
Fraction of high Ni affinity sites	0.038	This work (two-site model only).

Components: SOH, H^+, Na^+, Cl^-, carbonate, Ni^{2+}

Formation constants of surface species			Both models		Source
$K_{fm}(SO^-)$	$= \dfrac{[SO^-][H^+]}{[SOH]} \cdot \gamma_{H^+} \cdot e^{(-\psi_0)F/RT}$	=	$10^{-9.9}$		van Geen *et al. (1994)*
$K_{fm}(SOH_2^+)$	$= \dfrac{[SOH_2^+]}{[SOH][H^+]} \cdot \dfrac{1}{\gamma_{H^+}} \cdot e^{(\psi_0)F/RT}$	=	$10^{7.9}$		van Geen *et al. (1994)*
$K_{fm}(SO\text{-}Na)$	$= \dfrac{[SO-Na][H^+]}{[SOH][Na^+]} \cdot \dfrac{\gamma_{H^+}}{\gamma_{Na^+}} \cdot e^{(\psi_\beta - \psi_0)F/RT}$	=	$10^{-8.90}$		This study.
$K_{fm}(SOH_2\text{-}Cl)$	$= \dfrac{[SOH_2\text{-}Cl]}{[SOH][H^+][Cl^-]} \cdot \dfrac{1}{\gamma_{H^+}\gamma_{Cl^-}} \cdot e^{(\psi_0 - \psi_\beta)F/RT}$	=	$10^{8.84}$		This study.
carbonate = H_2CO_3:					
$K_{fm}(SOCO_2^-)$	$= \dfrac{[SOCO_2^-][H^+]}{[SOH][H_2CO_3]} \cdot \gamma_{H^+} \cdot e^{(-\psi_0)F/RT}$	=	$10^{-4.23}$		van Geen *et al. (1994)*
carbonate = CO_3^{2-}:					
$K_{fm}(SOCO_2^-)$	$= \dfrac{[SOCO_2^-]}{[SOH][H^+][CO_3^{2-}]} \cdot \dfrac{1}{\gamma_{H^+}\gamma_{CO_3^{2-}}} \cdot e^{(-\psi_0)F/RT}$	=	$10^{12.45}$		van Geen *et al. (1994)*
			One-site	Two-site	
$K_{fm}(SO^{II}Ni^+)$	$= \dfrac{[SO^{II}Ni^+][H^+]}{[SOH][Ni^{2+}]} \cdot \dfrac{\gamma_{H^+}}{\gamma_{Ni^{2+}}} \cdot e^{(\psi_0)F/RT}$	=	$10^{0.613}$	$10^{-0.5}$	This study.
$K_{fm}(SO^{I}Ni^+)$	$= \dfrac{[SO^{I}Ni^+][H^+]}{[SO^{I}H][Ni^{2+}]} \cdot \dfrac{\gamma_{H^+}}{\gamma_{Ni^{2+}}} \cdot e^{(\psi_0)F/RT}$	=	n/a	$10^{-0.5}$	This study.

[ ] denotes concentrations; γ is the activity coefficient for the indicated ion, calculated using the Davies equation (Davies, 1962); F is Faraday's constant (96480 C/mole e^-); R is the ideal gas constant; T is the absolute temperature; ψ_0 and ψ_β are the potentials at the surface and β plane, respectively.

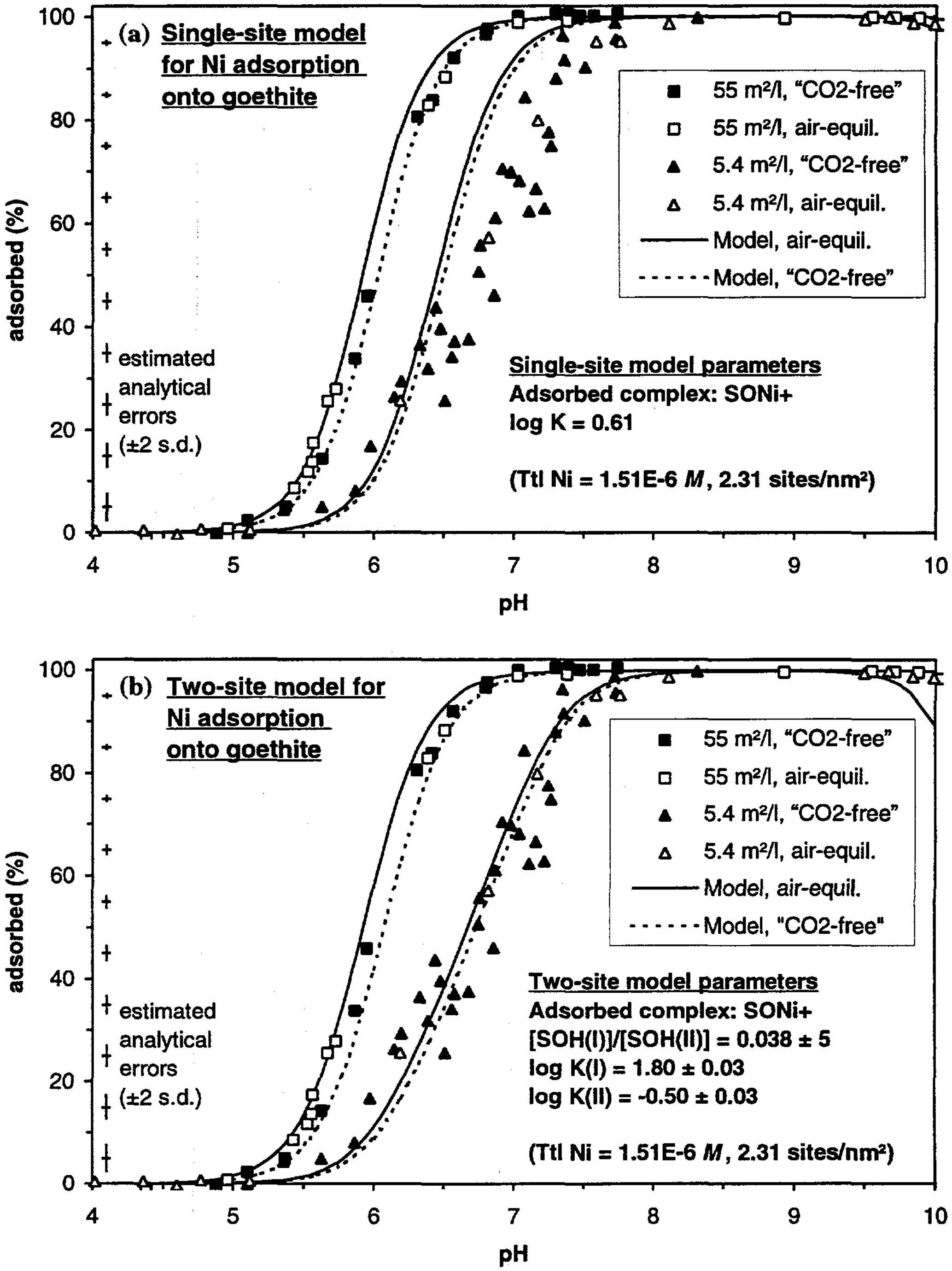

Figure 20. Optimized models of Ni adsorption onto goethite. a) Single-site model, with parameter fitting using FITEQL for each surface concentration separately. The average association constant is heavily weighted toward the 55 m^2/*l* curve. b) Two-site model calculated using HYDRAQL 94 and optimized visually. Quoted precisions are those which produce a perceptible worsening of fit to the experimental data, but carry no rigorous statistical significance.

predominantly Ni^{2+} to $NiCO_3^\circ$ and then to $Ni(CO_3)_2^{2-}$. The single-site model is more consistent with the experimental data, showing only slightly decreased adsorption at pH 10. The two-site model predicts a significant decrease in adsorption at pH for the low-goethite systems.

3.1.2. Triple-layer models for quartz and kaolinite

A preliminary surface complexation model for quartz was developed based on potentiometric and Ni adsorption studies carried out on Min-U-Sil 5, a reference quartz, at Sandia and at the British Geological Survey (Mark Crawford, letter to CHEMVAL2 participants dated 15 November 1993). Surface potentiometric data for Min U Sil are described in Ward *et al.* (1995a) and Ward (1995). A model for protolysis and electrolyte binding was developed using FITEQL to optimize $K_{fm}(SO^-)$, $K_{fm}(SO\text{-}Na)$, and C_1, assuming a site density of 6 nm^{-2} and a $pH_{ZPC} = 2$. As discussed in detail in Appendix A, Section A.4.5, it provides a better fit to our experimental data than that of the more commonly used model of Rea and Parks (1990) and was used as the basis for a model of Ni adsorption.

The triple-layer model for Ni adsorption by quartz is described in detail in Section A.4.5.2. Model parameters are listed in Table 5, below. In the model, Ni was assumed to form a unidentate outer-sphere complex ($SO\text{-}Ni^+$). A pH_{ZPC} of 2 was assumed, permitting the log K_{fm} values for SOH_2^+ and $SOH_2\text{-}Cl$ to be estimated. The model was visually optimized for the adsorption data set obtained in 0.01 M, giving a value for log $K_{fm}(SO\text{-}Ni^+) = -7.7$. As can be seen in Figure A.22, Appendix A, the model does not perform well. Qualitatively, the model exhibits the required dependency on ionic strength and total carbonate, but the slopes of the adsorption curves are poorly simulated especially at low ionic strengths. Under air-equilibrated conditions ($P_{CO_2} = 10^{-3.5}$ atm), calculated adsorption began declining above pH 8.1 after reaching a maximum of only 50%, whereas observed adsorption peaked at pH 9.3 at ~85%. Potential avenues for improvement of the model include modifying the stoichiometry of the adsorbed complex, adding additional adsorbing complexes involving the predominant Ni-bearing species at high pH, and considering variations in the affinities of adsorption sites for Ni^{2+} and Na^+ at near-neutral pH.

Attempts to develop a surface complexation model for kaolinite were more successful and are described in Appendix A, Section A.4.6. It is based on experimental work described above and previous work by Riese (1982), in which kaolinite flakes are modeled as a mixture of silanol and aluminol sites exposed in a 1:1 ratio. Model parameters are summarized in Table 5, below. The formation constant for the outer sphere complex $SiO\text{-}Ni^+$ was taken from the quartz model and Nickel was assumed to form an inner-sphere complex with the aluminol sites. With the aforementioned assumptions, the value of $K_{fm}(AlONi^+)$ was found by visual

Table 5. Triple-layer surface-complexation model parameters for quartz and kaolinite.

Surface	Site density (nm^{-2})	C_1 (F/m^2)	log K_{fm} (SO^-)	log K_{fm} (SOH_2^+)	log K_{fm} (SO-Na)	log K_{fm} (SOH_2-Cl)	log K_{fm} (SO-Ni^+)
Quartz (O.S.)	6	2.0	-6	-2	-7	-3	-7.7
Kaolinite	6*	2.4*					
>SiOH (O.S.)			-6.25*	NI	-3.5*	NI	-7.7
>AlOH (I.S.)			-7.4*	NI	-7.4*	NI	-2.1

O.S = outer-sphere; I.S. = inner-sphere. *Constants from Riese (1982). Ratio of alumina to silanol sites is 1:1. The value of C_2 is taken to be 0.2 F/m^2.

NI = not included in model

optimization using HYDRAQL 94 to be $10^{-2.1}$, over five orders of magnitude greater than that for the silanol sites. The fitted adsorption edge can be found in Figure 24 in the next section.

The model presented here differs from that of Riese in that at pH > 3, the complexes SOH_2^+ and SOH_2-Cl were assumed to be unimportant for silanol sites, analogous to the behavior of quartz surfaces at pH > pH_{ZPC}, and thus were omitted. As a result of this omission, the simplified kaolinite model used here lead to a low estimate of the intrinsic formation constant, K_{fm}($SONi^+$) and overestimates of the amount of kaolinite required to match Ni adsorption edges. Another important assumption in the model concerns the surface area of kaolinite: the effective surface area for the kaolinite in the Ni-adsorption experiments is taken to be 10 times the BET-measured surface area (246 m^2/g). This is based on studies of the kaolinite surface area accessible to protons and hydroxyls in solution (Xie and Walther, 1992). Additional discussion of the limitations of the model can be found in Section A.4.6 and in Ward (1995).

3.2. Conceptual Model for Adsorption of Ni and Li by Wedron Sand

The Ni and Li adsorption experiments described in this report were carried out to quantify the contribution of individual mineral constituents to the bulk adsorption properties of Wedron 510 sand. The adsorption properties of the bulk sand can be summarized as follows: Li adsorption by Wedron sand is relatively low and not strongly pH-dependent. With a 100 ppm total Li concentration, only a few % is adsorbed over the pH range 4-10 and a broad peak in adsorption occurs at around pH = 7–7.5. Ni adsorption by the sand is characterized by a sharp (strongly pH-dependent) adsorption edge with the 50% adsorption occurring at approximately pH 6.5 at a 1g/1m*l* solid:solution ratio. Above pH 7, nearly 100% of the Ni is adsorbed. The Ni adsorption edge is shifted to higher pH by high concentrations of Li (100 ppm), suggesting that Li competes with Ni for some adsorption sites.

Figure 21 summarizes our current conceptual model for adsorption of Li and Ni by the sand. The three most abundant minerals in the sand are quartz, kaolinite, and goethite. Quartz, accounting for more than 98% by weight of the total material, occurs as large grains coated with kaolinite and goethite. Its contributions to the total surface area and adsorption properties of the batch systems are probably small. Previous work (Siegel *et al.*, 1995) showed that adsorption of Ni by quartz (Min-U-Sil 5) is low, and that the sorption edge is at considerably higher pH than that of the sand.

The contribution of quartz to Li adsorption in the sand is also probably small. Chardymskaya *et al.* (1987) reported distribution coefficients that are orders of magnitude lower than that observed for Wedron sand. At concentrations of 10-100 ppm Li, they report only 0–10 ng Li (<0.1%) adsorbed per gram quartz. In addition, the shape of the adsorption curve for Li onto quartz is different from that for the

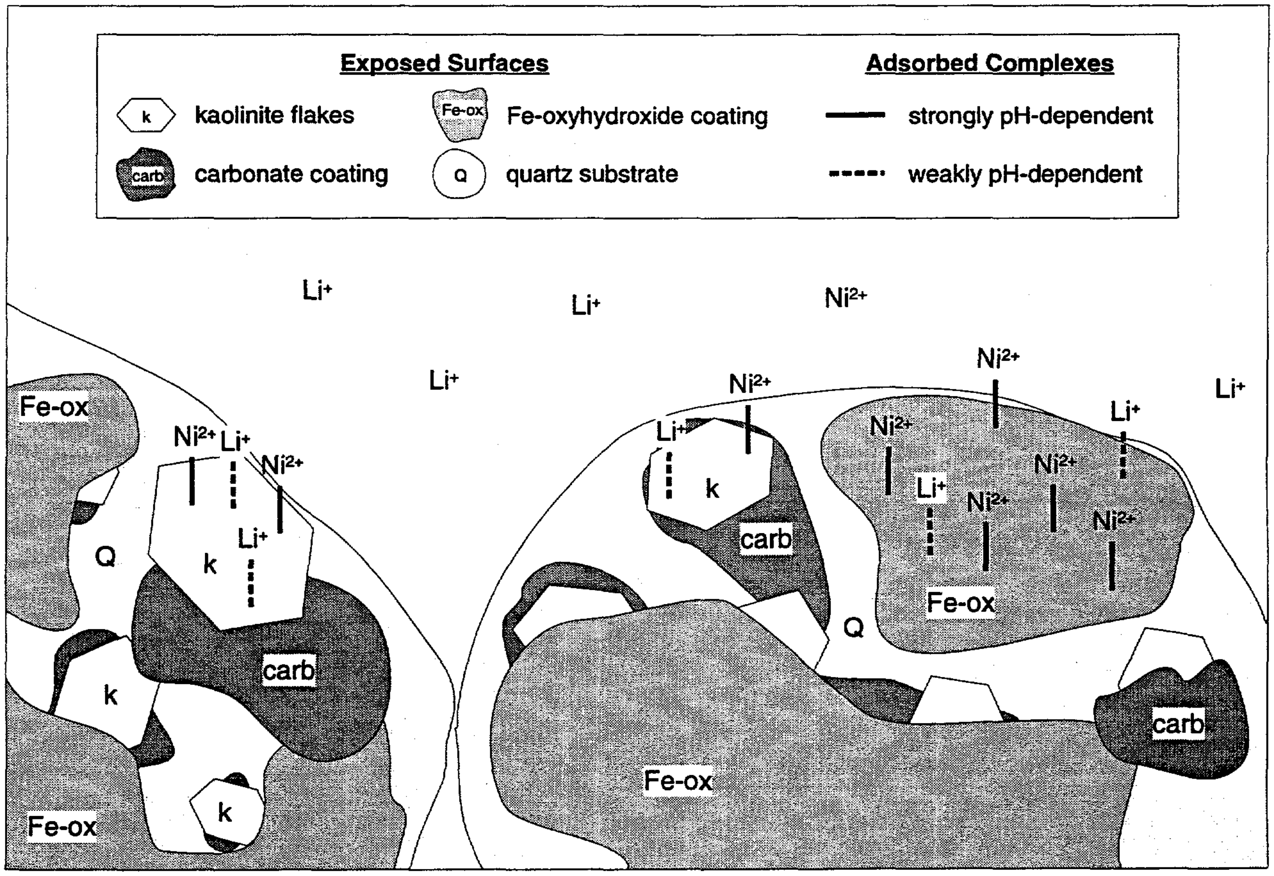

Figure 21. Conceptual model for adsorption of Ni and Li by Wedron 510 sand.

sand; the Li–quartz adsorption curve reported by Chardymskaya *et al.* increases steadily with pH rather than having a maximum around pH = 7 as observed for the sand.

Goethite as an Analog for Wedron 510 Sand. Iron oxyhydroxide has been visually identified in the sand as a coating on quartz grains, as shown in Figure 21. This coating is pervasive; the Fe oxyhydroxides give raw Wedron sand a slightly yellowish tint, compared to acid-washed sand. Although only 80 ppm Fe can be leached from the sand with 6 N HCl, goethite or an amorphous iron oxyhydroxide probably dominates Ni adsorption and accounts for a sizable fraction of the total surface area of the sand. The strongly pH-dependent Ni adsorption edge of the sand matches that of goethite for reasonable goethite concentrations and specific surface areas.

The two triple-layer surface-complexation models for goethite discussed in Section 3.1.1 were calibrated to simulate the behavior of Wedron sand under partially air-equilibrated conditions ($P_{CO_2} = 10^{-3.5}$ atm below pH 7.5) with a total Ni concentration of 130 ppb. For the single-site model, the optimal concentration of surface sites was found using FITEQL: Based on an initial guess for the goethite surface area, FITEQL optimized the total SOH concentration to obtain the best fit to the sand adsorption edge. For the two-site model, the goethite concentration (surface concentration and concomitant values for total $SO^{I}H$ and $SO^{II}H$) were adjusted manually until a visual best-fit to the adsorption edge was obtained. The results are shown in Figure 22. The optimum goethite concentrations for the single-site model and the two-site model were 28 m^2/l and of 37 m^2/l, respectively.

The abilities of the two models to simulate the effect of changes in Ni concentration and ionic strength on Ni adsorption were compared next. Within the scatter of the data, Ni adsorption by the sand at total Ni concentrations of 130 and 230 ng/m*l* ($10^{-5.66}$ and $10^{-5.41}$ M) was identical. As illustrated in Figure 22, the single-site model was virtually unaffected by increasing total Ni from 130 to 230 ng/m*l*, whereas the two-site model exhibited slightly decreased adsorption (%). (In the figure, the adsorption curve for the single-site model was shifted by less than a line-width when the Ni concentration was increased from 130 ng/m*l* to 230 ng/m*l*, so only a single curve is plotted.) The difference in model behavior is due to the relative abundance of adsorption sites in the single-site model, whereas the two-site model shows slightly decreased adsorption due to the scarcity of high-affinity sites.

The effect of a change in ionic strength on adsorption is shown in Figure 23. Ni adsorption on sand was diminished when the ionic strength increased from 0.001 M to 0.1 M, shifting the adsorption edge to higher pH by ~0.5 units. Although the experimental data are somewhat scattered, the single-site model appears to most accurately simulate this shift, with the two-site model predicting a somewhat smaller shift.

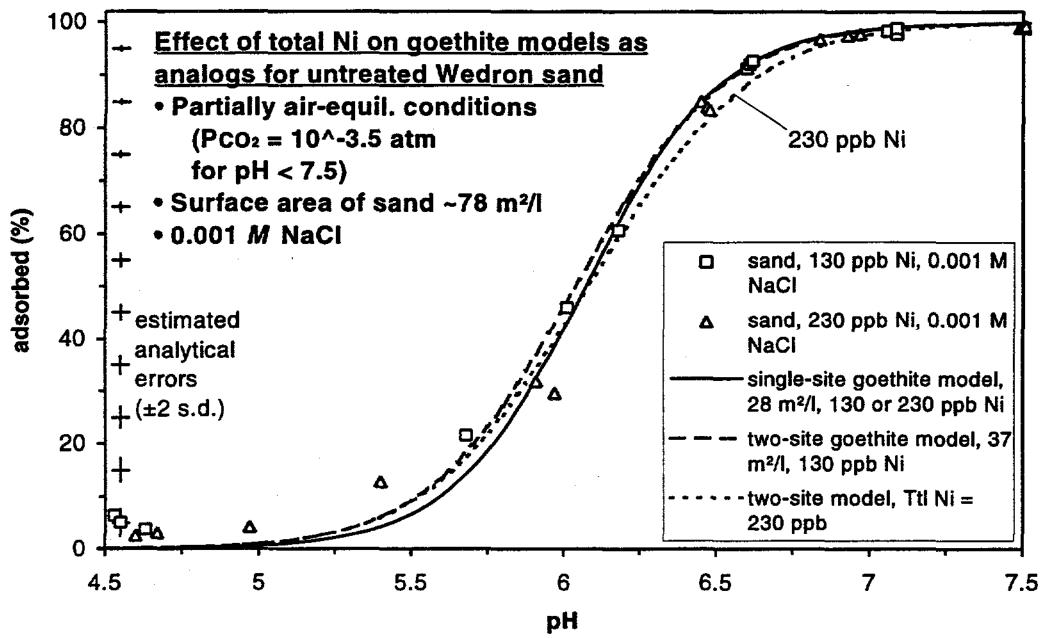

Figure 22. Performance of goethite-model analogs for Wedron sand under conditions of changing total Ni.

About 3% Li adsorption occurred in a 60 m^2/*l* goethite suspension over the pH range of 4-10 with an initial Li electrolyte concentration of 100 ppm. Li adsorption by goethite is independent of pH whereas adsorption by the sand exhibits slight pH-dependence. The difference in the shape of the adsorption curves suggests that goethite alone cannot be responsible for Li adsorption by the sand.

Evidence for Kaolinite in Wedron 510 Sand. Kaolinite has been identified in the fine fraction of the sand by XRD, and visually identified on the grain surfaces by SEM (Ward *et al.*, 1995). Its contribution to the total surface area of the sand is not known. The sand contains 0.28% Al by weight; some fraction of this may be substituting for Si in the quartz lattice, or occurring structurally in minerals other than kaolinite. The scarcity of cations in the sand, other than Si and Al (Table 5, Siegel *et al.*, 1995), suggests that most of the Al is in kaolinite rather than in another clay mineral. From the molecular weight of kaolinite, we can estimate that as much as 1.38% kaolinite by weight may be present, and it is probable that this mineral contributes significantly to the adsorption properties of the sand.

The triple-layer model for Ni adsorption presented in Section 3.1.2 was used to assess the amount of exposed kaolinite required to mimic the Ni adsorption edges measured for untreated and acid-washed Wedron sand. Calculations were carried out using HYDRAQL 94, and goodness of fit was assessed visually; results are portrayed in Figure 24. As discussed in Appendix A.4.6, recent studies have

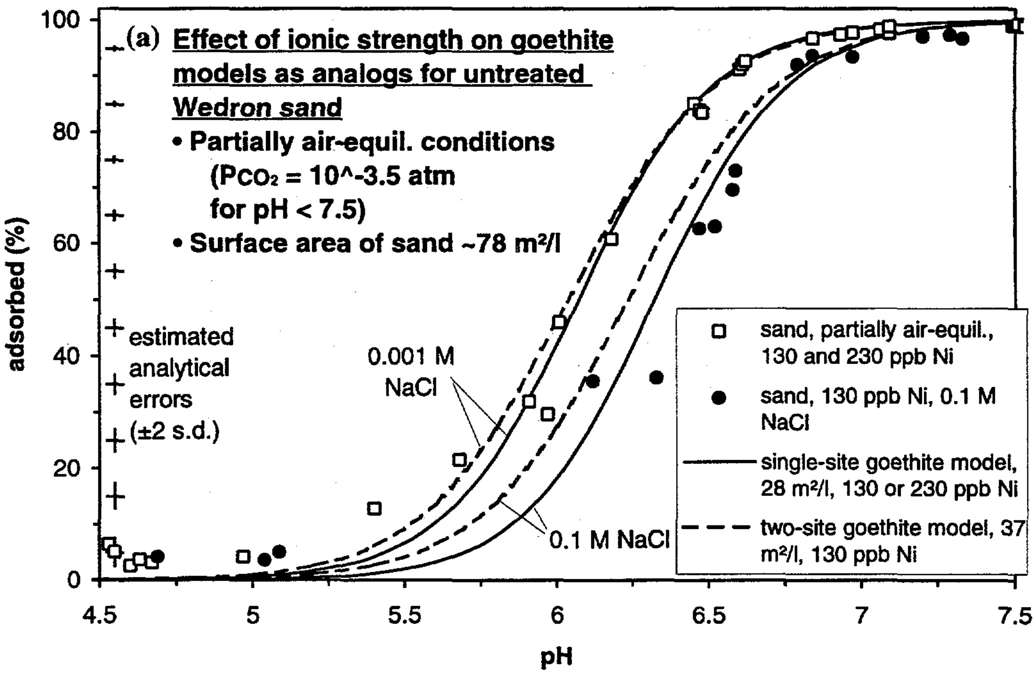

Figure 23. Performance of goethite-model analogs for Wedron 510 sand under conditions of changing ionic strength.

indicated that a realistic estimate of the surface area of kaolinite accessible to protons in solution may be 10 times the area measured by the BET method. Thus, adsorption of Ni by the acid-washed sand was closely simulated by the kaolinite model with a surface concentration of 60 m^2/l which corresponds to a BET-based surface concentration of 6 m^2/l. Nickel adsorption by untreated Wedron sand for total Ni = 130 ng/m*l* (2.21×10^{-6} M) was approximated by kaolinite calculations for a total kaolinite concentration of 3 m^2/l (corresponding to a BET-based surface concentration of only 0.3 m^2/l). The raw sand had a BET-based surface concentration of 78 m^2/l, so the predicted kaolinite concentration amounts to only 0.4% of the total. The steeper measured adsorption edge of the sand compared to the kaolinite model suggest that it is unlikely that kaolinite alone is solely responsible for Ni adsorption onto the untreated sand, and that the remaining 99.6% of the sand's surface is inert.

The Li adsorption curve for 124 m^2/l kaolinite (Figure C.5, Appendix C) has a maximum at pH = 7 – 7.5 and is qualitatively similar to that of the raw sand (Figure C.1, Appendix C). The amount of Li adsorbed by kaolinite is similar to that of the sand (about 3-4%) for similar surface areas. This suggests that kaolinite may be an important phase for Li adsorption by the sand. The desorption data described above and in Appendix C are consistent with the interpretation that Li is primarily adsorbing onto kaolinite in the sand. Those experiments indicate that Li adsorbs

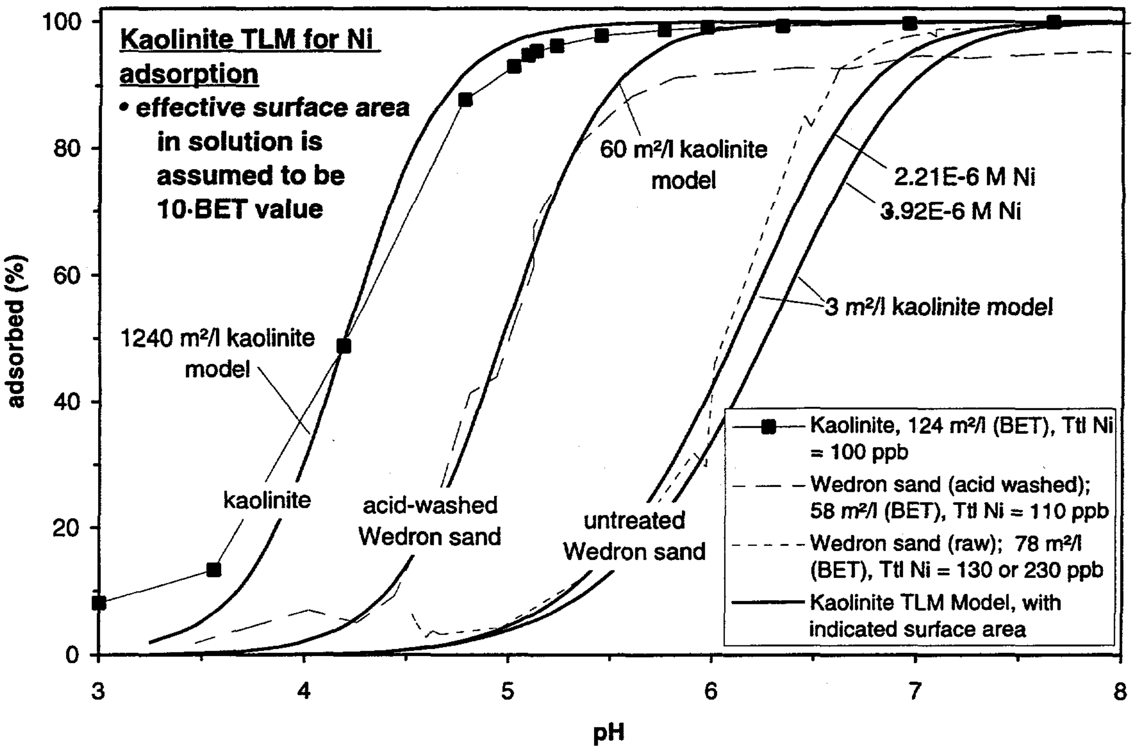

Figure 24. Triple-layer model for Ni adsorption onto kaolinite. Surface area of kaolinite in aqueous media taken to be a factor of 10 greater than the measured BET value (Xie and Walther, 1992). A value of $P_{CO_2} = 10^{-3.5}$ atm was used for all calculations. See text for further discussion.

irreversibly onto Wedron sand. Irreversible adsorption of Li by kaolinite has been reported by Anderson *et al.* (1989), who postulated that Li is strongly bound into octahedral edge sites in kaolinite. It most be noted, however, that they found that about 2/3 of the Li adsorbed onto kaolinite was so strongly bound that it could not be removed with 1 M CsCl, 1 M NH_4Cl, or 0.05 M HCl, while most of the Li adsorbed onto Wedron sand appears to be easily removable by lowering the pH of the electrolyte to ~2 (see Table C.3).

Three additional lines of evidence are discussed in Appendix A.5.2 that suggest that kaolinite is present in the sand in sufficient quantities to influence Ni adsorption: 1) Kaolinite is the dominant mineral present in the colloidal dispersion that forms in suspensions of the sand, even after acid-washing; 2) removal of goethite by acid washing enhances the similarities in Ni adsorption by kaolinite and the sand, i.e., adsorption of Ni onto acid-washed sand and kaolinite is weakly inhibited by CO_2, rather than enhanced, in contrast to goethite and raw sand; and 3) the presence of Li has the same effect on Ni adsorption by raw sand, acid-washed sand and kaolinite: the Ni adsorption curves are shifted to higher pH (cf. Figure 11 and Figure A.27.).

3.3. Comparison of Results of Batch and Transport Experiments

One long-term objective of this work was to obtain a self-consistent set of transport parameters from batch and column experiments for a relatively simple chemical and hydrological system. The parameters measured in batch sorption experiments included adsorption coefficients and adsorption rate constants. Parameters, measured directly or obtained by numerical fits to breakthrough curves obtained in column experiments, include dispersivity, adsorption rate constants and retardation factors. Columns were run at different flow velocities and influent concentrations to allow for correlation between the results of kinetic and isotherm batch experiments and transport experiments. The results are summarized in see Table 2.

We attempted to compare the accuracies of a simple K_d model and a simple first-order rate model for descriptions of Li and Br transport in the lab-scale columns . We observed that Li adsorption is non-linear and irreversible, and that the reaction rates are slow on the time scale of the column experiments. Although a multi-site non-linear kinetic adsorption model would be required to obtain an exact fit to the Li breakthrough curve (BTC), a reasonably good fit was obtained using the CXTFIT code with a single site, kinetic linear-sorption model. The apparent retardation factor, obtained from the BTC can also be shown to be consistent with the equilibrium and kinetic adsorption parameters obtained in batch studies when analyzed by the model of Kuhn and Peters (1981). This model is based on a theoretical relationship between the apparent retardation factor and the number of theoretical mass transfer units along a column. A detailed discussion of this work is given in Appendix D.

The BTC's for Ni in the low and high velocity bench-scale columns are more difficult to predict from the batch sorption data. Because column data (BTC's) are available at two flow velocities, comparisons between batch data and column BTC's involved consideration of both equilibrium and kinetic effects. Batch adsorption data presented in Appendices A, B and E show that the extent and rate of Ni adsorption are very sensitive to pH. The K_d for the sand ranges from 0.5 to >90 m*l*/g over the pH range 5.9 – 7.5; the adsorption rate constant ranges from 6.6×10^{-4} min^{-1} at pH 6.5 to 1.06×10^{-1} min^{-1} at pH 7.0. In order to relate the batch sorption data to the observed BTC's, it was necessary to make assumptions about the effective pH, K_ds and adsorption rates within the columns. Details of the analysis are given in Appendix E.

The *in situ* pH in both of the columns and the caisson is difficult to measure or estimate due to potential outgassing of CO_2. Measurements on influent and effluent samples suggest that in the columns the pH varied within the range 6.2 to 7.7. A corresponding range of equilibrium K_ds within the columns can be estimated from a linear regression between K_d and pH obtained from the batch sorption data (Fig. E.6). For example; the estimated K_d ranges from 7 to 48 from pH 6.5 to 7. These K_d values can be compared to apparent K_ds and corresponding pH's calculated from the retardation factors obtained from the CXTFIT fit of the BTC's.

The effective K_d obtained from the CXTFIT fit of the BTC of the low velocity column is 14.2 m*l*/g; the pH estimated from the linear regression in Fig. E.6 is 6.6. Thus, for the low velocity column, the retardation factor obtained from the column BTC is consistent with the equilibrium batch sorption data only at the lower end of the pH range measured in the column. Similarly, the apparent K_d of the fast column was 3.2 m*l*/g; this value falls in the lower end of the K_d range that corresponds to the observed pH range of 6.2 to 6.8. Thus, if adsorption kinetics is ignored, the batch adsorption data are consistent with the column BTC's only at low pH. If the pH of the column pore waters actually did change during the experiment, then the above analysis based solely on the equilibrium adsorption data is inadequate.

The effect of adsorption rate on the goodness or lack of agreement between the batch and column data was also examined in this study. Details of this analysis are given in Appendix E. The analysis of Kuhn and Peters (1981) was applied to predict the apparent retardation, R_{ap}, of the Ni BTC for the high and low velocity columns in a manner similar to that described for Li transport above. A detailed discussion is given in Appendix E. The apparent retardation factors calculated for the BTC's by CXTFIT fall within the range predicted from the relationship between n, the number of mass transfer units, and R_{ap}, the apparent retardation factor, for both columns at two different flow velocities at pH values of 6.5 and 7.0. Thus, consideration of both adsorption equilibria and adsorption kinetics allows for a more meaningful comparison of batch adsorption data and column breakthrough curves.

3.4. Suggestions for Future Work

3.4.1. Introduction: Review of the caisson experiment.

The joint Los Alamos/Sandia Caisson Experiments was designed to provide a relatively simple hydrological and geochemical system for the development of a framework for model validation. The objective of the work described in this report was to provide the geochemical data required to model tracer transport in the caisson. Construction of the test bed for the transport experiment, however, proved to be more difficult than originally foreseen. The hydrological and geotechnical properties of Wedron 510 sand were not well predicted by early design calculations (Siegel *et al.*, 1992). When the caisson was filled with the sand and saturated with water, the bottom boundary plate partially collapsed and many of the water samplers did not work. A higher flow rate and degree of saturation than originally planned was required to obtain water samples from the interior of the caisson; even at the higher water fluxes it was difficult to obtain reliable pH measurements from the hollow-fiber water samplers. Distribution of water at the top of the caisson was not uniform; a disproportionate amount of fluid trickled onto the center of the sand bed through loose fittings. This created a high velocity central channel through which tracer transport was more rapid than predicted from the steady-state flow model. The first LiBr pulse traveled much more rapidly through the caisson than expected; sufficient water samples were not taken to define the leading edge of the breakthrough curve.

The Caisson Experiments was scheduled to end in Fiscal Year 1994. Introduction of the tracers, however, was delayed repeatedly due to the problems described above, inclement weather and environmental regulations. The final tracer pulse was not completed until the end of August 1994, allowing little time for analysis of the solution samples and no time for transport modeling before the end of Fiscal Year 1994. Funding for analysis of samples from the second Li pulse was not available in the FY95 budget and therefore have not been carried out. An accurate description of flow within the caisson was not available as of March 1995, when the project was concluded.

The geochemical properties of Wedron 510 sand also proved to more complex than our original expectations. The laboratory studies described in this and previous reports revealed that trace minerals controlled the adsorption properties of the sand and that Ni adsorption extent and rate were very sensitive to pH over the pH range possible in the caisson. Measurements of pH both in laboratory columns and in the caisson were more difficult than expected; after sampling, the pH of solution may rise due or fall due to degassing or uptake of CO_2, respectively, depending on its original carbonate content.

The questions raised at the initiation of this project and described in Table 1, above, are important to the development of improved geochemical transport models, model validation and ultimately public confidence in the performance assessment models used to carry out risk assessment for high level waste disposal. The original plan for this project stressed validation of transport models by demonstration that the models could be used to make accurate *predictions* of solute transport from hydraulic and geochemical data obtained in the laboratory, prior to fielding of the experiments in the caisson. The problems in caisson construction described above have precluded achieving this original objective, however, the results of the caisson experiments can still be used to develop a framework for model validation. The results of the laboratory studies and analyses of caisson samples comprise a high quality data set for the exercise of alternative models for transport. A series of sensitivity analyses designed to model tracer transport will identify limitations in currently available computer codes, thermodynamic and kinetic data and monitoring techniques. This analysis would provide benefits to model validation that are analogous to the benefits that the TSPA exercises (Wilson *et al.*, 1994) provide to development of the Performance Assessment Methodology. Several additional studies are required to complete the work begun in this project. These include chemical analyses of the water samples collected during the second LiBr pulse, use of transport codes that simulate the processes that are now recognized to be important for this geochemical system and development of improved in-situ measurement techniques to characterize solutions in laboratory columns, intermediate-scale systems like the caisson, and field sites.

3.4.2. Additional Studies

1. **Complete analysis of waters samples from second Li pulse in caisson.** The breakthrough curves for Br tracer are the primary constraints on flow velocities. Due to the problems described above, the BTC for Br from only the second LiBr pulse was defined in sufficient detail to calculate a flow velocity. Use of this water velocity to describe a steady-state velocity for all three tracer pulses in the caisson may not be realistic. Based on observations of the non-uniform and transient application of water and tracer to the top of the caisson, it is possible that the water flow field was variable over the duration of the experiment. The BTC for Li provides a secondary constraint on the water velocity. If the model for Li transport can be validated, then the Li BTC data from the first LiBr pulse could be used to estimate the flow velocity during the early stages of the experiment. The Li transport model could be validated by successfully predicting the second Li BTC using the batch Li adsorption kinetics data obtained in the laboratory and the flow velocity obtained from Br BTC of the second LiBr pulse. The two velocities obtained from the LiBr pulses could then be used to bracket the flow velocity during the Ni pulse. This information is needed for calculation of Ni transport using the LEHGC or CXTFIT codes.

2. **Model Ni transport in column and caisson with the LEHGC code.** Transport of Ni in the laboratory columns was probably strongly dependent on the pH of the pore waters. The LEHGC code can simulate the transport of tracers whose adsorption depends on pH. The code could be used to bracket the possible chemical conditions within the columns and caisson in response to slow dissolution of carbonate and diffusion of CO_2. Success on placing corresponding bounds on Ni transport would be a useful demonstration of the possibility of placing bounds on

similar coupled processes important to performance assessment and retardation sensitivity analysis. When a reliable description of the flow within the caisson is obtained, Ni transport should also be modeled with the LEHGC code. Laboratory data suggest that adsorption equilibrium was not attained in either the column experiments or the caisson. Therefore, accurate simulation of Ni transport will not be possible with the LEHGC code because it only models only equilibrium processes. When completed, LEHGC Version 2 will be able to include effects of both non-linear sorption and slow adsorption kinetics on transport. The data sets from the laboratory studies and the caisson will provide an opportunity to validate this model.

3. Develop in-situ methods to measure pH of column and caisson solutions. Uncertainty in the in-situ pH of laboratory columns and the caisson prevents reliable prediction of Ni transport. Currently-available techniques, including measurements of pH on extracted water samples or continuous monitoring by electrodes in flow-through sample chambers, require relatively large volumes of water and calibration of electrodes. In-situ fiber optic probes have been developed to monitor pH of solutions in fermentation processes and waste water treatment (Agayn and Walt, 1993 and cited references). Such probes should be evaluated for use in future laboratory-scale, caisson-scale and field-scale transport experiments.

4. Summary

An intermediate-scale experiment was carried out by Sandia National Laboratories and Los Alamos National Laboratory for the Yucca Mountain Site Characterization Project to demonstrate a strategy to validate key geochemical and hydrological assumptions in performance assessment models. The experiment involved the detection and prediction of the migration of fluid and tracers through a 6-m high x 3-m diameter caisson filled with a processed quartz sand, mined from the St. Peter sandstone. The role of Sandia National Laboratories in the Caisson Experiment was to study the characteristics of the sand that would control chemical interactions between the tracers, fluid and substrates. This report describes the results of the following studies: 1) obtaining Li and Ni adsorption data for components of the raw sand, 2) studying reversibility of Ni and Li sorption by the sand, 3) studying the competition between Li and Ni for sorption sites on the sand and its components, 4) examining transport of Li and Ni in well-controlled bench-scale columns to provide an intermediate link between static batch sorption tests and the caisson transport experiment, and 5) obtaining data on breakthrough of a Ni pulse in the caisson. Several questions raised at the beginning of the experiment and described in the introductory sections of this report can be addressed using the results of these studies.

1. Can we model adsorption properties of raw sand as a mixture of two components: goethite and kaolinite, and ignore the quartz? Is goethite the only important adsorbent in the sand for Ni? Do Li and Ni adsorb onto the same sites? Is goethite an important phase for Li adsorption?

Wedron 510 sand is more than 99% quartz in bulk mineralogy, yet its adsorption behavior is dominated by iron oxyhydroxide and kaolinite, two trace components. The presence of Fe-oxyhydroxide is inferred from the quantity of Fe leached during an acid wash. Fe-oxyhydroxides probably coat most (50 – 80%) of the available surface area in the raw sand. Kaolinite platelets were observed on sand grain surfaces by SEM. Qualitatively, the adsorption properties of the sand can be adequately modeled as a two-component system. Ni adsorption occurs primarily on the iron oxyhydroxide, on sites where Li does not compete; some of the Ni adsorbs to kaolinite, and competes with Li for adsorption sites on that mineral. The presence of Li leads to diminished Ni adsorption by both the raw sand and pure kaolinite. Ni adsorption by goethite is insensitive to the presence of Li, suggesting that in the sand, iron oxyhydroxide could not be the site of the Li-Ni competition. Acid-washed sand adsorbs Ni in a manner similar to that of kaolinite. Acid stripping removes a substantial fraction of the kaolinite from the sand but may expose additional reactive surfaces by dissolving carbonate cement and iron oxyhydroxides. The presence of the cement is inferred from potentiometric titration of the raw sand and the amount of Ca and Mg that is leached by acid-stripping. Li adsorbs irreversibly, suggesting that kaolinite is the only important phase in the sand with respect to Li adsorption.

2. Are carbonato-complexes important for Ni adsorption by sand or its components? Are the formation constants for Ni carbonato-complexes reported in the literature reliable?

Two triple-layer surface-complexation models have been developed for simulating Ni adsorption onto goethite. The models were fit to Ni adsorption data in batch systems with approximately 5 and 50 m^2/l goethite, under both CO_2-free and air-equilibrated conditions. The adsorption stoichiometry is modeled as a 1:1 $SONi^+$ inner-sphere complex. The simpler one-site model performs poorly at lower surface concentrations when optimized at the higher surface concentration. The two site model contains a small fraction of high energy sites and fits data for both goethite concentrations. A quantitative model of Ni adsorption onto kaolinite was also developed; attempts to develop a model for quartz were less successful. Thermodynamic calculations were carried out with HYDRAQL 94 (Ward, 1995), a revised version of HYDRAQL (Papelis *et al.*, 1988), using an internally consistent set of formation constants for aqueous Ni species. The formation constants for Ni carbonato-complexes are two orders of magnitude lower than the values commonly used in the literature. The lower values are consistent with the results of Ni solubility measurements in batch systems with low concentrations of CO_2 and Ni adsorption experiments at high pH. In the proposed model, Ni carbonato complexes are not important as either aqueous or adsorbed species over the pH range of interest.

3. Can transport of Ni and Li in lab-scale columns be predicted from batch adsorption studies? Is Ni or Li adsorption by the sand fast and reversible? Is a linear equilibrium adsorption model adequate for Li and Ni transport?

Batch studies revealed that adsorption of Li by sand was non-linear, relatively slow and dominantly, irreversible. Similar studies of Ni sorption revealed that extents and rates of adsorption were pH dependent and partially irreversible. Many available transport models rely on simple geochemical assumptions such as linear reversible sorption. More sophisticated codes such as HYDRUS (Kool and van Genuchten, 1992), CXTFIT (Parker and van Genuchten, 1984) and LEHGC (Yeh, 1995) incorporate non-linear sorption, kinetics or surface complexation models, however, none of the transport codes examined in this project could model the full complexity of the adsorption behavior of these tracers on these substrates. It was shown, however, that the breakthrough curves for Ni and Li were consistent with the batch sorption data. Specifically, the differences between the shapes of the 1 and 17.4 ppm BTCs for Li were consistent with the non-linear sorption observed in the batch systems. Second, apparent retardation factors of both of the Li BTCs were consistent with the equilibrium batch K_d and adsorption rate constants and the pore water velocity of the columns. Third, although, both the K_d and rate of Ni sorption are strongly dependent on pH, and the pH of the Ni columns varied, the calculated retardation factor of slow and fast flowing columns were within the bounds predicted from the batch experiment data and the pore water velocity.

4. Which geochemical models adequately describe tracer migration? How is this study relevant to the validation of transport models for performance assessment (PA)?

Previously (Kent *et al.*, 1988), it has been asserted that the Surface Complexation Modeling (SCM) approach provides a useful framework to collect and evaluate adsorption data. The results of the present study provide support for that assertion. Although a unique quantitative adsorption model based on the properties of the component minerals of Wedron sand has not yet been obtained, the adsorption properties of Wedron sand can be qualitatively understood in terms of the properties of its components. Attempts to quantify the effects of solution parameters on adsorption revealed many trends that may have not been noticed using a more empirical approach to collection of adsorption data. These trends include: effect of pH, P_{CO_2}, ionic strength and substrate surface area on adsorption, and the competition between Ni and Li for adsorption sites on the sand and on kaolinite.

The studies described in this report provide a basis for predictions of transport of Ni, Li and Br through porous media similar to the reference sand. Techniques were developed for obtaining parameter values for surface complexation and kinetic adsorption models for the sand and its mineral components. The techniques have been described in this report and in a previous report (Siegel *et al.*, 1995). The general approach and methods should be useful for characterization of other natural materials in support of coupled hydrogeochemical transport calculations. Such models will be required for contaminant transport calculations for complex chemical systems in which a simple K_d model can not predict tracer retardation.

In heterogeneous groundwater systems, adsorption may be controlled by trace amounts of reactive minerals or coatings of inert materials that are preferentially concentrated along flow paths or other structural features. Proper characterization of mineral surfaces and formulation of an adsorption model for mixtures of minerals are required for site characterization because studies of metal adsorption by bulk rocks may not provide information about the most important adsorption sites. It is important for performance assessment calculations to determine if radionuclide discharges could be substantially different from those calculated using K_d values obtained from the bulk rock.

The work described in this report provides some insights into the comparative advantages and disadvantages of SCM's and K_ds for reactive-transport modeling and PA. Because K_ds are easily measured but difficult to evaluate, they have been obtained for many rock/water/solute combinations and can be used in transport codes for Monte Carlo simulations in PA calculations. In contrast, SCM data for systems relevant to HLW disposal are scarce and codes that use SCM parameters in PA calculations are not available.

Use of a robust surface complexation model requires a more detailed description of the chemical system than does use of a K_d. However, as this study demonstrates, the additional data requirements are not a weakness of the SCM's. By providing a structured way to examine experimental data obtained in batch adsorption studies, application of the SCM in this study reduced the chance that extraneous effects were introduced into the adsorption experiments. A great deal of experimental and theoretical work was required to obtain surface complexation constants, however, this additional information and the use of a thermodynamic framework in the calculations led to greater confidence that the model does accurately describe the most important aspects of the geochemical system.

If the required data are obtained for radionuclides and rocks relevant to Yucca Mountain, SCM models could be used in coupled hydrogeochemical transport models such LEHGC (Yeh, 1995) to demonstrate that the simplifying geochemical assumptions used in PA calculations are applicable under site-specific conditions. Briefly, modeling of transport using a code like LEHGC requires the following steps: 1) characterization or estimation of the relevant geochemical properties of the geomedia (mineralogical composition, specific surface area, mineralogical distribution) along the flow path; 2) measurement of adsorption as a function of relevant solution parameters (pH, concentrations of complexing ligands and competing cations, Eh, etc.); and 3) representation of the hydrologic flow field. A complete description of such modeling is beyond the scope of this report, however, examples of the use of coupled hydrogeochemical transport models to model transport on laboratory and field scales can be found in Yeh (1995).

Simplified (lumped) models used in performance assessment calculations may not include descriptions of many potentially important phenomena. As discussed in Siegel (1993) model validation in support of PA should involve showing that the effects of these *missing* phenomena on the regulatory performance measures are advantageous, nonexistent or relatively small under site-specific conditions. Confidence in the models used in performance assessment can be gained by demonstrating that the errors in the regulatory performance measures, due to the use of lumped geochemical models, are acceptable when compared to other errors in the total systems PA calculations. This can be done by comparing discharges calculated using the coupled comprehensive model to those calculated using the lumped models.

5. References

Agayn, V. I., and D. R. Walt, 1993: "Fiber-optic Sensor for Continuous Monitoring of Fermentation pH," *Biotechnology*, **11**, 726-729.

Anderson, M.A., P.M. Bertsch, and W.P. Miller, 1989: "Exchange and Apparent Fixation of Lithium in Selected Soils and Clay Minerals," *Soil Sciences*, **148**, 46-52.

Balistrieri, L.S., and J.W. Murray, 1979: "Surface of Goethite (αFeOOH) in Seawater," *Chemical Modeling in Aqueous Systems*, E.A. Jenne, ed., American Chemical Society Symposium Series **93**, 275-298.

Balistrieri, L.S., and J.W. Murray, 1981: "The Surface Chemistry of Goethite (alpha FeOOH) in Major Ion Seawater," *American Journal of Science*, **281**, 788-806.

Brunauer, S., P.H. Emmett, and E. Teller, 1938: "Adsorption of Gases in Multimolecular Layers," *Journal of the American Chemical Society*, **60**, 309-319.

Bryan, C.R., D.B. Ward, and M.D. Siegel, 1995: "Ni Sorption and Solubility Studies," in *Characterization of Materials for a Reactive Transport Model Validation Experiment, Appendix A*, Siegel, M.D., D.B. Ward, C.R. Bryan, and W.C. Cheng, SAND94-0189, Sandia National Laboratories, Albuquerque, NM, 32 pp.

Chardymskaya, E. Yu., M.P. Sidorova, and E.V. Kulepova, 1987: "Determination of EDL Potentials on SiO_2 surfaces in CsCl and LiCl solutions from Adsorption Measurements," *Colloid Journal of the USSR*, **48**, 645-649.

Cheng, W.C., M.D. Siegel, and C.R. Bryan, 1995: "Column Studies in Support of the Caisson Experiments: Design and Preliminary Results for Li and Br," in *Characterization of Materials for a Reactive Transport Model Validation Experiment, Appendix C*, Siegel, M.D., D.B. Ward, C.R. Bryan, and W.C. Cheng, SAND94-0189, Sandia National Laboratories, Albuquerque, NM, 36 pp.

Davies, C.W., 1962: *Ion Association*, Butterworths, London.

Davis, J.A., R.O. James, and J.O. Leckie, 1978: "Surface Ionization and Complexation at the Oxide-Water Interface. 1. Computation of Electrical Double Layer Properties in Simple Electrolytes," *Journal of Colloid and Interface Science*, **63**, 480-499.

Davis, J.A., and D.B. Kent, 1990: "Surface Complexation Modeling in Aqueous Geochemistry, in Mineral-Water Interface Geochemistry," *Reviews in Mineralogy*, **23**, M.F Hochella and A.F. White, eds., Mineralogical Society of America, Washington, D.C., 177-260.

Dzombak, D.A., and F.M.M. Morel, 1990: *Surface Complexation Modeling*, John Wiley & Sons, Inc., New York, 393 pp.

Kent, D.B., V.S. Tripathi, N.B. Ball, J.O. Leckie, and M.D. Siegel, 1988: *Surface–Complexation Modeling of Radionuclide Adsorption in Subsurface Environments*, SAND86-7175, Sandia National Laboratories, Albuquerque, NM, 113 pp.

Kester, D.R., and R.M. Pytkowicz, 1975: "Theoretical Model for the Formation of Ion-Pairs in Seawater," *Marine Chemistry*, **3**, 365-374.

Kool, J.B., and M. T. van Genuchten, 1992: *HYDRUS, One-Dimensional Variably Saturated Flow and Transport Model, Including Hysteresis and Root Water Uptake*. Research Report No. 124, U. S. Salinity Laboratory, USDA, ARS, Riverside, CA.

Kuhn, W.L. and R.D. Peters, 1981: "WRIT Leaching and Transport Modeling," *Waste/Rock Interactions Technology Program FY-80 Information Meeting*, J.F. Relyea Editor, PNL-3887, Pacific Northwest Laboratory, Richland, Wa., 268-276.

Mattigod, S.V. and G. Sposito, 1977: "Estimated Association Constants for Some Complexes of Trace Metals with Inorganic Ligands," *Soil Science Society of America*, **41**, 1092-1097.

Meijer, A., 1992: "A Strategy for Derivation and Use of Sorption Coefficients in Performance Assessment Calculations for the Yucca Mountain Site", in *Proceedings of the DOE/Yucca Mountain Site Characterization Project Radionuclide Adsorption Workshop at Los Alamos National Laboratory, September 11-12, 1990*, compiled by J.A. Canepa, LA-12325-C, Los Alamos National Laboratory, Los Alamos, NM, 9-41.

Papelis, C., K.F. Hayes, and J.O. Leckie, 1988: *HYDRAQL: A Program for the Computation of Chemical Equilibrium Composition of Aqueous Batch Systems Including Surface-Complexation Modeling of Ion Adsorption at the Oxide/Solution Interface*, Technical Report 306, Stanford University Department of Civil Engineering, Stanford, 130 pp.

Parker, J.C., and M. T. van Genuchten, 1984: "Determining Transport Parameters from Laboratory and Field Tracer Experiments," *Virginia Agricultural Experiment Station Bulletin 84-3,* ISSN 0096-6088.

Rea, R. L., and G. A. Parks, 1990: "Numerical Simulation of Coadsorption of Ionic Surfactants with Inorganic Ions on Quartz," in *Chemical Modeling of Aqueous Systems II,* Melchior and Bassett, eds., ACS Symposium Series 416, American Chemical Society, Washington, D.C., 261-271.

Relyea, J.F., 1982: "Theoretical and Experimental Considerations for the Use of the Column Method for Determining Retardation Factors," *Radioactive Waste Management and the Nuclear Fuel Cycle,* **3**, 151-166.

Riese, A.C., 1982: *Adsorption of Radium and Thorium onto Quartz and Kaolinite: A Comparison of Surface Complexation Models,* Unpublished Ph.D. thesis, Colorado School of Mines, Golden, Colorado, 292 pp.

Siegel, M.D., 1993: "Towards a Realistic Approach to Validation of Reactive Transport Models for Performance Assessment," *Proceedings, FOCUS 93: Site Characterization and Model Validation,* Las Vegas, NV, September 26-29, 1993. (SAND93-2507C)

Siegel, M. D., P. L. Hopkins, R.J. Glass, and D.B. Ward, 1992: "Design of an Intermediate-Scale Experiment to Validate Unsaturated-Zone Transport Models.", *High Level Radioactive Waste Management: Proceedings of the Third International Conference,* April 12-16, 1992, Las Vegas, Nevada, pp. 1972-1984.

Siegel, M. D., D. B. Ward, W. C. Cheng, C. Bryan, C. S. Chocas, and C.G. Reynolds, 1993: "Preliminary Characterization of Materials for a Reactive Transport Model Validation Experiment," *High Level Radioactive Waste Management: Proceedings of the Fourth International Conference,* April 26-30, 1993, Las Vegas, Nevada, pp. 348-358.

Siegel, M.D., D.B. Ward, C.R. Bryan, and W.C. Cheng, 1995: *Characterization of Materials for a Reactive Transport Model Validation Experiment,* SAND94-0189, Sandia National Laboratories, Albuquerque, NM, 277 pp.

Siegel, M.D., 1994: "Towards a Realistic Approach to Validation of Reactive Transport Models for Performance Assessment", *Proceedings FOCUS 93, Site Characterization and Model Validation,* Las Vegas NV, September 26-29, 1993.

Springer, E.P, M.D. Siegel, P.L. Hopkins, and R.J. Glass, 1993: "Testing Models of Flow and Transport in Unsaturated Porous Media, " in *Proceedings of the Fourth Annual International Conference on High Level Radioactive Waste*, V. 1, 336-347, Las Vegas, NV, April 26-30, 1993.

Tripathi, V.S., 1983: *Uranium (VI) Transport Modeling: Geochemical Data and Submodels*, Ph.D. thesis, Stanford University Department of Applied Earth Science, Stanford, 297 pp.

van Geen, A., A.P. Robertson, and J.O. Leckie, 1994: "Complexation of Carbonate Species at the Goethite Surface: Implications for Adsorption of Metal Ions in Natural Waters," *Geochimica et Cosmochimica Acta*, **58**, 2073-2086.

Ward, D.B., M.D. Siegel, and C.R. Bryan, 1995a: "Characterization of Wedron 510 Sand for the Intermediate-Scale (Caisson) Transport Experiment," in *Characterization of Materials for a Reactive Transport Model Validation Experiment, Appendix A,* Siegel, M.D., D.B. Ward, C.R. Bryan, and W.C. Cheng, SAND94-0189, Sandia National Laboratories, Albuquerque, NM, 43 pp.

Ward, D.B., C.R. Bryan, W.C. Cheng, and C.R. Boyle, 1995b: "Experimental Procedures Used in the Characterization Study," in Siegel, M.D., D.B. Ward, C.R. Bryan, and W.C. Cheng, *Characterization of Materials for a Reactive Transport Model Validation Experiment, Appendix E,* SAND94-0189, Sandia National Laboratories, Albuquerque, New Mexico, 114 pp.

Ward, D.B., 1995: *Nickel Adsorption on a Natural Sand and Goethite, Kaolinite, and Quartz: Single- vs. Multi-Site Models and the Role of* CO_2, unpublished Ph.D. thesis, University of New Mexico, Albuquerque, New Mexico.

Westall, J.C., 1982: *FITEQL -- A Computer Program for Determination of Chemical Equilibrium Constants from Experimental Data, Version 2.0*, Report 82-02, Dept. of Chemistry, Oregon State University, Corvallis, Oregon, 61 pp.

Wilson, M. L., Gauthier, J.H., and others, 1994: *Total-System Performance Assessment for Yucca Mountain - SNL Second Iteration (TSPA-1993),* SAND93-2675, Sandia National Laboratories, Albuquerque, NM.

Xie, Z., and J.V. Walther, 1992: "Incongruent Dissolution and Surface Area of Kaolinite," *Geochimica et Cosmochimica Acta*, **56**, 3357-3363.

Yeh, G.T., 1995: *User's Manual for LEHGC: A Lagrangian-Eulerian Finite Element Model of Hydrogeochemical Transport Through Saturated-Unsaturated Media, Version 1.0*, SAND93-7081, Sandia National Laboratories, Albuquerque, NM.

Appendix A.
Ni Adsorption by End-Member Components of Wedron 510 Sand

D. B. Ward, C. R. Bryan, and M. D. Siegel

Contents

A.1. Introduction

Our previous work (Siegel *et al.*, 1995) has shown that Wedron 510 sand contains several mineralogical components that are potentially important contributors to its aggregate surface chemistry and adsorption of Ni. Specifically, quartz, Fe-oxyhydroxide, kaolinite, and Ca-Mg carbonate phases were identified. Ni adsorption measurements were reported for the raw sand under both CO_2-free conditions and conditions of partial equilibration with air, and for synthetic goethite and quartz (Min-U-Sil 5) under CO_2-free conditions. Potentiometric titrations on acid-washed sand produced anomalous results, implying much greater effective surface area than measured by N_2-BET and the presence of another phase in addition to quartz. Based on the goethite data, we proposed a tentative model in which Ni adsorption onto the raw sand was accounted for by Fe-oxyhydroxides that effectively covered 50–80% of the surface of the sand.

We now have additional Ni adsorption measurements on acid-washed sand and goethite under both CO_2-free and atmospheric conditions, and on kaolinite and Min-U-Sil 5 quartz under atmospheric conditions only. Ca-Mg carbonate is ignored as a possible adsorbent, based on the published work of Zachara *et al.* (1991), who report an adsorption edge for Ni on calcite with a pH_{50} (the pH of 50% adsorption) of 8.5 at a surface area of 5 m^2/l and $I = 0.1$ M. No published values were found for Ni adsorption onto high-Mg calcite or dolomite. These data, in combination with results from a study of competition between Ni and Li for adsorption sites, allow us to propose a more refined and realistic model of the surface chemistry of Wedron 510 sand, in which kaolinite as well as Fe-oxyhydroxides is important, and a negligible role is played by quartz and Ca-Mg carbonate.

A.2. Methods

A.2.1. Preparation of Adsorbents

Batch adsorption experiments were conducted using raw (untreated) Wedron 510 sand, acid-washed Wedron 510 sand, Min-U-Sil 5 (a quartz reference material, U.S. Silica Corp., Berkeley Springs, West Virginia); kaolinite (kaolin powder, "Baker Analyzed" #2242-01, U.S.P., J.T. Baker Co.), and freshly synthesized goethite. The acid-washed sand, Min-U-Sil 5 quartz, and kaolinite were prepared by the boiling-HCl method (Ward *et al.*, 1995a), which consisted of bringing a suspension of the adsorbent refluxing in 6 *N* HCl for 45 min, and rinsing with deionized water to neutral pH. A second aliquot of Min-U-Sil 5 was obtained from Mark Crawford of the British Geological Survey. It had been treated by the ignition-$HClO_4$ method, in which the sample was ignited at 500 °C for 48 h prior to leaching in boiling $HClO_4$. The two cleaning methods were found to be equivalent for Min-U-Sil 5, with no detectable differences in surface chemistry. After drying, the Min-U-Sil 5 and kaolinite were resuspended in deionized water whereas the sand was stored dry. X-ray diffraction patterns and SEM observations of grain morphology show that crystallinity of the Min-U-Sil 5 and kaolinite was not degraded by acid-washing.

Goethite was synthesized according to the method of Tripathi (1983), which is based on the procedure of Atkinson *et al.* (1967): the pH of a solution of $Fe(NO_3)_3$ was rapidly raised to pH 11.8–12 by addition of NaOH and then aged for 5 days at 63 °C to allow conversion of the $Fe(OH)_3$ precipitate to goethite (α-FeOOH). The goethite was washed repeatedly with deionized water until the pH was less than 8. CO_2-free reagents and deionized water were used throughout the synthesis, and the headspace of all containers was purged with Ar whenever they were opened. Five batches were prepared. The first three batches were used for technique development, and will not be discussed further.

A.2.2. Surface-Area Measurements

Surface areas were measured using the BET method (Brunauer *et al.*, 1938) with either Kr or N_2 as the adsorbing gas at five values of P/P_0. Measurements using Kr were performed on a Micromeritics Digisorb 2600 operated in "research mode", with a 1% acceptance tolerance for P/P_0 measurements and determinations of saturation pressure every 15 min. Measurements using N_2 were performed on a Micromeritics ASAP2000 operated in standard mode, with a 5% acceptance tolerance and determination of saturation pressure at the start of each analysis. A cross-sectional area of 0.210 nm^2 was used for Kr and 0.162 nm^2 for N_2 in surface-area calculations. Sample mass was 0.3–2 g if the expected surface area was > 2 m^2/g, and 15–20 g for Wedron sand (with expected surface area << 1 m^2/g). Samples were outgassed under vacuum at 100–200 °C (depending on mineralogy) until the outgas rate was below 100 torr/sec. Consistent serial surface-area determinations were taken to indicate sufficient outgassing.

A.2.3. Batch Adsorption Experiments

Ni adsorption measurements under nominally CO_2-free conditions were carried out in batch systems as described in our previous report (Ward *et al.*, 1995b). The procedure for adsorption measurements under air-equilibrated conditions was modified to provide near-equilibrium quantities of total dissolved CO_2 at high pH. In our previous work under atmospheric conditions, referred to in this report as "partially air-equilibrated", CO_2 was added by sparging each batch system with air for several minutes. This was adequate to achieve equilibrium in solution (P_{CO_2} =

$10^{-3.5}$ atm) for pH values up to ~7.5, but at higher pH values the quantity of CO_2 that must be absorbed into the solution increases by a factor of 10 or more for each unit of pH increase, due to dissociation of H_2CO_3. The degree of equilibration with air in these systems is estimated by measurements on representative systems containing only electrolyte. Total carbonate was calculated using mass-action and charge-balance equations (Table A.1) from the final pH and the concentration of Na (added as NaOH). As shown in Figure A.1, total carbonate was constant above pH 7.5 at a concentration of $10^{-3.74}$ M, and one datum at pH 7.3 was in equilibrium with air. Thus it seems probable that in batch systems for Ni adsorption, the dissolved carbonate species were in equilibrium with air below pH 7.5. The work of Girvin *et al.* (1991), also illustrated in Figure A.1, showed similar behavior. Their amorphous Fe suspension was in contact with air for up to 24 hr before the start of adsorption experiments, and after pH adjustment the suspensions were in contact with air for up to 5 min before being sealed.

Rather than rely on the slow uptake of CO_2 by the electrolyte, the present measurements were made by using both NaOH and $NaHCO_3$ to increase the pH of the systems. Such systems are referred to in this report as "air-equilibrated". The quantity of $NaHCO_3$ required was calculated from the target pH, the concentration of the $NaHCO_3$ stock solution, and the volume of the system by assuming equilibrium carbonate speciation. The relevant equilibria are summarized in Table A.1. It was assumed that activities equaled concentrations, and that the partial pressure of CO_2 in the laboratory atmosphere was $10^{-3.5}$ atm. Actual P_{CO_2} in the laboratory was probably somewhat lower because of the reduced atmospheric pressure at 1,675 m above sea level. After adding the requisite amounts of HCl, NaOH, and $NaHCO_3$, the batch systems (including adsorbent) were sealed and pre-equilibrated for 1–3 d, then spiked with Ni and sparged with humidified air for at least 3 min, sealed, and equilibrated for 2–4 d before centrifuging and sampling. These times appear to have been sufficient for close approach to equilibrium (See Appendix B in this report).

Table A.1. Equations used to calculate addition of NaOH and $NaHCO_3$ to batch systems.

Reaction	Equilibrium Constant
$H_2O \leftrightarrow H^+ + OH^-$	$K_W = 1.01 * 10^{-14}$
$CO_2(g) + H_2O \leftrightarrow H_2CO_3$	$K_H = 0.03405$
$H_2CO_3 \leftrightarrow H^+ + HCO_3^-$	$K_1 = 4.45 * 10^{-7}$
$HCO_3^- \leftrightarrow H^+ + CO_3^{2-}$	$K_2 = 4.69 * 10^{-11}$
<u>Charge Balance</u>	
$[H^+] + [Na^+] = [OH^-] + [HCO_3^-] + 2[CO_3^{2-}]$	

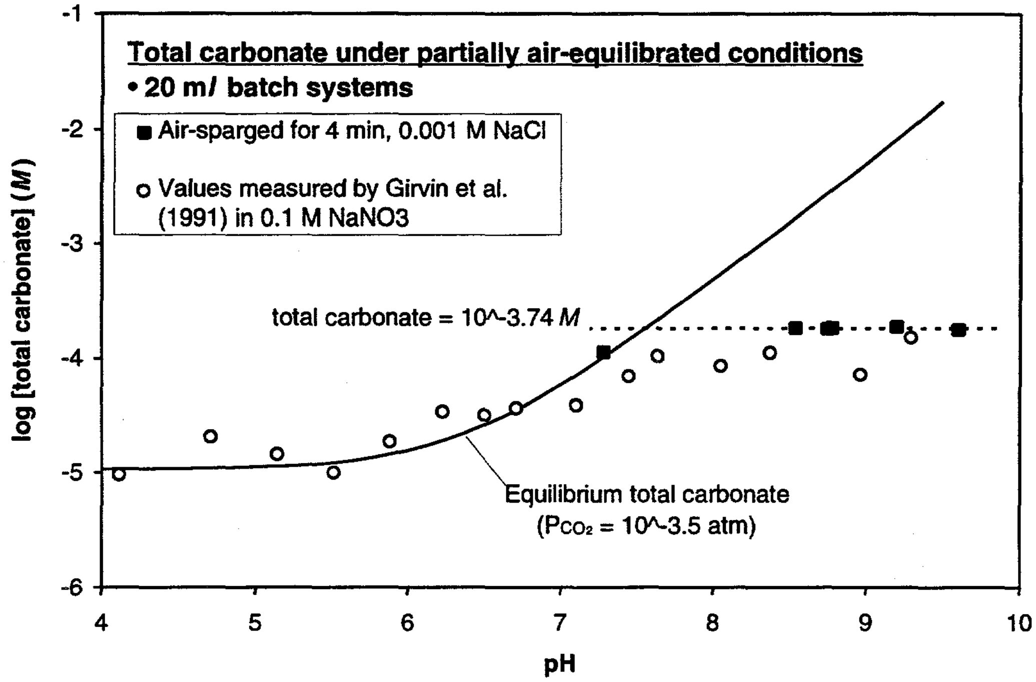

Figure A.1. Probable total carbonate in batch systems partially equilibrated with air. The systems (solution only) were equilibrated by sparging with air for 4 minutes. Values were calculated from potentiometric data; solid line is theoretical curve for systems in equilibrium with atmosphere. Equilibrium was probably achieved for pH < 7.5. At higher pH values, total carbonate was probably nearly constant at ~$10^{-3.74}$ M. Batch systems (with goethite) from Girvin *et al.* (1991) were prepared open to air but not sparged.

Oak Ridge-style 50 m*l* centrifuge tubes were used as reaction vessels. For "air-equilibrated" conditions, either polyallomar or polycarbonate tubes were used — measurements were not affected by the type of plastic. For nominally CO_2-free conditions, which lack the buffering capacity of the dissolved carbonate species, only polyallomar tubes were used because this plastic is not subject to acidic contamination from the washing procedure and displays no detectable buffering tendencies.

A.2.4. Li/Ni Sorption Competition

Batch Li/Ni site sorption competition experiments were conducted with Wedron sand, goethite, and kaolinite. The experiments were carried out under both CO_2-free and nominally atmospheric conditions, at initial Li concentrations of 100 µg/m*l* and 1000 µg/m*l* (0.014 M and 0.14 M), and initial Ni concentrations of 80–5000 ng/m*l* (1.36×10^{-6} M to 8.5×10^{-4} M). The experimental conditions for each study are summarized in Table A.2. Sodium bicarbonate solution was added to the electrolyte in experiments involving goethite and kaolinite to insure that sufficient bicarbonate was present for high-pH samples to reach equilibrium with atmospheric CO_2. Samples were then sparged with air to remove any excess CO_2. When samples of electrolyte containing 100 ppm or 1000 ppm Li electrolyte were assayed for Ni by graphite furnace atomic adsorption (GFAA), they were run with standards in a similar matrix.

The Wedron sand experiments were run using a solid:solution ratio of 1 g/m*l*; Kr-BET surface area measurements suggest that this corresponds to a surface area of ~80 m^2/l. The goethite concentration used was 1.25 mg/m*l* or 60 m^2/l, assuming the surface area of the goethite to be 48.5 m^2 (Balistrieri and Murray, 1979; Tripathi, 1983). The kaolinite concentration used was 5 mg/m*l*, or 124 m^2/l, using a measured N_2-BET surface area of 24.3 m^2/g.

The Li/Ni competition studies on pure minerals were run using 100 ppm Li (added as LiBr) and 100 ppb Ni. In an effort to evaluate the effect of irreversible sorption, each sample group was split into 2 subsets; half the samples were spiked with Li first, the other half with Ni. After equilibrating for 3–4 days, each set was then spiked with the other element, and allowed to re-equilibrate for 4–7 days before sampling.

A.2.5. Potentiometric Titrations

Potentiometric titrations involve monitoring the pH of a suspension as known amounts of acid or base are added. The difference between the observed pH at each

Table A.2. Experimental conditions for batch Li/Ni adsorption competition studies.

Study #	[Li] ppm	[Ni] ppb	P_{CO_2} (atm)	pH	Substrate	$\frac{\text{Solid}}{\text{Solution}}$ (g/m*l*)	SA (m^2/l)	Comments
1	100	100	0	4–10	Wedron sand	1	80	Moderate Li competition with Ni
2	1000	100	$10^{-3.5}$	4–10	Wedron sand	1	80	Moderate Li competition with Ni
3	100	100	$10^{-3.5}$	4–10	Goethite	1.24	60	No Li competition with Ni
4	100	100	$10^{-3.5}$	4–10	Kaolinite	5	124	Strong Li competition with Ni
5	0.1–10	80–5000	$10^{-3.5}$	~7.7	Wedron sand	1	80	Some Ni competition with Li

step and that expected for electrolyte alone (without any suspended material) is due to protonation/deprotonation of the surfaces of the suspensate. The electrostatic charge on the surfaces is then calculated from knowledge of its surface area and a model of surface complexation.

Potentiometric titrations followed the procedure described in Ward *et al.* (1995b), modified as follows. To minimize uptake of CO_2 from the air, fresh reagents were prepared at the beginning of each series of titrations. HCl was diluted from concentrated reagent-grade stock with Ar-sparged deionized water, and NaOH was prepared from the solid, using pellets from a bottle which was only opened under Ar purge. Reagents were standardized based on the volume required to change the pH of 300 m*l* 0.001 M NaCl from 4 to 10 (for NaOH) or 10 to 4 (HCl). This was repeated until three consistent values were obtained (Ward, 1995).

Titrations were performed from pH 10 down to 4 and then back to 10. Solid NaCl was then added to increase the ionic strength, and the titrations were repeated. The pH was considered to be stable after addition of an increment of reagent when 4 pairs of back-to-back readings of the electrode potential differed by less than ±0.15 mV. The required equilibration time was typically less than 1 min, so that elapsed time for the titration at each ionic strength was 80–180 min.

Both ionic strength and net added acid were calculated from mass balance, beginning from a well-defined set of initial conditions (initial ionic strength, total system volume, and pH), and strictly accounting for the effects of all reagent additions (HCl, NaOH, and NaCl) on ionic strength and net added acid (cf. Ward *et al.*, 1995b, Appendix E.6 Equation 7). Several minor adjustments were made to compensate for distinct jogs in the titration curves due to bubbles in the reagent tubing (these appeared as segments with an unusually small change in pH for the amount of reagent added) or refilling of a syringe (2–3 μl of reagent are expelled at the end of a filling cycle as the check valves are reseated, giving rise to segments with an unusually large change in pH for the amount of reagent added).

A.2.6. Precision and Accuracy of Measurements

BET. Xie and Walther (1992) have suggested that the effective surface area for kaolinite in contact with aqueous fluids may be an order of magnitude greater than the BET surface area. This discrepancy highlights the shortcoming of the BET method: the surface area is determined under vacuum with respect to adsorption of an inert gas but is being used to estimate the surface area in contact with an aqueous solution. Under aqueous conditions, interlayer surfaces of clays may become accessible, and gel layers can swell and become permeable, both leading to an increase in the available surface area. Although the reproducibility of the N_2-BET measurements is usually better than 1% at surface areas of 3 m^2/g or greater for separate aliquots of the same material, the accuracy varies widely among different materials so that differences from material to material of 20% or even more may not be meaningful. Surface area determinations for materials with very low specific surface areas are often difficult to reproduce; replicate determinations on some aliquots of sand varied by nearly 6%, providing an indication of the magnitude of statistically significant differences for surface areas < 0.1 m^2/g.

pH. The protocol used for pH measurements is described in Ward *et al.* (1995b, Appendix E.1). In buffered systems (e.g., "air-equilibrated"), pH measurements were reproducible to better than ± 0.03 pH units and display a similar level of accuracy relative to the calibration buffers (pH 4, 7 and 10). Two pairs of near replicate experiments provide the basis for this estimate. One pair examined fractional Ni adsorption by untreated Wedron sand at 100 ppb and 200 ppb total Ni (Ward *et al.*, 1995a). The two adsorption curves were indistinguishable. The second pair examined Ni adsorption by goethite alone or in the presence of 100 ppm Li (this study, section A.3.6.2). Again, the two curves were indistinguishable.

In unbuffered systems (e.g., nominally CO_2-free), the pH is extremely sensitive to perturbation from a variety of sources, including uptake by the sample of small quantities of CO_2 due to imperfect exclusion of air and contamination by the electrode from the electrolyte flowing from its porous. The precision of these measurements is best estimated from the scatter of the adsorption data about a best-fit curve.

Ni concentration. Measurement of Ni by graphite-furnace atomic absorption spectrophotometry is described in Siegel *et al.* (1995, Appendix E.3). Analyses of standards as unknowns indicates a precision of ± 1% or 0.2 ppb, whichever is greater. Deviations of actual samples may be slightly larger due to imperfect compensation of matrix effects, particularly at high pH in air-equilibrated systems where the ionic strength exceeds 0.5 M. Calculation of the fraction of Ni adsorbed in a batch experiment requires normalizing all Ni measurements to the measured concentration of the Ni spike, thus introducing an additional absolute uncertainty of ± 1%, for a total uncertainty of ± 2%. The relative uncertainty for adsorption measurements in the same experiment, however, remains only 1%.

Error bars are shown in the following graphs only when the errors exceed the size of the plotted symbols. In CO_2-free systems, the approximate errors are readily apparent from the scatter in the data.

A.3. Results

A.3.1. Surface Area Measurements

Surface areas of the adsorbents are reported in Table A.3. The surface area of Wedron 510 sand was previously reported as 0.12 m^2/g, measured by N_2-BET (Ward *et al.*, 1995a). The N_2-BET method, however, is poorly suited to determinations on materials with such low surface areas, and Kr-BET is preferable. The new Kr-BET measurements averaged 0.08 m^2/g for the raw sand and 0.06 m^2/g following acid-washing, and are used in this report. Numerous aliquots of Min-U-Sil 5 have been measured, with surface areas ranging from 4.05 to 5.81 m^2/g using N_2, and 2.93 to 3.84 m^2/g using Kr. The N_2-BET method is generally reliable at these surface areas (Davis and Kent, 1990), and the N_2 values are used in this report. Variations from aliquot to aliquot are thought to reflect true relative differences which arose either

Table A.3. Surface area determinations using the BET method. Either Kr or N_2 was the adsorbing gas.

Sample ID	n	Area (m²/g)	Precision (± 1 s.e.)	Outgassing T (°C)	Outgassing Time (h)
Krypton Measurements					
Min-U-Sil 5 -- SNL #1 (untreated)	2	3.84	± 0.07	200	2
Min-U-Sil 5 -- SNL #1 (acid-washed)	3	2.93	± 0.22	200	2 or 15
Wedron 510 Sand (untreated)	2	0.0798	± 0.0001	200	2 or 15
Wedron 510 Sand (acid-washed)	2	0.0590	± 0.0003	200	2 or 15
Nitrogen Measurements					
Goethite #4	3	39.9	± 0.01	100	60
Goethite #5	3	45.4	± 0.03	100	60
Kaolinite	3	24.6	± 0.03	100	15
"clay" from Wedron 510 sand	3	26.5	± 0.04	150	15
Min-U-Sil 5 -- SNL #1 (acid-washed, stored wet)	3	4.05	± 0.01	200	15
Min-U-Sil 5 -- SNL #2 (acid-washed, stored dry)	3	5.54	± 0.002	200	15
Min-U-Sil 5 -- SNL #2 (acid-washed, stored wet)	3	5.81	± 0.003	200	15
Min-U-Sil 5 -- BGS	3	4.70	± 0.01	200	15
Std.#A50118 -- 218 m²/g	6	216.3	± 0.3	90 or 350	1 or 4

during initial processing by U.S. Silica or during cleaning. The N_2-BET surface area of the kaolinite was determined to be 24.6 m^2/g

Measurements of surface area by N_2-BET on the goethite were 39.9, and 45.4 m^2/g. Prior to measurement, the powdered suspension residues were outgassed overnight (~15 h) under vacuum at 100 °C — higher temperatures would have risked loss of structural water and possible conversion to hematite. The differences in measured surface areas are probably attributable to variations in aging temperature, especially during the few minutes immediately following basification. Crystallite coarsening during prolonged storage cannot be ruled out, however, as the measured values are inversely correlated with length of storage as a suspension. Using material synthesized by the same method, Balistrieri and Murray (1979, 1981) have reported N_2-BET surface areas of 48.5 and 51.8 m^2/g, and van Geen *et al.* (1994) have reported a value of 45 m^2/g.

A.3.2. Goethite

Ni adsorption onto goethite was measured in batch systems with 0.001 M NaCl background electrolyte containing 3.7–5.4 or 41–55 m^2/l goethite surface area under both "CO_2-free" and air-equilibrated protocols. These measurements are plotted in Figure A.3. Adsorption at the higher surface concentrations is similar to that seen on Wedron sand in systems containing 78 m^2/l (Bryan *et al.*, 1995) and is consistent with the hypothesis that Fe-oxyhydroxide is the dominant adsorbent in the raw sand.

Ni-adsorption data for goethite rinsed with Ar-sparged water, plotted in Figure A.3, shows a negligible dependence on P_{CO_2}. For goethite batch #5, the "CO_2-free" and air-equilibrated data sets define essentially identical adsorption edges at goethite concentrations of 54 and 5.4 m^2/l. Goethite batch #4 had a lower specific surface area, which led to 10% lower goethite concentrations in the batch adsorption systems. Qualitatively, this appears to explain the observed differences in Ni adsorption between the two batches of goethite.

Potentiometric titrations were performed on goethite batch #5, with results plotted as surface charge (C/m^2) vs pH in Figure A.2. Changes in ionic strength over the course of each titration were due to the effects of reagent addition and the inherent leakage of 3 M KCl from the porous junction in the combination-pH electrode. The intersection of the curves for each ionic strength is the pH of zero salt effect (pH_{ZSE}), which in the absence of specific interactions between solution species (other than H^+) and the surface is the same as the pH of zero proton charge (pH_{ZPC}) and the pH of zero net charge (pH_{ZNC}). In these titrations, H^+ is the only

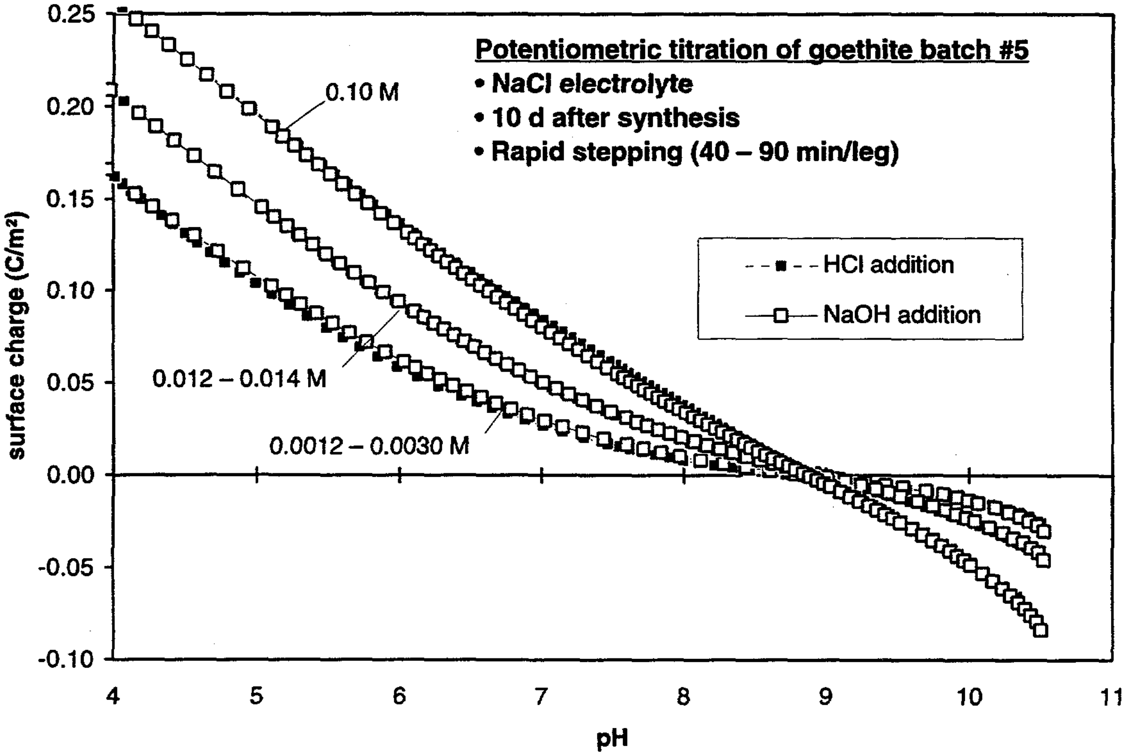

Figure A.2. Potentiometric titration of goethite batch #5.

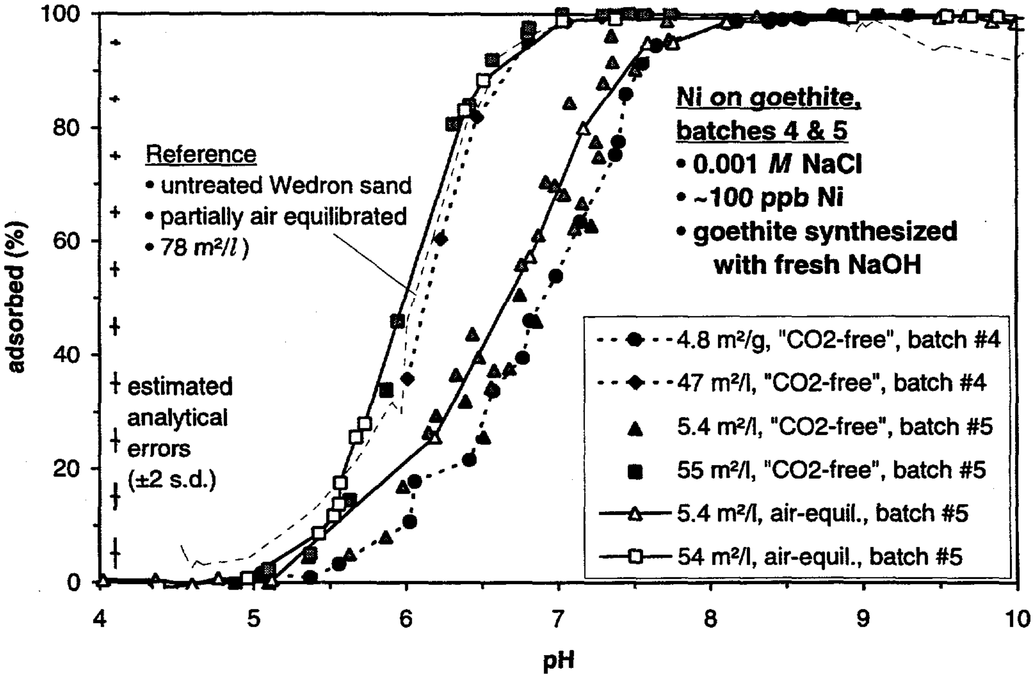

Figure A.3. Ni adsorption onto goethite. The data show the influence of variations in surface area and P_{CO_2} (nominally CO_2-free, or equilibrated with air), A curve for Wedron 510 sand is shown for reference (Bryan *et al.*, 1995).

potential-determining ion, and the pH of intersection will be referred to as the pH_{ZPC}.

Potentiometric titrations for goethite #5 (Figure A.2) define a $pH_{ZPC} = 8.9$, identical to that obtained by van Geen *et al.* (1994) but substantially higher than that reported by earlier workers (cf. Balistrieri and Murray, 1981). van Geen *et al.* suggest that earlier measurements were made in the presence of significant quantities of CO_2, which lowers the pH_{ZSE} by introducing another potential-determining ion (CO_3^{2-}).

A.3.3. Acid-washed Wedron 510 Sand

Ni adsorption onto acid-washed Wedron 510 sand in batch systems composed of 0.001 M NaCl background electrolyte and sand in a proportion of 1 m*l*:1 g (for an adsorbent surface area of 60 m^2 per liter of electrolyte) was measured under both CO_2-free and air-equilibrated conditions, as shown in Figure A.4. Reference curves for the raw sand under the same conditions are also shown. The acid-washed curves parallel the curves for the raw sand but are displaced toward lower pH by just over one unit. The pH_{50} values of the acid-washed sand are 4.9 and 5.0, respectively, for CO_2-free and air-equilibrated systems. Unexpectedly, acid-washing has left behind a much more reactive surface with respect to Ni adsorption. This observation is consistent the potentiometric titration data for the acid-washed sand (Ward *et al.*, 1995a), which implied that the effective surface area for the acid-washed sand in aqueous solution may be an order of magnitude greater than the 0.06 m^2/g measured by Kr-BET.

The effect of CO_2 on Ni adsorption by the acid-washed sand is reversed from that on the raw sand, with pH_{50} shifted to higher pH by ~0.1 instead of lower pH by ~0.2. Separate batches of sand were used for the air-equilibrated and "CO_2-free" experiments, however, so this variation is not significant. Adsorption on the acid-washed sand plateaus at 90–95% and then declines gradually with increasing pH. The similar but less pronounced effect seen above pH 9 for the raw sand was attributed to colloids penetrating the 0.2 μm filters used to sample the suspensions (Bryan *et al.*, 1995); the same phenomenon may have occurred to a greater extent with the acid-washed sand. Observations during sampling are consistent with this hypothesis — systems above pH 5 were visually turbid and difficult to force through the 0.2 μm syringe filters.

A.3.4. Min-U-Sil 5 Quartz

Ni adsorption onto Min-U-Sil 5 quartz, cleaned by boiling HCl or ignition/$HClO_4$, is shown in Figure A.5 along with reference curves for untreated

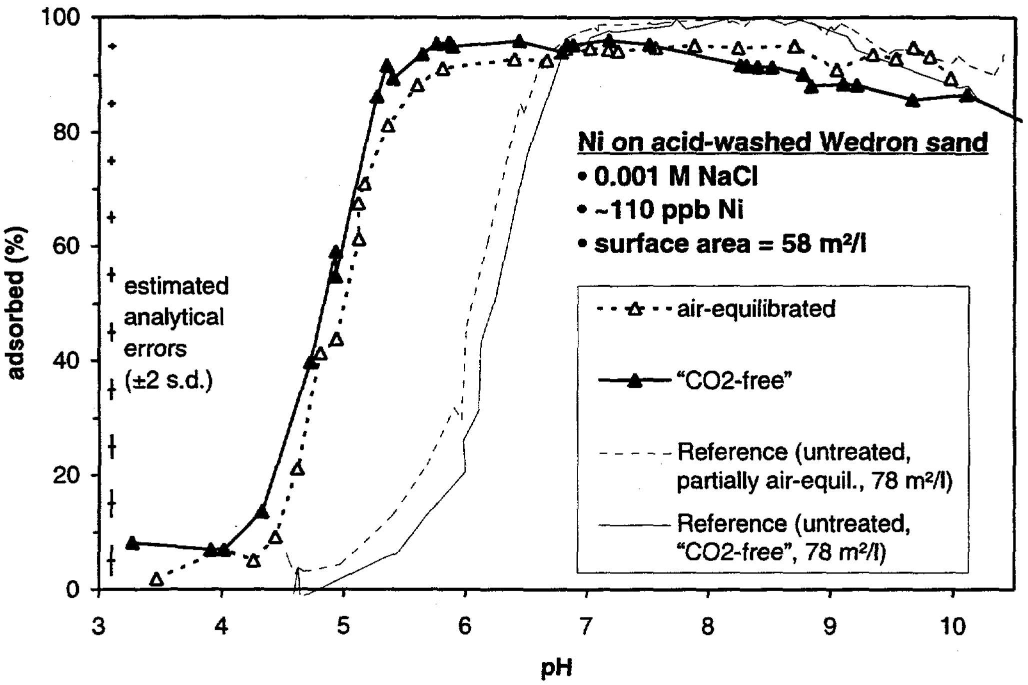

Figure A.4. Ni adsorption onto acid-washed Wedron sand. Air-equilibrated systems show slightly diminished adsorption relative to "CO_2-free" systems, probably attributable to variations among batches of acid-washed sand. Reference curves for raw Wedron 510 sand under similar P_{CO_2} conditions (Bryan *et al.*, 1995) show the opposite effect. Both curves were measured on aliquots taken from the same carefully homogenized container, so variations in the adsorbent are unlikely.

Wedron sand. In 0.001 M NaCl under CO_2-free conditions, Ni shows only a gradual increase in adsorption with increasing pH, without a sharp adsorption edge. This curve lacks any resemblance to either the raw or the acid-washed sand.

In 0.01 M NaCl equilibrated with air, with 50% less surface area, adsorption was substantially diminished and showed a dramatically different profile. At low pH, adsorption increased very slowly with pH, reaching only 20% at pH 7.5. Above this pH, an adsorption edge is apparent, with $pH_{50} = 8.3$, but with maximal adsorption of only 83% at pH 9.4 followed by a steep decline. Differences between the 0.001 and 0.01 M NaCl curves were not due to pretreatment, as results in 0.01 M NaCl using HCl-washed SNL stock (not shown) were essentially the same as for the ignition/$HClO_4$ BGS stock. Ni-carbonato species are present in inconsequential amounts at lower pH values, and the direct effect of dissolved CO_2 on Ni adsorption appears to be small, as seen in the curves for untreated Wedron sand, acid-washed sand and goethite (Figures A.3 and A.4). Therefore, the primary factor contributing

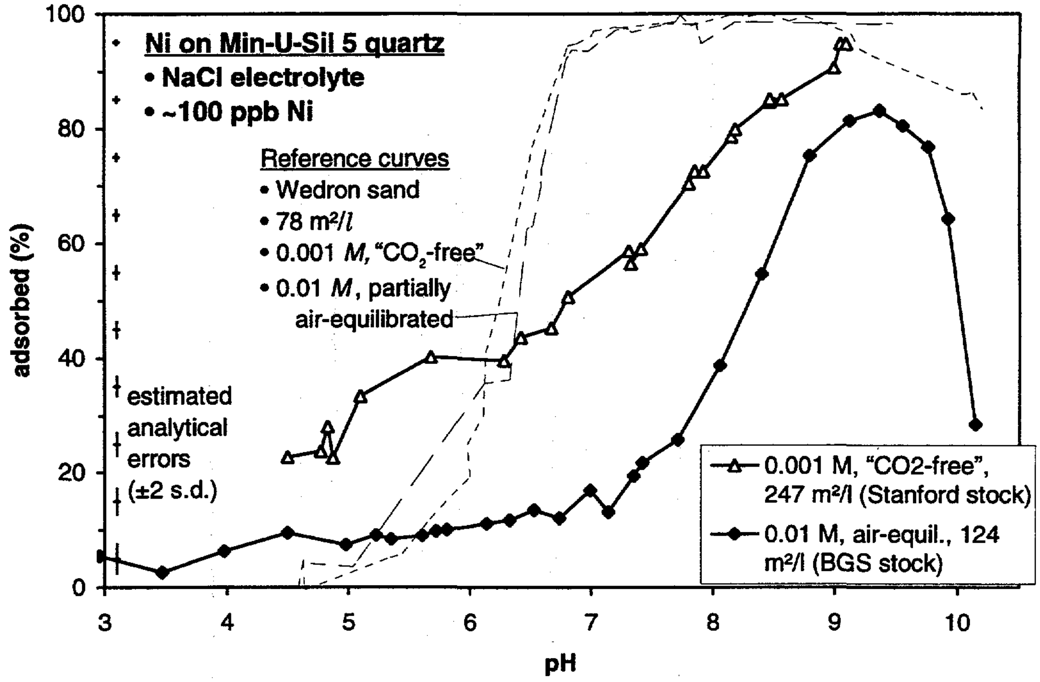

Figure A.5. Ni adsorption onto Min-U-Sil 5 quartz. Curves for untreated Wedron sand at similar ionic strengths are included for reference.

to diminished adsorption at 0.01 M NaCl is probably the order-of-magnitude increase in ionic strength.

As shown by the reference curves in Figure A.5, sensitivity to ionic strength is not a characteristic of the raw sand (Bryan *et al.*, 1995). This, and the dramatic difference in shape of the adsorption curves between Min-U-Sil 5 quartz and Wedron 510 sand suggest that quartz surfaces play a negligible role in Ni adsorption onto the sand in both the raw and acid-washed states.

A.3.5. Kaolinite

Ni adsorption onto kaolinite is shown in Figure A.6, along with reference curves for acid-washed and raw Wedron 510 sand, all under air-equilibrated conditions in 0.001 M NaCl. For an estimated BET-measured surface area of 124 m^2/l, the kaolinite shows an adsorption edge at $pH_{50} = 4.2$ with a profile much like the sand curves. If kaolinite were the major adsorbent in the acid-washed sand, application of the law of mass action suggests that in order to shift the adsorption edge to $pH_{50} = 5.0$, the concentration of kaolinite should be reduced by a factor of $10^{-(5.0-4.2)} = 0.16$, giving a surface area (19.8 m^2/l) that accounts for only about 34% of that exposed by the acid-washed sand. If the remaining area were quartz, its

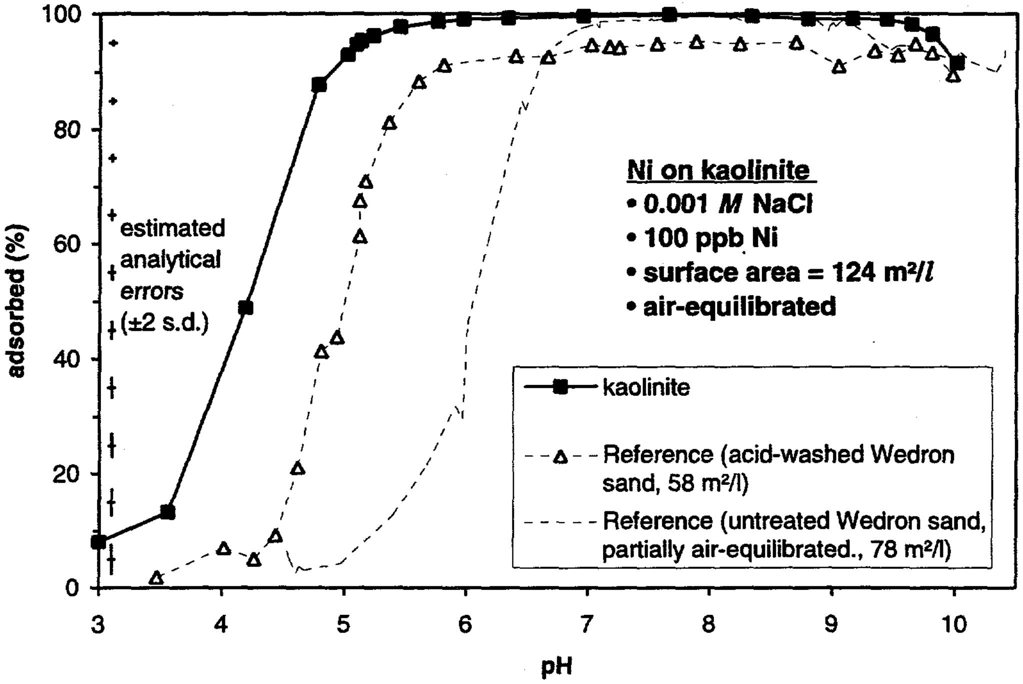

Figure A.6. Ni adsorption onto kaolinite. Curves for both acid-washed (see Figure A.4) and untreated (Bryan, *et al.*, 1995) Wedron 510 sand are included for reference.

contribution to Ni adsorption would be undetectable. If the effective surface area of the kaolinite is greater than the BET-measured surface area, as discussed previously, then the unreactive surface area of the sand would be even greater.

A.3.6. Sorption Competition Studies

A.3.6.1 Wedron Sand studies

Figure A.7 shows the results of the 100 ppm Li/100 ppb Ni test on Wedron sand that was run in a glove box under CO_2-free conditions. As with previous competition studies at lower Li concentrations (10-17 ppm) (Bryan *et al.*, 1995), the Ni sorption curve is shifted towards higher pH relative to the Li-free Ni adsorption curve, suggesting that Li competes with Ni. The order in which the tracer elements are added has a slight effect on the location of the adsorption curves; Ni adsorption appears to be slightly higher in those samples to which Ni was added first. This suggests that some of the Ni is adsorbing irreversibly. Alternatively, because kinetic studies show that Li adsorption is slow to reach equilibrium, perhaps Li/Ni

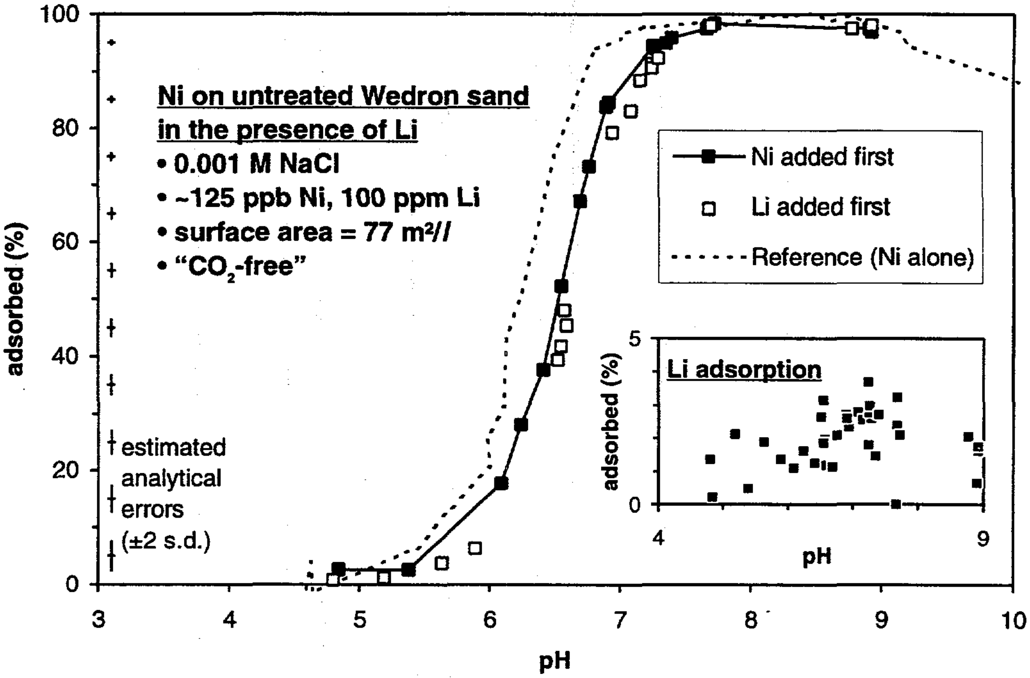

Figure A.7. Ni adsorption onto Wedron sand in the presence of 100 ppm Li. Adsorption of Ni alone is shown for reference. Inset shows Li adsorption onto the sand in the same experiment.

exchange is also slow, and insufficient time was allowed for equilibrium to be reached.

The 1000 ppm Li/100 ppb Ni experiment was run in equilibrium with atmospheric CO_2. The data are somewhat scattered (Figure A.8), as the high LiBr concentration in the electrolyte resulted in changes in the graphite furnace response during Ni analysis, causing severe drift and erratic response. The adsorption edge is not shifted relative to the edge for Ni in 100 ppm Li electrolyte. At low pH, the curve levels out at about 20% adsorption. The given adsorption curve was calculated assuming 35 ng/g exchangeable Ni in the sand, a number determined from several previous experiments (Bryan *et al.*, 1995). If this number is reduced to 12 ng/g, then the Ni adsorption curve levels out at 0% adsorbed rather than 20%.

Figure A.9 summarizes the results of the study conducted at higher Ni concentrations and several Li concentrations to determine the effect of Ni/Li competition on Li adsorption by Wedron sand under atmospheric conditions. Only the 1 ppm Li curve shows a decrease of adsorption with increasing Ni concentration; curves at higher and lower Li concentrations, 10 ppm and 100 ppb, respectively, show no systematic variation in Li adsorption with Ni concentration.

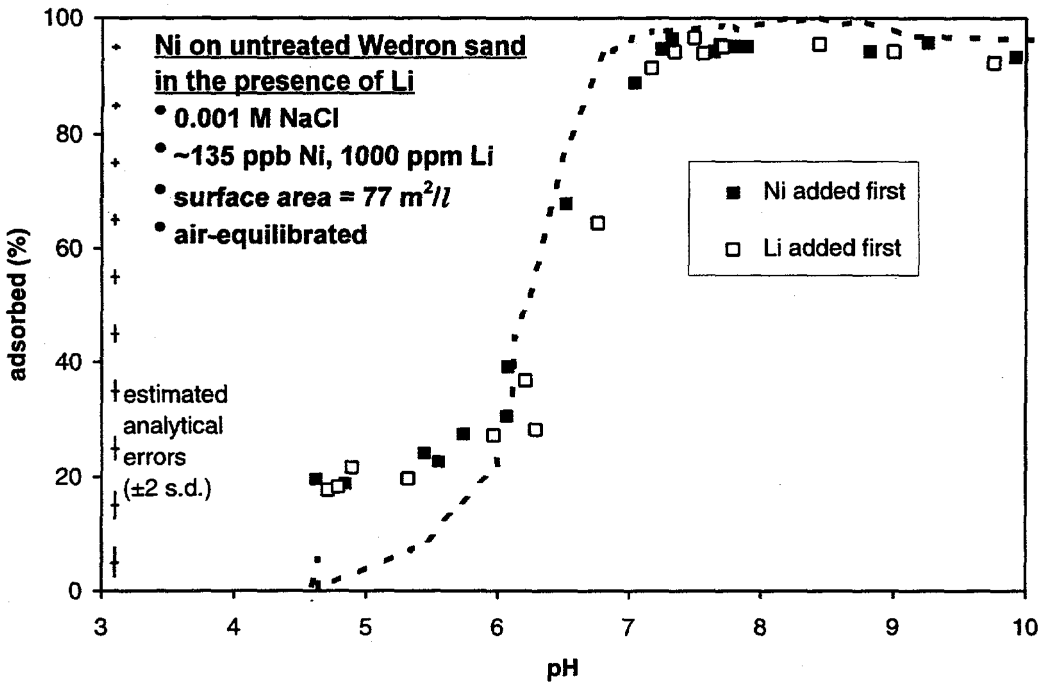

Figure A.8. Ni adsorption onto Wedron sand in the presence of 1000 ppm Li. The adsorption curve for 100 ppb Ni in a Li-free Wedron sand system is included for reference.

A.3.6.2. Goethite study

The site-competition study on goethite yielded very different results from those on the sand. The experiment was run under atmospheric conditions, using synthetic goethite with an estimated surface area of 60 m^2/*l*. The adsorption curves for 100 ppb Ni in the presence of 100 ppm Li and for a Li-free 100 ppb Ni system coincide perfectly, indicating that Li does not compete with Ni on the goethite (Figure A.10).

A.3.6.3. Kaolinite study

The kaolinite site-competition study was run under atmospheric conditions, using kaolinite with a BET-estimated surface area of 124 m^2. The results (Figure A.11) show that Li competes strongly with Ni for adsorption sites on kaolinite. The 100 ppb Ni/100 ppm Li adsorption curve is shallower and is shifted to higher pH than the Li-free 100 ppb Ni curve. The shape and slope of this curve is very different than that produced by Wedron sand or goethite under similar conditions (Figure A.3 on p. A-13). There is a pronounced hump in the curve is a result of the shallowing of the slope above pH = 5.5; this is probably caused by an increase in

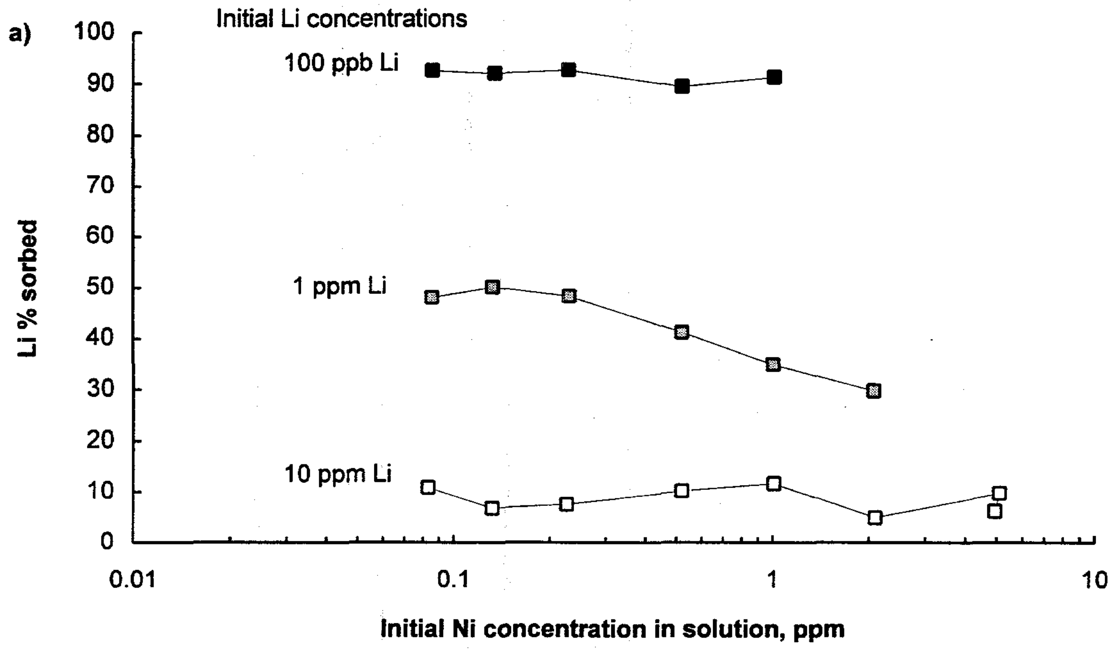

Figure A.9. The effect of Ni solution concentration on the adsorbance of Li by Wedron 510 sand at pH ~7.7. Run under atmospheric conditions.

competition with Li; Li adsorption increases significantly above this pH (see inset graph in Figure A.11).

A.4. Thermodynamic Modeling

A.4.1. Introduction

Goethite is a promising analog for Ni adsorption onto Wedron 510 sand, giving an adsorption edge which closely resembles that for the sand. Of the two other important components of the sand, kaolinite also has the potential to explain the observed patterns of Ni adsorption, whereas quartz is comparatively inert over the pH range of interest. A triple-layer model of surface complexation of Ni^{2+} onto goethite was developed in Siegel *et al.* (1995) based on a single set of Ni adsorption data at a presumed surface concentration of 6 m^2/l in 0.001 M NaCl partially equilibrated with air. Ni^{2+} was modeled as an inner-sphere complex adsorbing to a single deprotonated surface site according to the reaction $SO^- + Ni^{2+} \leftrightarrow SONi^+$. Aqueous Ni-carbonato species thought to be favored at high pH were eliminated from consideration by setting $P_{CO_2} = 10^{-6}$ atm in the model, and the equilibrium constant for adsorption was adjusted to obtain a visual best-fit to the experimental

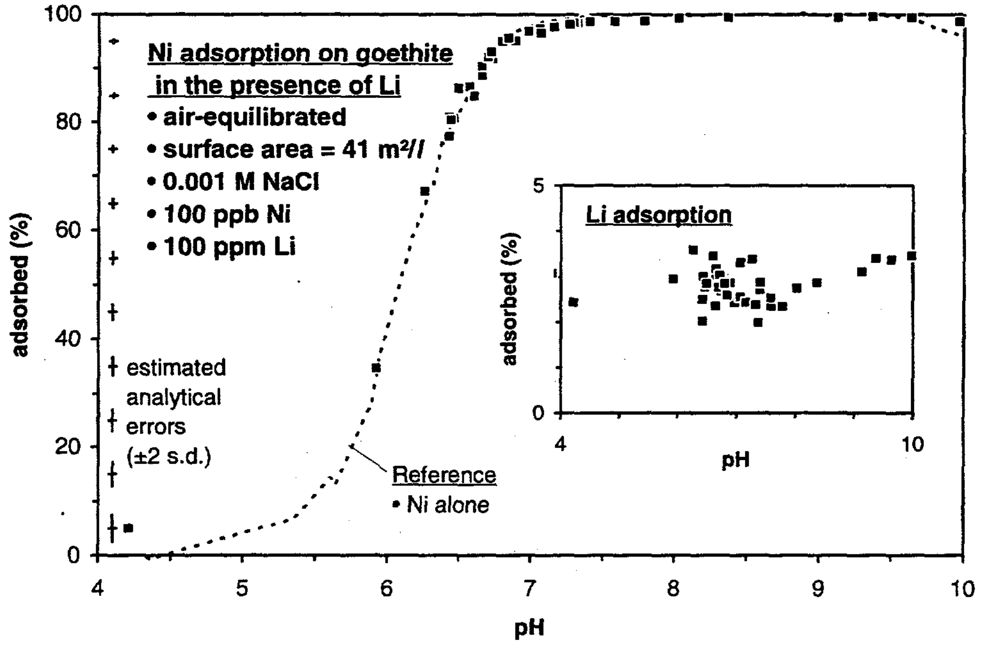

Figure A.10. Ni adsorption onto goethite in the presence of Li. Adsorption of Ni alone shown for reference. Inset shows Li adsorption onto goethite in the same experiment.

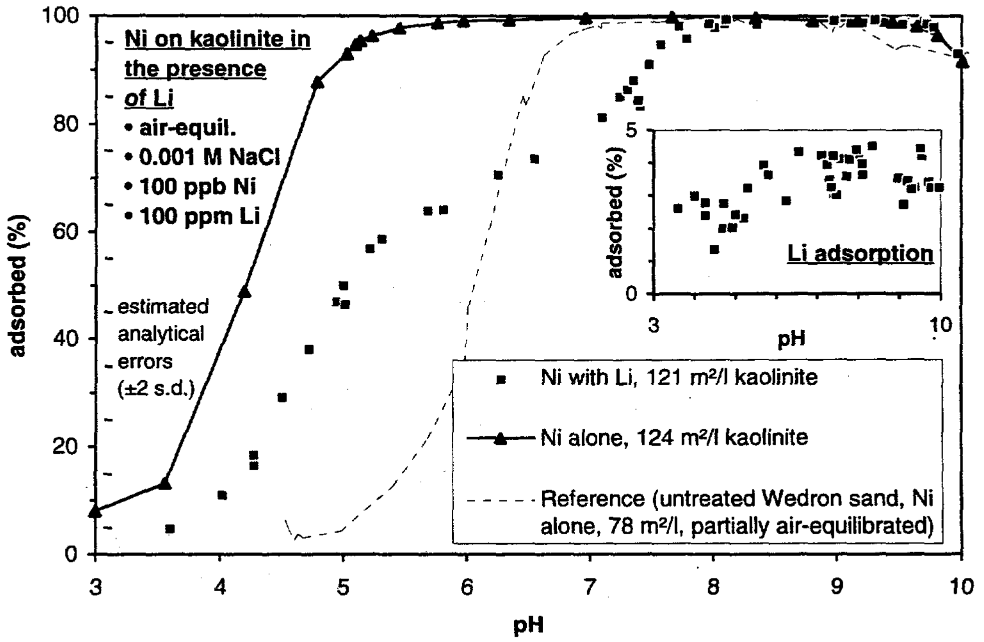

Figure A.11. Ni adsorption onto kaolinite in the presence of Li. Adsorption of Ni alone shown for reference, to illustrate the much greater affinity of kaolinite for Ni. Inset shows Li adsorption onto kaolinite in the same experiment.

data, giving log $K_{fm}(SONi^{+}) = -1$. Next, the surface area of goethite necessary to mimic the sand (65 m^2/l) was found by increasing the surface area in the goethite model until the calculated curve fit the observed adsorption of Ni onto raw Wedron 510 sand in 0.001 M NaCl partially equilibrated with air. The equilibrium-speciation and surface-complexation code HYDRAQL (Papelis, 1988) was used to perform these calculations.

Although internally consistent, this model is perhaps too simplistic and has several shortcomings: 1) The experimental data only poorly constrain the shape and location of the adsorption edge. More recent data (cf. Figure A.3) show that the adsorption edge at low goethite concentration has a shallower slope than was previously assumed (i.e., parallel to the adsorption edge for Wedron sand). 2) The role of CO_2 on the goethite surface was ignored. This is unrealistic in light of the new data presented here suggesting an important role for irreversibly adsorbed CO_2, and in consideration of the recent study by van Geen *et al.* (1994) measuring reversible CO_2 adsorption at the goethite surface. 3) The role of CO_2 in stabilizing dissolved Ni was bypassed by setting P_{CO_2} in the model to an unrealistically low value. A review of the literature failed to find any experimental determinations of stability constants for Ni-carbonato complexes, so the current experimental work may have interesting implications. 4) The specific surface area of the goethite used in the earlier study (goethite batch #1) had not yet been measured; its actual value appears to have been 35.5 m^2/g instead of the presumed 48.5 m^2/g. Such a difference is not critical, being easily compensated for by adjustments to other model parameters, but hinders intercomparison with other studies.

In this section, a more rigorous and complete model for Ni adsorption by goethite, kaolinite and quartz is presented. An internally consistent set of equilibrium constants for plausible aqueous Ni species is developed, based in part on experimental constraints on the stability of Ni-carbonato complexes and probable P_{CO_2} values for the "CO_2-free" goethite batch systems. Thermodynamic calculations are carried out with HYDRAQL 94 (Ward, 1995), a revised version of HYDRAQL. Two models (single-site and two-site) are proposed for Ni adsorption onto goethite and used to predict the possible fraction of surfaces in Wedron sand covered by Fe-oxyhydroxides. A preliminary surface complexation model for quartz is developed based on potentiometric and Ni adsorption studies carried out at Sandia and at the British Geological Survey (Mark Crawford, letter to CHEMVAL2 participants dated 15 November 1993). Finally, a surface complexation model for Ni adsorption by kaolinite is developed based on experimental work described above and previous work by Riese (1982).

A.4.2. Modeling Software

Two programs were used for chemical speciation and surface-complexation calculations: FITEQL 2.0 (Westall, 1982), a generalized least-squares non-linear regression program, and HYDRAQL 94 (Ward, 1995), a modified version of HYDRAQL (Papelis *et al.*, 1988). These programs were used to adjust selected equilibrium constants and surface-complexation parameters by obtaining a best-fit between calculated and measured adsorption and surface-charge curves.

Although tedious to use, FITEQL allows exact specification of the concentrations of all components at each step in a titration or series of batch adsorption experiments. Functionally, it minimizes the sum of the squares of the residuals (weighted by the estimated precision of the data) for those components whose free and total concentrations are specified. The value of this sum, divided by the number of degrees of freedom is the variance of the experimental measurements with respect to the model. Unfortunately, the standard version of FITEQL can accommodate only 10 components, whereas twelve are necessary to completely specify the two-site triple-layer model of Ni adsorption as a function of ionic strength. As a result of the present limitations, manual corrections for ionic strength were made, eliminating the need for one component, and mathematically optimized adsorption parameters could thus be obtained for the single-site model.

HYDRAQL is a convenient tool for generating titration, solubility, or adsorption curves from a specified set of formation constants and initial and boundary conditions. Optimization of speciation and surface-complexation parameters was achieved by visually estimating the best fit between calculated and measured adsorption and surface-charge curves. Activity corrections are made using the Davies equation (Davies, 1962), which is valid up to an ionic strength of 0.5 M, but charge balance is not required (except in the electrical double layer), so that calculations for systems containing a species with fixed activity (e.g. $a_{H_2CO_3}$ when P_{CO_2} is fixed) or activity product (e.g., $a_{Ni^{2+}}$ controlled by the solubility of $Ni(OH)_2$) can indicate large charge imbalances due to the absence of an automatically introduced counter-ion. Additionally, a bug was encountered during pH-stepping operation in which activity corrections to the intrinsic equilibrium constants were not updated after the first pH step. For aqueous species involved in surface reactions, HYDRAQL uses the activity model of Hayes and Leckie (1987), which subsumes all activity corrections into the electrostatic term. The program was modified, fixing the pH-stepping bug, permitting overall charge-balance optimization, and including the Davies activity correction for aqueous species involved in surface reactions. The modified version is referred to as HYDRAQL 94, and is documented in Ward (1995).

Several test problems were calculated using FITEQL and HYDRAQL 94 to verify that the problems had been properly posed for each program and that each program produced the same output given identical input. For speciation of the system Na^+– Cl^-– CO_3^{2-} at pH 9.5 the two programs were in exact agreement with each other (to the limit of the output precision of three significant figures) as well as with the manually calculated value. For calculation of surface charge on goethite as a function of pH, the agreement was close, with deviations attributable at least in part to rounding errors as the input data were translated from one format to the other (FITEQL uses $\log[H^+]$ instead of pH, and FITEQL was supplied with apparent equilibrium constants whereas HYDRAQL 94 calculated activity corrections from the species concentrations).

A.4.3. Thermodynamic Database for Ni Speciation

An internally consistent set of formation constants (K_{fm}) for expected aqueous complexes in the system H_2O–Na^+–Cl^-–CO_3^{2-}–Ni^{2+} is presented in Table A.4, and corresponding free energies of formation (ΔG_f^o) are presented in Table A.5. These values differ slightly in some cases from those used in Siegel *et al.* (1994) or in the HYDRAQL database (Papelis *et al.*, 1988), but do not cause significant changes in calculated Ni speciation. Constants for Ni complexes have been traced back at least to their first appearances in critical compilations, or to the original work in the case of $NiCl^+$. See Ward (1995) for a more detailed discussion of literature sources.

No published experimental work on aqueous Ni-carbonato species has been found. The work of Mattigod and Sposito (1977) provides the only available estimates of the stabilities of $NiHCO_3^+$ and $NiCO_3^o$, based on the electrostatic ion-pairing model of Kester and Pytkowicz (1975), and of $Ni(CO_3)_2^{2-}$, based on the empirical model of Van Panthaleon Van Eck (1953) for the relationship between the first association constant, the stepwise association constant, and the number of coordinating ligands at each step. An in-depth review of these methods is beyond the scope of this discussion.

The P_{CO_2} of these systems cannot be reconstructed from the experimental data, however, because of the large uncertainty in the total amount of added acid because of the Ar contamination problems. A rough inference is obtained from estimates of P_{CO_2} in the goethite batch systems, in which a maximum total carbonate concentration of 5×10^{-5} M was calculated for batch systems equilibrated in a glove bag under N_2 for less than a week (cf. section A.4.4.2 *Apparent Partial Pressures of CO_2 in Goethite Batch Experiments*). When the solubility of $Ni(OH)_2$ is calculated using the constants of Mattigod and Sposito (1977), only agreement with the observations was obtained. As depicted in Figure A.12, Ni solubility at low pH is underestimated by several orders of magnitude when $K_{fm}(Ni(OH)_2)$ was chosen so as to fit the observations at high pH (curve with — - — - pattern). Although some

Table A.4. Thermodynamic equilibrium constants for formation (K_{fm}) of important species. The chemical system is defined by the components H_2O–Na^+–Cl^-–CO_3^{2-}–Ni^{2+}. In some cases, K_{fm} values were calculated from the change in free energy for the reaction (ΔG°_{rxn}) using the ΔG_f° values listed Table A.5 and the relation $\log(K_{fm}) = -\Delta G^{\circ}_{rxn} / 5.707$.

Reaction	log K_{fm}	Reference
Aqueous Ni Species		
$Ni^{2+} + H_2O = NiOH^+ + H^+$	-9.86	Baes and Mesmer (1976)
$Ni^{2+} + 2H_2O = Ni(OH)_2^{\circ} + 2H^+$	-19.	Baes and Mesmer (1976)
$Ni^{2+} + 3H_2O = Ni(OH)_3^- + 3H^+$	-30.	Baes and Mesmer (1976)
$Ni^{2+} + 4H_2O = Ni(OH)_4^{2-} + 4H^+$	-44.	Baes and Mesmer (1976)
$2Ni^{2+} + H_2O = Ni_2OH_3^+ + H^+$	-10.7	Baes and Mesmer (1976)
$4Ni^{2+} + 4H_2O = Ni_4(OH)_4^{4+} + 4H^+$	-27.74	Baes and Mesmer (1976)
$Ni^{2+} + Cl^- = NiCl^+$	-0.43	Libus and Tialowska (1975)
$Ni^{2+} + 2Cl^- = NiCl_2^{\circ}$	0.96	Mattigod and Sposito (1977)
$Ni^{2+} + CO_3^{2-} = NiCO_3^{\circ}$	6.87	Mattigod and Sposito (1977)
	4.87	This study.
$Ni^{2+} + 2CO_3^{2-} = Ni(CO_3)_2^{2-}$	10.11	Mattigod and Sposito (1977)
	8.11	This study.
$Ni^{2+} + CO_3^{2-} + H^+ = NiHCO_3^+$	12.47	Mattigod and Sposito (1977)
Other Aqueous Species		
$H_2O = H^+ + OH^-$	-13.99	Stumm and Morgan (1981)
$CO_3^{2-} + H^+ = HCO_3^-$	10.33	*calculated from* ΔG_f°
$CO_3^{2-} + 2H^+ = H2CO_3^{\circ}$	16.69	*calculated from* ΔG_f°
$CO_3^{2-} + 2H^+ = H_2O + CO_2(g)$	18.16	*calc. from* ΔG_f°; P_{CO_2} in atm.
$Na^+ + CO_3^{2-} = NaCO_3^-$	0.77	Butler and Huston (1970)
$Na^+ + CO_3^{2-} + H+ = NaHCO_3^{\circ}$	10.03	Butler and Huston (1970)
Solid Ni compounds		
$Ni^{2+} + 2H_2O = Ni(OH)_2 + 2H^+$	-12.73	*calculated from* ΔG_f°
aged at 110 °C	-10.8	Baes and Mesmer (1976)
freshly precipitated	-13.3	Baes and Mesmer (1976)
	-11.6	This study.
$Ni^{2+} + CO_3^{2-} = NiCO_3$	6.85	*calculated from* ΔG_f°

Table A.5. Free energies of formation (ΔG_f°) for components and important species in the system H_2O–Na^+–Cl^-–CO_3^{2-}–Ni^{2+}. To ensure internal consistency, ΔG_f° values from the critical compilation of Wagman *et al.* (1982) form the basis set for values calculated from equilibrium formation constants (K_{fm} values, Table A.4). Standard states are 1 molal activity for electrolytes, 0.1 MPa (1 bar) for gases, at 298.15 K. To convert to units of atm for a reaction, $\Delta G_{rxn}^\circ(atm) = \Delta G_{rxn}^\circ(MPa) + 0.03263n$, where n is the net increase in moles of gas.

Species	ΔG_f° (kJ/mole)	Reference	Species	ΔG_f° (kJ/mole)	Reference
Components			*Other Aqueous Complexes*		
H^+	0.000	*(by definition)*	OH^-	-157.261	*calculated from K_{fm}*
H_2O	-237.129	Wagman *et al.* (1982)	HCO_3^-	-586.77	Wagman *et al.* (1982)
Na^+	-261.905	Wagman *et al.* (1982)	$H2CO_3^\circ$	-623.08	Wagman *et al.* (1982)
CO_3^{2-}	-527.81	Wagman *et al.* (1982)	$CO_2(g)$	-394.36	Wagman *et al.* (1982)
Cl^-	-131.228	Wagman *et al.* (1982)	$NaCO_3^-$	-794.1	*calculated from K_{fm}*
Ni^{2+}	-45.6	Wagman *et al.* (1982)	$NaHCO_3^\circ$	-847.0	*calculated from K_{fm}*
Aqueous Ni Complexes			*Solid Ni compounds*		
$NiOH^+$	-226.5	*calculated from K_{fm}*	$Ni(OH)_2$	-447.2	Wagman *et al.* (1982)
$Ni(OH)_2^\circ$	-411.4	*calculated from K_{fm}*	aged	-458.	*calculated from K_{fm}*
$Ni(OH)_3^-$	-585.8	*calculated from K_{fm}*	fresh	-444.	*calculated from K_{fm}*
$Ni(OH)_4^{2-}$	-743.0	*calculated from K_{fm}*	$NiCO_3$	-612.5	Wagman *et al.* (1982)
$Ni_2OH_3^+$	-267.3	*calculated from K_{fm}*			
$Ni_4(OH)_4^{4+}$	-972.6	*calculated from K_{fm}*			
$NiCl^+$	-174.4	*calculated from K_{fm}*			
$NiCl_2^\circ$	-313.5	*calculated from K_{fm}*			
$NiCO_3^\circ$	-612.6	*calculated from K_{fm} of Mattigod and Sposito (1977)*			
$Ni(CO_3)_2^{2-}$	-1113.	*calculated from K_{fm} of Mattigod and Sposito (1977)*			
$NiHCO_3^+$	-645.	*calculated from K_{fm} of Mattigod and Sposito (1977)*			

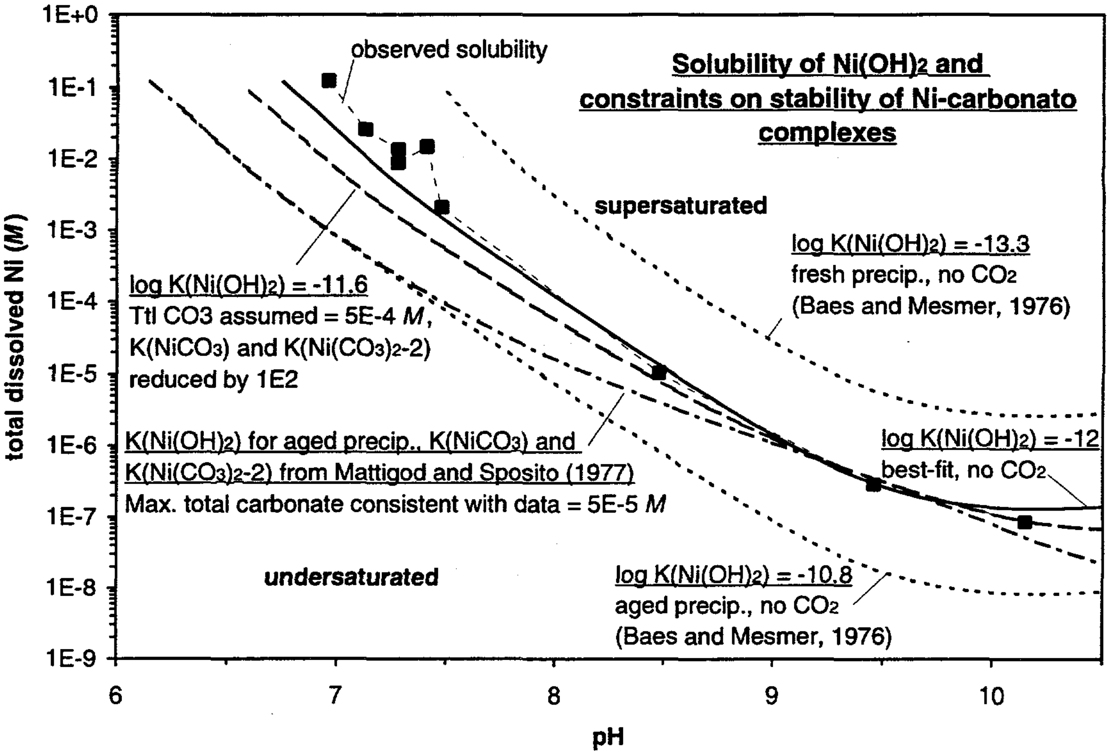

Figure A.12. Measured and calculated Ni solubility. Measurements are from Bryan *et al.* (1995). A reasonable fit to the experimental data was obtained by reducing the formation constants for $NiCO_3$ and $Ni(CO_3)_2^{2-}$ by two orders of magnitude each.

variation with pH of the properties of the precipitate are possible, it seems unlikely that such variations could account for such a large discrepancy. Alternatively, the K_{fm} values for the Ni carbonato species are too large. An alternate set of values is derived below.

The first step was to obtain a realistic estimate of total CO_2 present in the batch systems used for the solubility measurements. In consideration of the tortuous history of the Ni-solubility batch systems, and that they were equilibrated in air on the laboratory benchtop, the value estimated above for the glove-bag equilibrated batch systems 5×10^{-5} M is probably too low. The total CO_2 in the solubility experiment was certainly higher but by an unknown amount. An arbitrary value an order of magnitude larger was selected, 5×10^{-4} M, for speciation calculations. Because this value is somewhat larger than that inferred for partially air-equilibrated batch systems (~2×10^{-4} M), the results of these calculations may constitute a lower limit on the stability of Ni carbonato complexes.

Using the thermodynamic equilibrium constants presented in Table A.4, total dissolved Ni in equilibrium with solid $Ni(OH)_2$ was calculated as a function of pH using HYDRAQL 94. Two limiting cases are shown in Figure A.12 (shown by the ------- pattern): systems without CO_2 in equilibrium with (1) freshly precipitated or (2) aged $Ni(OH)_2$. These cases bracket the experimental data, which are well described by an intermediate value of $K_{fm}(Ni(OH)_2)$ in the absence of CO_2. As mentioned above, when the "CO_2-free" batch-system total carbonate value of 5×10^{-5} M is used, a reasonable fit can be obtained for the points at pH 8.5, but only at the expense of seriously underestimating Ni solubility at low pH (<8). When the estimated total carbonate value of 5×10^{-4} M is used, a more reasonable fit is obtained when the formation constants for $NiCO_3^o$ and $Ni_2(CO_3)_2^{2-}$ were reduced by two orders of magnitude each. This gives the fit shown in Figure A.12 by long dashes (— — —). The third Ni-carbonato complex, $NiHCO_3^+$, is not an important species in solution and thus has little effect on calculated solubilities, so its formation constant was not adjusted.

The probable aqueous speciation of Ni can now be calculated, and is shown in Figure A.13 for the case in which CO_2 is entirely absent, and for air-equilibrated conditions ($P_{CO_2} = 10^{-3.5}$ atm) with the equilibrium constants of Mattigod and Sposito (1977) or the reduced constants proposed above. As may be seen in Figure A.13b, the reduced constants extend the predominance of Ni^{2+} to nearly pH 8.5, so that Ni-carbonato species are of little concern over the pH range of interest for adsorption (pH 5–8). Calculated Ni speciation for the upper and lower limits of total CO_3^{2-} in the solubility experiment is shown in Figure A.14. All Ni adsorption modeling performed in this study uses the reduced values of the Ni-carbonato complexation constants. Had the larger values of Mattigod and Sposito been used, calculated adsorption would have been substantially lower at high pH, inconsistent with experimental observations.

A.4.4. Triple-Layer Surface-Complexation Model for Goethite

A.4.4.1. Triple-Layer Model for Protolysis and Electrolyte Binding Constants

A list of parameters for the triple-layer surface-complexation model (Yates *et al.*, 1974; Davis *et al.*, 1978), their definitions and values, and their sources is presented in Table A.6. The species vs. component matrix required to implement the model in FITEQL is given in Table A.7. FITEQL was used to extract optimum values of three parameters for the triple-layer model, including the inner-layer capacitance (C_1), and formation constants for electrolyte binding ($K_{fm}(SO\text{-}Na)$ *and* $K_{fm}(SOH_2\text{-}Cl)$). Model performance is not usually improved by allowing more parameters to be adjustable (Hayes *et al.*, 1990). Formation constants for the protonated and deprotonated surface species ($K_{fm}(SOH_2^+)$ and $K_{fm}(SO^-)$) were taken

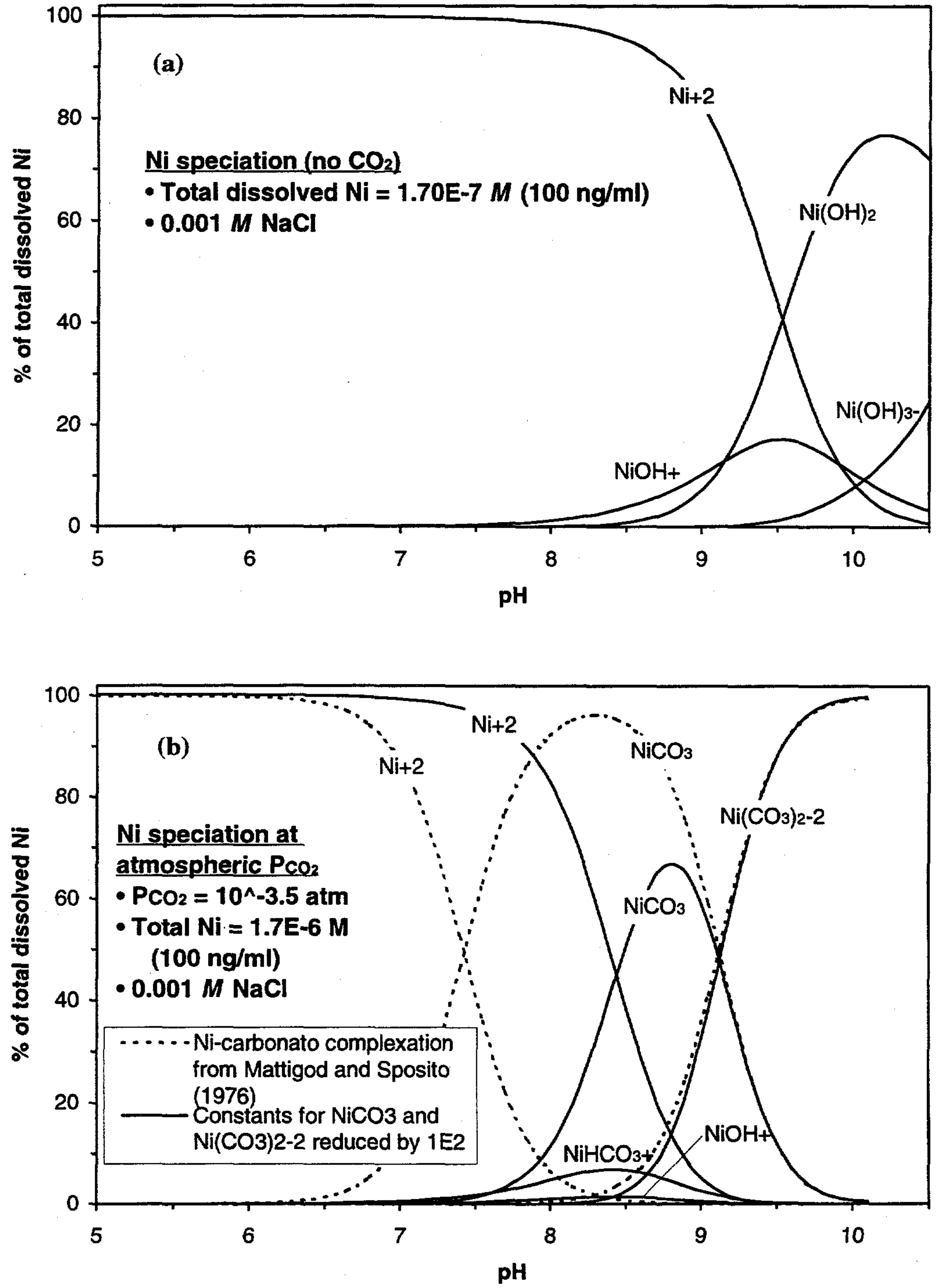

Figure A.13. Calculated speciation of Ni in 0.001 M NaCl. Possible precipitation of $Ni(OH)_2$ was not considered. (a) CO_2 absent. (b) A comparison of the effects of Ni-carbonato complexes at atmospheric P_{CO_2} for literature values of the stability constants and for the proposed reduced constants.

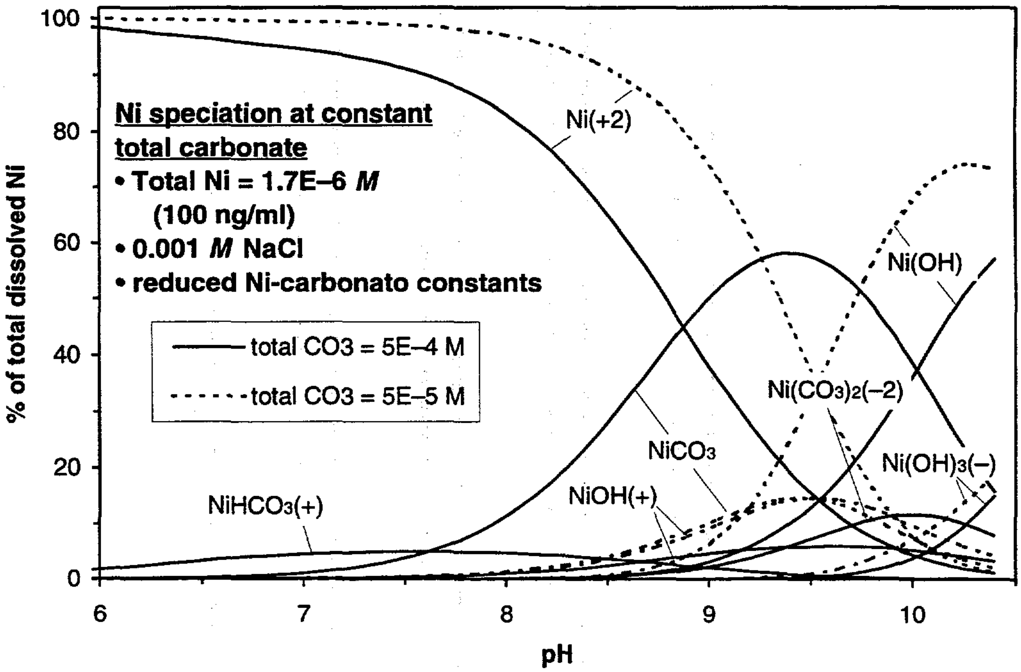

Figure A.14. Calculated speciation of Ni at constant total CO_3^{2-}. Speciation was calculated for upper and lower limits of total CO_3^{2-} in the solubility experiment.

from the work of van Geen *et al.* (1994) in order to reduce the number of adjustable parameters and because their values are consistent with the observed pH_{ZPC}. Their model (stoichiometry and formation constant) for adsorption of CO_3^{2-} by goethite was also used. The outer-layer capacitance (C_2) was fixed at the value proposed by Davis *et al.* (1978) for consistency with zeta-potential measurements, and the site density value (2.31 sites/nm^2) is that advocated by Davis and Kent (1990) to facilitate intercomparison of modeling efforts.

For FITEQL optimization, subsets of the potentiometric titration data on goethite #5 were selected to minimize the change in ionic strength from start to finish of each curve (the ionic strength specified for the electrical double layer model in FITEQL is separate from that for the bulk solution and may not be adjusted during iteration on ionic strength). Only the curves titrated with NaOH were used, and although many points were omitted in order to make the FITEQL input file more manageable, the precision of the fitted parameters should not have been affected (Hayes *et al.*, 1990). The selected points and the FITEQL model are shown in Figure A.15. FITEQL was run in ionic-strength-iteration mode, enabling it to report intrinsic rather than apparent formation constants. Because C_1 is not a parameter for which FITEQL can optimize, runs were made over a range of values of C_1 and the resulting electrolyte binding constants and goodness-of-fit value

Table A.6. Parameters and values for the triple-layer surface-complexation models of Ni adsorption onto goethite.

Parameter	Value	Source
Inner-layer capacitance (C_1)	1.20 F/m^2	This work.
Outer-layer capacitance (C_2)	0.20 F/m^2	Davis *et al.* (1978)
Site density	2.31 sites/nm^2	As advocated by Davis and Kent (1990).
Fraction of high Ni affinity sites	0.038	This work (two-site model only).

Components: SOH, H^+, Na^+, Cl^-, carbonate, Ni^{2+}

Formation constants of surface species		Both models	Source
$K_{fm}(SO^-) = \frac{[SO^-][H^+]}{[SOH]}\cdot\gamma_{H^+}\cdot e^{(-\psi_0)F/RT}$	=	$10^{-9.9}$	van Geen *et al. (1994)*
$K_{fm}(SOH_2^+) = \frac{[SOH_2^+]}{[SOH][H^+]}\cdot\frac{1}{\gamma_{H^+}}\cdot e^{(\psi_0)F/RT}$	=	$10^{7.9}$	van Geen *et al. (1994)*
$K_{fm}(SO\text{-}Na) = \frac{[SO\text{-}Na][H^+]}{[SOH][Na^+]}\cdot\frac{\gamma_{H^+}}{\gamma_{Na^+}}\cdot e^{(\psi_\beta-\psi_0)F/RT}$	=	$10^{-8.90}$	This study.
$K_{fm}(SOH_2\text{-}Cl) = \frac{[SOH_2\text{-}Cl]}{[SOH][H^+][Cl^-]}\cdot\frac{1}{\gamma_{H^+}\gamma_{Cl^-}}\cdot e^{(\psi_0-\psi_\beta)F/RT}$	=	$10^{8.84}$	This study.
carbonate = H_2CO_3:			
$K_{fm}(SOCO_2^-) = \frac{[SOCO_2^-][H^+]}{[SOH][H_2CO_3]}\cdot\gamma_{H^+}\cdot e^{(-\psi_0)F/RT}$	=	$10^{-4.23}$	van Geen *et al. (1994)*
carbonate = CO_3^{2-}:			
$K_{fm}(SOCO_2^-) = \frac{[SOCO_2^-]}{[SOH][H^+][CO_3^{2-}]}\cdot\frac{1}{\gamma_{H^+}\gamma_{CO_3^{2-}}}\cdot e^{(-\psi_0)F/RT}$	=	$10^{12.45}$	van Geen *et al. (1994)*

		One-site	Two-site	
$K_{fm}(SO^{II}Ni^+) = \frac{[SO^{II}Ni^+][H^+]}{[SOH][Ni^{2+}]}\cdot\frac{\gamma_{H^+}}{\gamma_{Ni^{2+}}}\cdot e^{(\psi_0)F/RT}$	=	$10^{0.613}$	$10^{-0.5}$	This study.
$K_{fm}(SO^{I}Ni^+) = \frac{[SO^{I}Ni^+][H^+]}{[SO^{I}H][Ni^{2+}]}\cdot\frac{\gamma_{H^+}}{\gamma_{Ni^{2+}}}\cdot e^{(\psi_0)F/RT}$	=	n/a	$10^{-0.5}$	This study.

[ ] denotes concentrations; γ is the activity coefficient for the indicated ion, calculated using the Davies equation (Davies, 1962); F is Faraday's constant (96480 C/mole e^-); R is the ideal gas constant; T is the absolute temperature; ψ_0 and ψ_β are the potentials at the surface and β plane, respectively.

Table A.7. Matrix of stoichiometric coefficients for mass-action and mass-balance equations for the two-site goethite TLM, used to set up the FITEQL input file. Components used in the HYDRAQL model were the same, except that carbonate was defined to be CO_3^{2-} rather than H_2CO_3, and the dummy variable NiAds (required by FITEQL in order to fit adsorption data) was omitted. The single-site matrix is identical but for the omission of the component SO^IH.

IDNum			170	50	13	14	5	103	101	1	2	160	161	162
	Components		Activity	H(+)	Ni(+2)	NiAds**	Na(+)	Cl(–)	H_2CO_3	SO(II)H	SO(I)H	Psi(0)	Psi(β)	Psi(d)
	Species	**Charge**	n/a	1	2	0	1	-1	0	0	0	n/a	n/a	n/a
170	Activity	n/a	n/a											
50	H(+)	1	0	1										
100	OH(–)	-1	-2	-1										
101	H_2CO_3	0	0						1					
12530	HCO_3(–)	-1	-2	-1					1					
12540	CO_3(–2)	-2	-6	-2					1					
5	Na(+)	1	0				1							
103	Cl(–)	-1	0					1						
2000	$NaCO_3$(–)	-1	-2	-2			1		1					
2005	NaHCO3	0	0	-1			1		1					
13	Ni(+2)	2	0		1									
6780	NiCl(+)	1	4		1			1						
6781	$NiCl_2$	0	6		1			2						
7590	NiOH(+)	1	2	-1	1									
7592	$Ni(OH)_2$	0	2	-2	1									
7593	$Ni(OH)_3$(–)	-1	0	-3	1									
7594	$Ni(OH)_4$(–2)	-2	-4	-4	1									
7595	Ni_2OH(+3)	3	-2	-1	2									
7596	$Ni_4(OH)_4$(+4)	4	-4	-4	4									
7597	$NiCO_3$	0	2	-2	1				1					
7598	$Ni(CO_3)_2$(–2)	-2	-4	-4	1				2					
7599	$NiHCO_3$(+)	1	2	-1	1				1					
1	SOH	0*	0							1				
86105	SO(–)	0*	-1	-1						1		-1		
86110	SOH_2(+)	0*	1	1						1		1		
86115	SO-Na	0*	0	-1			1			1		-1	1	
86120	SOH_2-Cl	0*	2	1				1		1		1	-1	
86125	$SOCO_2$(–)	0*	-1	-1					1	1		-1		
80013	SO(II)Ni(+)	0*	3	-1	1	1				1		1		
80014	SO(I)Ni(+)	0*	3	-1	1	1					1	1		

* considered to have zero charge for purposes of activity stoichiometry and calculated ionic strength.

** dummy variable used by FITEQL during optimization of adsorption data.

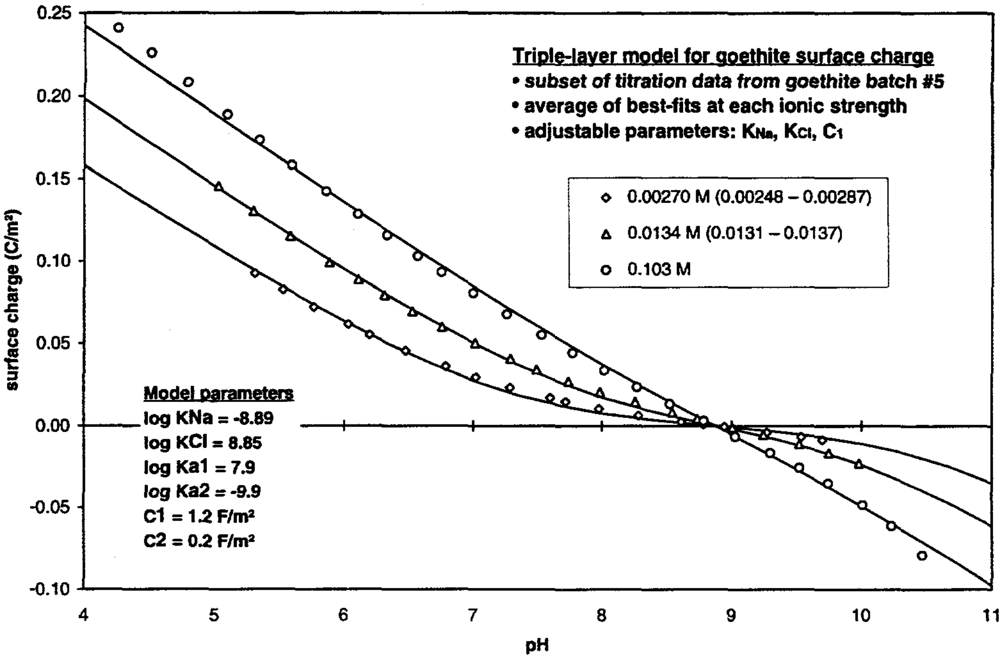

Figure A.15. Triple-layer surface-complexation model of surface charge on goethite in NaCl electrolyte.

(SOS/DF, the sum of the squares of the residuals divided by the degrees of freedom) were recorded. Plots of calculated surface charge vs. pH were compared with the experimental measurements to permit a visual estimate of goodness-of-fit as well. The optimum value of C_1 was selected by minimizing the weighted sum of SOS/DF for the three ionic strengths, using the square roots of the ionic strengths as the weighting factors. The optimum weighted SOS/DF was 6.1, using FITEQL's default precision estimates, indicating a reasonably good fit. Although this scheme is probably not statistically rigorous, it provides a solution consistent with the visual evidence, distributing the degree of misfit equitably among the three titration curves, and provides somewhat greater weight to the data obtained at higher ionic strength where the effects of electrolyte binding on surface charge are greater. The values of the electrolyte binding constants consistent with the selected value of C_1 are the logarithmic means of the values obtained at each ionic strength.

A.4.4.2. Apparent Partial Pressures of CO_2 in Goethite Batch Experiments

A quantitative estimate of P_{CO_2} in the "CO_2-free" batch systems can be calculated from the measured pH values combined with the total added acid (or base) and the triple-layer surface-complexation model outlined above. FITEQL was used to calculate a table of total acid vs. values of log [H_2CO_3] for each batch system;

the values of log [H_2CO_3] and total carbonate compatible with the known value of total acid were then read from the table. P_{CO_2} was calculated from [H_2CO_3] using the Henry's Law constant for CO_2 ($K_H = 0.034$ M/atm). Adsorption of Ni was included, using the model presented in Siegel *et al.* (1995). This model included both direct Ni complexation and Ni binding to adsorbed CO_2 (log $K_{fm}(SONi^+) = -1.6$ and log $K_{fm}(SOCO_2Ni^+) = 3.21$). The literature values of equilibrium constants for Ni-carbonato species were also used (Mattigod and Sposito, 1977). Because the total Ni concentration (~10^{-6} M) is only about 10% of the inferred value for total CO_3^{2-} (~10^{-5} M), errors in the model for Ni speciation and binding will not have a significant effect on the calculated total CO_3^{2-} values.

Calculated P_{CO_2} values in "CO_2-free" goethite batch systems are presented graphically in Figure A.16a. For systems with ~5 m^2/l goethite, calculated P_{CO_2} is relatively constant up to pH ~7 and then begins to decline linearly with pH. For pH > 7, total carbonate was nearly constant at $3\text{–}5 \times 10^{-5}$ M (Figure A.16b). As discussed previously, an conservative upper limit of 5×10^{-4} M total CO_2 was used in calculations of Ni solubility in the CO_2-free systems.

For systems with higher goethite concentrations (55 m^2/l), calculated P_{CO_2} was substantially lower, as expected due to adsorption of CO_2 by the goethite, but also varied erratically as shown in Figure A.16. Attempts to model the titration behavior of these systems (TtlH vs. pH) at fixed P_{CO_2} could not realistically bracket the observations as shown in the figure. This suggests that these systems may have been contaminated by base, and that the actual P_{CO_2} was probably substantially higher than calculated. As a limiting case, then, the P_{CO_2} for adsorption calculations in these batch systems was taken to be $10^{-4.8}$ atm over the pH range 5–8, maximizing the difference between the air-equilibrated and "CO_2-free" systems.

A.4.4.3. Triple-Layer Model for Ni Surface Complexes on Goethite

Two triple-layer surface-complexation models have been developed for simulating Ni adsorption onto goethite. Both models rely on the same basic triple-layer model outlined above to determine the electrostatic properties of the solution/solid interface. The adsorption stoichiometry is presumed to be 1:1, forming an $SONi^+$ inner-sphere complex, as is typical for adsorption of divalent cations onto insoluble oxides (Dzombak and Morel, 1990). As discussed in Siegel *et al.* (1995), other stoichiometries were investigated but rejected because of poorer fits to the experimental data.

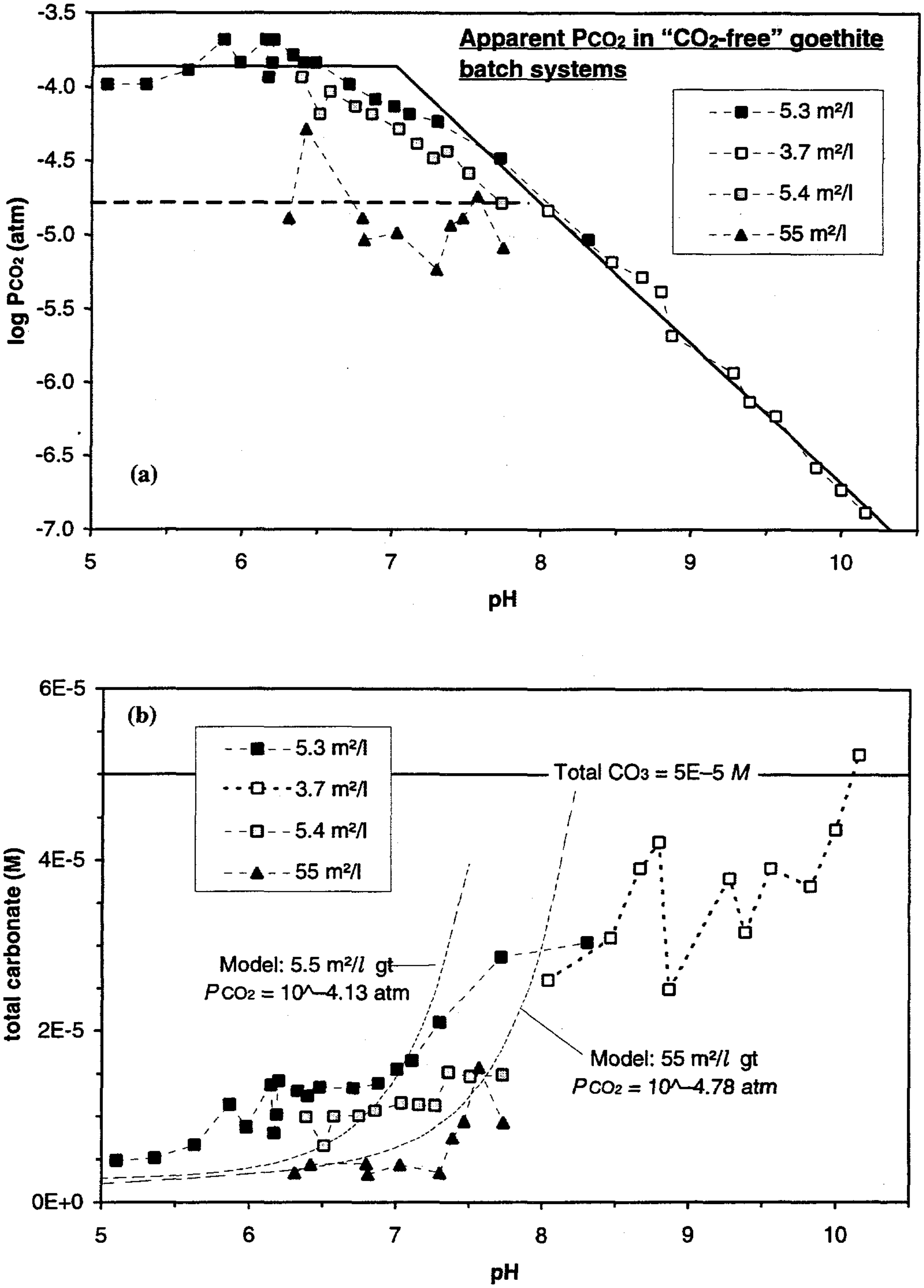

Figure A.16. Apparent CO_2 in goethite batch adsorption experiments conducted under "CO_2-free" protocol. a) Calculations plotted as P_{CO_2} vs. pH. b) Calculations plotted as total carbonate vs. pH. Theoretical total CO_2 at constant P_{CO} plotted as dotted lines.

A.4.4.3.1. Single-Site Model

The simpler of the two is a single-site model similar to that proposed in Siegel *et al.* (1995). Using FITEQL, values for $K_{fm}(SONi^+)$ were extracted from the Ni-adsorption data from goethite batch #5. Only data lying within the region of the adsorption edge were considered (pH 4.8–7.4 for ~55 m^2/l, and pH 5.1–7.6 for 5.4 m^2/l systems), and log $[H_2CO_3]$ was fixed at –4.97 for air-equilibrated systems and –6.25 or –5.32 for "CO_2-free" systems with ~55 m^2/l or 5.4 m^2/l goethite ($P_{CO_2} = 10^{-4.78}$ and $10^{-4.13}$), respectively. Iteration on ionic strength could not be used because FITEQL permits only 10 components. In the triple-layer model, four components are necessary to describe the charged surface, two components are necessary for the electrolyte ions (which form outer-sphere complexes with the surface, influencing the charge profile of the electrical double layer), one component is necessary for carbonate, one for H^+, and two for Ni (Ni^{2+}, and NiAds, a dummy variable used to keep track of the number of surface sites occupied by Ni, as described in Westall and Herbelin, 1992). In place of iterating on ionic strength, the intrinsic formation constants were corrected by hand to their apparent values at an ionic strength of 0.001 M using the Davies equation (Davies, 1962) and the reaction stoichiometries listed in Table A.7. Adsorption measurements were input as the total apparent concentration of adsorbed Ni at each point (i.e., total concentrations for NiAds).

In order to obtain realistic variances, FITEQL's default assumptions about the precision of input data were modified for the concentration of total adsorbed Ni (NiAds) for each batch system. These values were specified to have a precision of the larger of $\pm 1\%$ or $\pm 1 \times 10^{-8}$ M (the defaults are $\pm 1\%$ or $\pm 1 \times 10^{-6}$ M) because FITEQL could not accommodate the true error structure. The amount adsorbed is found by difference between the amount added to the system and the amount remaining in solution after equilibration, yielding adsorption values that are quite precise at high values, but that become increasingly less precise (both relative and absolute error) as measured adsorption decreases. Thus FITEQL gives more weight at low values of adsorption and less weight at high values than is merited by the precision of the data. The resulting model may be no more valid, statistically, than a visually optimized model.

The results of FITEQL optimizations for the single-site model are given in Table A.8, and adsorption edges calculated using the weighted average $K_{fm}(SONi^+)$ are displayed in Figure A.17a. The weighted average was calculated using the reciprocals of the variance, SOS/DF, as weighting factors. As reflected by the large variance, the single site model performs poorly at the lower surface concentration. The FITEQL-optimized curve for 5.4 m^2/l (not shown) passes through the midpoint of the experimental data but underestimates adsorption at lower pH and overestimates adsorption at higher pH — its slope is too steep. (The steep slope of the adsorption edge is inherent to the single-site model with 1:1 stoichiometry at pH values well removed from the pH_{ZPC}.) The single-site model using the weighted average $K_{fm}(SONi^+)$ performs even less well at lower goethite concentration, passing to the low-pH side of all the data above 30% adsorbed at 5.4 m^2/l goethite concentration. The standard deviations listed in Table A.8 reflect the internal precision of the optimizations rather than the scatter of the data relative to the model, and correspond to the smallest change in log K_{fm} that would cause a statistically significant increase in the variance of the model.

A.4.4.3.2. Two-Site Model

The decrease in slope of the adsorption edge with a decrease in surface concentration is symptomatic of "non-linear" behavior and indicates that the assumption of a single type of surface site binding with Ni is too simplistic. The alternative adopted here is to postulate that a subset of the surface sites have a high affinity for the ion of interest. In such a model, as the high-affinity sites become mostly occupied, further adsorption must occur at less favorable sites and thus requires a larger increase in pH to effect the same change in amount adsorbed. If the affinities of the two types of sites differ greatly, the adsorption "edge" will have a plateau where all of the high-affinity sites have been occupied but where the pH is too low for significant adsorption by the low-affinity sites. Additional parameters required by the high-affinity sites are: 1) their fractional abundance, and 2) their equilibrium constant for complexing with Ni.

The implementation of the two-site model is similar to that used by Dzombak and Morel (1990) for hydrous ferric oxide, in which two surface components are required: type I (SO^IH) for the high-affinity sites and type II ($SO^{II}H$) for the total number of sites. Only one new reaction is required — Ni adsorption by the high-

Table A.8. Results of FITEQL optimizations for Ni binding by the single-site model. Optimizations were performed for each surface area using apparent formation constants for 0.001 M NaCl. The resulting $K_{fm}^{app}(SONi^+)$ values were converted to intrinsic parameters using the appropriate activity corrections for aqueous species calculated using the Davies equation. The average was calculated using the inverses of the variances as weighting factors.

Surface area	log K_{fm}^{app}	std.dev.	variance	log K_{fm}^{int}	Weight
5.4 m²/l	0.328	0.0081	106.60	0.375	0.009
55 m²/l	0.575	0.0076	3.81	0.621	0.262
Weighted average				0.61	

affinity site to form the inner-sphere complex SO^INi^+. The remaining surface and solution reactions are identical with those in the single-site model, with the surface component now being $SO^{II}H$ in place of SOH. Although the type I sites are defined to be a subset of the type II sites, this is strictly true only in the limiting case where the ratio of type I to type II sites approaches zero. In the more general case, the type I and type II sites must be thought of as distinctly separate populations in which the type II sites exhibit the usual amphoteric behavior and interact with electrolyte and carbonate ions, but the type I sites exhibit specialized behavior, interacting only with Ni^{2+}. The type-I sites still contribute to the net surface charge, however, when they become positively charged by exchanging a proton for Ni^{2+}.

HYDRAQL 94 was used to implement the two-site model, with goodness-of-fit determined by visual comparison of the model output with the experimental data. In modifying the HYDRAQL version of the single-site mode, the type II sites were identified with the standard surface component SOH (component 184), and the type I sites were installed as component 185. A comparison of the calculated surface charge with the surface charge obtained by summing the reported concentrations of all surface complexes with charge at the 0-plane showed that the contribution of SO^INi^+ to the overall surface charge is properly included in the electrostatic calculations.

The results of the two-site model with visually optimized parameters are summarized and illustrated in Figure A.17b. Its superior fit at the lower surface area is readily apparent in comparison to the single-site model in Figure A.17b. The model was optimized at $P_{CO_2} = 10^{-3.5}$ atm to produce essentially the same adsorption edge at ~55 m^2/l as was obtained from the single-site model while at the same time providing the best-looking fit to the 5.4 m^2/l data. HYDRAQL 94 was run in pH-stepping mode with charge-balance optimization enabled, so that a realistic ionic strength was maintained at all pH values. The indicated precisions are subjective, showing the magnitude of changes judged to produce a perceptible worsening of fit. The fraction of high-affinity sites was found to be ~0.04, about the same as the value of 0.025 accepted by Dzombak and Morel (1990) for hydrous ferric oxide after their comprehensive survey of the literature.

The performance of the two goethite models with respect to a decrease in P_{CO_2} is illustrated by the dotted lines in Figure A.17, obtained when P_{CO_2} was decreased to its apparent value appropriate for each surface concentration under nominally CO_2-free conditions. Both models predict decreased adsorption at decreased P_{CO_2}, with the two-site model being slightly more sensitive. Physically, this difference is expected due to the relatively high affinity of the goethite surface for CO_2. Because adsorbed CO_2 forms a negatively charged surface site ($SOCO_2^-$), an increase in P_{CO_2} at constant pH will cause the net surface charge to decrease, becoming less positive

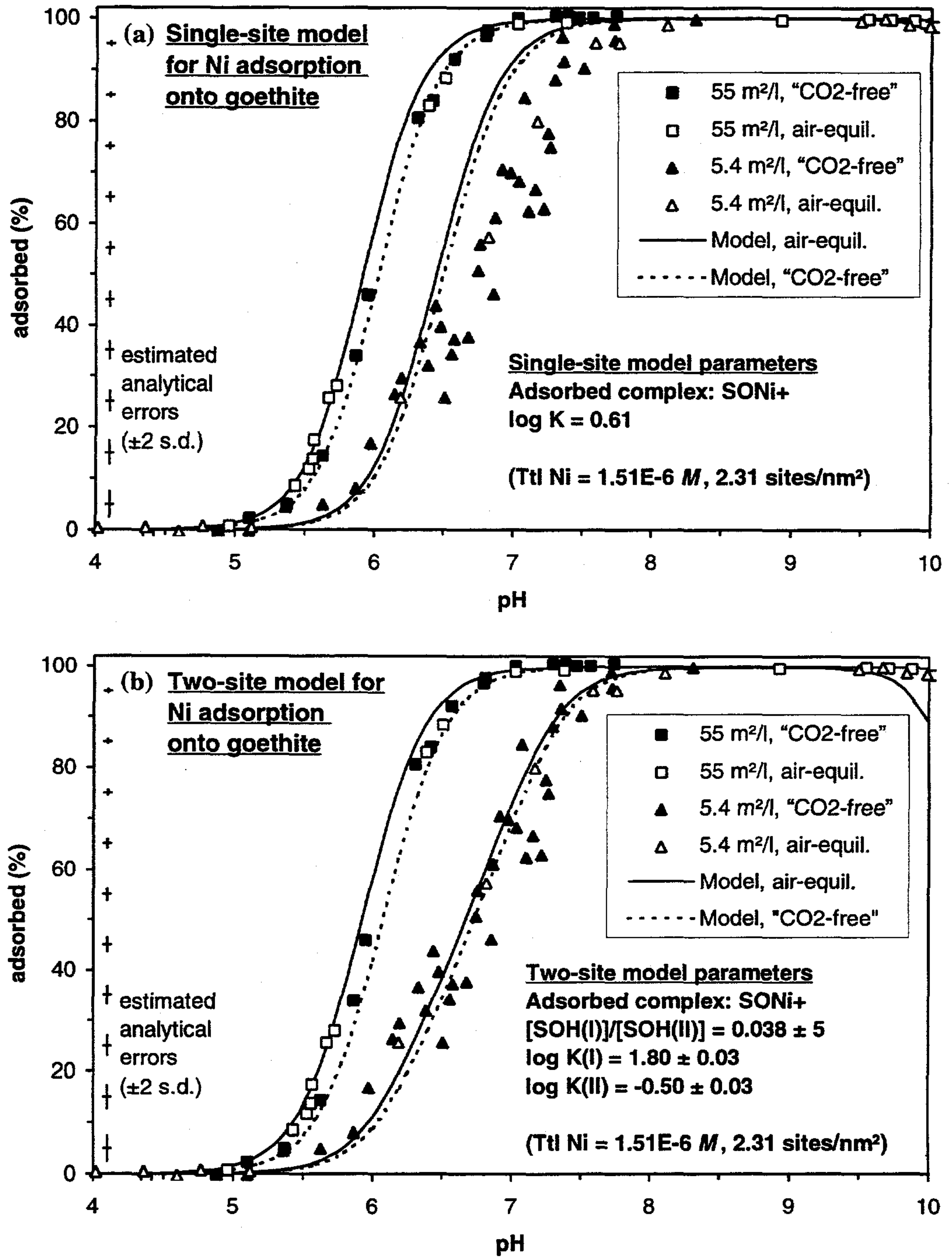

Figure A.17. Optimized models of Ni adsorption onto goethite. a) Single-site model, with parameter fitting using FITEQL for each surface concentration separately. The average association constant is heavily weighted toward the 55 m^2/l curve. b) Two-site model calculated using HYDRAQL 94 and optimized visually. Quoted precisions are those which produce a perceptible worsening of fit to the experimental data, but carry no rigorous statistical significance.

or more negative, resulting in a more favorable electrostatic interaction thus increasing Ni adsorption. This corresponds with the shift in pH_{ZNC} to lower values discussed earlier and noted by van Geen *et al.* (1994) as P_{CO_2} increases. For batch systems with 55 m^2/l goethite, both models over-predict the effect of CO_2. Recall, however, that the apparent P_{CO_2} values were selected to be as low as possible. In reality there may have been very little difference in P_{CO_2} between "CO_2-free" and air-equilibrated conditions.

The two models also differ in their predictions at high pH, where Ni speciation is modeled to undergo a transition from predominantly Ni^{2+} to $NiCO_3^{\circ}$ and then to $Ni(CO_3)_2^{2-}$. The single-site model is more consistent with the experimental data, showing only slightly decreased adsorption at pH 10. The two-site model predicts a significant decrease in adsorption at pH for the low-goethite systems.

The detailed behavior of the two-site model for Ni adsorption onto goethite is summarized in a speciation diagram (Figure A.18). The role played by outer-sphere complexes with the electrolyte ions is readily apparent — at extreme pH values and high ionic strengths, they occupy a significant fraction of the total surface sites. Also apparent is the relative efficacy of adsorption of Ni onto the high-affinity sites, (forming SO^INi^+) compared to the low-affinity sites (forming SO^INi^+) — over 90% of the adsorbed Ni is located on the high-affinity sites even though these sites constitute only ~4% of the total.

A.4.5. Triple-Layer Surface-Complexation Model for Quartz

A.4.5.1. Triple-Layer Model for Protolysis and Electrolyte Binding Constants

A preliminary single-site triple-layer surface-complexation model has been developed for quartz, based on the potentiometric titrations of Min-U-Sil 5 in NaCl electrolyte of this study. Because quartz has an unusually low pH_{ZPC} for an oxide, only $K_{fm}(SO^-)$ and K_{fm}(SO-Na) can be extracted from the experimental data. Typical values claimed for the quartz pH_{ZPC} are in the range 2–3 (Bolt, 1957; Tadros and Lyklema, 1968; Davis *et al.*, 1978; Riese, 1982); a value of 2 has been adopted for the present study. By assuming "symmetrical" adsorption of the electrolyte, $K_{fm}(SOH_2^+)$ and $K_{fm}(SOH_2\text{-}Cl)$ can be calculated from the pH_{ZPC}, and $K_{fm}(SO^-)$ or K_{fm}(SO-Na), respectively. In the triple-layer model with symmetrical adsorption, these formation constants must satisfy the following relations with the pH_{ZPC}:

$$\mathrm{pH_{ZPC}} = \frac{\log K_{\mathrm{fm}}(\mathrm{SOH_2^+}) - \log K_{\mathrm{fm}}(\mathrm{SO^-})}{2}\text{ , and} \tag{A.1}$$

$$\mathrm{pH_{ZPC}} = \frac{\log K_{\mathrm{fm}}(\mathrm{SOH_2\text{-}Cl}) - \log K_{\mathrm{fm}}(\mathrm{SO\text{-}Na})}{2}\text{ .} \tag{A.2}$$

These relations follow from the definitions of the formation constants and the fact that at the $\mathrm{pH_{ZPC}}$, $[\mathrm{SOH_2^+}] = [\mathrm{SO^-}]$, and $[\mathrm{SOH_2\text{-}Cl}] = [\mathrm{SO\text{-}Na}]$ for symmetrical adsorption. Quartz is also unusual in that it exhibits very low surface charge near its $\mathrm{pH_{ZPC}}$, not becoming significantly charged until pH 5 or 6. Thus for the pH range of interest here (pH 5–9), the protonated species ($\mathrm{SOH_2^+}$ and $\mathrm{SOH_2\text{-}Cl}$) can be omitted from the model, an approach adopted by Rea and Parks (1990).

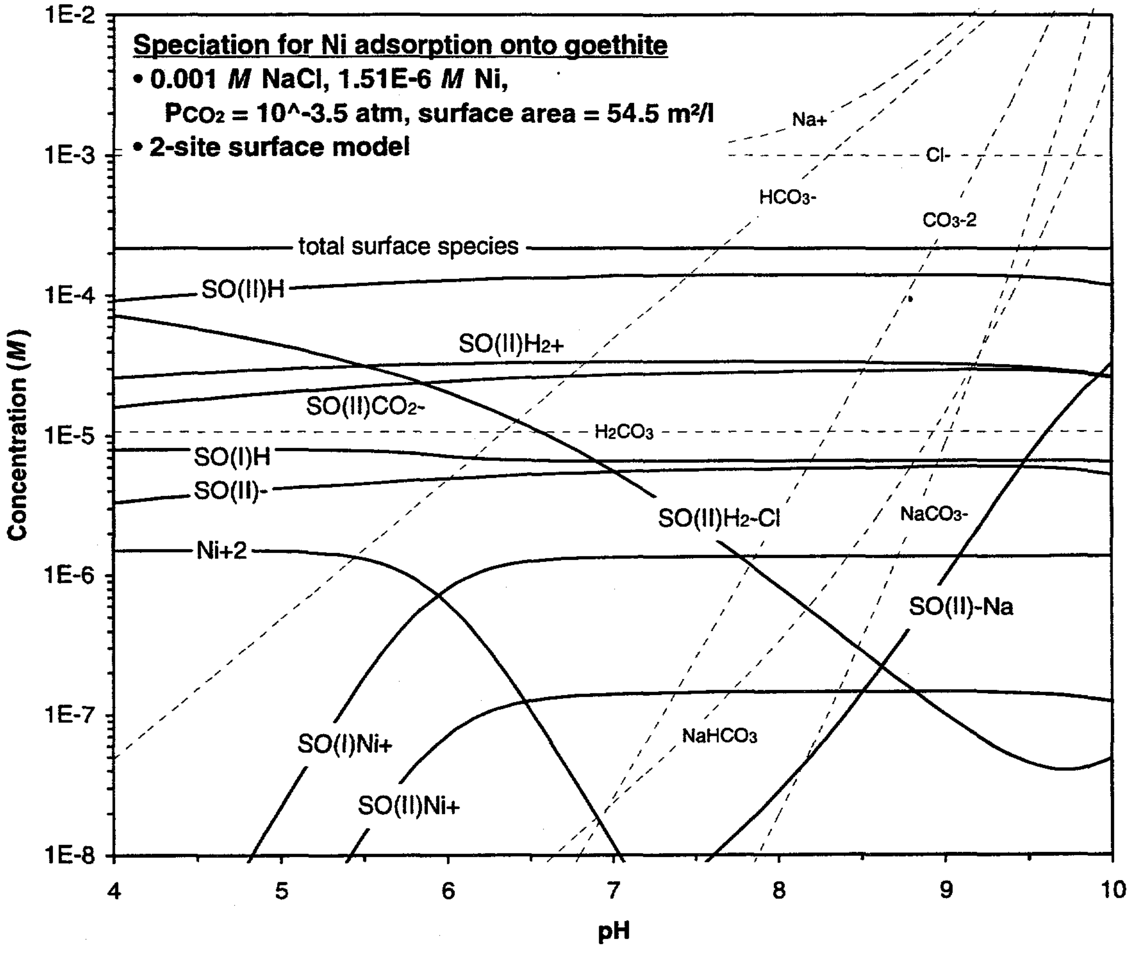

Figure A.18. Speciation model for Ni adsorption onto goethite. All aqueous and adsorbed species with concentrations greater than 10^{-8} M are shown.

The site density on quartz has been measured to be in the range 2–6 by tritium exchange and thermogravimetric methods by numerous investigators. A value of 6 sites/nm^2 was adopted in the early stages of this work and has been used throughout, although 5 sites/nm^2 is more commonly used (Riese, 1982; Rea and Parks, 1990). As was used for goethite, the outer-layer capacitance (C_2) was fixed at 0.2 F/m^2 in accordance with the arguments of Yates *et al.* (1974) and Davis *et al.* (1978) for obtaining agreement with observed zeta potentials.

Three models of surface charge on quartz were examined. In the first, values for K_{fm}(SO$^-$) and K_{fm}(SO-Na) were found using the double-extrapolation method (James *et al.*, 1978), as shown in Figure A.19. The extracted parameters (log K_{fm}(SO$^-$) = –7.8 and log K_{fm}(SO-Na) = –5.2) along with an assumed value for the inner layer capacitance (C_1) of 1.2 F/m^2 were then used to calculate surface charge as a function of pH, with results plotted in Figure A.20a. The calculated surface charge does not agree with the measured surface charge, predicting much more rapid charging as pH was increased than was actually observed. For comparison, the widely used model for silica of Davis *et al.* (1978) as implemented by Rea and Parks (1990) was used to calculate surface charge, with the results plotted in Figure A.20b. Their model used a site density of 5 nm^{-2}, with log K_{fm}(SO$^-$) = –7.2, log K_{fm}(SO-Na) = –6.7, and C_1 = 1.295 F/m^2. These calculated surface charges resemble the observations much more closely but still miss some of the details: at low pH, the observations show a significant increase in surface charge with increasing ionic strength, and at higher pH the data are concave downward, exhibiting an increasing rate of charging with increasing pH.

A final model was developed using FITEQL to optimize K_{fm}(SO$^-$), K_{fm}(SO-Na), and C_1, assuming a site 6 nm^{-2} and a pH$_{ZPC}$ = 2. The optimum value of C_1 was a function of ionic strength, ranging from less than 1 F/m^2 at 0.0005 M to more than 2.4 at 0.094 M. Weighted averages of the variances of each optimization, as used for goethite, were still declining at C_1 = 2.4 F/m^2, but such a high capacitance seemed unrealistic in comparison with other studies of quartz and silica (Riese, 1982) so a value of 2.0 F/m^2 was chosen for C_1. The results of this optimization are plotted in Figure A.21, and the optimized parameters are given in Table A.9. This model provides a better fit than that of Rea and Parks, and will be used as the basis for a model of Ni adsorption.

Several conclusions may be drawn from these models of surface charge on quartz. Firstly, these titrations on Min-U-Sil 5 are not very different from those obtained from other forms of silica, suggesting that acid-washing provides consistent preparations of the silica surface for potentiometric titrations. Secondly, the double-extrapolation method provides poor estimates of K_{fm}(SO$^-$) and K_{fm}(SO-Na) for quartz. Because of the unusual properties of quartz discussed earlier (low pH$_{ZPC}$ and small surface charge in the vicinity of the pH$_{ZPC}$), the double-

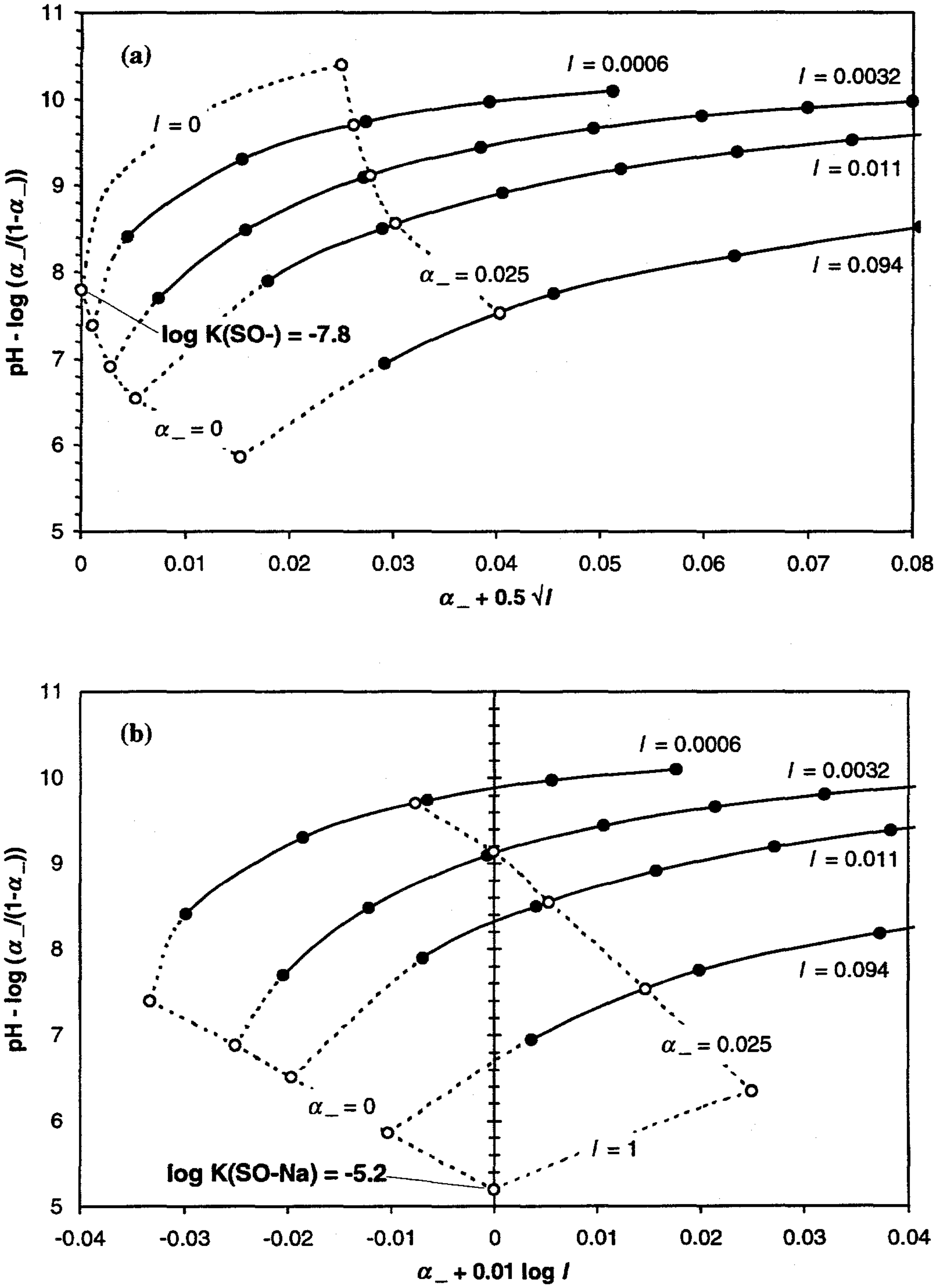

Figure A.19. Double-extrapolations of potentiometric titration data on quartz. a) $K_{fm}(SO^-)$, and b) K_{fm}(SO-Na). Filled symbols are measured values, open symbols are extrapolated or interpolated values.

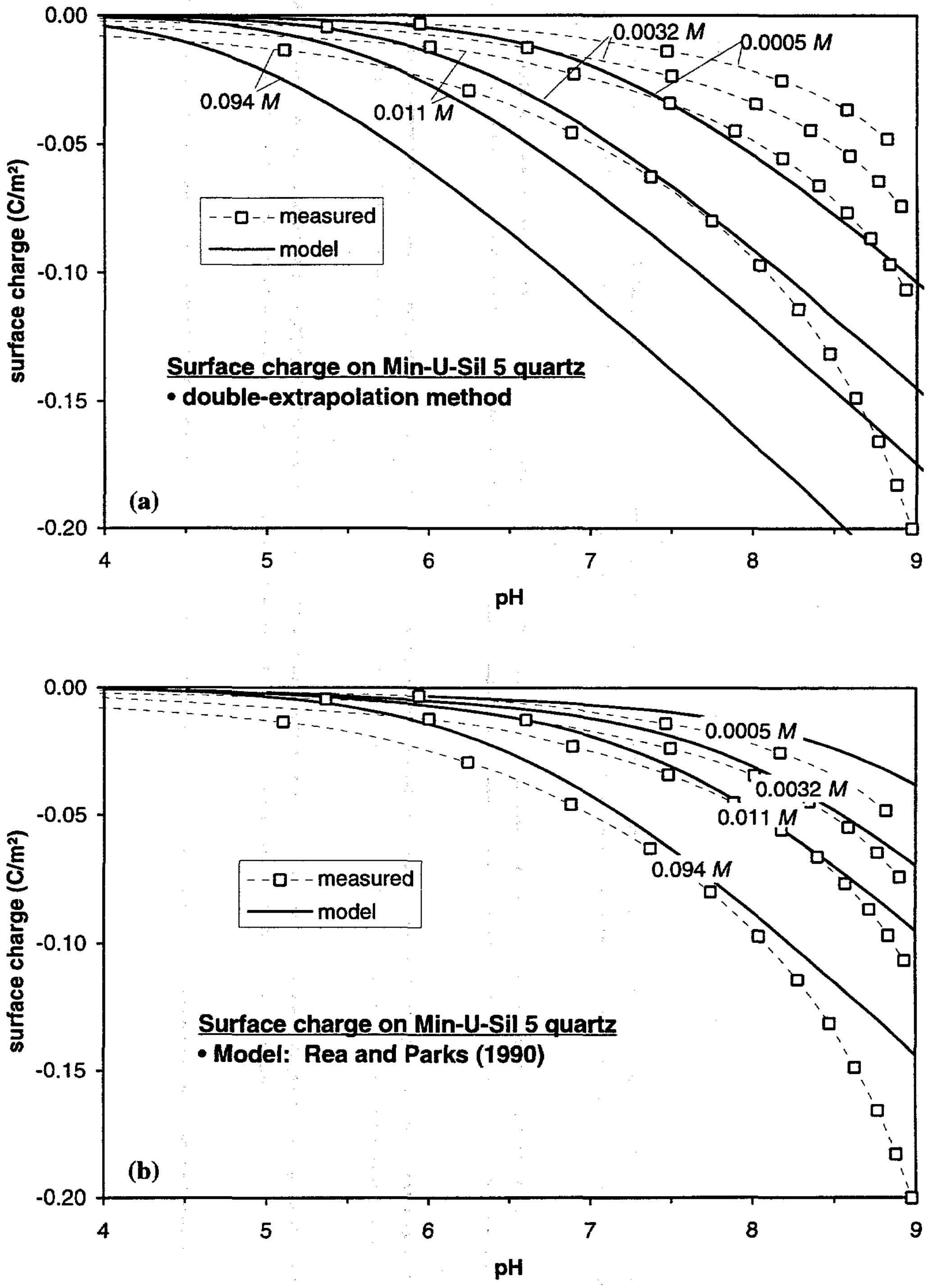

Figure A.20. Calculated surface charges compared to measurements on Min-U-Sil 5 quartz. a) $K_{fm}(SO^-)$ and K_{fm}(SO-Na) found by double-extrapolation. b) $K_{fm}(SO^-)$ and K_{fm}(SO-Na) from Rea and Parks (1990). Calculations performed using HYDRAQL 94.

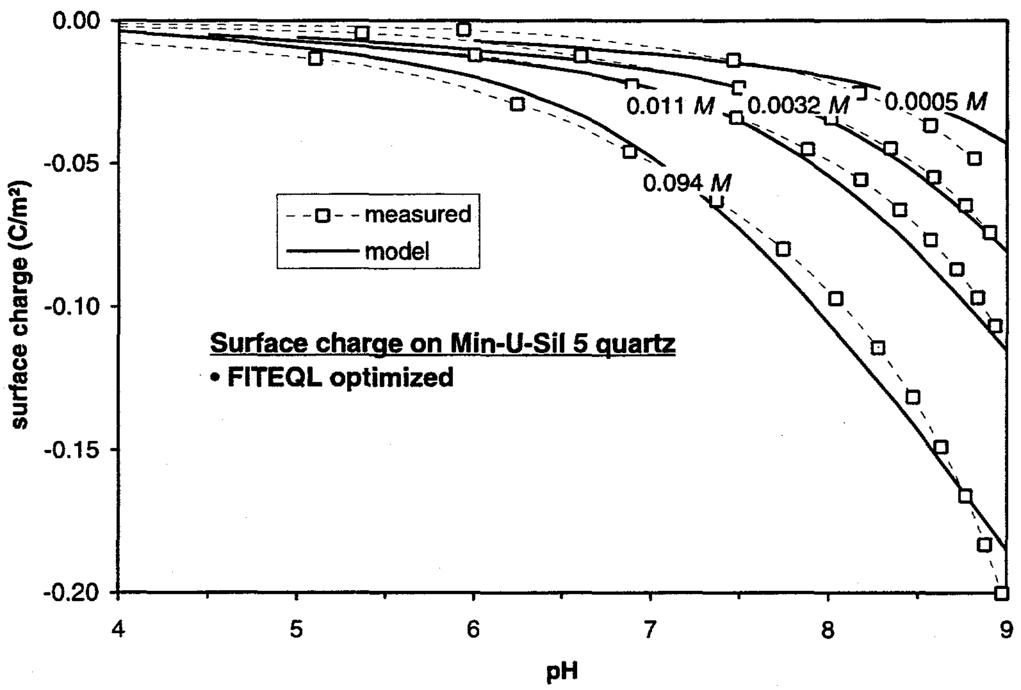

Figure A.21. FITEQL-optimized triple-layer-model parameters for surface charge on Min-U-Sil 5 quartz.

Table A.9. Quartz parameters for triple-layer surface-complexation model. Based on measurements on Min-U-Sil 5. Nickel forms an outer-sphere complex with single surface site (SO-Ni$^+$). A pH$_{ZPC}$ of 2 was assumed, permitting the log K_{fm} values for SOH_2^+ and SOH_2-Cl to be estimated.

Surface	Site density (nm^{-2})	C_1 (F/m^2)	log K_{fm} (SO$^-$)	log K_{fm} (SOH_2^+)	log K_{fm} (SO-Na)	log K_{fm} (SOH_2-Cl)	log K_{fm} (SO-Ni$^+$)
Quartz	6	2.0	-6	-2	-7	-3	-7.7

extrapolation method requires the practitioner to project slightly curved lines into a region of much greater curvature. Hence the extrapolation process becomes quite subjective, and curves that appear "beautiful in the eye of the beholder" may lead to constants that are inconsistent with the original observations. Such extrapolations, particularly for quartz, are of little value and should be abandoned in favor of the FITEQL approach. Thirdly, FITEQL cannot always be applied in a completely objective manner, as shown by the wide range in optimal values for C_1 as a function of ionic strength. This difficulty is either a reflection of shortcomings in the triple-layer model or indicates an inconsistency in the experimental observations. Recall that for these titrations of Min-U-Sil 5, the amount of acid added to lower the pH to the starting point of each titration was not precisely known, so it was treated as an adjustable parameter, and it was determined by visually extrapolating the data through the pH_{ZPC}. Thus each curve of surface charge vs. pH could be slightly misplaced by constant, though quite small (< 0.01 F/m^2), amounts of surface charge.

In spite of this, however, the shape of each titration curve would remain the same. Because all of the calculated surface-charge for each of the three models display decreasing curvature at high pH, it appears that this triple-layer model is incapable of precisely reproducing the observed trends, and that additional surface complexes and dissolved species should be considered. One refinement would be the incorporation of dissolved silica speciation. Kent *et al.* (1988, p.85) suggest that errors due to dissolved silica are negligible below pH 9, but the experience of the British Geological Survey (Mark Crawford, letter to CHEMVAL2 participants dated 15 November 1993) shows that the influence of dissolved silica can be important. Because of the slow kinetics of silica dissolution, and the likelihood of different rates of dissolution for different forms of silica, an equilibrium solubility model should not be relied upon. Instead, dissolved silica should be determined analytically at appropriate intervals.

A.4.5.2. Triple-Layer Model for Ni Surface Complexes on Min-U-Sil

Data obtained in NaCl electrolyte as described previously and Ni adsorption curves obtained from the British Geological Survey (Mark Crawford, letter to CHEMVAL2 participants dated 15 November 1993) in $NaNO_3$ electrolyte were used as a basis for the triple-layer model for Ni adsorption by quartz. The results of modeling Ni adsorption onto quartz are shown in Figure A.22. Although the experimental data are a combination of runs in $NaNO_3$ and in NaCl electrolytes, this should present no inconsistency as only Na^+ interacts with the quartz surface, not the anion, at pH > 5. In the model, Ni was assumed to form a unidentate outer-sphere complex ($SO\text{-}Ni^+$). This stoichiometry was based on the general observation that simple cations rarely bind to more than one site (Dzombak and Morel, 1990), and outer-sphere geometry was selected because of the sensitivity of Ni adsorption to ionic strength— placing the Ni^{2+} ions in the same plane as the electrolyte counter-ion (Na^+) allows for much greater competition between the two compared to the inner-sphere geometry used for Ni^{2+} on goethite. The experimental P_{CO_2} was not reported for the BGS data ($NaNO_3$ electrolyte) but the suspensions were in at least partial contact with air during their 1 h equilibration periods. As a first approximation, the constant total CO_2 found to apply to the partially-air-equilibrated batch experiments at pH > 7.5 (1.82×10^{-4} atm) was used for these data. The model was visually optimized for the 0.01 M data set, giving a value for $\log K_{fm}(SO\text{-}Ni^+) = -7.7$. All model calculations were performed assuming a surface concentration of 265 m^2/*l*.

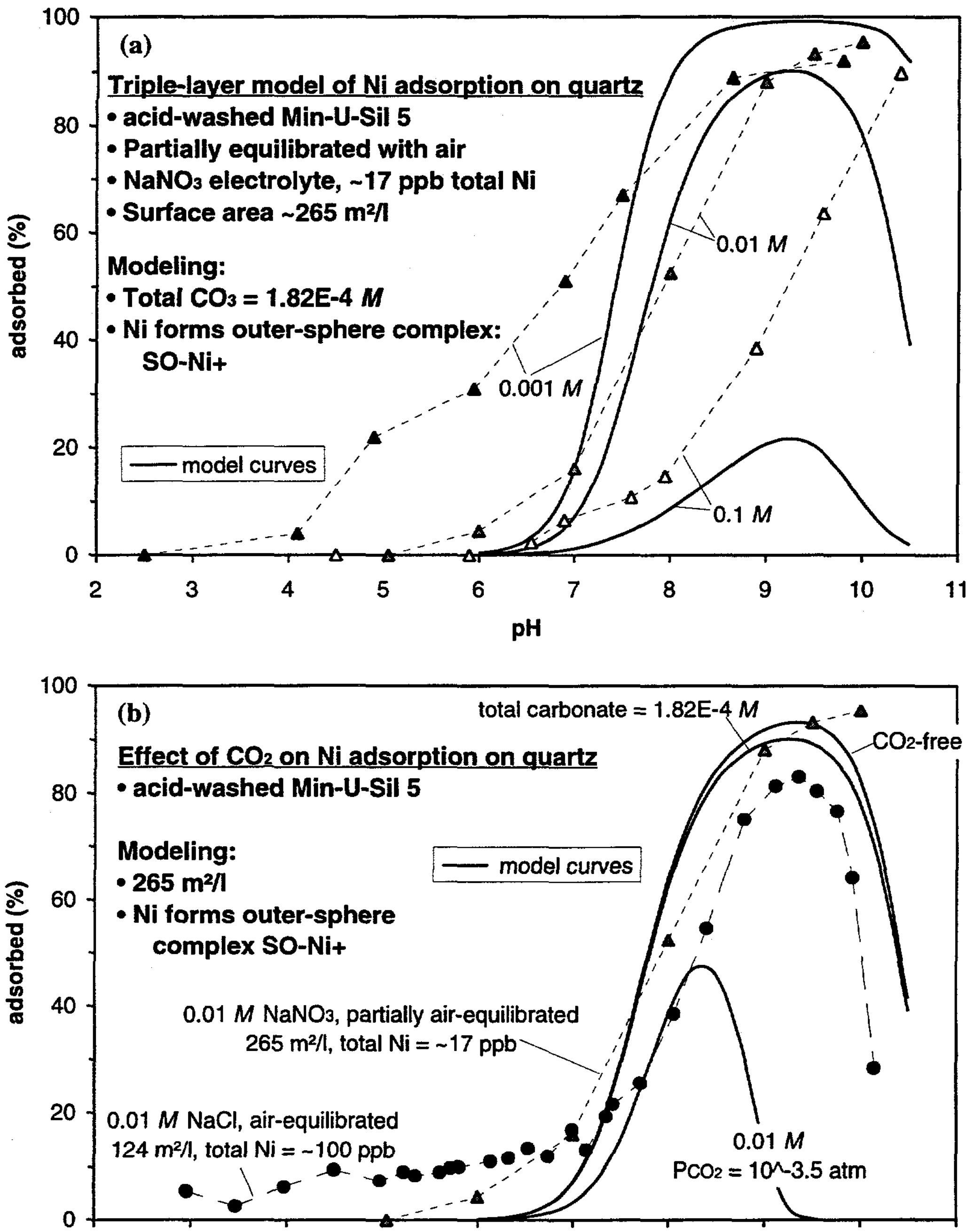

Figure A.22 Triple-layer model of Ni adsorption on quartz. The FITEQL-optimized surface-charge parameters were used in the calculations. Experimental data were obtained from the British Geological Survey on BGS stock except for the air-equilibrated data in b, which were measured in this study on BGS stock. a) Effect of ionic strength. Total carbonate was estimated to be 1.82×10^{-4} M (partially air-equilibrated conditions for pH > 7.5). b) Effects of varying P_{CO_2} in 0.01 M electrolyte. Model calculations assume 0.01 M NaCl.

The model does not perform well. Qualitatively, the model exhibits the required dependency on ionic strength and total carbonate, but the slopes of the adsorption curves are poorly simulated, and calculated adsorption begins declining above pH > 9.3 at all ionic strengths. Under air-equilibrated conditions ($P_{CO_2} = 10^{-3.5}$ atm), calculated adsorption began declining above pH 8.1 after reaching a maximum of only 50%, whereas observed adsorption peaked at pH 9.3 at ~85%. Low calculated adsorption at high pH was due to the predominance of aqueous Ni-carbonato and Ni-hydroxo complexes, successfully competing with the surface sites for Ni^{2+}. More realistic model behavior might be obtained by including surface complexes involving the dominant aqueous Ni species or by adopting a different stoichiometry for the adsorbed Ni complex. By analogy with observations on goethite systems, shallow slopes may indicate the availability of more than one type of site for Ni adsorption. At low ionic strength, the Ni^{2+} can compete more effectively with Na^+ for high-affinity sites than at higher ionic strengths. At higher ionic strengths, mass-action effects exclude Ni^{2+} from the surface until electrostatic interactions become more favorable, above pH ~6.

To summarize, the simple single-site outer-sphere model does not adequately describe Ni adsorption at the quartz surface. Its shortcomings suggest likely avenues for improvement, including modifying the stoichiometry of the adsorbed complex, adding additional adsorbing complexes involving the predominant Ni-bearing species at high pH, and considering variations in the affinities of adsorption sites for Ni^{2+} and Na^+ at near-neutral pH.

A.4.6. Triple-Layer Surface-Complexation Model for Kaolinite

Kaolinite is a layered aluminosilicate composed of alternating sheets of silica (composition $(Si_4O_{10})^{-4}$) and alumina (a gibbsite-type layer of composition $(OH)_6{-}Al_4{-}(OH)_2O_4$) joined by the apical oxygens of the silica tetrahedra to give a bulk composition of $Al_4(Si_4O_{10})(OH)_8$. Layers are joined by hydrogen bonding in one of several stacking sequences to yield either kaolinite *sensu stricto*, dickite, or nacrite. In halloysite, each silica-alumina layer is separated by a layer of water molecules, and the sheets are randomly stacked (Deer *et al.*, 1966). Kaolinite can exhibit a small capacity for cation exchange due to substitution of Al for Si in the silica layer, leading to permanent negatively charged sites (Wieland and Stumm, 1992 and references therein).

Models of surface charge have been developed along both crystallographic and chemical lines. In the crystallographic approach (cf. Wieland and Stumm, 1992), kaolinite flakes are modeled as platelets with three types of surfaces, each with its own sets of electrostatic and surface-complexation parameters. One type of basal surface is composed of only aluminol (Al-OH) sites, corresponding to the gibbsite-type layer. The second type of basal surface exposes only silanol (Si-OH) sites and fixed-charge sites, corresponding to the silica layer. The third type of surface is composed of both silanol and aluminol sites, corresponding to the exposed edges of the stacked sheets of gibbsite and silica.

In the chemical approach, kaolinite flakes are modeled as a mixture of silanol and aluminol sites exposed in a 1:1 ratio. Although less realistic than the crystallographic approach, it is more amenable to simplifying assumptions and has been the basis for several surface complexation models (cf. Riese, 1982; Xie and Walther, 1992 and references therein). Riese (1982) developed a triple-layer model for surface charge on kaolinite with the parameters summarized in Table A.10. In this model, CO_2 plays no direct role at the surface, but can still influence adsorption indirectly via its effect on ionic strength or by forming stable complexes with dissolved cations.

The model presented here is based on the model of Riese but includes a simplifying assumption: at pH > 3, the complexes SOH_2^+ and SOH_2-Cl were assumed to be unimportant for silanol sites, analogous to the behavior of quartz surfaces at $pH > pH_{ZPC}$, and thus were omitted. (Riese's model did not include the equivalent aluminol surface complexes.) As a result of this omission, the simplified kaolinite model used here predicts a more negatively charged surface near the pH_{ZPC} than does Riese's full model. Because the measured Ni adsorption edge is also near pH 4, the spurious electrostatic attraction arising between aqueous Ni^{2+} and the excessively negatively charged surface will lead to a low estimate of the intrinsic formation constant, $K_{fm}(SONi^+)$. When these parameters are applied to estimate the surface area of kaolinite required to match observed adsorption edges at higher pH values, the small formation constant will lead to overestimates of the amount of required kaolinite. With this caveat in mind, some useful inferences about the role of kaolinite can be obtained from the model. Additional discussion of the limitations of the model can be found in Ward (1995).

The surface area of kaolinite is a current topic of debate in the literature. Xie and Walther (1992) have presented a new analysis of data from Carroll-Webb and Walther (1988) and Sposito (1984) which shows that a realistic estimate of the surface area accessible to protons and hydroxyls in solution might be about 10 times the BET-measured surface area if a site density of 6 nm^{-2} is assumed. Their conclusion is based on the observation that a site density of ~170 sites/nm^2 is required in order to account for the surface charge measured by Carroll-Webb and Walther if the BET-measured surface area is used, whereas crystallographic calculations suggest a maximum site density of only 19.8 sites/nm^2. For this reason, the effective surface area for the kaolinite in the Ni-adsorption experiments is taken to be $10 \times 24.6 = 246$ m^2/g, for a surface concentration in the batch experiments of 1240 m^2/l.

Table A.10 Kaolinite parameters for two-site triple-layer surface-complexation model. Both sites are considered to reside on the same surface and hence share electrostatic properties. At pH > 3, the complexes SOH_2^+ and SOH_2-Cl are assumed to be unimportant for both sites, and thus were not included in the model. As usual the value of C_2 is taken to be 0.2 F/m^2.

Surface	Site density (nm^{-2})	Fraction of total sites	C_1 (F/m^2)	log K_{fm} (SO$^-$)	log K_{fm} (SO-Na)	log K_{fm} (SO?Ni$^+$)	Type of Complex
Kaolinite	6*		2.4*				
>SiO		0.5*		-6.25*	-3.5*	-7.7	O.S.
>AlO		0.5*		-7.4*	-7.4*	-2.1	I.S.

O.S = outer-sphere; I.S. = inner-sphere. *Constants from Riese (1982).

Nickel complexation on the silanol sites was assumed to resemble that for Ni on quartz, so the formation constant for the outer sphere complex SiO-Ni$^+$ was taken from the quartz model. Because Ni is so weakly adsorbed by quartz, this assumption effectively assures that all Ni adsorption will take place on the aluminol site on kaolinite. Nickel was assumed to form an inner-sphere complex with the aluminol sites because of the observed strength of the sorption interaction. No data at other ionic strengths are available to test this hypothesis, but strongly adsorbed transition metals typically form inner-sphere surface complexes (Dzombak and Morel, 1990). With the aforementioned assumptions, the value of K_{fm}(AlONi$^+$) was found by visual optimization using HYDRAQL 94 to be $10^{-2.1}$, over five orders of magnitude greater than that for the silanol sites.

With this calibrated model of Ni adsorption, it is possible to assess the *amount* of exposed kaolinite required to mimic the Ni adsorption edges measured for untreated and acid-washed Wedron sand. Calculations were carried out using HYDRAQL 94, and goodness of fit was assessed visually; results are portrayed in Figure A.23. Adsorption of Ni by the acid-washed sand was closely simulated by the kaolinite model with a surface concentration of 60 m^2/*l*, corresponding to a BET-based surface concentration of 6 m^2/*l*. Because the acid-washed sand had a surface concentration of 58 m^2/*l* based on BET measurement, kaolinite (if it were the active surface) would account for only 10% of the BET surface area of the sand. The remaining surface area of the acid-washed sand is presumably quartz, whose contribution to total adsorbed Ni would be negligible over this pH range (4–6). (Nickel adsorption in the experimental systems did not reach 100%, presumably due to colloidal particles penetrating the 0.2 μm filters used to extract the samples for Ni analysis.)

Nickel adsorption by untreated Wedron sand for total Ni = 130 ng/m*l* (2.21×10^{-6} M) was approximated by kaolinite calculations for a total kaolinite concentration of 3 m^2/*l*, corresponding to a BET-based surface concentration of only

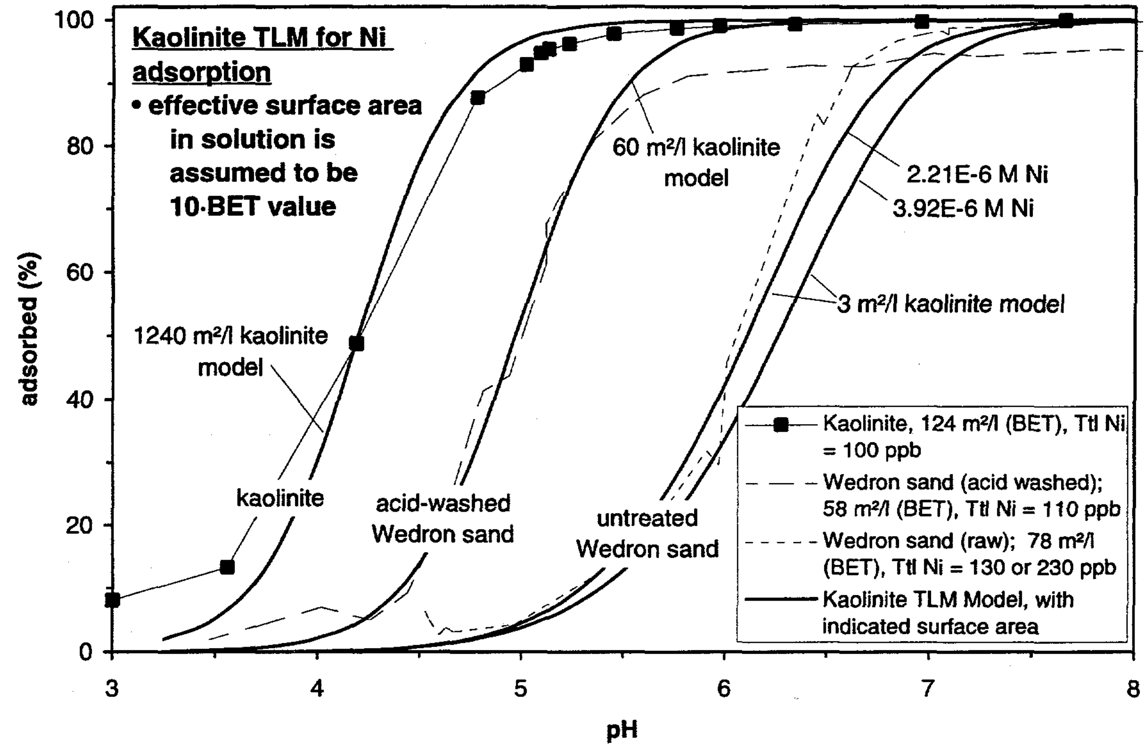

Figure A.23 Triple-layer model for Ni adsorption onto kaolinite. Surface area of kaolinite in aqueous media taken to be a factor of 10 greater than the measured BET value (Xie and Walther, 1992). A value of $P_{CO_2} = 10^{-3.5}$ atm was used for all calculations. See text for further discussion.

0.3 m^2/*l*. The raw sand had a BET-based surface concentration of 78 m^2/*l*, so the predicted kaolinite concentration amounts to only 0.4% of the total. The steeper measured adsorption edge of the sand compared to the kaolinite model suggest that it is unlikely that kaolinite alone is solely responsible for Ni adsorption onto the untreated sand, and that the remaining 99.6% of the sand's surface is inert. The slope of the calculated adsorption edge is shallower at this pH range than at lower pH ranges because the total SOH concentration is no longer in great excess relative to available Ni ($[\Sigma Ni^{2+}]/[\Sigma SOH\pm] = 0.07$). As would be expected due to the short supply of surface sites, increasing the total Ni to 230 ng/m*l* (3.92×10^{-6} M) resulted in a significant shift of the calculated adsorption edge toward higher pH. The untreated sand, on the other hand, exhibited no such shift due to increased Ni concentration, and also exhibited a steeper adsorption edge above 50% adsorbed.

A.5. Discussion

Previous results (Siegel *et al.*, 1995) and the results of adsorption studies described above suggest that Ni adsorption by Wedron sand is controlled predominately by iron oxyhydroxide coatings on the sand grains. In the following section, the ability of models of synthetic goethite to simulate the properties of the sand and the potential roles of the other minerals in the sand are discussed.

A.5.1. Goethite as an Analog for Ni Adsorption by Wedron 510 Sand

The two triple-layer surface-complexation models for goethite discussed above were calibrated to simulate the behavior of Wedron sand under partially air-equilibrated conditions ($P_{CO_2} = 10^{-3.5}$ atm below pH 7.5). For the single-site model, the optimal concentration of surface sites was found using FITEQL: Based on an initial guess for the goethite surface area, FITEQL optimized the total SOH concentration to obtain the best fit to the sand adsorption edge. The total SOH value and the site density were then used to refine the guess of the goethite surface area, and the cycle was repeated. Convergence to three significant figures was achieved after three cycles of this procedure. Adjustments of estimates of the goethite surface area by the above procedure are equivalent to revisions of the estimated specific surface area (m^2/g) of the iron oxyhydroxide coatings of the sand grains. Note that the concentration of leachable Fe from the sand (80 μg Ni/g sand; see Siegel *et al.*, 1995, Section III.B) provides an independent constraint on the amount of iron oxyhydroxide coating in the sand.

For the two-site model, the goethite concentration (surface concentration and concomitant values for total $SO^{I}H$ and $SO^{II}H$) were adjusted manually until a visual best-fit was obtained. In both models, optimization was carried out for a total Ni concentration of 130 ppb ($10^{-5.66}$ M). These simulations are shown in Figures A.24 and A.25, with an optimum goethite concentration for the single-site model of 28 m^2/l and for the two-site model of 37 m^2/l. The difference in apparent goethite concentration is attributable to the fact that most of the Ni in the two-site model adsorbs to the high-affinity sites, which are in comparatively short supply and thus results in a higher required goethite concentration.

The reference curve for Wedron sand is a composite of data collected at total Ni concentrations of 130 and 230 ng/m*l* ($10^{-5.66}$ and $10^{-5.41}$ M), and can be used to test model predictions at the higher concentration. Adsorption (%) of Ni by the sand was not measurably affected by these variations in concentration. As illustrated in Figure A.24, the single-site model was virtually unaffected as well by increasing total Ni from 130 to 230 ng/m*l*, whereas the two-site model exhibited slightly decreased adsorption (%). The difference in model behavior is because of the

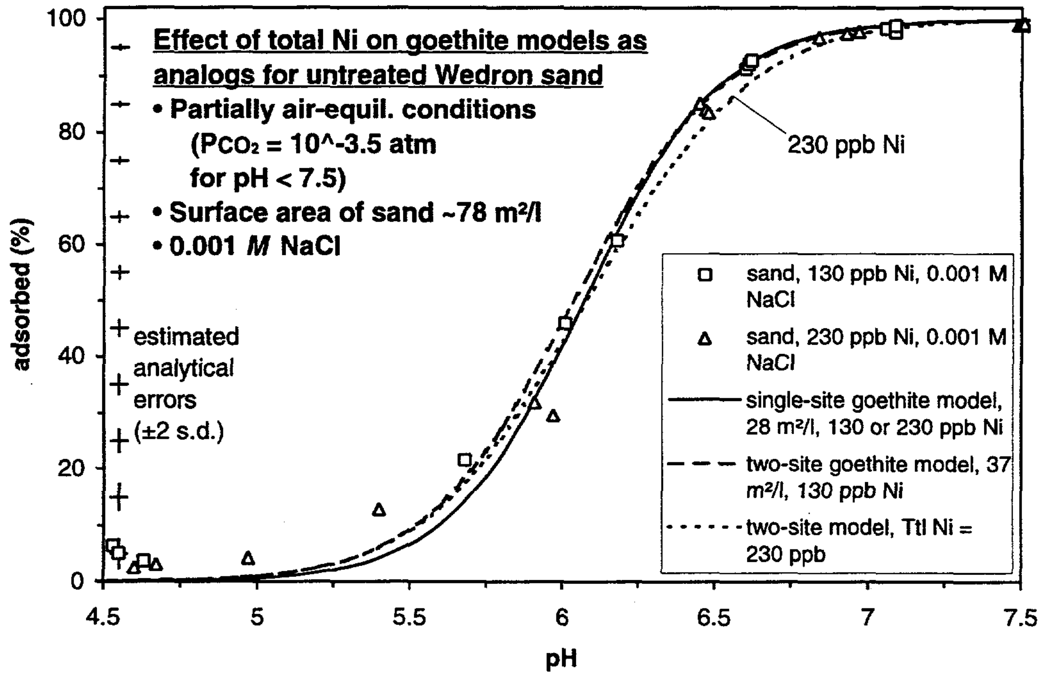

Figure A.24. Performance of goethite-model analogs for Wedron sand under conditions of changing total Ni. The single-site model, with a large surplus of unoccupied surface sites, was shifted by less than a line-width when the Ni concentration was increased from 130 ng/m*l* to 230 ng/m*l*, so only a single curve is plotted.

relative abundance of adsorption sites in the single-site model, whereas the two-site model shows slightly decreased adsorption due to the scarcity of high-affinity sites.

A second test is provided by examining the effect of a change in ionic strength. As shown in Figure A.25a, Ni adsorption on sand was diminished when the ionic strength increased from 0.001 M to 0.1 M, shifting the adsorption edge to higher pH by ~0.5 units. Although the experimental data are somewhat scattered, the single-site model appears to most accurately simulate this shift, with the two-site model predicting a somewhat smaller shift. No experimental data on goethite at higher ionic strength are available to evaluate the performance of these models on their native surface.

A third test for the models is provided by comparing their predictions in the absence of CO_2 with measurements on the sand under "CO_2-free" conditions, where the adsorption curve was shifted toward higher pH by ~0.3 units (cf. Figure A.25b). The actual P_{CO_2} in the "CO_2-free" sand systems can only be guessed at. It may have been as low as that assumed for the high-surface-area goethite systems ($P_{CO_2} = 10^{-4.8}$ atm), for which there was little difference in calculated adsorption between this P_{CO_2}

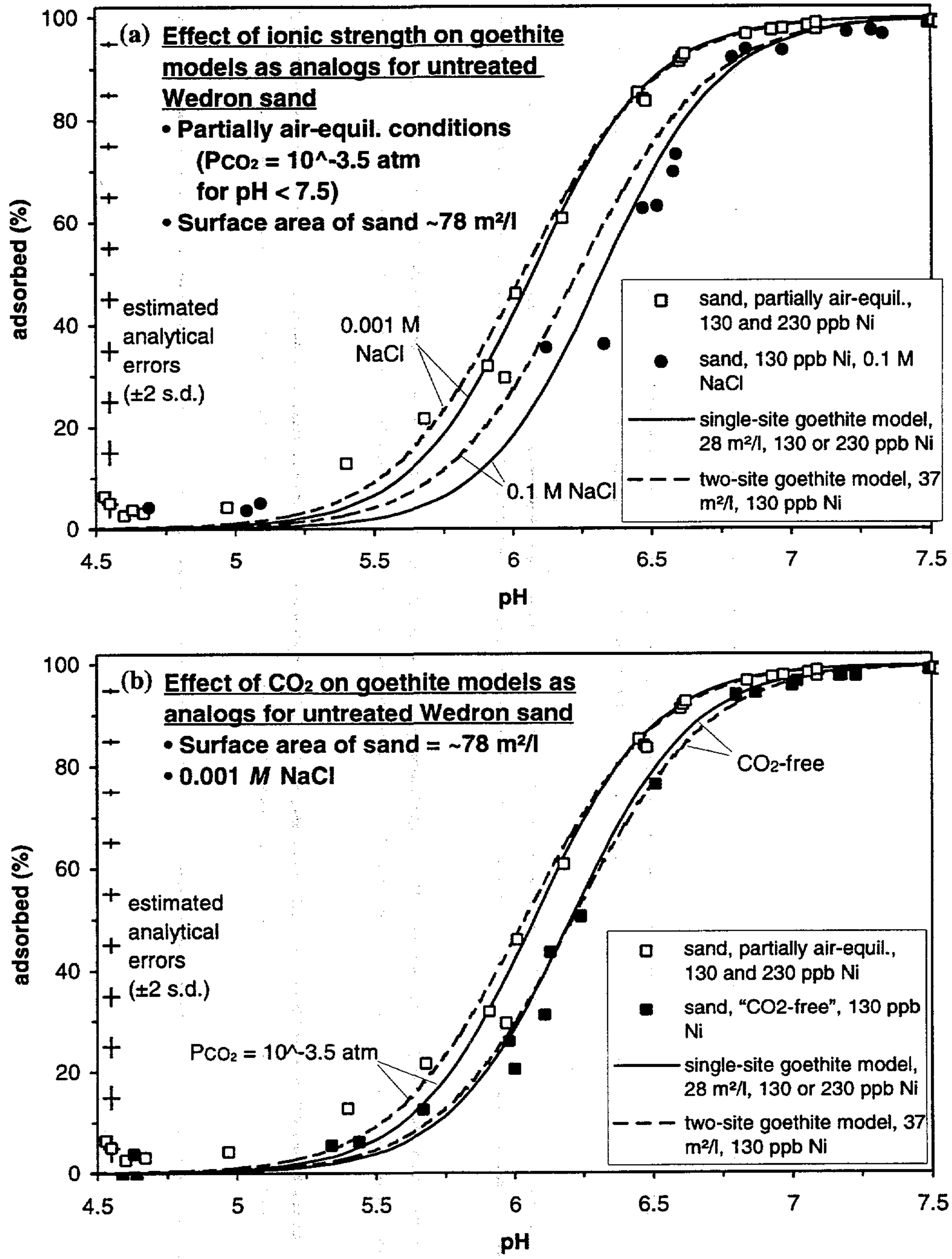

Figure A.25. Performance of goethite-model analogs for Wedron sand under conditions of changing ionic strength and P_{CO_2}. a) Effect of ionic strength (at $P_{CO_2} = 10^{-3.5}$ atm). b) Effect of P_{CO_2} (the models were run under conditions of both atmospheric P_{CO_2} and essentially zero CO_2).

and no CO_2 at all. More likely, it was closer to atmospheric ($10^{-3.5}$ atm) due to partial dissolution of Ca-Mg carbonate in the sand. A comparison of model predictions with observations on the sand shows that in the absence of CO_2, both models provide a reasonable simulation of the observed adsorption onto "CO_2-free" sand. Because the sand was far from free of CO_2, however, the success of the models may be merely fortuitous and they might not provide a quantitative understanding about the underlying processes and effects of CO_2 adsorption at the sand surface.

A.5.2. Evidence for Exposed Kaolinite

Although the goethite models can be adjusted to reasonably simulate the behavior of the sand with respect to adsorption of Ni, the mineralogy of the sand suggests that kaolinite, quartz, and carbonate are also potentially active surfaces (Ward *et al.*, 1995a). As may be seen from Figure A.5 (p. A-16), quartz does not appear to be a reasonable analog for the sand, and is thus dismissed from further consideration here. Further discussion of the role of quartz can be found in Ward (1995). The role of Ca-Mg carbonate as a Ni adsorber is assumed to be minor as well, based on the published work of Zachara *et al.* (1991), who reported an adsorption edge for Ni on calcite with a pH_{50} of 8.5 at a surface area of 5 m^2/l and $I =$ 0.1 M. No published values were found for Ni adsorption onto high-Mg calcite or dolomite. This leaves the role of kaolinite to be explored.

A.5.2.1. Adsorption Density Calculations for Raw Sand

The arguments favoring kaolinite as the second adsorbent in the raw sand are reinforced by the measurements of Ni adsorption in the presence of various concentrations of a second sorbate. Lithium was chosen because it adsorbs only weakly to the sand and to quartz (Abendroth, 1970; Chardymskaya *et al.*, 1987) but is strongly adsorbed by kaolinite (Assaad and Elneklawy, 1986; Anderson *et al.*, 1989). A series of adsorption competition experiments were carried at varying Li/Ni ratios using initial Li concentrations of 100 μg/m*l* and 1000 μg/m*l* (0.014 M and 0.14 M), and initial Ni concentrations of 80–5000 ng/m*l* (1.36×10^{-6} M to 8.5×10^{-4} M). The results of the experiments were presented in Figure A.9 on p. A-20.

In Figure A.26, the effect of competition for adsorption sites is described by Γ, the adsorption density in moles/m², which was calculated for each sample using:

$$\Gamma,\ moles/m^2 = \left. \frac{\left(\%El_{sorbed}/100\right)(Total_{El})}{MW_{El}} \right/ SA,\ m^2 \qquad \{A.3\}$$

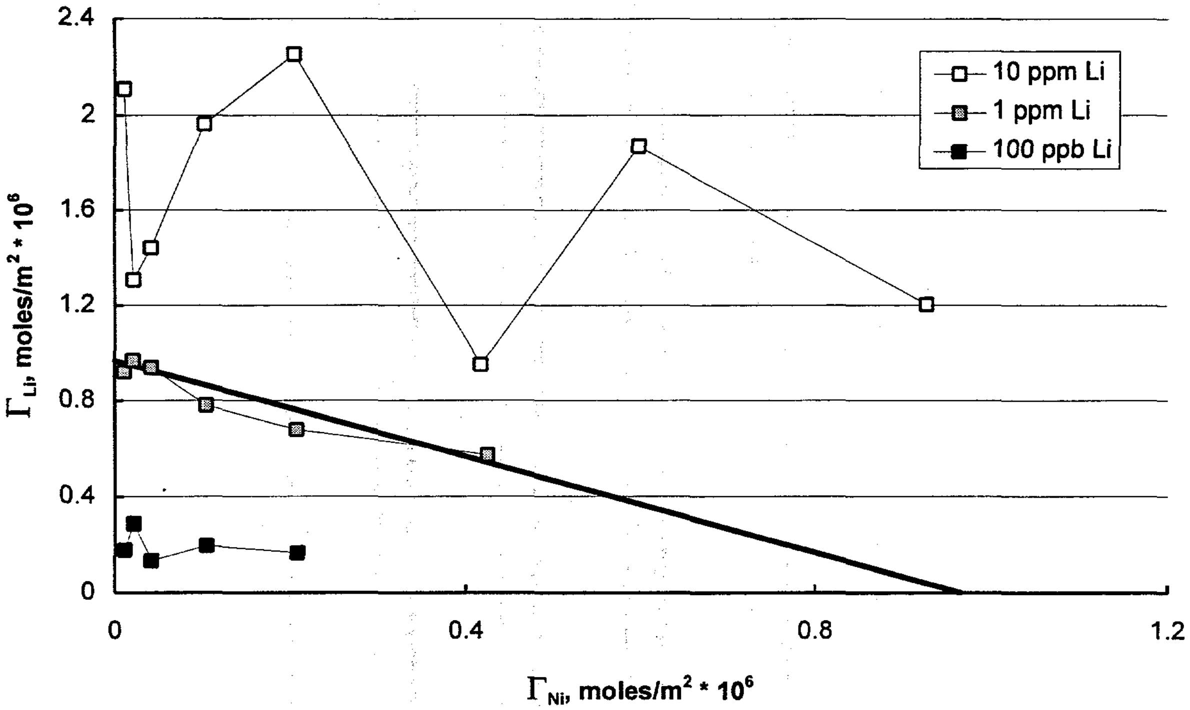

Figure A.26. The effect of Ni surface concentration on the adsorbance of Li. A reference line with a slope of –1, corresponding to a total adsorption density of 0.97 × 10^{-6} moles/m^2, is drawn through the 1 ppm Li points.

where *El* is either Ni or Li, *Total$_{El}$* is the total grams of the element added to the system, *MW* is mole weight, and *SA* is total surface area of the substrate in the system.

For samples with 10 ppm Li, the number of filled sites varies from 0.80 to 1.50 sites/nm^2 (1.32 to 2.45 μmoles/m^2), with considerable scatter.

These data suggest that adsorption may be occurring on a continuum of energetically different sites in the sand. The total number of occupied sites in the 1 ppm Li samples is far less than even the most conservative estimates of site densities in the sand (2.1 sites/nm^2 if the reactive sand surfaces are all goethite and a minimum of 16 sites/nm^2 if kaolinite the is dominant adsorbing phase). Despite this, Li adsorption in these samples is very sensitive to the amount of Ni adsorbed. The slope of the 1 ppm Li curve is -1, suggesting that Li and Ni are competing directly for relatively few favored adsorption sites. Li adsorption is higher in the 10 ppm samples, as energetically less favorable sites are being utilized at this higher concentration.

The total number of occupied sites per nm^2 can be calculated using:

$$\frac{\#\,filled\ sites}{nm^2} = \frac{\left[\frac{\left(\%Ni_{sorbed}/100\right)\left(Total_{Ni}\right)}{MW_{Ni}}\right] + \left[\frac{\left(\%Li_{sorbed}/100\right)\left(Total_{Li}\right)}{MW_{Li}}\right]}{SA,\ nm^2/N} \qquad \{A.4\}$$

where $Total_{Ni}$ and $Total_{Li}$ are the total grams of each added to the system, MW is mole weight, N is Avogadro's number (6.02×10^{23} atoms/mole), and SA is total surface area of the substrate in the system.

The 100 ppb Li curve does not show the effects of Ni competition because only about 0.11 sites/nm^2 are filled; so many empty sites are present that the slight decrease in available sites due to Ni adsorption does not produce a measurable change in Li adsorption. The 1 ppm Li curve is very sensitive to Ni concentration, decreasing linearly with increasing Ni adsorption. The number of occupied sites for the samples on this curve is between 0.53 and 0.60 sites/nm^2 (0.93–0.99 µmoles/m^2).

A.5.2.2. Effects of Li Competition on Ni Adsorption Edges

The results of a series of experiments using an initial Ni concentration of 100 ppb and an initial Li concentration of 100 ppm or 1000 ppm were summarized in Figures A.7, A.8, A.10 and A.11 in a previous section. Changes in Li concentration due to adsorption were minor, because the high concentration used in these experiments is 2–3 orders of magnitude greater than that needed to occupy all of the available adsorption sites. Competitive effects were manifested only as pronounced changes in the behavior of Ni.

On the raw sand, Ni adsorption was slightly diminished in the presence of Li, as shown in Figure A.7, with the adsorption edge shifting from $pH_{50} = 6.3$ to 6.5. The slightly decreased Ni adsorption apparent when Li is added first (~2 h earlier than Ni) may be due to irreversible adsorption of Li at sites that would otherwise irreversibly adsorb Ni. Within the framework of surface-complexation theory, mechanisms by which Li displaces Ni from the surface are limited to two: 1) Li may directly displace some Ni cations; and 2) the increase in ionic strength from 0.001 to 0.014 M will tend to collapse the electrical double-layer, leading to reduced electrostatic attraction for adsorbed cations that do not reside precisely at the mineral surface.

Ni adsorption onto goethite in the presence of Li under air-equilibrated conditions is shown in Figure A.10, along with the air-equilibrated goethite curve for Ni alone for reference. It is apparent that Li has no measurable effect on Ni adsorption, and the inset graph shows that Li adsorption onto goethite is quite small compared to the amount in solution and is independent of pH. Thus adsorbed Ni on goethite must be located close to the surface as an inner-sphere complex, whereas Li must form an outer-sphere complex, or may be present only as a counter-ion in the diffuse layer.

For kaolinite the scenario is quite different. As shown in Figure A.11, Ni adsorption is diminished by the presence of Li, producing a curve with shallower slope at low pH and then nearly leveling off between pH 5 and 6 before reaching complete adsorption near pH 7.5. A scenario that explains the Ni curve would place both Ni and Li at the kaolinite surface, but with Ni forming a substantially stronger complex. Below the adsorption edge for Li at pH 5, a small but increasing amount of Li is adsorbed, interfering with Ni adsorption and thus producing the shallower slope in the Ni curve. In the vicinity of pH 5, as shown in the inset on Figure A.11, Li adsorption becomes energetically favorable, leading to a rapid increase in the amount of Li adsorbed and thus preventing further Ni uptake. Finally, above pH 6, adsorption energetics shift again in the favor of Ni, permitting adsorption to reach 100%. This simple scenario is undoubtedly more complex in reality, as kaolinite is a mixture of at least two types of adsorption sites — silanol (>Si-OH) sites on the basal 001 faces and aluminol (>Al-OH) sites on the edges. Xie and Walther (1992) have shown that even some of the interlayer sites may be accessible to aqueous cations. A quantitative mechanistic model for Li adsorption onto kaolinite would probably require at least two sites, but would largely be an exercise in parameterization due to the paucity of constraining data. At the very least, however, it appears that the presence of kaolinite sites could explain the shift in the Ni adsorption edge seen for the sand in the presence of Li.

Ni adsorption by kaolinite may explain the high affinity of acid-washed Wedron sand for Ni. As shown by studies of Ni adsorption onto kaolinite alone (cf. Figure A.6 (p. A-17), and the quantitative adsorption model described in Section A.4.6, kaolinite has a much greater affinity for Ni than goethite, quartz, or Ca-Mg carbonate. After acid-washing, the surface of any remaining kaolinite would now be exposed, whereas previously it would have been covered by a thin coating of Fe-oxyhydroxide. Thus, acid-washing may have converted the surfaces in the sand from predominantly goethite and Ca-Mg carbonate with minor kaolinite to quartz and substantially more kaolinite.

To test this hypothesis, Ni adsorption onto the acid-washed sand was measured in the presence of Li, with results shown in Figure A.27. While not conclusive, the data are consistent with adsorption onto kaolinite, showing a strong competitive effect between Li and Ni over the same pH range at which it was strongest on pure kaolinite (Figure A.11 on p. A-21, pH 5.3–7.5). Above pH 6, there is an indication of irreversible adsorption of Li when it is added first, similar to that noted previously for the sand.

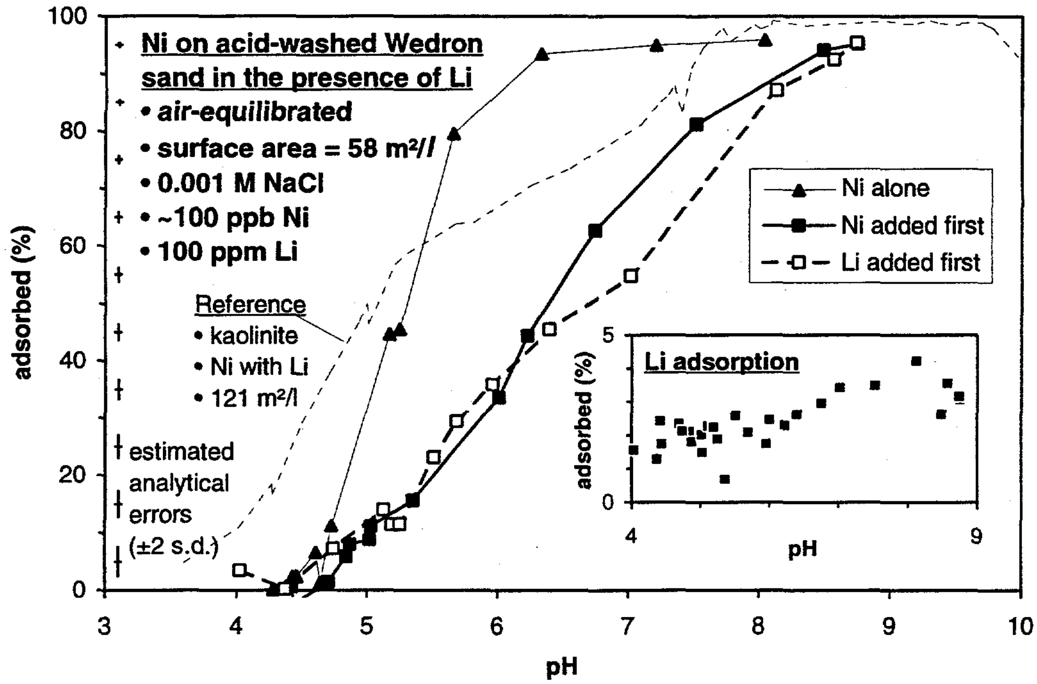

Figure A.27. Ni adsorption onto acid-washed Wedron sand alone and in the presence of Li. Adsorption of Ni onto kaolinite in the presence of Li shown for reference.

SEM observations, however, suggest that the washing procedure removed essentially all of the kaolinite particles adhering to the quartz grains (Ward, 1995). The alternative hypothesis to explain the strong Ni adsorption by the acid-washed sand is that the surfaces of the acid-washed quartz sand grains had been affected by weathering, leaching, and re-precipitation processes during their long exposure to surface- and groundwaters. The outer few nanometers may have become microporous, been converted to amorphous silica, or been coated with a silica gel. Before being quarried, this surface could have been covered by natural iron oxyhydroxide coatings. Thus, the quartz surfaces exposed by the acid washing may have dramatically different surface properties than the freshly fractured quartz surfaces such as those present in Min-U-Sil 5 quartz powder. There are insufficient data to rule out either hypothesis. Definitive evidence might be obtainable from X-ray photo-electron spectroscopy and high-resolution transmission electron microscopy on the acid-washed sand.

A.6. Summary

Our observations on the effects of CO_2 and Li on the adsorption of Ni onto Wedron 510 sand and the pure end-member surfaces of quartz, goethite, and kaolinite are summarized in Table A.11. Wedron 510 sand, with more than 99% quartz in bulk mineralogy, appears to display two types of mineral surfaces to aqueous solutions, neither of which is quartz. Quartz adsorbs Ni so weakly that its contribution to the mixture is completely overshadowed. The presence of Fe-oxyhydroxide is inferred from several lines of evidence: the yellow tinge of the untreated sand, the quantity of Fe leached during the acid wash, and the reasonable surface coverage by goethite needed to account for Ni adsorption by the raw sand.

The Li/Ni site-competition experiments described in this Appendix suggest that kaolinite, too, is an important phase with respect to Ni adsorption onto the sand. On Wedron sand, Li competition for adsorption sites is limited; the Ni adsorption curve is shifted to slightly higher pH relative to the Li-free system. Li does not shift the Ni adsorption curve for goethite at all; hence, goethite alone does not adequately describe the Ni adsorption behavior of Wedron sand. Li competes strongly with Ni for kaolinite adsorption sites; addition of 100 ppm Li shifts the 100 ppb Ni adsorption curve by as much as 2 pH units. Thus, the results of the Li/Ni site competition experiments are consistent with both goethite *and* kaolinite contributing to the adsorption properties of the sand.

Washing the sand with acid causes the affinity of the sand for Ni to increase dramatically, shifting the adsorption edge to lower pH by more than one unit. Our *a priori* expectation was that acid-washing would leave a nearly pure unreactive quartz surface; both Fe-oxyhydroxides and discrete particles of kaolinite in the sand are removed by acid-washing. Our observations, however, may suggest the persistence of a significant amount of kaolinite, present as thin overgrowths on the quartz grains that are no longer be sequestered by a coating of Fe-oxyhydroxide. Alternatively, the acid wash may expose an activated "weathered" quartz surface whose properties are much different than those of freshly fractured quartz surfaces.

Quantitative modeling has focused on developing an accurate description of Ni adsorption onto quartz, kaolinite and goethite. A single-site surface complexation model for Min-U-Sil quartz was developed but does not perform well. Although the model exhibits the required relationships between Ni adsorption, ionic strength and total carbonate, adsorption under alkaline conditions is lower than observed in batch systems. Possible modifications to improve the model such as changes in proposed adsorption stoichiometry are beyond the scope of this work, particularly since it appears that the quartz surface plays a minor role in Ni adsorption by Wedron sand.

Table A.11. Effects of P_{CO_2}, competition with Li, and ionic strength on Ni adsorption onto Wedron sand and pure end-members. pH_{50} is the pH at which 50% of the total exchangeable Ni is adsorbed onto the surface. Not all possible combinations were investigated.

	pH_{50} for Ni*					
Substrate	**no Li, no CO_2**	**atm. CO_2**	**Li and CO_2**	**Effect of CO_2**	**Effect of Li**	**Comments**
Wedron 510 sand • untreated • 78 m^2/*l*	6.3	6.1	6.5**	pH_{50} lowered by 0.2	pH_{50} raised by 0.2	Adsorption of Ni enhanced by CO_2, diminished by Li and increased ionic strength. Both Fe-oxyhydroxide and kaolinite surfaces may be exposed.
Wedron 510 sand • acid-washed • 58 m^2/*l*	4.9	5.0		pH_{50} raised by 0.1		Adsorption diminished by CO_2 but unexpectedly enhanced by acid-washing, which may have exposed more kaolinite or activated the "weathered" grain surfaces.
quartz (Min-U-Sil 5) • 247 m^2/*l*	6.9					Slope of adsorption curve much shallower than for sand; Ni only weakly adsorbed; very sensitive to ionic strength. Not an important surface in the sand.
goethite • 55 m^2/*l*	6.0	6.0	6.0	none	none	Adsorption unaffected by CO_2, Li, or ionic strength, but sensitive to total Ni. Accurate modeling required two types of surface sites.
kaolinite • 124 m^2/*l*		4.2	~5		pH_{50} raised by 0.8	Adsorption of Ni greatly diminished by Li, especially above the Li adsorption edge at pH 5.

* in 0.001 M NaCl   ** Li only; CO_2-free.

The surface complexation model for kaolinite assumes that adsorption is dominated by formation of an inner-sphere complex with aluminol sites and that the actual surface area accessible to Ni cations is 10x the BET-measured surface area. With the aforementioned assumptions, the value of $K_{fm}(\text{AlONi}^+)$ was found by visual optimization using HYDRAQL 94 to be $10^{-2.1}$, over five orders of magnitude greater than that for the silanol sites.

Two models have been developed for Ni adsorption by goethite. A single-site model performs well at high goethite concentrations (~55 m^2/*l*) but over-predicts adsorption and exhibits too steep an adsorption edge at lower goethite concentrations. The decrease in slope of the adsorption edge with a decrease in goethite concentration is symptomatic of "non-linear" behavior, caused by the presence of sites with differing affinities for Ni. The two-site model, in which 3.8% of the sites have a high affinity for Ni, successfully simulates Ni adsorption at both high and low goethite concentration. Both models predict reduced Ni adsorption at reduced P_{CO_2}, a consequence of adopting the van Geen *et al.* (1994) model for reversible CO_2 adsorption onto goethite, but appear to over-predict the magnitude of this effect. Both models predict sensitivity to ionic strength, in apparent contrast to the behavior observed in the presence of 100 μg/m*l* Li, where no change in adsorption behavior was noted in spite of an increase in ionic strength from 0.001 M to 0.015 M. When calibrated as analogs to the sand, the single-site goethite adsorption model is superior to the two-site model, showing the same decrease in adsorption with an increase in ionic strength, the same insensitivity to changes in total Ni concentration and the proper effect of variations in P_{CO_2} on Ni adsorption as were observed on the sand.

Qualitatively, the adsorption properties of Wedron sand can be adequately modeled by treating it as a two-component system. Ni adsorption occurs primarily on goethite, on sites where Li does not compete; some of the Ni adsorbs to kaolinite, and does exchange with Li--hence the shift in the Ni adsorption curve in the sand Li/Ni competition studies. As discussed in Appendix C, all of the Li adsorbs irreversibly onto the sand, suggesting that kaolinite is the only important phase in the sand with respect to Li adsorption. This model accounts for the important surface processes in the sand with respect to adsorption of Ni and can be used in transport modeling to interpret the results of the caisson experiment.

A.7. References Cited

Abendroth, R.P., 1970: "Behavior of a Pyrogenic Silica in Simple Electrolytes," *Journal of Colloid and Interface Science*, **34**, 591-596.

Anderson, M.A., P.M. Bertsch, and W.P. Miller, 1989: "Exchange and Apparent Fixation of Lithium in Selected Soils and Clay Minerals," *Soil Science*, **148**, 46-52.

Assaad, F.F., and A.S. Elneklawy, 1986: "The Relation of Physico-Chemical Properties of Alkaline Metal Cations to the Exchange Selectivity on Kaolinite Clay," *Z. Phys. Chemie*, Leipzig, **267**, 1135-1144.

Atkinson, R.J., A.M. Posner, and J.P. Quirk, 1967: "Adsorption of Potential-Determining Ions at the Ferric Oxide-Aqueous Electrolyte Interface," *Journal of Physical Chemistry*, **71**, 550-558.

Baes, Jr., C.F., and R.E. Mesmer, 1976: *The Hydrolysis of Cations*, Krieger Publishing Company, Malabar, FL, 489 pp.

Balistrieri, L.S., and J.W. Murray, 1979: "Surface of Goethite (αFeOOH) in Seawater," *Chemical Modeling in Aqueous Systems*, E.A. Jenne, ed., American Chemical Society Symposium Series **93**, 275-298.

Balistrieri, L.S., and J.W. Murray, 1981: "The Surface Chemistry of Goethite (alpha FeOOH) in Major Ion Seawater," *American Journal of Science*, **281**, 788-806.

Ball, J.W., D.K. Nordstrom, and E.A. Jenne, 1980: *Additional and Revised Thermochemical Data and Computer Code for WATEQ2 — A Computerized Model for Trace and Major Element Speciation and Mineral Equilibria of Natural Waters*, WRI 78-116, U.S. Geological Survey Water Resources Investigations.

Bolt, G.H., 1957: "Determination of the Charge Density of Silica Sols," *Journal of Physical Chemistry*, **61**, 1166-1169.

Brunauer, S., P.H. Emmett, and E. Teller, 1938: "Adsorption of Gases in Multimolecular Layers," *Journal of the American Chemical Society*, **60**, 309-319.

Bryan, C.R., and C. Boyle, 1995: "Appendix C: Li Adsorption by Wedron 510 Sand and Pure Minerals: Reversibility and Kinetic Studies," in *Batch and Column Studies of Adsorption of Li, Ni, and Br by a Reference Sand for Contaminant Transport Experiments, Appendix C*, Siegel, M.D., D.B. Ward, C.R. Bryan, and C. Boyle, SAND95-0591, Sandia National Laboratories, Albuquerque, NM, 23 pp.

Bryan, C.R., D.B. Ward, and M.D. Siegel, 1995: "Appendix B: Ni Sorption and Solubility Studies," in M.D. Siegel, D.B. Ward, C.R. Bryan, and W.C. Cheng, *Characterization of Materials for a Reactive Transport Model Validation Experiment, Appendix B*, Siegel, M.D., D.B. Ward, C.R. Bryan, and W.C. Cheng, SAND94-0189, Sandia National Laboratories, Albuquerque, New Mexico, 31 pp.

Butler, J.N., and R. Huston, 1970: "Activity Coefficients and Ion Pairs in the Systems Sodium Chloride-Sodium Bicarbonate-Water and Sodium Chloride-Sodium Carbonate-Water," *Journal of Physical Chemistry*, **74**, 2976-2983.

Carroll-Webb, S.A., and J.V. Walther, 1988: "Kaolinite dissolution at 25°, 60°, and 80° C," *American Journal of Science*, **290**, 797-810.

Chardymskaya, E.Yu., M.P. Siderova, and E.V. Kulepova, 1987: "Determination of EDL Potentials on SiO_2 Surfaces in CsCl and LiCl Solutions from Adsorption Measurements," *Kolloidnyi Zhurnal*, **48**, 645-649.

Davies, C.W., 1962: *Ion Association*, Butterworths, London.

Davis, J.A., and D.B. Kent, 1990: "Surface Complexation Modeling in Aqueous Geochemistry, in Mineral-Water Interface Geochemistry," *Reviews in Mineralogy*, **23**, M.F. Hochella and A.F. White, eds., Mineralogical Society of America, Washington, D.C., 177-260.

Davis, J.A., R.O. James, and J.O. Leckie, 1978: "Surface Ionization and Complexation at the Oxide-Water Interface. 1. Computation of Electrical Double Layer Properties in Simple Electrolytes," *Journal of Colloid and Interface Science*, **63**, 480-499.

Deer, W.A., R.A. Howie, and J. Zussman, 1966: *An Introduction to the Rock-forming Minerals*, Longman Group Limited, London, 528 pp.

Dzombak, D.A., and F.M.M. Morel, 1990: *Surface Complexation Modeling*, John Wiley & Sons, Inc., New York, 393 pp.

Garrels, R.M., and C.L. Christ, 1965: *Solutions, Minerals, and Equilibria*, Jones and Bartlett, Boston, MA, 450 pp.

Girvin, D.C., L.L Ames, A.P. Schwab, and J.E. McGarrah, 1991: "Neptunium Adsorption on Synthetic Amorphous Iron Oxyhydroxide," *Journal of Colloid and Interface Science*, **141**, 67-77.

Hayes, K.F., and J.O. Leckie, 1987: "Modeling Ionic Strength Effects on Cation Adsorption at Hydrous Oxide/Solution Interfaces," *Journal of Colloid and Interface Science*, **115** (2), 564-572.

Hayes, K.F., G. Redden, E. Ela, and J.O. Leckie, 1990: *Application of Surface Complexation Models for Radionuclide Adsorption: Sensitivity Analysis of Model Input Parameters Final Report*, NUREG/CR-5547, U.S. Nuclear Regulatory Commission, Washington, D.C., 81 pp.

James, R.O., J.A. Davis, and J.O. Leckie, 1978: "Computer Simulation of the Conductometric and Potentiometric Titrations of the Surface Groups on Ionizable Latexes", *Journal of Colloid and Interface Science*, **65** (2), 331-344.

Kent, D.B., V.S. Tripathi, N.B. Ball, J.O. Leckie, and M.D. Siegel, 1988: *Surface–Complexation Modeling of Radionuclide Adsorption in Subsurface Environments*, SAND86-7175, Sandia National Laboratories, Albuquerque, NM, 113 pp.

Kester, D.R., and R.M. Pytkowicz, 1975: "Theoretical Model for the Formation of Ion-Pairs in Seawater," *Marine Chemistry*, **3**, 365-374.

Leckie, J.O., A.R. Appleton, N.B. Ball, K.F. Hayes, and B.D. Honeyman, 1984: *Adsorptive Removal of Trace Elements from Fly-Ash Pond Effluents onto Iron Oxyhydroxide*, EPRI RP-910-1, Electric Power Research Institute, Palo Alto, California.

Libus, Z., and H. Tialowska, 1975: "Stability and Nature of Complexes of the Type MCl^+ in Aqueous Solution (M = Mn, Co, Ni and Zn)," *Journal of Solution Chemistry*, **4**, 1011-1022.

Mattigod, S.V., and G. Sposito, 1977: "Estimated Association Constants for Some Complexes of Trace Metals with Inorganic Ligands," *Soil Science Society of America*, **41**, 1092-1097.

Mattigod, S.V., A.S. Gibali, and A.L. Page, 1979: "Effect of Ionic Strength and Ion-Pair Formation on the Adsorption of Nickel by Kaolinite," *Clays and Clay Minerals*, **27**, 411-416.

Nieboer, E., and W.A.E. McBryde, 1973: "Free-Energy Relations in Coordination Chemistry. III. A Comprehensive Index to Complex Stability," *Canadian Journal of Chemistry*, **51**, 2512-2524.

Papelis, C., K.F. Hayes, and J.O. Leckie, 1988: *HYDRAQL: A Program for the Computation of Chemical Equilibrium Composition of Aqueous Batch Systems Including Surface-Complexation Modeling of Ion Adsorption at the Oxide/Solution Interface*, Technical Report 306, Stanford University Department of Civil Engineering, Stanford, 130 pp.

Rea, R.L., and G.A. Parks, 1990: "Numerical Simulation of Coadsorption of Ionic Surfactants with Inorganic Ions on Quartz," in *Chemical Modeling of Aqueous Systems II*, Melchior and Bassett, eds., ACS Symposium Series 416, American Chemical Society, Washington, D.C., pp. 261–271.

Riese, A.C., 1982: *Adsorption of Radium and Thorium onto Quartz and Kaolinite: "A Comparison of Solution/Surface Equilibria Models*, Unpublished Ph.D. thesis, Colorado School of Mines, Golden, Colorado, 292 pp.

Siegel, M.D., D.B. Ward, C.R. Bryan, and W.C. Cheng, 1995: *Characterization of Materials for a Reactive Transport Model Validation Experiment*, SAND94-0189, Sandia National Laboratories, Albuquerque, NM, 277 pp.

Sillen, L.G., and A.E. Martell, 1964: *Stability Constants of Metal-Ion Complexes*, Special Publication 17, The Chemical Society, London, 754 pp.

Smith, R.M., and A.E. Martell, 1976: *Critical Stability Constants: Volume 4. Inorganic Complexes*, Plenum Press, New York, 257 pp.

Sposito, G., 1984: *The Surface Chemistry of Soils*, Oxford University Press, New York.

Stumm, W., and J.J. Morgan, 1981: *Aquatic Chemistry*, 2nd Ed., John Wiley and Sons, New York, 780 pp.

Tadros, T.F., and J. Lyklema, 1968: "Adsorption of Potential-Determining Ions at the Silica-Aqueous Electrolyte Interface and the Role of Some Cations," *Electroanalytical Chemistry and Interfacial Chemistry*, **17**, 267-275.

Theis, T.L., and R.O. Richter, 1980: "Adsorption Reactions of Nickel Species at Oxide Surfaces," in *Particulates in Water: Characterization, Fate, Effects, and Removal, Advances in Chemistry,* **189**, M.C. Cavanaugh and J.O. Leckie, eds., American Chemical Society, Washington, D.C., p.73-96.

Tripathi, V.S., 1983: *Uranium (VI) Transport Modeling: Geochemical Data and Submodels*, Ph.D. thesis, Stanford University Department of Applied Earth Science, Stanford, 297 pp.

van Geen, A., A.P. Robertson, and J.O. Leckie, 1994: "Complexation of Carbonate Species at the Goethite Surface: Implications for Adsorption of Metal Ions in Natural Waters," *Geochimica et Cosmochimica Acta,* **58**, 2073-2086.

Van Panthaleon Van Eck, C.L., 1953: "On the Mutual Stability Relationship of MeA Complexes Consisting of a Metal Ion Me and a Ligand A in Aqueous Solution, for Consecutive Values of n," *Recuel des Travaux Chimiques des Pays-Bas*, **72**, 529-537.

Wagman, D.D., W.H. Evans, V.B. Parker, R.H. Schumm, I. Halow, S.M. Bailey, K.L. Churney, and R.L. Nuttall, 1982: "The NBS Tables of Chemical Thermodynamic Properties: Selected Values for Inorganic and C1 and C2 Organic Substances in SI Units," *Journal of Physical and Chemical Reference Data*, **11:2**, 392 pp.

Ward, D.B., 1995: *Nickel Adsorption on a Natural Sand and Goethite, Kaolinite, and Quartz: Single- vs. Multi-Site Models and the Role of* CO_2, unpublished Ph.D. thesis, University of New Mexico, Albuquerque, New Mexico.

Ward, D.B., M.D. Siegel, and C.R. Bryan, 1995a: "Characterization of Wedron 510 Sand for the Intermediate-Scale (Caisson) Transport Experiment," in M.D. Siegel, D.B. Ward, C.R. Bryan, and W.C. Cheng, *Characterization of Materials for a Reactive Transport Model Validation Experiment, Appendix A*, Siegel, M.D., D.B. Ward, C.R. Bryan, and W.C. Cheng, SAND94-0189, Sandia National Laboratories, Albuquerque, New Mexico, 43 pp.

Ward, D.B., C.R. Bryan, W.C. Cheng, and C.R. Boyle, 1995b: "Experimental Procedures Used in the Characterization Study," in M.D. Siegel, D.B. Ward, C.R. Bryan, and W.C. Cheng, *Characterization of Materials for a Reactive Transport Model Validation Experiment, Appendix E*, Siegel, M.D., D.B. Ward, C.R. Bryan, and W.C. Cheng, SAND94-0189, Sandia National Laboratories, Albuquerque, New Mexico, 114 pp.

Wieland, E., and W. Stumm, 1992: "Dissolution Kinetics of Kaolinite in Acidic Aqueous Solutions at 25° C," *Geochimica et Cosmochimica Acta*, **56**, 3339-3355.

Westall, J.C., 1982: *FITEQL -- A Computer Program for Determination of Chemical Equilibrium Constants from Experimental Data, Version 2.0*, Report 82-02, Dept. of Chemistry, Oregon State University, Corvallis, Oregon, 61 pp.

Westall, J.C., and A. Herbelin, 1992: *Sample Problem VI. Adsorption of Zn(II) on Hydrous Ferric Oxide as a Function of pH*, Addendum to FITEQL 2.0 Manual, Dept. of Chemistry, Oregon State University, Corvallis, Oregon, 7 pp.

Xie, Z., and J.V. Walther, 1992: "Incongruent Dissolution and Surface Area of Kaolinite," *Geochimica et Cosmochimica Acta*, **56**, 3357-3363.

Yates, D.E., S. Levine, and T.W. Healy, 1974: "Site-Binding Model of the Electrical Double Layer at the Oxide/Water Interface," *Journal of the Chemical Society of London Faraday Transactions*, **70**, 1807-1818.

Zachara, J.M., C.E. Cowan, and C.T. Resch, 1991: "Sorption of Divalent Metals on Calcite," *Geochimica et Cosmochimica Acta*, **55**, 1549-1562.

Appendix B.

Kinetics of Ni Adsorption/Desorption with Wedron 510 Sand

Charles R. Bryan and David B. Ward

Contents

B.1. Introduction

Previous studies (Bryan *et al.*, 1995) determined that the kinetics of Ni adsorption onto Wedron 510 sand at pH ~7.6 are moderately fast, reaching equilibrium in 2 – 4 h, but the rate and extent of desorption, and the pH dependence of both adsorption and desorption, were not examined. Evaluation of these factors is important in interpreting the results of the 200 ppb Ni pulse through the Sandia/Los Alamos caisson, described in Appendix F of this report. Breakthrough of the Ni pulse occurred more rapidly than predicted, suggesting that Ni adsorption under the pH conditions in the caisson may have been slower than previous laboratory batch experiments, run at higher pH, had indicated. The studies described here provide information on rates of adsorption and desorption of Ni on Wedron sand as a function of pH.

B.2. Methods

B.2.1. Adsorption Studies

Two experiments were run to examine the kinetics of Ni adsorption. The first was run at pH ~7.7, using 20 g Wedron 510 sand and 20 m*l* of 0.001 M NaCl in screw-cap polycarbonate centrifuge tubes. After pre-equilibrating for two days on hematology mixers, each tube was spiked with 200 μ*l* of 10 ppm Ni, neutral pH solution, yielding an initial electrolyte Ni concentration of 100 ppb. Each tube was shaken violently to homogenize the sand and electrolyte, and then mixed steadily by hand or on a hematology mixer until the desired equilibration time, from 1 minute to 24 hours, had elapsed. Samples of the electrolyte were extracted from the tube with a 10 ml disposable plastic syringe, forced through a 0.2 μm membrane filter, and acidified to 2% HNO_3 for later Ni analysis by GFAA. The pH of the remaining electrolyte was measured immediately after Ni aliquots were extracted. The experiment was run under atmospheric P_{CO_2}, and the pH of the systems was buffered by carbonate naturally present in the sand; the mean and standard deviation of the measured pH values was 7.70 ± 0.10. The pH did not vary with equilibration time.

The second adsorption experiment was run in duplicate at pH ~6.3, on the steep part of the Ni adsorption edge. In order to avoid the small pH variations which occur when multiple small batch systems are used, a single 250 m*l* bottle was used for each system, consisting of 80 m*l* electrolyte, 80 g sand, and 2.4 m*l* of 50 mmol HCl (added to lower the pH to 6.3). After two days pre-equilibration on a hematology mixer, each system was sparged with air to remove excess CO_2 and spiked with 100 ppb Ni. Each system was agitated violently to mix the sand and electrolyte and returned to the mixer. Aliquots of the electrolyte were collected at timed intervals from 1 minute to 24 hours; ~1.5 m*l* electrolyte was withdrawn using a 10 ml disposable plastic syringe, forced through a 0.2 µm membrane filter, and acidified for later Ni analysis. The pH of the systems was measured before the first sampling interval (1 minute), and after collection of the final (24 hr) sample; an upward pH drift of ~0.12 units was observed in each system.

B.2.2. Desorption Studies

One batch desorption experiment was run using 20 g sand and 20 m*l* 0.001 M NaCl in screw-cap centrifuge tubes. Samples were pre-equilibrated at pH ~7.7 for two days on hematology mixers and spiked with 200 µ*l* of 10 ppm Ni solution, yielding an initial electrolyte Ni concentration of 100 ppb. After equilibrating for two days, samples were taken to verify that Ni adsorption was ~100%, as determined by previous studies at this pH (Bryan *et al.*, 1995). Acid (50 mmol HCl) was then added to each tube, in amounts varying from 210 to 1000 µ*l*, and each tube was sampled after the appropriate re-equilibration interval, from ½ hour to 130 hours. Sampling was done as described above for the adsorption experiments.

The other desorption experiment was performed using an autotitrator (described in detail in Siegel *et al.*, 1995; Appendix E.6), with the standard reactor jar replaced by a 1 *l* polyethylene bottle immersed in a 25 °C constant-temperature water bath. A paddle-type stirrer turning at ~800 rpm was used to maintain the sand in suspension. The electrode was isolated from the direct flow of the suspension, and thus from the sedimentation potential (~1 mV) by a plastic shield constructed from a 10 m*l* syringe body. The suspension was sampled using a 1/8″ O.D. tube connected to a disposable plastic syringe by a sleeve of 3/32″ I.D. vinyl tubing. During sampling, the stirrer was set to maximum (> 1000 rpm) to maximize mixing, and a 5 m*l* sample was withdrawn. The electrolyte was separated from the sand by forcing it through a 0.2 µm syringe filter, after which it was acidified and later analyzed for Ni. Ni analysis by GFAA is described in Siegel *et al.* (1995, Appendix E.3).

The reactor bottle was filled with a 1:1 suspension of Wedron 510 sand in 0.001 M NaCl (722 g sand + 722 m*l* electrolyte), capped, and equilibrated overnight with Ar-purge of its headspace (~0.6 *l*/min at ambient pressure) while being stirred vigorously. The system was spiked with $1.23 \cdot 10^{-6}$ moles Ni to give a total added Ni concentration of ~100 ng/m*l*. After allowing 2 h for adsorption to reach equilibrium, the pH was adjusted downward by addition of acid until the next target pH was reached. For pH adjustment, 0.5 N HNO_3 and 0.64 N NaOH were used. During equilibration, the autotitrator was used as a pH-stat to maintain constant pH as the carbonate in the sand dissolved. This equilibration and adjustment loop was repeated until pH 4 was reached. Samples were taken immediately before and after pH adjustment, and also after the initial ~2 h equilibration if the next pH adjustment was not going to take place immediately. At the end of the first day (at pH 6.7), stirring was stopped and the autotitrator was shut down, but Ar-purge was continued until the experiment was resumed 41 h later. After the second day of measuring (at pH 5.1), stirring continued while the autotitrator maintained pH 5.1 for the next 38.5 h until the experiment was resumed.

Total exchangeable Ni was determined at the end of the experiment by acidifying the system to pH 3 and allowing it to equilibrate for several weeks with occasional agitation before sampling it for Ni-GFAA analysis. Total exchangeable Ni was found to be 126 ng/m*l* at the end of the experiment, consistent with the addition of ~100 ng/m*l* Ni plus ~35 ng/g Ni naturally present in the sand. Analytical precision is estimated to have been better than ± 1.8% or 0.4 ppb, whichever is larger, for dissolved Ni, and better than ± 0.05 pH units for pH measurements.

All adsorption and desorption kinetics experiments, save for the one run in a constant temperature water bath, were run under ambient laboratory conditions. Examination of daily pH electrode calibration records, which record temperature data, indicates that laboratory temperatures varied nonsystematically from 17.5 to 22.3 °C over the course of these experiments. Mean temperature was 19.2 ± 1.7 °C.

B.3. Results

B.3.1. Adsorption Studies

The results of experiments to examine the kinetics of Ni adsorption are summarized in Figure B.1. The *total exchangeable Ni* includes both 100 ng/g added Ni and about 35 ng/g Ni which occurs naturally in an exchangeable state in the sand. At pH 7.7, all of the naturally-occurring Ni is initially adsorbed, so the total exchangeable Ni adsorbed is 35 of 135 ng/g, or about 26%, at time $t = 0$ (just after spiking). At pH 6.3, about 8 ng/g of the naturally-occurring exchangeable Ni desorbs during pre-equilibration, so about 27 of 135 ng/g Ni, or 20 %, is adsorbed at $t = 0$.

Equilibrium adsorption studies (Bryan *et al.*, 1995) found that 100% and 70 % of Ni in 100 ppb solutions was adsorbed by Wedron sand within 48 hours at pH 7.7 and pH 6.3, respectively. The results of the present kinetic experiment at pH ~7.7 are consistent the previous equilibrium studies. Adsorption was extremely rapid; about 66% of the added Ni (75% of the total exchangeable Ni) was adsorbed within

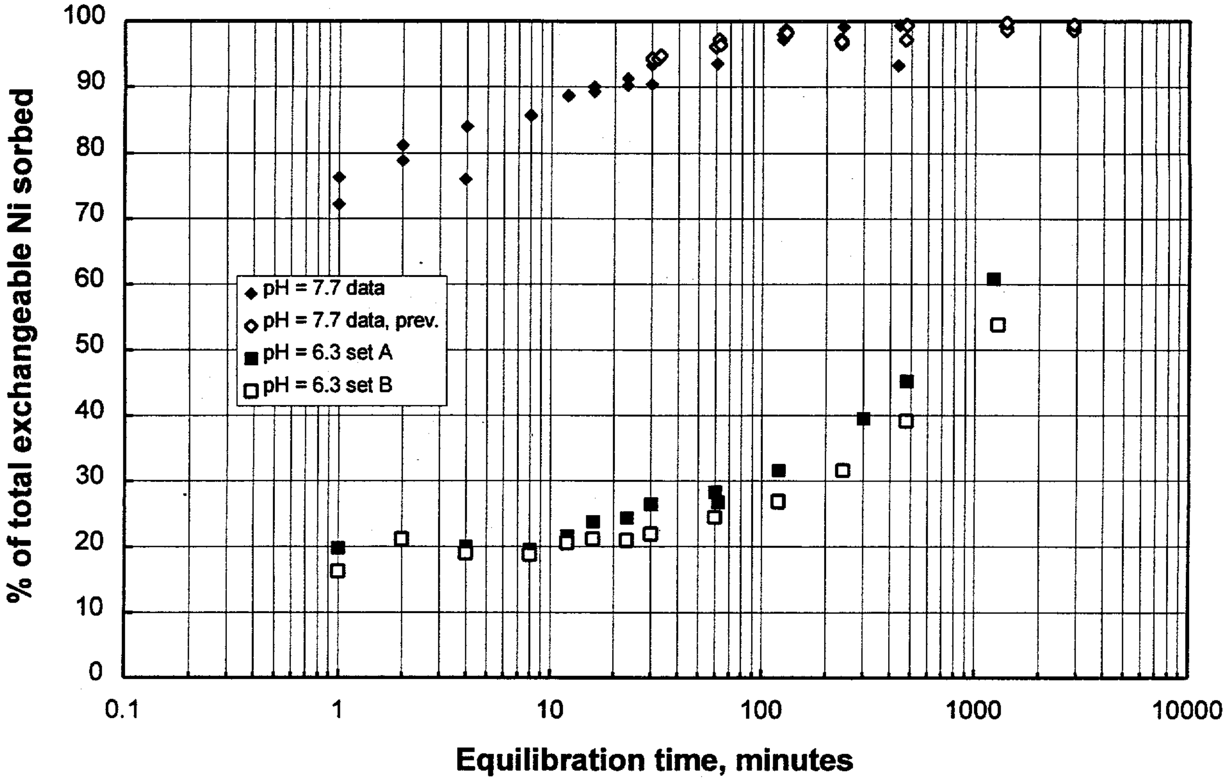

Figure B.1. Adsorption of Ni by Wedron 510 sand at pH 7.7 and pH 6.3. Total Ni = 135 ppb. Previous data are from Bryan *et al.* (1995). At pH 7.7 and 6.3, 100 % and 70%, respectively, of the Ni is adsorbed at equilibrium.

one minute, 90% was adsorbed within ½ hr, and equilibrium was reached after 2 – 4 hours. Measured pH values for the individual batch systems were 7.70 ± 0.10.

The pH of the systems run at ~6.3 varied slightly. In the first (set A), the pH increased from 6.30 initially to 6.43 after 24 hours; in the second (set B), the pH rose from 6.15 to 6.27 in 24 hours. Adsorption is considerably slower at pH 6.3 than at 7.7. There was no measurable adsorption for several minutes after addition of the spike, and only about 40 % of the total exchangeable Ni was adsorbed after 4 hours. Equilibrium (70% adsorbed) was not reached even after 24 hours. Even the small pH difference between the two replicates caused a significant difference in adsorption rate; adsorption was slower in the slightly more acidic set B.

First-order reaction rate constants were calculated for Ni adsorption onto Wedron 510 sand at the two different pH values. If adsorption is a first order reaction, then the following equation applies:

$$-\ln(C) + \ln(C_o) = kt$$

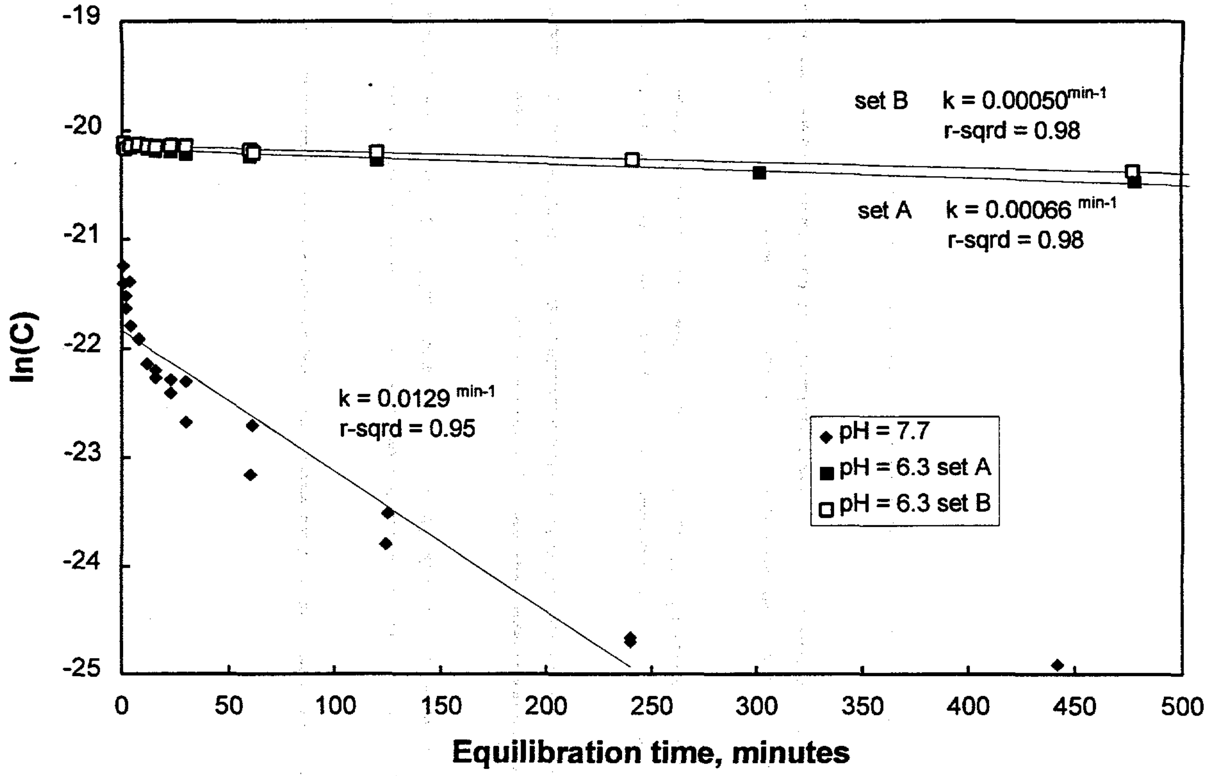

Figure B.2. Calculated first-order rate constants for adsorption data. Best-fit lines, determined by least squares regression, are shown.

where C is the concentration of Ni in solution at time *t*, C_o is the original amount of Ni in solution, and *k* is the rate constant. On a plot of -ln(C) versus time, the data should fall on a straight line with a slope of *k* (Figure B.2). The pH 6.3 data form linear trends on this plot, indicating that adsorption at this pH can be approximated as a first-order reaction; calculated rate constants for data sets A and B were 0.00066 min^{-1} and 0.00050 min^{-1}, respectively. The pH 7.7 data is non-linear on this plot, suggesting either that Ni adsorption at this pH is a higher-order reaction, or that more than one adsorption mechanism or adsorption site is involved. A best fit line for this data is given for comparison with the pH 6.3 data; given the nonlinearity of the data, little significance should be attached to this line.

The stochiometry of probable adsorption reactions derived from the batch adsorption data indicates that adsorption of Ni onto Wedron 510 sand is a first-order reaction (Appendix A, this report); hence, no attempt was made to fit the data using higher-order reactions. It is possible to model the pH = 7.7 data as the sum of two first-order reactions (Figure B.3); a rapid reaction (1), occurring early in the experiment (<20 minutes), with a rate constant of 0.0455 min^{-1}, and a slower reaction (2), occurring throughout the experiment, with a rate constant of 0.0106

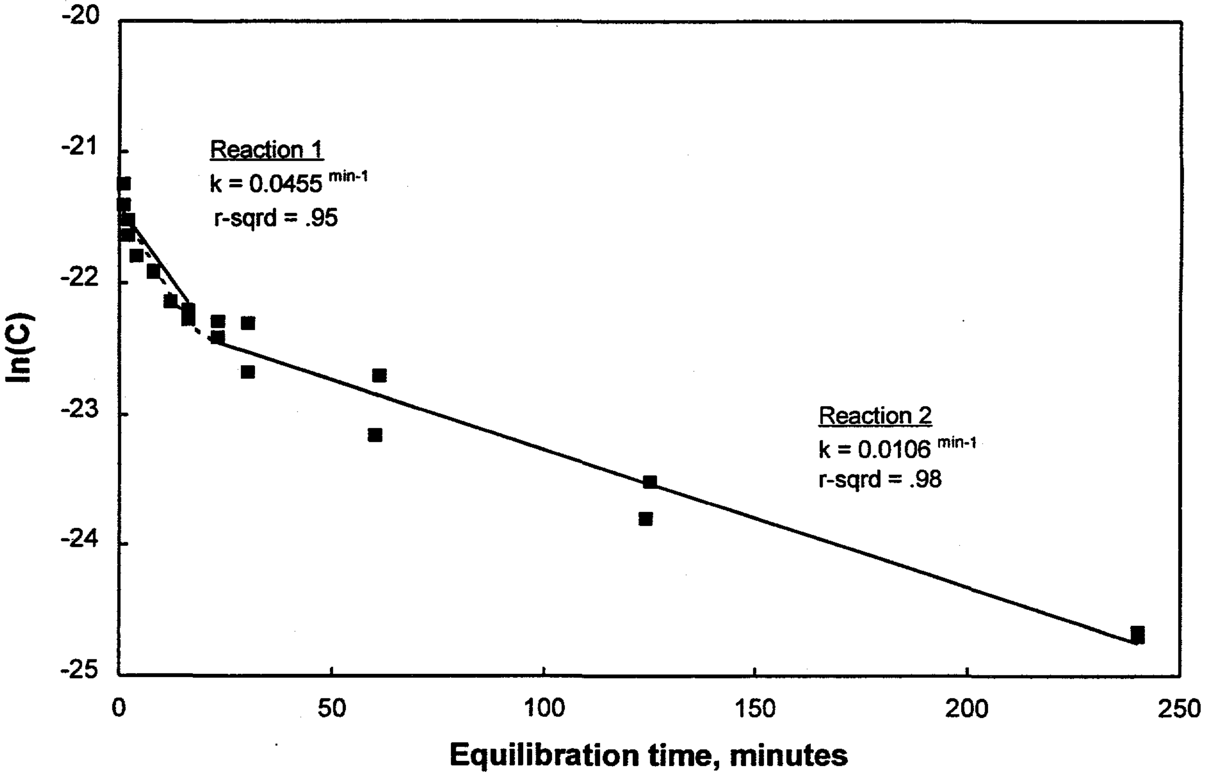

Figure B.3. Modeling pH = 7.7 data as a function of two first-order reactions. At *t* < 20 both Reaction 1 and 2 are occurring; results are additive (dotted line). At *t* > 20, only Reaction 2 is occurring.

min^{-1}. For *t* < 20 minutes, both reactions are occurring, and the results are additive (dotted line in Figure B.3); for *t* > 20 minutes, only reaction 2 is occurring. This is consistent with rapid adsorption onto a high-energy site, which either becomes saturated or reaches equilibrium with respect to the Ni in solution in ~ 20 minutes, and slower adsorption onto an energetically less favorable site. This is consistent with results of modeling discussed in Appendix A, which suggest that adsorption is occurring at two different sites (assuming goethite is the major active substrate in the sand with respect to Ni adsorption); a relatively rare high-energy site, and a much more abundant lower-energy site.

B.3.2. Desorption Studies

Samples for the batch desorption experiment were equilibrated with 100 ppb Ni at pH 7.7; electrolyte samples collected after two days showed that Ni adsorption was ~100%. Acid was then added to each tube to lower the pH, so that the samples no longer fell on the equilibrium Ni adsorption curve. This provided the driving force for desorption.

The results of the batch desorption experiment are shown in Figure B.4, along with a reference curve showing equilibrium adsorption as determined from batch systems run under atmospheric conditions. Solid lines connect samples to which different amounts of acid were added, but which had equal desorption time. The dotted lines connect samples to which equal amounts of acid were added; they form desorption trajectories for sand/electrolyte systems. The amount of Ni adsorbed in each sample decreased with desorption time until the systems were once more in equilibrium. The pH of samples increased with re-equilibration time, due to continued dissolution of carbonate in the sand.

The samples with a final pH greater than 6.0 reached equilibrium during the

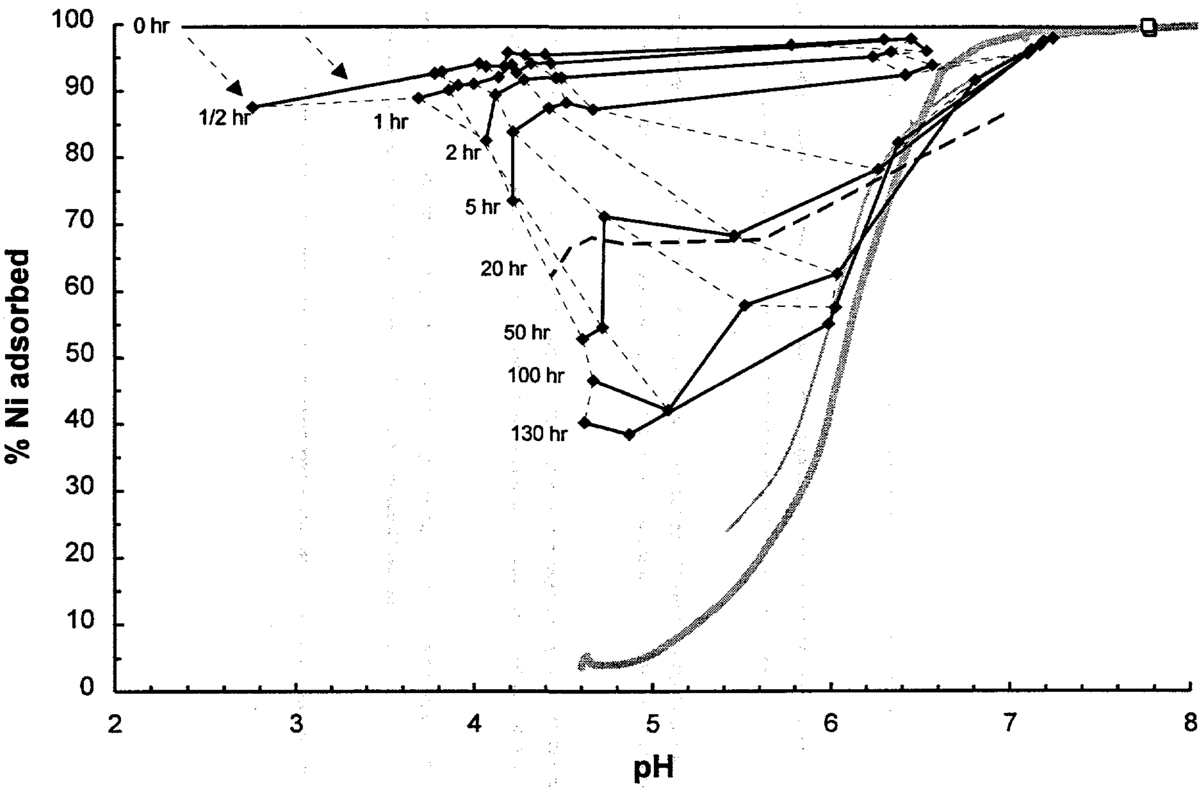

Figure B.4. Desorption of Ni from Wedron 510 sand. Solid lines connect samples of equal re-equilibration time; the 20 hr line, determined later, is inconsistent with the others, and is dashed. Dotted lines connect samples to which equal amounts of acid were added. The heavy shaded line is the equilibrium Ni adsorption curve for Wedron sand under atmospheric conditions, from Bryan (1995). The thinner shaded line is an apparent equilibrium desorption curve; below pH 5.8, the curve is speculative.

experiment, and define an equilibrium desorption curve (light shaded line). This curve is offset slightly from the 100 ppb Ni reference adsorption curve (heavy line), which was derived under similar experimental conditions. Several samples intersected the equilibrium curve before reaching a stable pH; these moved up along the curve, re-adsorbing Ni as the pH continued to increase. Those samples with a lower final pH did not reach the equilibrium Ni curve prior to the conclusion of the experiment. It should be noted however, that while higher pH samples reached equilibrium faster, the amount of Ni desorbing per unit time is far greater in the low-pH samples.

It is not possible to derive desorption rate constants from this data. Such constants must be obtained at constant pH; the Ni solution concentrations and desorption trajectories shown in Figure B.4 are affected both by desorption and by pH change due to carbonate dissolution.

Results for the autotitrator desorption experiment are shown in Figure B.5 along with a reference curve showing equilibrium adsorption as determined from CO_2-free batch systems. The system response as acid was added during pH

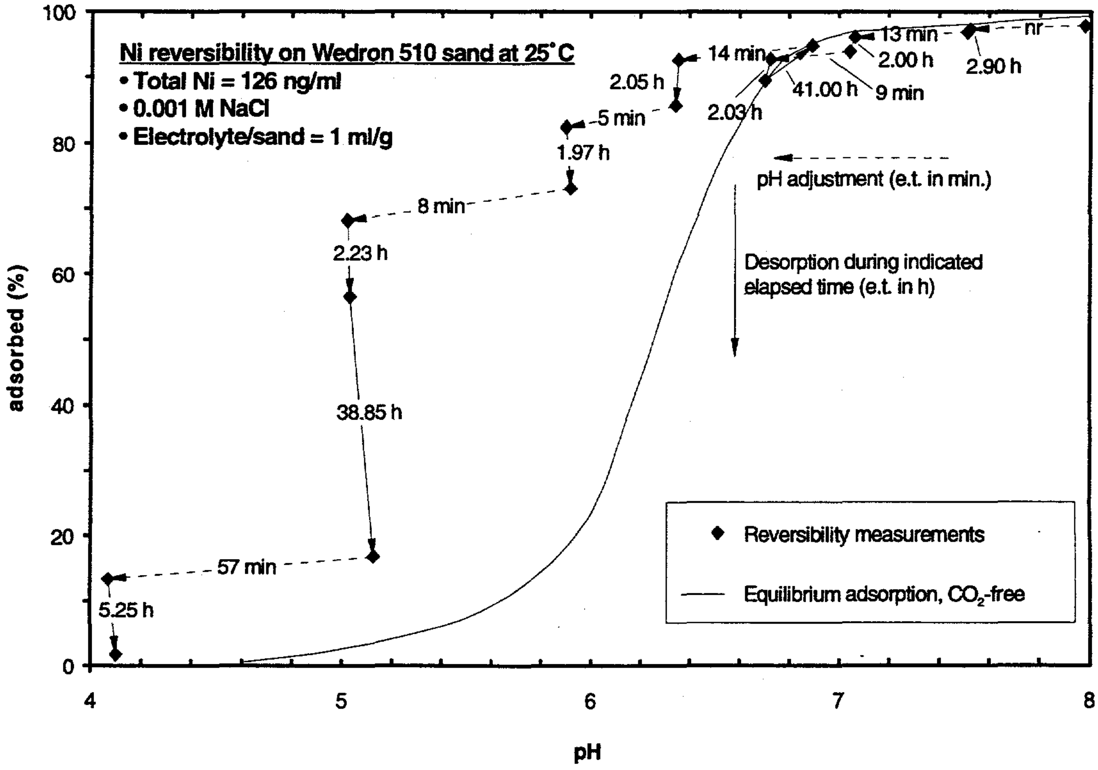

Figure B.5. Ni reversibility on Wedron 510 sand at 25 °C. Dashed arrows show pH decreases as a result of acid addition (e.t. in min; nr = not recorded); solid arrows show amount of Ni desorption and pH drift during the indicated equilibration period (e.t. in H^+). Analytical uncertainties are similar to the data symbols in size.

adjustment is shown by the dashed arrows, labeled with elapsed times measured in minutes from the beginning of acid addition. System response during the equilibration periods between pH adjustments is shown by the solid black arrows labeled with the time elapsed since the previous point, measured in hours. Below pH 7, detectable desorption occurred over periods of several minutes during pH adjustment, as indicated by the sloping rather than flat-lying arrows — this coincides approximately with the upper end of the desorption edge. At higher pH, adsorption was high and deviations from the equilibrium curve were small, so any desorption on the scale of a few minutes was obscured by analytical scatter. At lower pH (6.5 – 4), desorption appears to be sluggish, requiring much more than 2 h and perhaps not even reaching equilibrium after (38.85+2.23=) 41.08 h at pH 5.1.

B.4. Discussion

Rates of Ni adsorption by Wedron 510 sand are extremely pH-dependent. At pH ~7.7, adsorption is extremely rapid; about 66% of 100 ppb added Ni is adsorbed within one minute and equilibrium is reached after 2 – 4 hours. At pH 6.3, no adsorption occurs for several minutes, and has only reached about half of the expected level after 4 – 8 hours; equilibrium is not reached even after 24 hours.

It is unclear why adsorption is slower at low pH. Increased site competition with H^+ at lower pH is one possible mechanism. Protonation of surface sites:

$$SO^- + H^+ \rightarrow SOH$$

decreases the total number of sites available for adsorption. However, the triple-layer model for Ni adsorption onto the sand discussed in Appendix A indicates that $[SO^-]$ is relatively insensitive to pH; the change in site abundance between pH 6.3 and 7.7 is less than a factor of 2 (Appendix A, Figure A.18). Hence, it is unlikely that competition with H^+ alone can account for the observed change in the Ni adsorption rate with pH.

Alternatively, the change in the electrical double layer with pH may be important. For goethite, the dominant surface of Ni adsorption in Wedron sand, the surface potential increases from 0.02 C/m^2 at pH ~7.7 to 0.06 C/m^2 at pH ~6.3 (See Appendix A, this report). A greater positive surface charge decreases the rate of cation adsorption (Hayes, 1987), so the effect of surface charge should be to decrease adsorption rates at lower pH, as experimentally observed. Another possibility is that different adsorption reactions are occurring at different pH; the stochiometry of the reaction, or perhaps the speciation of the surface sites or of the aqueous Ni species, may change with pH.

The stochiometries of adsorption reactions derived from batch adsorption data, listed in Appendix A, Table A.6, indicate that adsorption is a first-order reaction. The kinetic data at pH 7.7 are nonlinear on a plot of -ln(C) vs. equilibration time, suggesting that more than one mechanism, or more than one adsorption site, is important. The data can be modeled as a two first-order reactions, one of which is very rapid, and reaches equilibrium within 20 minutes. The other is much slower, taking two to four hours to reach equilibrium. These reactions probably represent adsorption onto two different surface sites. One is highly favored, and is the dominant adsorption site in the early stages of equilibration. Once this site becomes filled, or reaches equilibrium with respect to the Ni in solution, adsorption onto less energetically favorable sites begins to dominate, and the rate of adsorption decreases. This is consistent with the triple layer complexation model results discussed in Appendix A, which conclude that Ni adsorption onto goethite, the dominant sorbing phase in the sand, occurs at two sites, a high-energy site, comprising about 4% of the total, and a lower-energy site, comprising the remainder.

A similar pattern is not observed in the pH 6.3 data; either the same reactions are not occurring, or adsorption is so slow that changes in the adsorption rate cannot be discerned.

Chemical reaction rates are highly temperature-dependent. However, total variation in ambient laboratory temperatures over the duration of these experiments was less than 5 °C, and was nonsystematic. It seems unlikely that any of the observed trends or differences in adsorption reaction rates can be attributed to laboratory temperature fluctuations.

The Ni batch desorption data are difficult to interpret. The effect of both site competition and surface charge should be to increase desorption rates at lower pH. The experimental results show that although the amount of Ni desorbed per unit time increased with decreasing pH, equilibrium was reached more slowly than at higher pH. At pH > 6, equilibrium was re-established within several hours of pH adjustment. At lower pH, equilibrium was not reached by the end of the experiment. The equilibrium curve generated by desorption is offset slightly relative to the adsorption reference curve generated under similar experimental conditions; it falls below that curve at pH >7, and above it for pH <7. A consistent offset above the adsorption curve would indicate that irreversible adsorption is occurring; the pattern actually obtained is difficult to interpret.

The autotitrator desorption data are consistent with the batch data, and support the interpretation that Ni is being adsorbed onto several sites, with a continuum of site energies. As pH was lowered from pH 8, Ni desorbed fairly quickly from low-energy sites, reaching equilibrium within the allotted two hours. By pH 6.5, however, Ni adsorbed to easily exchangeable sites had already been lost, so that further loss was less favorable energetically, and thus slower kinetically. As with the batch experiment, the desorption equilibrium curve was offset slightly from the adsorption reference curve.

Both of the desorption experiments described here are inappropriate for determining rate constants. Similar experiments should be run on pre-treated, carbonate-free sand, or on pure mineral components, goethite and kaolinite, to derive meaningful desorption rate constants.

B.5. Summary

The studies described here provide information on adsorption and desorption rates of Ni on Wedron sand as a function of pH. Adsorption experiments were carried out under atmospheric conditions at pH 6.3 and 7.7, using 1:1 sand:electrolyte systems with initial Ni concentrations of 100 ppb ($1.7 \cdot 10^{-9}$ moles/*l*) and equilibrating for intervals from 1 minute to 24 hours. Adsorption rate constants were calculated at both pH values. Desorption experiments were run under both atmospheric and CO_2-free conditions, using Wedron sand that had been pre-equilibrated with electrolyte containing 100 ppb Ni at pH 7.7–8.0. At these pH values, adsorption is ~100%. Acid was added to each sample to lower the pH, and following a period of re-equilibration, the electrolyte was sampled to determine the rate of Ni desorption. The desorption data are not suitable for the derivation of rate constants.

The results show that Ni adsorption onto Wedron 510 sand is strongly pH-dependent; it is considerably slower at pH 6.3 than at pH 7.7. Possible causes for this include increased site competition with H^+ and higher positive surface charge at lower pH; alternatively, different adsorption/desorption reactions may be occurring. The data at pH 6.3 are consistent with Ni adsorption being a first-order reaction, with a rate constant of 0.00058 min^{-1} (avg. of 2). At pH 7.7, Ni adsorption is extremely rapid initially, but slows after the first ~20 minutes. First-order rate constants calculated for the fast and slow components of Ni adsorption at pH 7.7 are 0.0455 min^{-1} and 0.0106 min^{-1}, respectively. The data are consistent with adsorption at two different sites. The more favored site either becomes filled or reaches equilibrium with the solution within 20 minutes; subsequently, adsorption kinetics are governed by the second, less favorable, site. Alternatively, adsorption reactions involving 2 different adsorbing species may be occurring; a very rapid reaction which is dominant for the first ~20 minutes, and then ceases to be important, and a second, slower reaction which continues to operate. The two site interpretation is preferred, as the triple-layer complexation model described in Appendix A predicts the presence of two adsorption sites of differing energies.

Desorption is also somewhat pH-dependent. Although more Ni per unit time desorbed at low pH, samples reached equilibrium more slowly than at high pH. Desorption at low pH was far slower than expected.

These studies provide some insight on the behavior of Ni in the Los Alamos/Sandia caisson experiment. The previous adsorption rate study, at pH 7.7, indicated that the kinetics of Ni adsorption onto Wedron sand are extremely fast; the new data show that adsorption rate is pH-dependent. The pH in the caisson during the Ni pulse was not well characterized (see Appendix F, this report); if the pH in the caisson was ~7 or less, then the kinetics of Ni adsorption may have been an important control on Ni transport within the caisson. Ni desorption appears to be fairly rapid at pH values similar to those in the caisson.

B.6. References

Bryan, C.R., D.B. Ward, and M.D. Siegel, 1995: "Appendix B: Ni Sorption and Solubility Studies," in *Characterization of Materials for a Reactive Transport Model Validation Experiment, Appendix B*, M.D. Siegel, D.B. Ward, C.R. Bryan, and W.C. Cheng, SAND94-0189, Sandia National Laboratories, Albuquerque, New Mexico, 32 pp.

Hayes, K.F., 1987: "Equilibrium, Spectroscopic, and Kinetic Studies of Ion Adsorption at the Oxide/Aqueous Interface," Ph.D. dissertation, Stanford University, 259 p.

Siegel, M.D., D.B. Ward, C.R. Bryan, and W.C. Cheng, 1995: *Characterization of Materials for a Reactive Transport Model Validation Experiment*, SAND94-0189, Sandia National Laboratories, Albuquerque, NM, 277 pp.

Appendix C.

Li Adsorption by Wedron 510 Sand and Pure Minerals: Reversibility and Kinetic studies

Charles R. Bryan and Connor Boyle

CONTENTS

C.1. Introduction

Several batch adsorption experiments were conducted to characterize Li adsorption onto Wedron 510 sand in the presence of 100 ng/m*l* ($1.7 \cdot 10^{-6}$ M) Ni, under both CO_2-free and nominally atmospheric conditions, at initial Li concentrations of 100 μg/m*l* and 1000 μg/m*l* (0.014 M and 0.14 M). Samples from two 100 ppm Li adsorption experiments were subsequently used to evaluate Li desorption.

In addition, Li adsorption/desorption studies were conducted on goethite and kaolinite, two important trace mineral phases in the sand. These experiments were run under atmospheric conditions ($P_{CO2} = 10^{-3.5}$), using Li and Ni initial concentrations of 100 μg/m*l* and 100 ng/m*l*, respectively.).

To adequately model Li transport in porous media, it may also be necessary to consider non-equilibrium, or time dependent, sorption. Therefore, a batch kinetic study was done to ascertain an apparent rate law and rate constant to be used in Li transport modeling. Several kinetic reaction equations were used to describe the sorption of Li on Wedron 510 sand.

The experimental conditions for each study are summarized in Table C.1.

C.2. Experimental Methods

The experimental methods used in the adsorption/desorption studies are those described in Bryan *et al.* (1995), with minor changes. Sodium bicarbonate solution was added to the electrolyte in those experiments involving goethite and kaolinite to insure that sufficient bicarbonate was present for high-pH samples to reach equilibrium with atmospheric CO_2. Samples were then sparged with air to remove any excess CO_2. In previous experiments run under nominally atmospheric conditions, summarized in Siegel *et al.* (1995), high-pH samples were probably not sparged with air long enough for true equilibrium with atmospheric CO_2 to be achieved.

The adsorption and kinetics experiments run on Wedron sand used a solid:solution ratio of 1g/m*l*; Kr-BET surface area measurements suggest that this corresponds to a surface area of ~80 m^2/l. The goethite experiment was run on synthesized goethite at a concentration of 1.25 mg/m*l*. or 41 m^2/l (see Appendix A for further details). The kaolinite experiment was run using reagent-grade kaolin powder purchased from VWR Scientific ("Baker Analyzed" #2242-01), and washed with 6 N HCl to remove iron oxide-hydroxide coatings. The kaolinite concentration

Table C.1. Experimental conditions for batch adsorption/desorption studies

Study #	Type	[Li] ppm	[Ni] ppb	P_{CO_2}	pH	Substrate	Solid / Solution	SA m^2/l	Comments
1	Li adsorption	100	0	$10^{-3.5}$	4 – 10	Wedron sand	1g/m*l*	80	Broad adsorption peak at pH~7.5
2	Li adsorption	100	100	0	4 – 10	Wedron sand	1g/m*l*	80	Broad adsorption peak at pH~7.5
3	Li adsorption	1000	100	$10^{-3.5}$	4 – 10	Wedron sand	1g/m*l*	80	Adsorption low, insensitive to pH
4	Li adsorption	100	100	$10^{-3.5}$	4 – 10	Goethite	1.24 mg/m*l*	60	Adsorption insensitive to pH
5	Li adsorption	100	100	$10^{-3.5}$	4 – 10	Kaolinite	5 mg/m*l*	124	Broad adsorption peak at pH~7.5
6	Li desorption	100	0	$10^{-3.5}$	4, 7, 10	Wedron sand	1g/m*l*	80	No desorption
7	Li desorption	100	100	0	4 – 10	Wedron sand	1g/m*l*	80	No desorption
8	Li desorption	20	100	$10^{-3.5}$	2, 7	Wedron sand	1g/m*l*	80	Only acidified samples desorb
9	Li kinetics	10	0	$10^{-3.5}$	~7.7	Wedron sand	1g/m*l*	80	

used was 5 mg/m*l*, or 124 m^2/l, using a N_2-BET surface area measurement of 24.3 m^2/g.

C.2.1. Desorption at moderate pH

The Li desorption experiments were run using samples from two different 100 ppm Li adsorption studies. The first was run under atmospheric conditions; Wedron sand was equilibrated with 100 ppm Li (added as LiBr) electrolyte at three different pH's, and the electrolyte was sampled to determine the amount of adsorbed Li and the Li concentration of the electrolyte. As much electrolyte as possible was then siphoned off of the sand with a pipette; the moist sand was weighed to determine the amount of liquid remaining. Fresh, Li-free electrolyte was added to each sample tube; the concentration of Li in the electrolyte at this point could be calculated from the Li concentration in the spiked electrolyte prior to siphoning, the weight of the electrolyte remaining in the moist sand after siphoning off the free liquid, and the amount of fresh electrolyte added. The tube was closed, mixed and re-equilibrated for a fixed time interval, and re-sampled. The second study was run under CO_2-free conditions over a range of pH, using 100 ppm Li. It was run in a similar manner, but pH of the Li-free electrolyte added after siphoning was carefully adjusted to match that of the electrolyte prior to siphoning. Also, each tube was sampled after siphoning and addition of fresh electrolyte to determine the initial Li concentration during re-equilibration. Tubes were re-sampled after a fixed time interval; it was assumed that any change in concentration was caused by desorption.

C.2.2. Desorption at low pH

In a separate study, 20 g sand was equilibrated with neutral-pH 0.001 M NaCl containing 20 ppm Li and then quickly (~2 minutes) rinsed three times with fresh neutral electrolyte. After the final rinse, neutral-pH electrolyte was added to half the sample tubes, and pH = 2 electrolyte was added to the rest. The tubes were shaken and immediately sampled, and then allowed to equilibrate for 3 days and re-sampled.

C.2.3 Adsorption kinetics

The kinetics experiment was done as a batch process, using 50 m*l* polyallomar centrifuge tubes. The experiment was run under atmospheric P_{CO_2}, using 20 g sand / 20 ml electrolyte (0.001 M NaCl). Sets of three samples, containing sand and 0.001 M NaCl electrolyte, were pre-equilibrated on hematology mixers for 48 hours. After pre-equilibration, 0.203 g of 997 ppm Li as LiBr was pipetted into each tube, resulting in a final Li concentration of about 10 ppm. The time was noted and the tube placed back on the mixer.

Aliquots were taken from each set at elapsed times of 0, 0.5, 1, 2, 4, 5, 7, 10, 15, 20, 30, 46, 60, 100, and 120 hours. The aliquots were withdrawn from the centrifuge tubes using a 10 ml disposable syringe, filtered through a 0.2 μm membrane filter, and the time noted. The set corresponding to an elapsed time of zero was done slightly differently. Immediately after the Li spike was added the tube was capped and shaken by hand, then sampling was done as described above.

Sample pH values were not measured. However, previous experiments indicate that carbonate in the sand buffers a 20 g Wedron sand / 20 ml electrolyte mixture at pH ~7.7 under atmospheric conditions.

C.3. Results

The results of the Li batch adsorption and desorption studies are discussed below. Reported pH measurements have an accuracy of ~0.05 units. Measured Li concentrations have an accuracy of ± 1 – 2 %; for those experiments run with a high Li concentrations (≥ 100 ppm), dilution of samples to the operational range of the

Atomic Adsorption Spectrometer (AAS), which is < 20 ppm, introduced additional error. While these factors contribute to the scatter in the following figures, the dominant cause for the scatter is the small amount of solute that adsorbed. The concentration in solution changes little during the experiment, thus small errors in Li concentration correspond to large relative errors in % adsorbed and in K_ds.

C.3.1. Li adsorption

C.3.1.1. Wedron sand

Adsorption curves for Wedron 510 sand in equilibrium with 0.001 M NaCl with initial Li concentrations of 10 and 17 ppm have been described by Siegel *et al.* (1995). Additional data has since been collected at concentrations of 100 and 1000 ppm Li. Two 100 ppm Li experiments were run, the first under nominally atmospheric conditions, and the second under CO_2-free conditions in an N_2-filled glove box.

The results of the two 100 ppm Li studies are shown in Figure C.1. The curves are similar for both sets of conditions; over the pH range 4.8 to 9.5, sorption is low, less than 5 %; and both show broad sorption peaks between pH = 6.8 and 7.5, with sorption decreasing towards higher and lower pH. Maximum adsorption is ~3.5 % for the atmospheric curve, and perhaps 0.7% lower for the CO_2-free curve. The difference is probably an artifact of the experimental procedure. Ni was present in the samples defining the lower curve, and Ni competition with Li should decrease Li adsorption. However, because the Li concentration was almost 4 orders of magnitude higher than that of Ni (molar concentration) the effect of Ni can be ignored. The possible effect of the partial pressure of CO_2 on Li adsorption has not been examined systematically.

The 1000 ppm Li adsorption experiment was run under partial equilibrium with atmospheric CO_2. Results for the 1000 ppm Li adsorption experiment are shown in Figure C.2. Adsorption is about 1 % over the pH range examined; showing no dependence on pH.

The general shape of the adsorption curves at 100 ppm Li are consistent with previous curves obtained at lower Li concentrations, reported in Cheng *et al.* (1995); all show a broad adsorption maximum near pH = 7. Adsorption decreases with increasing Li concentration in the electrolyte. Figure C.3 is an isotherm plot of the adsorption data from the batch experiments described here and in previous reports.

The 100 ppm and 1000 ppm data are consistent with results from most earlier Li adsorption experiments although an experiment designed specifically to define an adsorption isotherm, summarized in Cheng *et al.* (1995), yielded somewhat

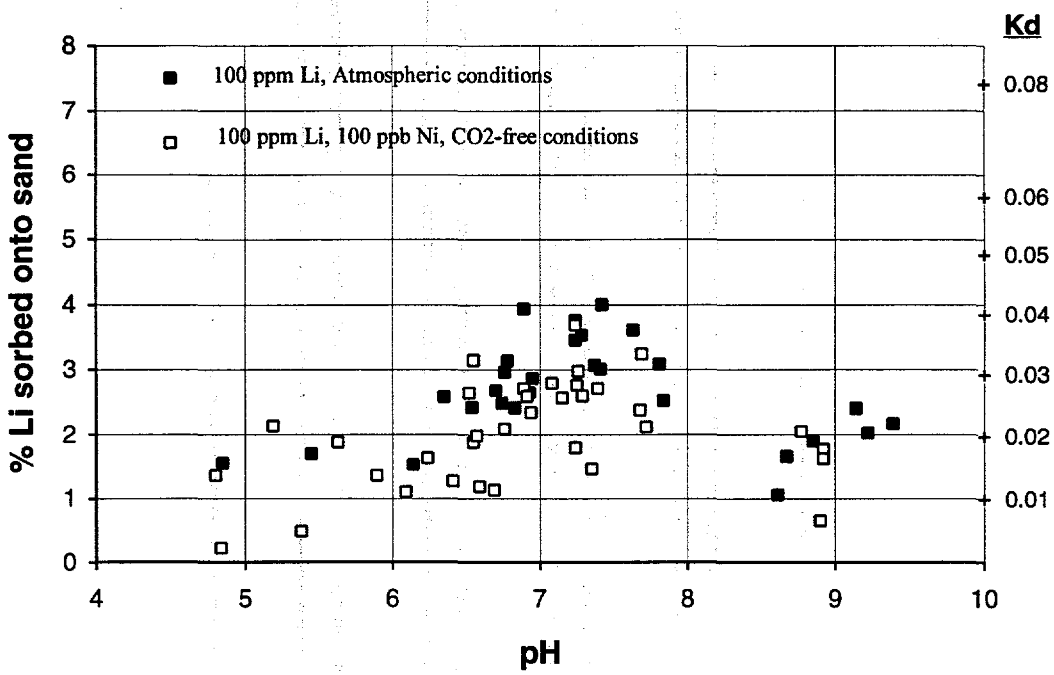

Figure C.1. Li adsorption curves for batch systems containing 1g/m*l* Wedron sand (80m²/*l*), and an initial Li concentration of 100 ppm.

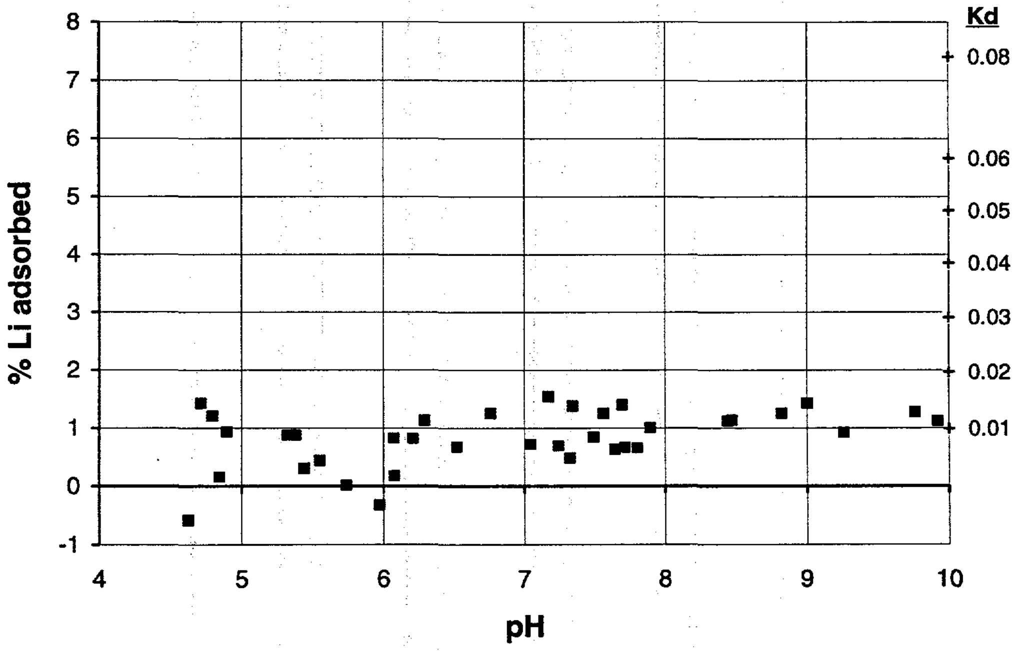

Figure C.2. Li adsorption curve for Wedron sand under atmospheric conditions, using 1g/m*l* sand (80 m²/*l*) and an initial Li concentration of 1000 ppm.

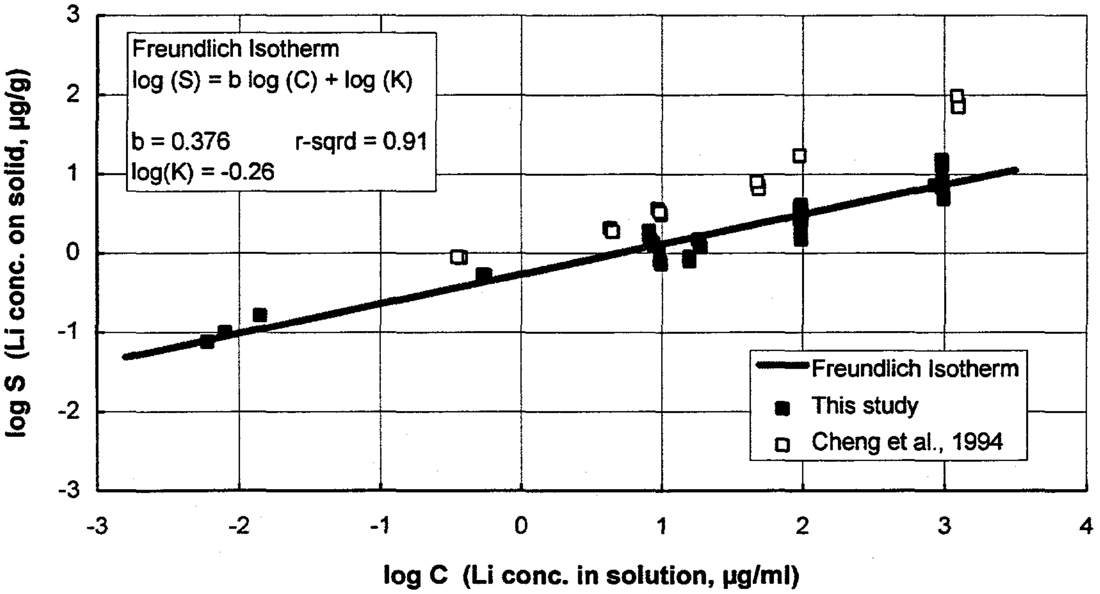

Figure C.3. Li adsorption isotherm plot for Wedron 510 sand. The isotherm data from Cheng *et al.* (1995) was not used in calculating the Freundlich fit shown here.

discordant results. This is probably due to problems with the Atomic Adsorption analytical technique used in the earlier study; at the time, no ionization suppressant was being used, and a malfunctioning air-pressure regulator made oxidant flow erratic.

The adsorption data is best described by a Freundlich rather than a linear (K_d) or a Langmuir isotherm. Only data in the pH range 6.9 – 8 was used to parameterize the isotherm equation (Table C.2).

C.3.1.2. Goethite

Li sorption onto goethite was carried out under atmospheric conditions ($P_{CO2} = 10^{-3.5}$), using 100 ppm Li and a goethite surface area of 41 m^2/l. The results are summarized in Figure C.4; though scatter is relatively large, percent adsorption is constant at ~3% over the pH range 4 to 10.

C.3.1.3. Kaolinite

Li adsorption onto kaolinite was carried out under atmospheric conditions, using an initial Li concentration of 100 ppm and 124 m^2/l of substrate. The results are shown in Figure C.5; adsorption varies somewhat with pH, increasing from

Table C.2. Li adsorption data used to generate the Freundlich isotherm in Figure C.3.

pH	C, µg/g	S, µg/g	Kd
1000 ppm Li, 100 ppb Ni, atmospheric cond.			
7.04	858	7.21	0.008
7.24	986	6.94	0.007
7.32	984	4.84	0.005
7.64	980	6.30	0.006
7.80	975	6.58	0.007
7.17	957	15.5	0.016
7.34	964	13.9	0.014
7.49	968	8.49	0.009
7.56	965	12.6	0.013
7.69	962	14.0	0.014
100 ppm Li, atmospheric conditions			
7.24	97.5	3.50	0.036
7.24	96.8	3.81	0.039
7.28	97.3	3.57	0.037
7.37	97.9	3.11	0.032
7.41	97.3	3.04	0.031
7.42	96.7	4.06	0.042
7.63	96.2	3.65	0.038
7.81	96.7	3.12	0.032
7.84	97.4	2.55	0.026
100 ppm Li, 100 ppb Ni, atmospheric cond.			
7.08	95.0	2.81	0.030
7.15	96.1	2.58	0.027
7.24	94.8	3.70	0.039
7.24	96.8	1.81	0.019
7.25	95.7	2.78	0.029
7.26	95.5	2.99	0.031
7.29	96.0	2.61	0.027
7.35	97.2	1.48	0.015
7.39	95.9	2.72	0.029
20 ppm Li, 100 ppb Ni, atmospheric cond.			
7.63	18.1	1.49	0.081
7.63	18.6	1.38	0.073
7.63	18.6	1.24	0.066
7.63	18.6	1.22	0.064
7.63	18.8	1.19	0.062
7.63	18.5	1.34	0.071
7.63	18.4	1.39	0.074
7.63	18.3	1.50	0.080
7.63	18.5	1.32	0.070
7.63	18.3	1.45	0.078
17 ppm Li, 200 ppb Ni, atmospheric conditions			
7.46	15.6	0.91	0.059
7.58	15.7	0.80	0.051
7.52	15.5	0.85	0.054
10 ppm Li, CO2-free conditions			
7.31	8.14	1.86	0.24
7.31	8.15	1.85	0.24
7.33	8.09	1.90	0.25
7.71	8.67	1.35	0.16
7.75	8.70	1.32	0.16
7.90	8.81	1.21	0.14
10 ppm Li, atmospheric conditions			
6.98	8.32	1.43	0.17
7.08	8.21	1.53	0.19
6.97	8.09	1.65	0.21
6.94	8.21	1.51	0.18
7.12	8.37	1.35	0.16
6.94	8.24	1.48	0.18
0.1–10 ppm Li, < 200 ppb Ni, atmospheric cond.			
7.73	9.78	0.73	0.074
7.71	9.65	0.80	0.083
7.71	9.43	1.17	0.12
7.72	0.55	0.52	0.94
7.69	0.55	0.51	0.93
7.77	0.53	0.54	1.01
7.77	0.01	0.16	11.7
7.83	0.01	0.10	12.6
7.76	0.01	0.08	12.7

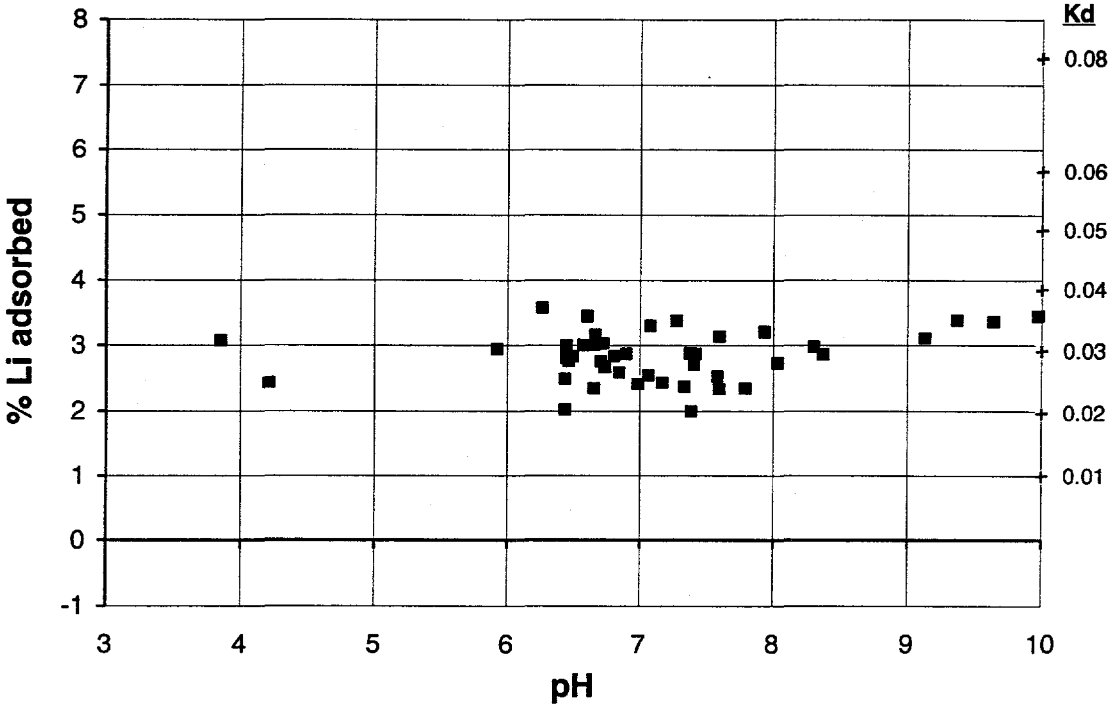

Figure C.4. Adsorption of 100 ppm Li onto 41 m^2/*l* goethite, under atmospheric conditions.

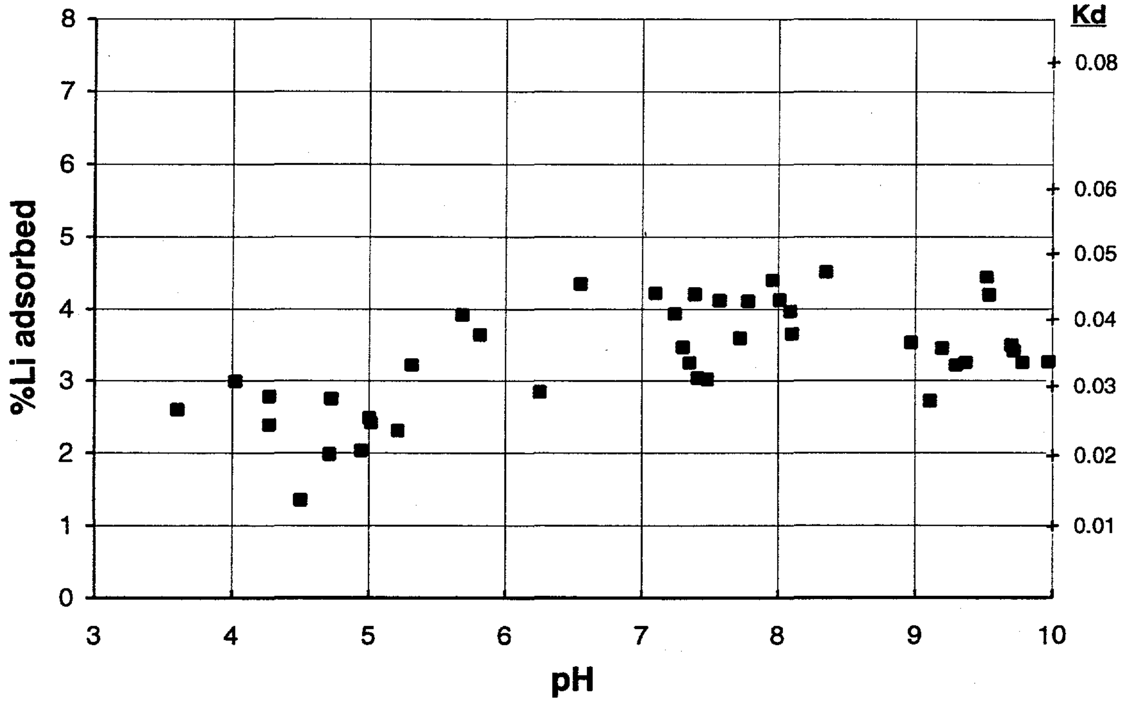

Figure C.5. Adsorption of 100 ppm Li onto 124 m^2/*l* kaolinite, under atmospheric conditions.

1.5% to 3% from pH 4 to pH 7 and then leveling off or dropping slightly with further increases in pH. This adsorption curve is broadly similar to that produced by Wedron sand (Figure C.1).

C.3.2. Li desorption

C.3.2.1. Desorption at moderate pH

Two experiments examined Li desorption in the pH range 4–10, using sand equilibrated with electrolyte containing 100 ppm Li; the first was run under atmospheric conditions, and the second under CO_2-free conditions. Results of both experiments are shown in Figure C.6. On these plots, the difference as % change between the initial (just after siphoning and addition of fresh electrolyte) and final Li concentrations in the electrolyte is plotted versus re-equilibration time. In the first experiment (Figure C.6a), the initial concentrations were not measured. Instead, they were calculated from the volume and Li concentration of the electrolyte remaining in the sand after siphoning, and the volume of fresh added electrolyte. In the second experiment (Figure C.6b), the initial concentration in each sample was measured. The results from both studies are similar; the concentration of Li in the electrolyte did not increase with time, indicating that no significant Li desorption occurred.

C.3.2.2. Desorption at low pH

Table C.3 compares desorption under acidic (pH 2) and neutral conditions for sand originally equilibrated with electrolyte containing 20 ppm Li. For those samples re-equilibrated at neutral pH, the Li concentration actually dropped slightly, indicating that no desorption occurred; in fact, sorption continued. Li desorbed rapidly from the sand in those samples re-equilibrated at pH = 2; even the immediate samples are elevated relative to the neutral pH samples. After 3 days, 85 – 92 % of the sorbed Li had desorbed. This assumes that naturally occurring exchangeable Li in the sand is negligible, an assumption supported by leaching experiments; only 0.1 μg Li / g sand was leachable with 6 N HCl.

C.3.3. Li adsorption kinetics

The results of the 10 ppm Li adsorption kinetics study are shown in Figure C.7. It is evident that some scatter in the data is present, especially at time = 0 hours. The scatter and unusually high Li concentration at time = 0 hrs may be due to errors in the sampling technique. To obtain a sample that was as close to time = 0 hrs as possible, an effort was made to minimize the contact time between the sand

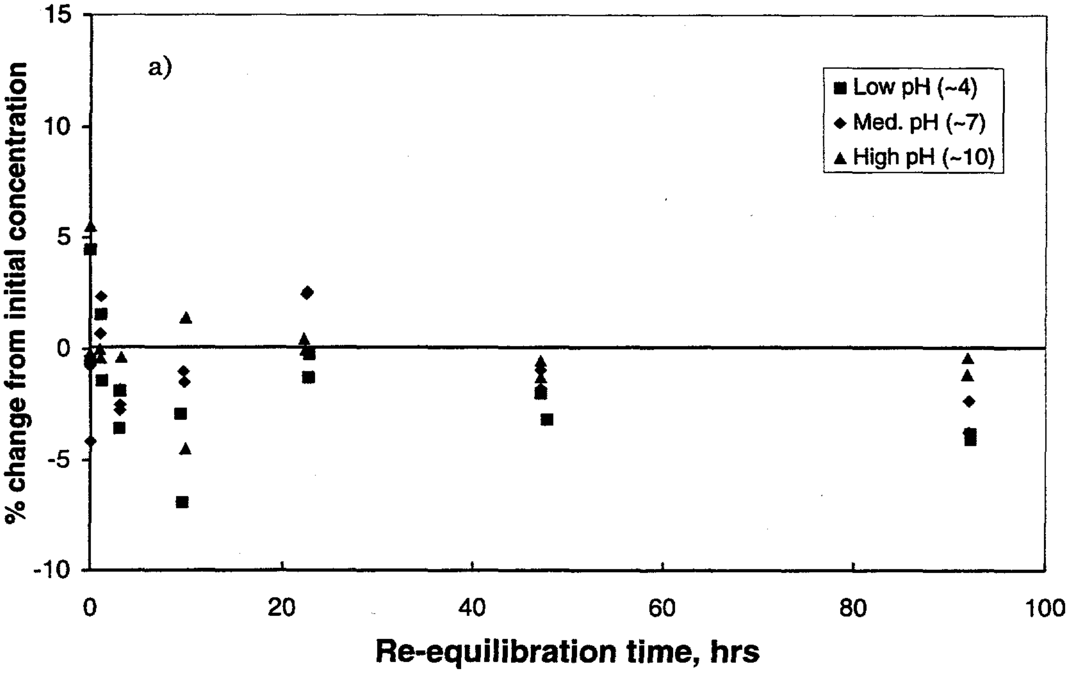

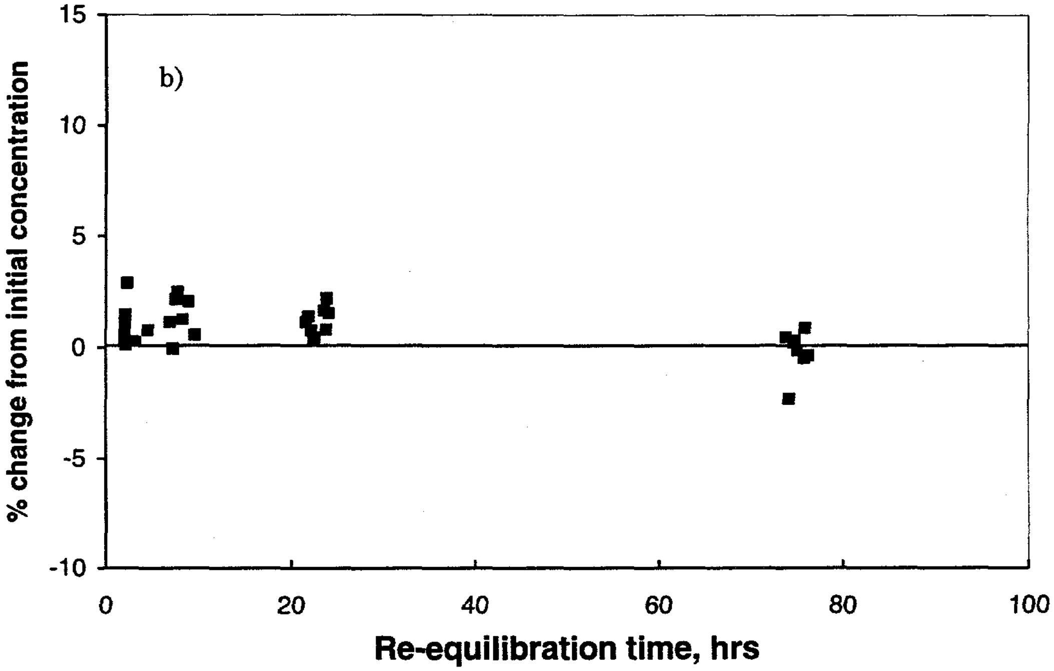

Figure C.6. Extent of Li desorption from Wedron sand, expressed as the % change in the Li concentration of the electrolyte with time. For batch systems containing 1g/m*l* (80m^2/*l*) sand. **a)** Atmospheric conditions, desorption examined at pH 4,7 and 10. **b)** CO_2-free conditions, pH = 4 – 10.

Table C.3. Results of Li stripping experiment.

Li, % sorbed at pH ~7.7	Li adsorbed, µg/g sand	Final pH, after re-equilibration	Li ppm init. sample	Li ppm 3 days later	Li desorbed, µg/g sand *	% Li desorbed
7.46	1.49	7.71	0.09	0.08	-0.01	-0.4
6.92	1.38	7.75	0.09	0.09	0.00	-0.2
6.25	1.24	7.74	0.09	0.08	-0.01	-0.9
6.11	1.22	1.99	0.31	0.93	1.06	87.3
5.98	1.19	2.00	0.27	0.99	1.10	91.9
6.71	1.34	2.00	0.28	1.01	1.13	84.8

* assuming 0.09 µg/m*l* Li carryover after 3 rinses.

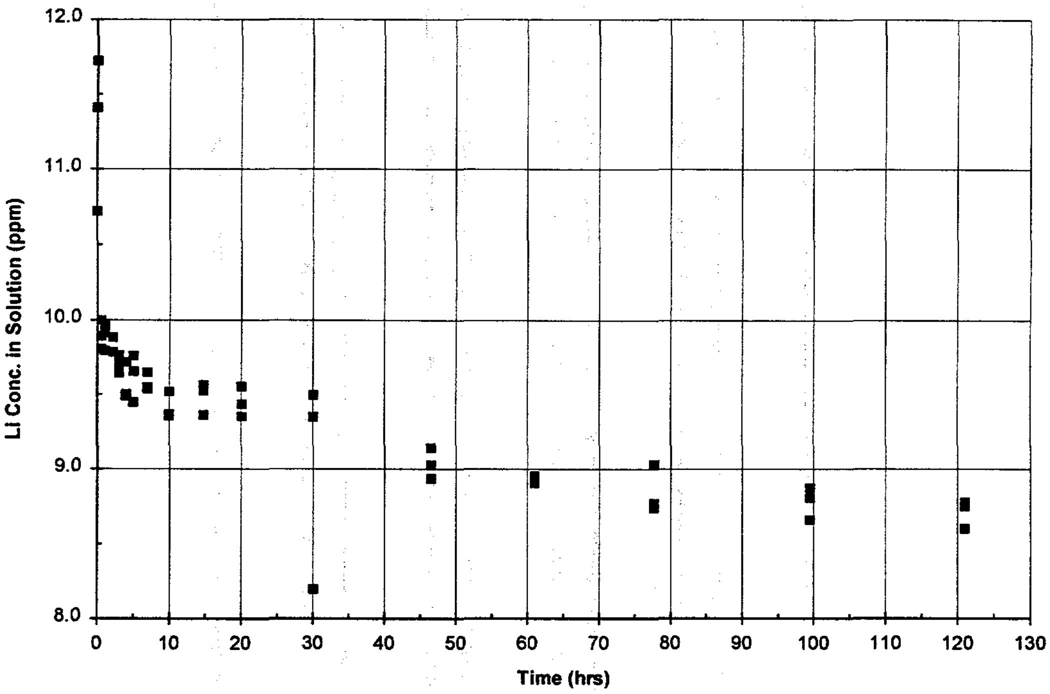

Figure C.7. Adsorption of 10 ppm Li on Wedron 510 sand as a function of time. Determined using batch systems containing 1g/m*l* (80 m^2/l) sand, at pH ≈ 7.7.

and Li. As a result, the Li spike may not have mixed with the full volume of electrolyte present in the centrifuge tube before the sample aliquot was taken. This would cause a higher than expected final Li concentration because dilution was not complete at the time of sampling. For this reason these data points are not included in subsequent plots or calculations. The low data point at time = 30 hrs appears to be an anomaly, and is therefore also omitted. Figure C.8 shows the resulting average Li concentration values for each time interval.

These data were used to model Li sorption as a first-order kinetic reaction (Equation 1) and a second-order kinetic reaction (Equation 2). Modeling the data as a first order reaction, seen in Figure C.9, gave an apparent rate constant of 0.0011 hr^{-1}, but the fit was poor as indicated by a regression coefficient (r^2) value of 0.877.

$$\ln C = \ln Co - k_a t \tag{1}$$

$$\frac{1}{C} - \frac{1}{Co} = k_a t \tag{2}$$

where:

C = Concentration of Li in solution at time t.
Co = Initial concentration of Li at time zero.
k_a = Apparent rate constant

A second order kinetic model (Figure C.) gave a slight improvement over the first order, but was still a statistically poor fit. The data was next fitted with two first-order equations (Figure C.10), one for the time interval from zero to 10 hours, and the other from 10 to 120 hours. This appeared to describe the data well, based on r^2 values for the two lines of about 0.9.

C.4. Discussion

C.4.1. Li adsorption

The Li adsorption experiments described in this report were carried out to determine the adsorption properties of Wedron sand, and, if possible, to identify and quantify the contribution of the individual mineral constituents in the sand. The results of the Li adsorption experiments show that Li adsorption by Wedron sand is relatively low; using a 100 ppm initial concentration, only a few % adsorbed over the pH range examined. These experiments and previous ones at lower Li concentrations show that a broad peak in Li adsorption occurs around pH = 7–7.5; at lower and higher pH, adsorption is less.

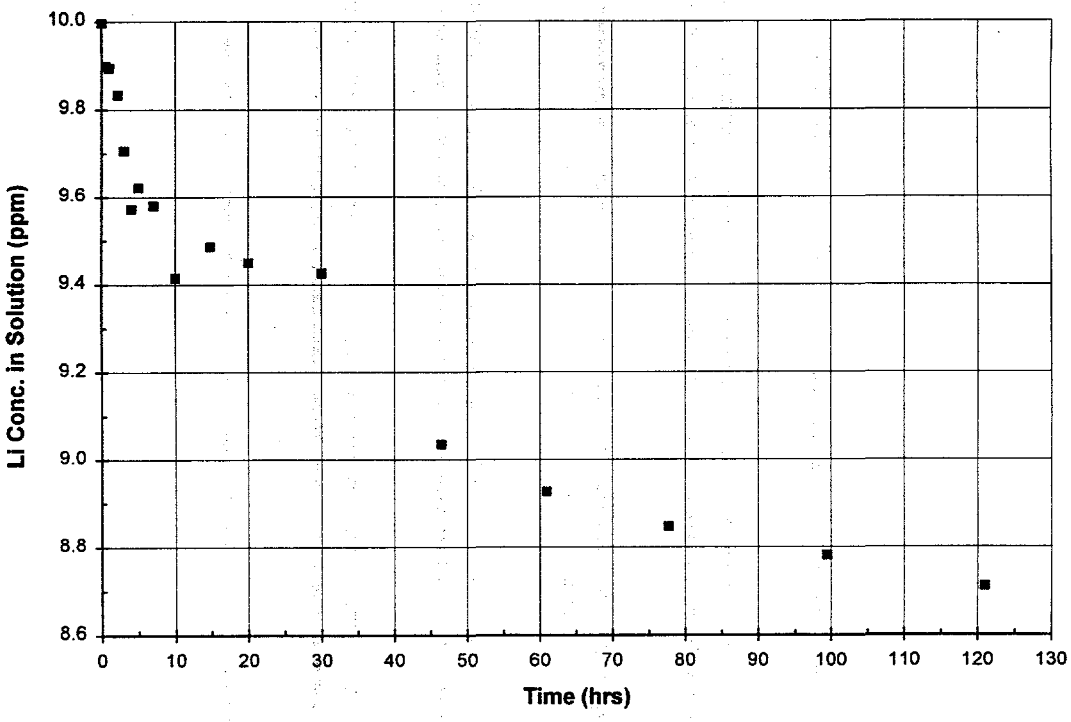

Figure C.8. Average of the three data points at each time interval. Data for t=0 is excluded.

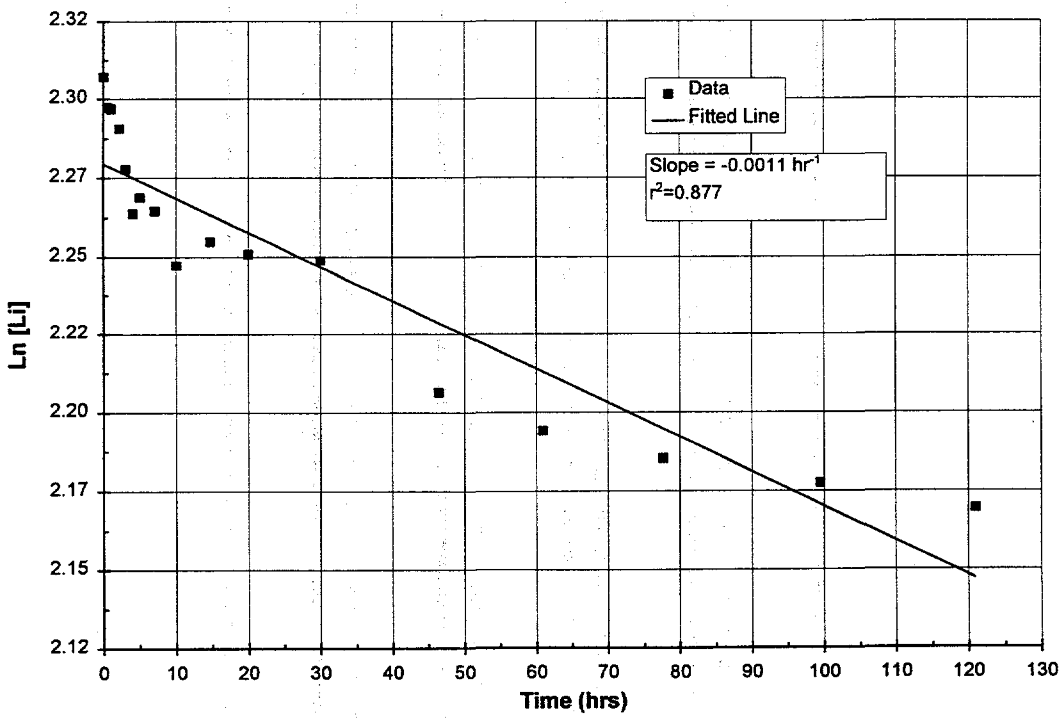

Figure C.9. First order kinetic model for 10 ppm Li sorption on Wedron sand.

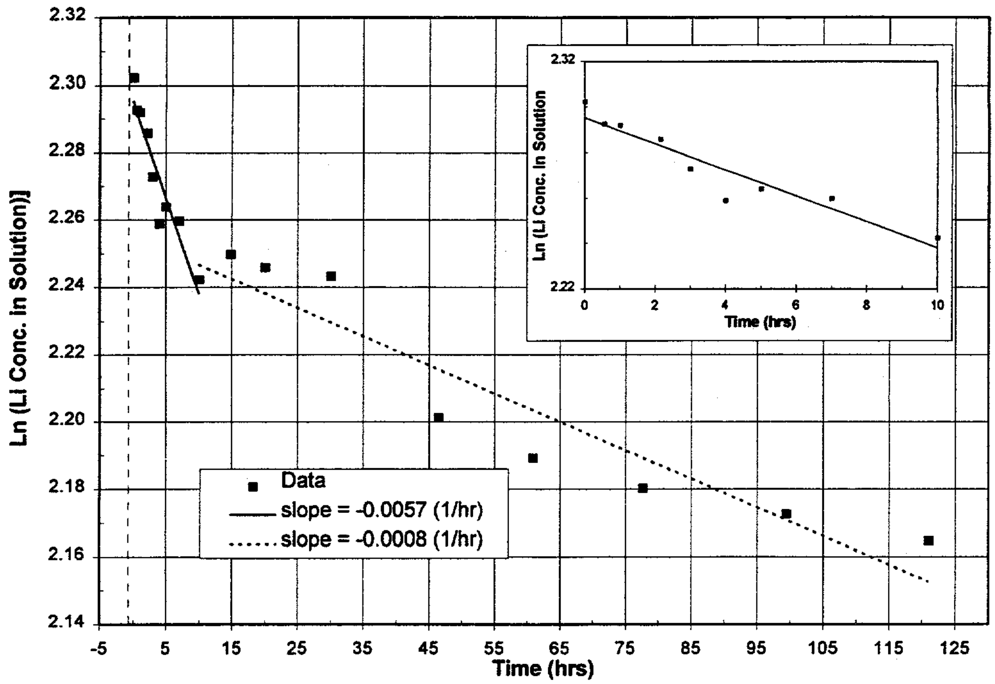

Figure C.10. Multiple first-order equations for 10 ppm Li sorption onto Wedron sand. The time interval 0<t<10 hrs is shown inset.

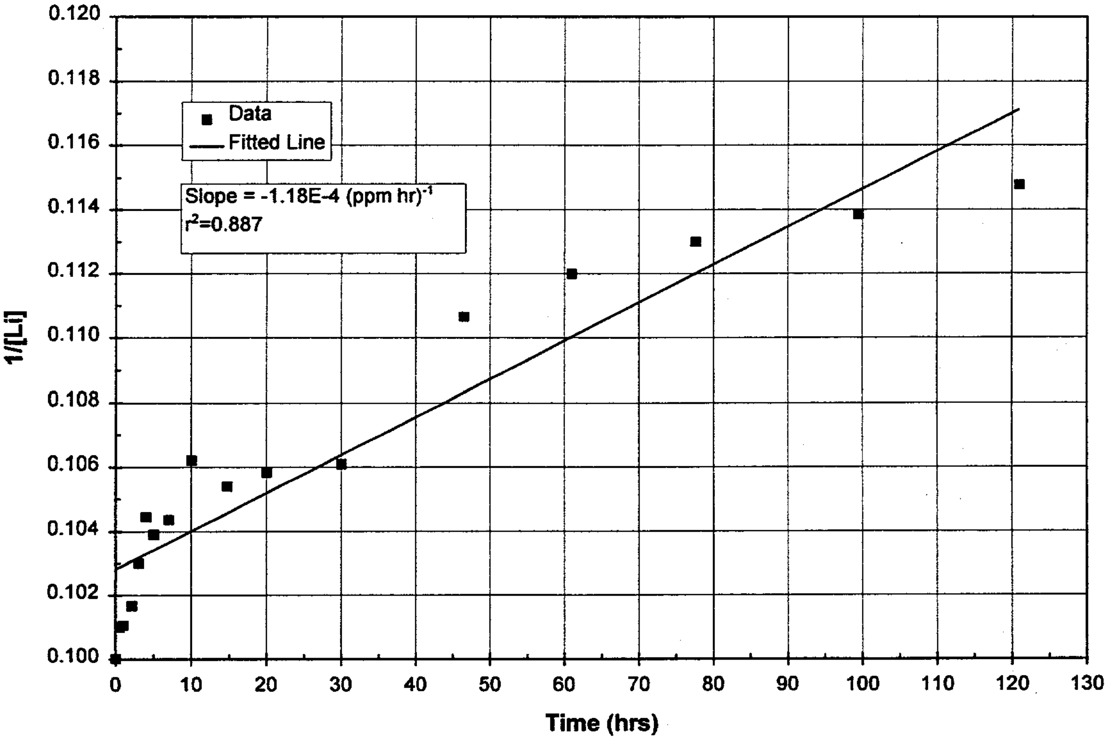

Figure C.11. Second order kinetic model for 10 ppm Li sorption on Wedron sand.

The three most abundant mineral constituents in the sand are quartz, kaolinite, and goethite. Quartz dominates the sand, accounting for more than 98% by weight of the total material; however, it occurs as large grains, and these grains are coated with kaolinite and goethite. Its contribution to the total surface area of the system, and to the Li adsorption properties of the sand, is probably small. Chardymskaya *et al.* (1986) have reported Li distribution coefficients that are orders of magnitude too low to account for those seen for Wedron sand; i.e., at concentrations of 10-100 ppm Li, they report only 0–10 ng Li (<0.1%) adsorbed per gram quartz. In addition, the shape of the adsorption curve for Li onto quartz obtained by Chardymskaya *et al.* is different from that of Wedron sand. The Li – quartz adsorption curve increases steadily with pH, whereas the Li – Wedron sand adsorption curve peaks at pH ~7.

Leaching experiments and previous adsorption experiments (Siegel *et al.*, 1995) suggest that goethite, occurring as coatings on grain surfaces, represents a significant fraction of the total surface area of the sand. Li adsorption by 41 m^2/l goethite is independent of pH; for an initial Li electrolyte concentration of 100 ppm, about 3% adsorption occurred over the pH range of interest.

Kaolinite has been identified in the fine fraction in the sand by XRD, and visually identified on the grain surfaces by SEM (Ward *et al.*, 1995); however, its contribution to the total surface area of the sand is not known. The sand contains 0.28% Al by weight; some fraction of this may be substituting for Si in the quartz lattice, or occurring structurally in minerals other than kaolinite, but the scarcity of cations in the sand other than Si and Al (Table 5, Siegel *et al.*, 1995) suggests that it is mostly in kaolinite. Thus, as much as 1.38% kaolinite by weight may be present in the sand, and it is probable that this mineral contributes significantly to the surface area and adsorption properties of the sand.

The adsorption curve for 124 m^2/l kaolinite (Figure C.5) shows a similar trend to that of the raw sand (Figure C.1); adsorption increases with pH to a maximum at pH = 7 – 7.5. It is unclear whether adsorption decreases at higher pH or levels out. The amount of Li adsorbed (about 3-4%) is also very similar. The general shape of these two adsorption curves suggests that kaolinite is probably an important phase in the sand with respect to Li adsorption.

C.4.2. Li desorption

The results of the desorption experiments indicate that Li does not desorb from Wedron sand under conditions of moderate pH. This is consistent with the adsorption study results which indicate that kaolinite is an important adsorbing phase with respect to Li; irreversible adsorption of Li by kaolinite has been reported by Anderson *et al.* (1989), who postulated that Li is strongly bound into octahedral edge sites in kaolinite. Studies also indicate that most or all of the Li can be stripped off of Wedron sand by lowering the pH of the electrolyte to 2 or less; this is inconsistent with the results of Anderson *et al.*, who found that Li bound to kaolinite did not desorb under even more acidic conditions. However, their stripping experiments lasted less than one hour, while that described here lasted two days. If Li desorption rates are as slow as Li adsorption rates, their experiments may not have reached equilibrium.

C.4.3. Li kinetics

Table C.4 is a summary of the kinetic reaction equations that were fitted to the Li sorption data including r^2 values, the standard error of the estimate, SE (a measure of the scatter of the data about the fitted line), and the slopes of the fitted lines.

The first and second-order equations do not adequately describe the kinetic data as seen by the low values of r^2. The parabolic equation has the highest r^2 value but also the highest SE. Fitting two separate first-order reaction equations to the sorption data described the data well for the time intervals 0-10 hrs and 10-120 hrs. The relatively high r^2 values and low SE values show this to be the best model. The multiple slopes may indicate the presence of two different sites or mechanisms for sorption. Another explanation may be a change in physical properties of the sand due to abrasion caused by the mixing action.

While two straight lines may describe the data well, Skopp (1986) cautions that this is not proof that two first-order reactions are occurring. He suggests that an incomplete description of the reaction mechanism exists, or multiple reactions in parallel may be occurring. Skopp also states that the interpretation of semilog plots is only appropriate when the kinetic data is far from equilibrium; therefore, only the initial line segment should be used for estimating rate constants.

One way to determine if the sorption reaction is first-order is to perform another sorption experiment at a different initial concentration, at least double or half the original concentration (Bunnett, 1986). If the reaction is first-order, the

Table C.4. Summary of kinetic equations used to model the Li sorption data.

Model	r^2	SE	Slope of Fitted Line
First-order	0.877	1.62E-2	-0.0011 hr^{-1}
Second-order	0.887	1.66E-3	0.0001 $(ppm\ hr)^{-1}$
Multiple First-order			
First line	0.898	6.76E-3	-0.0057 hr^{-1}
Second line	0.902	1.17E-2	-8.5E-4 hr^{-1}

rate constant should be the same for both concentrations.

Using data from a similar experiment (Figure C.12) with an initial Li concentration of 5 ppm (Cheng *et al.*, 1995, Figure C.6) for the time interval from 0-15 hr., an apparent first-order rate constant of 0.0043 hr^{-1} was found using the first-order kinetic reaction equation.

A comparison of the apparent rate constant obtained from the 5 ppm Li kinetic experiment with that of the 10 ppm Li kinetic experiment show a close agreement, 0.0057 hr^{-1} vs. 0.0043 hr^{-1}. The same procedure was followed in performing both experiments; however, errors and differences in measuring, sampling and analysis techniques may explain why the values are not identical. Nonetheless, the apparent rate constants are in close enough agreement to suggest a first-order kinetic reaction can adequately model the first 10 to 15 hours of Li sorption on Wedron sand.

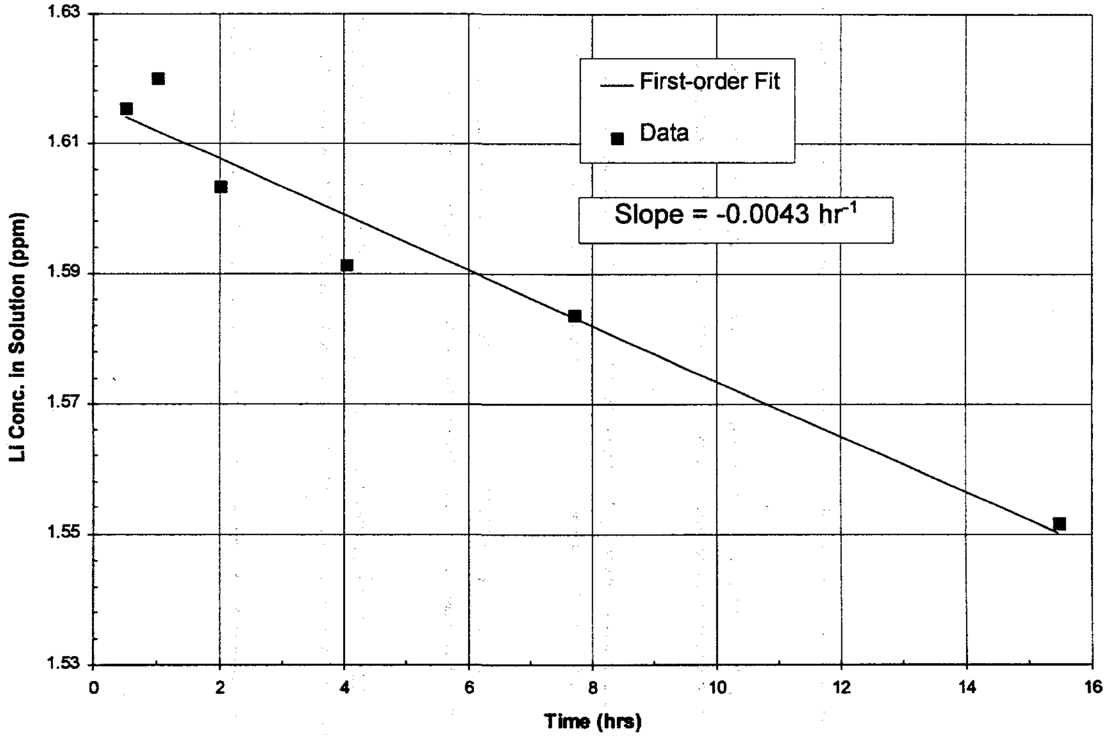

Figure C.12. Five ppm Li sorption on Wedron 510 sand modeled by the first-order kinetic reaction equation. (Data from Cheng *et al.* 1995)

C.5. Summary

The Li adsorption and desorption experiments described in this paper have yielded information on the role of the individual mineral phases in adsorption of Li by Wedron 510 sand. Leaching experiments and previous adsorption experiments (Siegel *et al.*, 1995) suggest that goethite, occurring as coatings on grain surfaces, represents a sizable fraction of the total surface area of the sand. Kaolinite is also a significant trace mineral phase in the sand; it has been identified by SEM and XRD as small particles coating the sand grains, and the Al content of bulk Wedron sand suggests that it might comprise as much at 1.38% of the sand by weight.

Both the adsorption and desorption studies suggest that that kaolinite is the only important phase in the sand with respect to Li adsorption. The Li adsorption curve of the sand is similar to that of kaolinite; both exhibit a broad peak in adsorption at near-neutral pH values. Conversely, Li adsorption onto goethite is pH-independent; the adsorption curve is flat. The desorption studies indicate that Li does not desorb readily from Wedron sand; this is consistent with adsorption by kaolinite, which adsorbs Li irreversibly.

The batch kinetics experiment was conducted to determine the time dependence sorption of Li onto Wedron 510 sand. The kinetic sorption data was not modeled well by either the first or second-order rate equations, based on low r^2 values.

Using multiple first-order rate equations for the time intervals from 0-10 hrs and 10-120 hrs described the data well. The apparent rate constant for the interval 0-10 hrs agreed closely with a first-order apparent constant derived from previous 5 ppm Li kinetic sorption data. This confirms that for Li sorption on Wedron sand, for sorption times up to 15 hrs, the reaction can be modeled as first-order with an apparent rate constant in the range 0.0043 hr^{-1} to 0.0057 hr^{-1}.

C.6. References

Anderson, M.A., P.M. Bertsch, and W.P. Miller, 1989: "Exchange and Apparent Fixation of Lithium in Selected Soils and Clay Minerals," *Soil Sciences*, 148, 46-52.

Bryan, C.R., D.B. Ward, and M.D. Siegel, 1995: "Ni Sorption and Solubility Studies," in *Characterization of Materials for a Reactive Transport Model Validation Experiment, Appendix B,* Siegel, M.D., D.B. Ward, C.R. Bryan, and W.C. Cheng, SAND94-0189, Sandia National Laboratories, Albuquerque, NM, 32 p.

Bunnett, J. F., 1986: "Kinetics in Solution", in *Investigations of Rates and Mechanisms of Reactions, Part I,* 4th ed, Claude F. Bernasconi, ed. Wiley-Interscience, New York, 171-250.

Chardymskaya, E. Yu., M.P. Sidorova, and E.V. Kulepova, 1986: "Determination of EDL Potentials on SiO_2 surfaces in CsCl and LiCl solutions from Adsorption Measurements," *Colloid J. of the USSR*, 48, 645-649.

Cheng, W.C., M.D. Siegel, and C.R. Bryan, 1995: "Column Studies in Support of the Caisson Experiments: Design and Preliminary Results for Li and Br," in *Characterization of Materials for a Reactive Transport Model Validation Experiment, Appendix C,* Siegel, M.D., D.B. Ward, C.R. Bryan, and W.C. Cheng, SAND94-0189, Sandia National Laboratories, Albuquerque, NM, 36 pp.

Siegel, M.D., D.B. Ward, C.R. Bryan, and W.C. Cheng, 1995: *Characterization of Materials for a Reactive Transport Model Validation Experiment, SAND94-0189*, Sandia National Laboratories, Albuquerque, NM, 271 pp. (in press).

Skopp, J., 1986: "Analysis of Time-dependent Chemical Processes in Soils", *Journal of Environmental Quality,* 15, 205-213.

Ward, D.B., M.D. Siegel, and C.R. Bryan, 1995: "Characterization of Wedron 510 Sand for the Intermediate-Scale (Caisson) Transport Experiment," in *Characterization of Materials for a Reactive Transport Model Validation Experiment, Appendix A,* Siegel, M.D., D.B. Ward, C.R. Bryan, and W.C. Cheng, SAND94-0189, Sandia National Laboratories, Albuquerque, NM, 43 pp.

Appendix D.

Transport of Lithium in a Saturated Bench-Scale Sand Column

Connor Boyle

Table of Contents

D.1. Introduction

A saturated, laboratory-scale column experiment was conducted using 1 ppm Li (as LiBr) as a tracer. The column breakthrough curve (BTC) was modeled using input parameters derived from batch sorption studies. Values for the Li distribution coefficient, K_d, and kinetic adsorption rate constant, k, obtained from previous batch studies were used as input for the computer codes CXTFIT and HYDRUS. The code CXTFIT was used to numerically fit the one dimensional convective-dispersive transport equation to the effluent Li and Br breakthrough curves (BTC), resulting in values for the transport parameters hydrodynamic dispersion, D, and retardation factor, R. The code HYDRUS was used to simulate breakthrough curves based on a non-linear, Freundlich adsorption isotherm equation derived from batch studies.

D.2. Experimental Methods

The methods used in this experiment follow those described in Siegel *et al.* (1995). A 5 cm diameter by 30.5 cm long Plexiglas column was filled with 1073.4 g of Wedron 510 sand and saturated with 179.6 g of 0.001 M NaCl solution. The corresponding values for bulk density, ρ_b, and porosity, η, were 1.8 g/m*l* and 0.30, respectively. Care was taken to eliminate or minimize layering of sand and the accumulation of air bubbles within the column. Slightly more than one pore volume of the 0.001 M NaCl solution was pumped through the column after saturation to strip any background Li from the sand, and to remove air bubbles inside the column.

A LiBr pulse was pumped into the column at a constant rate of 0.42 g/min resulting in a pore water velocity (V_w) of 0.071 cm/min. Column effluent was collected in 16 mm sample vials for 30 minutes at a time. After 54.1 g of 1 ppm Li (as LiBr) tracer was pumped into the column (about 0.3 pore volumes), the pump was turned off and a feed bottle of 0.001 M NaCl solution was connected to the input of the column. The LiBr tracer pulse was then flushed with a total of ~6 pore volumes of the 0.001 M NaCl solution. The experimental setup for this column experiment is shown in Figure D.1.

Two computer codes were used to model the Li and Br breakthrough curves: the multi-parameter optimization program, CXTFIT, of Parker and van Genuchten (1984) and HYDRUS, a numerical linear finite element program for simulation of solute transport, by Kool and van Genuchten (1992). Both models incorporate the processes of reversible adsorption into the one-dimensional convection-dispersion equation.

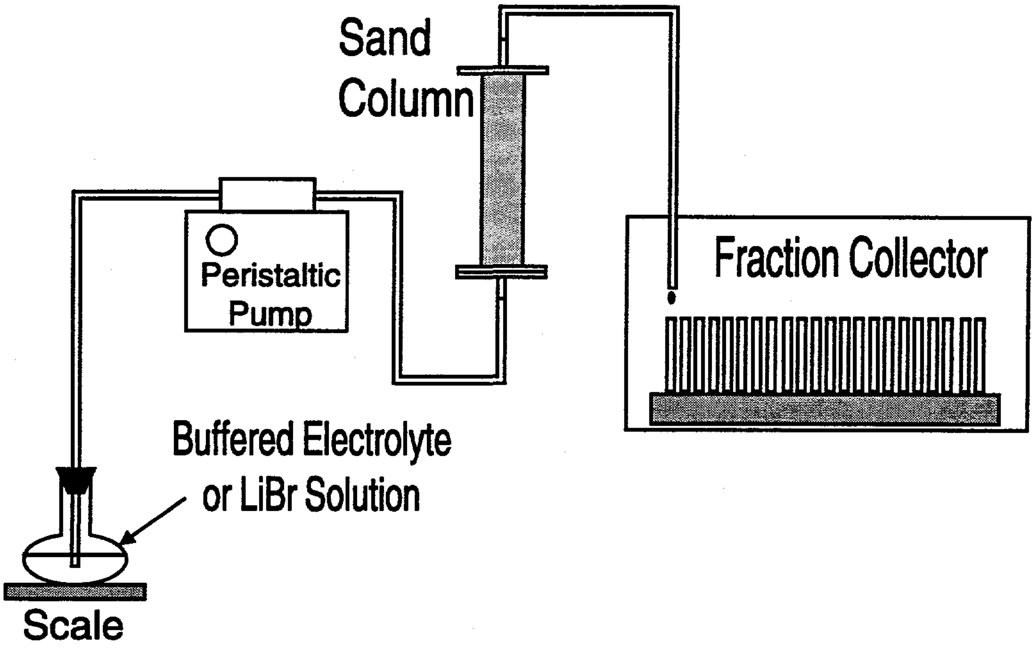

Figure D.1. Experimental set up for column experiment.

The computer code CXTFIT was used to obtain transport parameters by fitting a BTC to the experimental data. This code can either predict a BTC given the transport parameters, or determine the parameters based on a fitted BTC. Two CXTFIT models were used to fit the column data: the linear equilibrium adsorption model and the two-site/two-region nonequilibrium (or kinetic) model. Both assume that a linear isotherm describes the adsorption of the solute onto the solid phase. The linear equilibrium adsorption model treats all adsorption sites as being in equilibrium, whereas the kinetic model separates the total adsorption sites into two fractions. In one fraction, F, the adsorption sites are in equilibrium and the other fraction, 1-F, is modeled by a first-order adsorption rate constant.

Additional variable parameters used in the CXTFIT kinetic model include β, the fraction of instantaneous retardation, and ω, the Damkohler number which represents the ratio of hydrodynamic residence time to the characteristic time of sorption (1/k). As the degree of nonequilibrium decreases in the column, β and ω increase in magnitude (Brusseau, 1991). The value of the retardation factor (R) used by CXTFIT is the equilibrium R, the effective or apparent R can be found by multiplying the equilibrium R by β. Definitions for β and ω are shown below.

$$\beta = \frac{1 + F\left(\frac{\rho_b}{\eta}\right)K_d}{R} \tag{D-1}$$

$$\omega = \frac{k(1-\beta)RL}{V_w} \tag{D-2}$$

where all variables are as defined previously and L = column length.

The code HYDRUS differs from CXTFIT in several ways. The code cannot estimate transport parameters based on a given BTC, however it will simulate the BTC from user-specified transport and adsorption parameters. This code is also capable of simulating non-linear (Freundlich) sorption, while CXTFIT can only model linear sorption. HYDRUS also assumes only reversible, equilibrium sorption, and cannot simulate sorption rates.

The sorption of Li onto Wedron sand has been shown to be irreversible (Bryan and Boyle, Appendix C, this report). Both HYDRUS and CXTFIT assume reversible sorption, therefore, the mass of Li in the effluent (rather than the influent) was used as the pulse input mass for both computer codes for some simulations.

Estimates for parameters required for the models were obtained from previous laboratory studies. In batch adsorption experiments (Ward, Bryan, and Siegel Appendix A, this report) containing 1 ppm Li with either 100 ppb or 200 ppb Ni were equilibrated with an equal mass of sand. Measured Li K_ds of ~1 ml/g were obtained for both solutions (Ward, Bryan and Siegel, Figure A.9, this report). This agrees with the interpolated K_d value for a 1 ppm Li concentration based on previous batch studies (Cheng *et al.*, 1995, Figure C.9, in Siegel *et al.*, 1995).

A 10 ppm Li kinetic study (Bryan and Boyle, Appendix C, this report) gave an apparent adsorption rate constant of 9.5×10^{-5} min^{-1} (5.7×10^{-3} hr^{-1}). This agreed closely with an apparent rate constant of 7.2×10^{-5} min^{-1} (4.3×10^{-3} hr^{-1}) obtained from data from a previous 5 ppm Li kinetic study (Cheng *et al.*, 1995, Figure C.9, in Siegel *et al.*, 1995). The apparent rate constant value of 9.5×10^{-5} min^{-1} was used as input to the CXTFIT kinetic model.

It has been shown by Bryan and Boyle (Appendix C, this report) that Li adsorption, for a Li concentration range of 0.001 - 1000 ppm, is best described by the Freundlich adsorption isotherm described below. The constants K and n were determined from the batch studies and used as input to HYDRUS.

$$S = KC^n \tag{D-3}$$

where

S = mass of solute sorbed (μg/g)
C = concentration of solute in solution (ppm)
K and n are empirical constants, found to be 0.55 and 0.376 respectively

D.3. Results

The observed BTC's for Br and Li are shown Figure D.2. Both curves are similar to other Br and Li BTC's derived from previous experiments (Cheng *et al.*, 1995, in Siegel *et al.*, 1995). The Br BTC displays a retardation factor of ~1 with little or no adsorption while the Li BTC indicates some retardation and attenuation of the pulse with a noticeable tailing effect.

The Br pulse was adequately modeled using the CXTFIT linear equilibrium model, assuming a constant pore water velocity of 0.071 cm/min. Allowing the code to calculate values for retardation and dispersion gave a fitted curve with a r^2 value of 0.994 (see Figure D.3). The calculated values for D and R were 0.005 cm^2/min and 1.0, respectively. The computed value of $R=1.0$ corresponds to the batch K_d of 0. Using the kinetic model, and allowing D, R, F, and k to vary, gave a slightly better fitting curve (Br BTC #2, not shown) but produced a physically-meaningless, negative value for F, the fraction of total adsorption sites in equilibrium.

Li breakthrough curves were calculated using three different models: the CXTFIT equilibrium model, the CXTFIT kinetic model, and the HYDRUS Freundlich sorption model. Values obtained in batch experiments for K_d and k, and

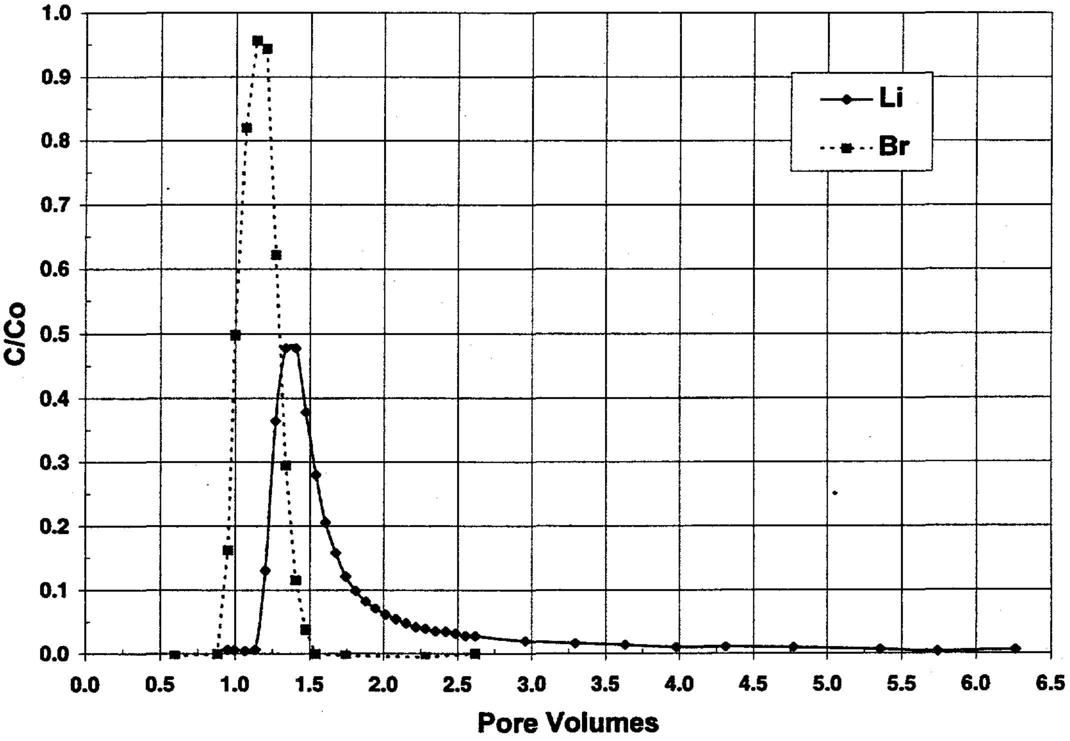

Figure D.2. Experimental Li and Br breakthrough curves for a 0.3 pore volume pulse input of 1 ppm Li as LiBr.

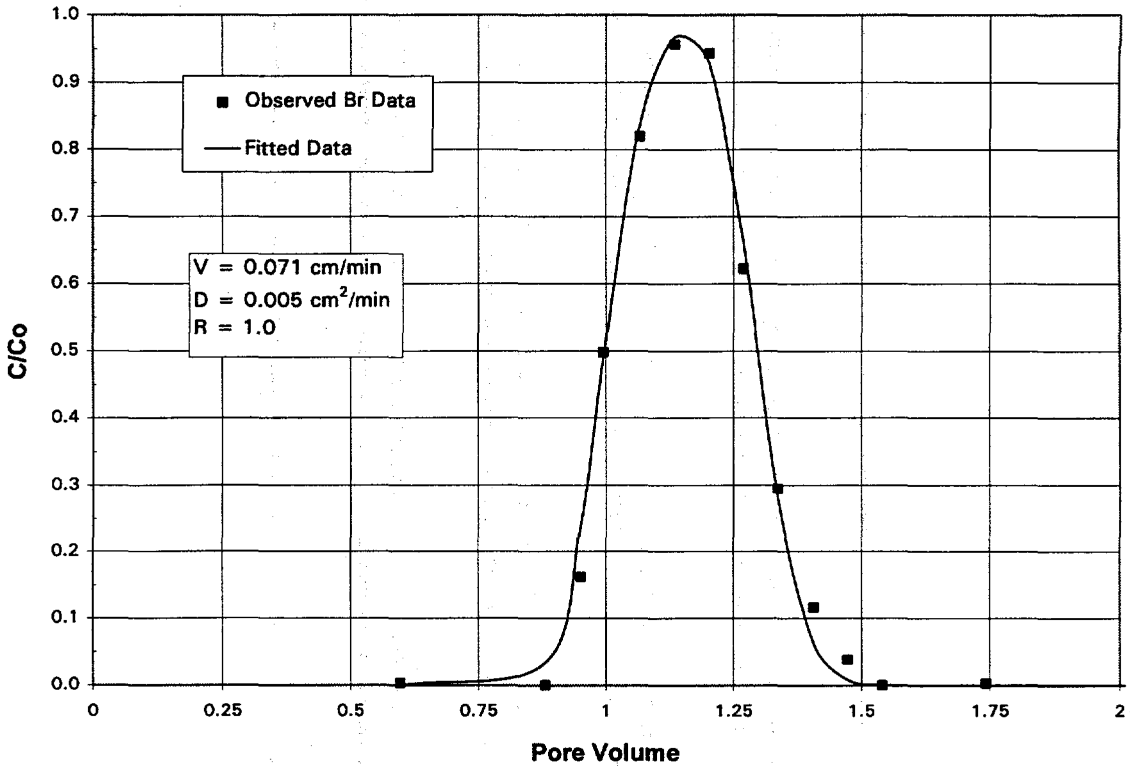

Figure D.3. Br data from Figure D.2 fitted using the CXTFIT linear equilibrium model (Br BTC #1).

the Freundlich constants K and n were used for the models. Because of the long flow path (30.5 cm) and relatively high average pore water velocity, it was assumed that mechanical dispersion was the dominant form of mixing. Thus, molecular diffusion was considered insignificant and the value of dispersion obtained from the fitted Br curve was used for all three models. In the CXTFIT kinetic model all the sites were assumed to be kinetic sites (F=0). Figure D.4 compares the predicted BTC's (Li BTC's #1, #2, and #4) to the actual breakthrough curves. It is apparent that none of these simulated BTC's adequately model the observed data.

The CXTFIT equilibrium model was used to model the BTC by using the value of D from Br BTC #1, and allowing R to vary. The resulting BTC (Li BTC#3 shown in Figure D.5.) was symmetrical and greatly over estimated the peak concentration and tracer mass. Because the kinetic model more closely modeled the observed data, a series of fitted curves were generated using the kinetic model, with different combinations of fixed and variable parameters. The pore water velocity was the only input value held constant and combinations of D, R, k, and F, were allowed to vary. The Li BTC (Li BTC #5) shown in Figure D.5. was obtained by allowing k and F to vary. This BTC gave the best fit to the data while still producing parameters

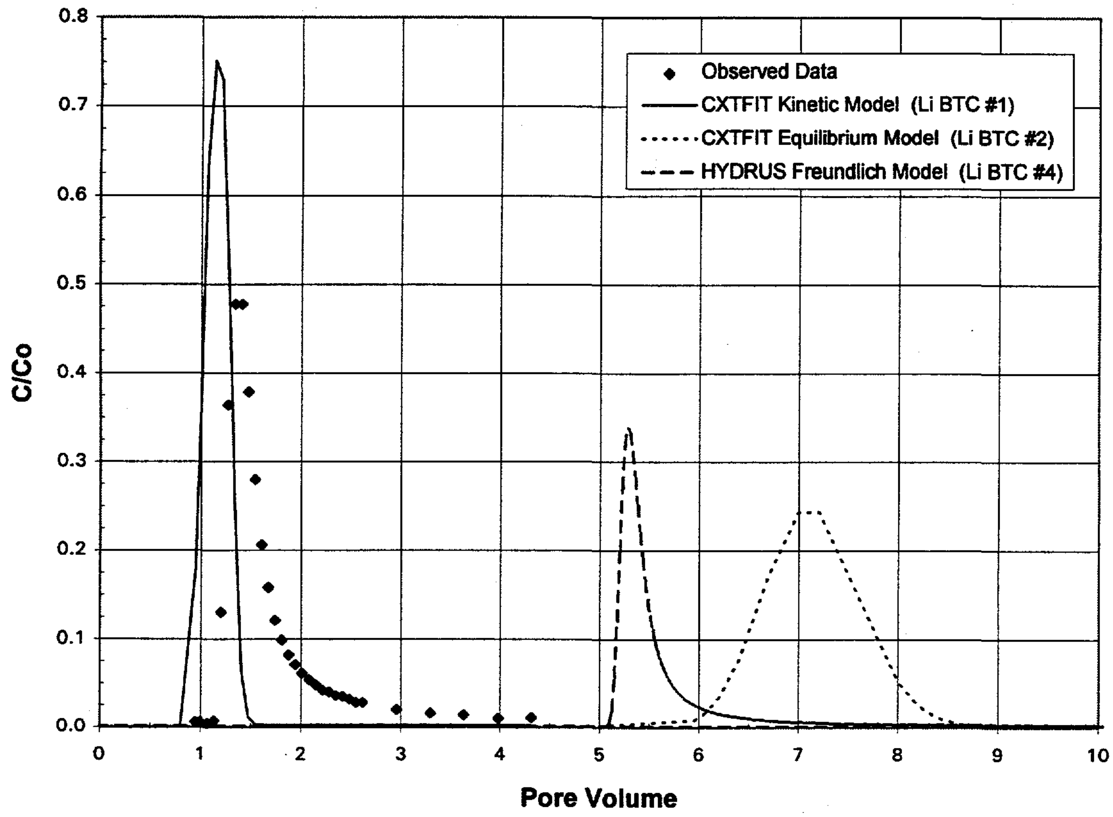

Figure D.4. Predicted 1 ppm Li BTC's, using the CXTFIT equilibrium and kinetic models, and the HYDRUS Freundlich model. The constants K_d, k, K, n, obtained from laboratory studies (Appendix C, this report), and the value of D obtained from the Br BTC, were used as input for the models. $V_w = 0.071$ cm/min for all models.

that were close to the batch values obtained in batch studies. The curve, however, did not account for the tailing of the Li pulse.

The best fit to the observed data came by letting all parameters vary, including the mass of the Li input pulse. As can be seen in Figure D.6, the modeled curve (Li BTC #6) fits the data well, including the tail of the pulse. The calculated values for the transport parameters, however, were very different from the measured batch values for K_d and k, and the value of D obtained from the Br pulse. In addition, the mass of the Li input pulse obtained by CXTFIT was 40 μg. The actual effluent Li mass is 47 μg, indicating the CXTFIT kinetic model cannot completely account for the tail of the BTC.

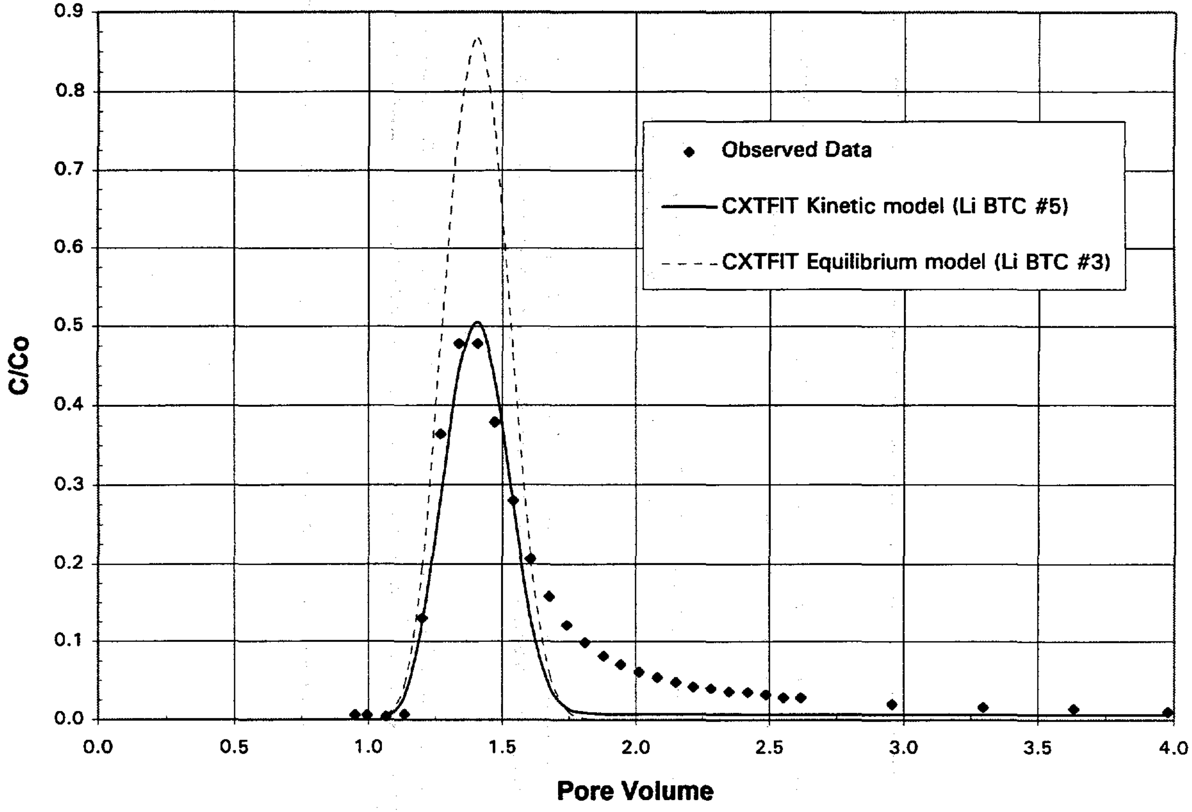

Figure D.5. CXTFIT kinetic and equilibrium models fitted to the Li data. Li BTC #5 was obtained by letting F and k vary, and Li BTC #3 was obtained by varying R only.

D.4. Discussion

The CXTFIT computer code can predict BTC's if the transport parameters are known, or can determine the parameters by fitting them to observed laboratory data. The code uses a least-squares inversion method to solve the one-dimensional conductive-dispersive transport equation using a linear adsorption isotherm (Parker and van Genuchten, 1984). In addition, CXTFIT assumes reversible adsorption in the two-site/two-region kinetic model.

CXTFIT was able to adequately fit the Br experimental column data and produce reasonable values for the transport parameters. However, this was expected because Br is a non-sorbing tracer for which the linear isotherm and equilibrium adsorption assumptions in CXTFIT are valid. When the kinetic model was used to fit the data, a better fit was obtained, but the transport parameters for D and F were unrealistic. Therefore, the equilibrium model should be used to model Br and not the kinetic model.

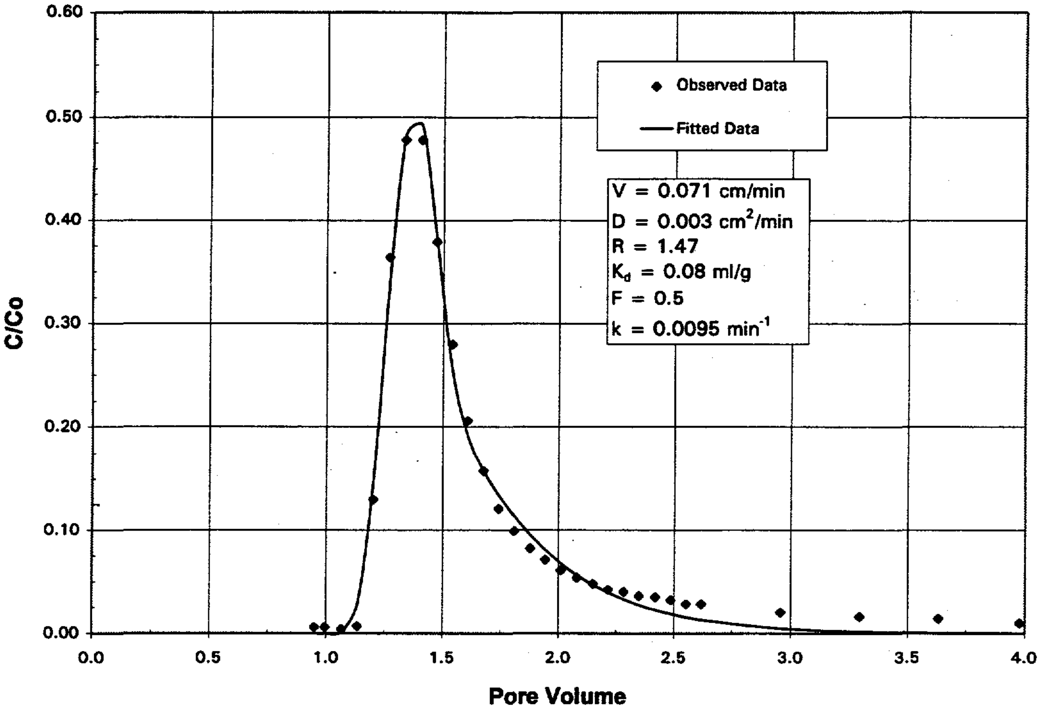

Figure D.6. Li BTC #6 using the CXTFIT kinetic model and allowing all parameters to vary.

The Li data, however, were not modeled well by either CXTFIT or HYDRUS. Table D.1 is a summary of the attempts to both fit the data and produce transport parameters which agreed with the parameters derived from batch adsorption experiments. The CXTFIT equilibrium and kinetic models, and HYDRUS were first used to predict the Li BTC using laboratory derived values for K_d of 1 m*l*/g, k of $9.5x10^{-5}$ min^{-1} , Freundlich K and n of 0.55 and 0.376 respectively. The results can be seen in Models Li BTC's #1, #2, and #4. CXTFIT and HYDRUS do not provide r^2 values for predicted BTC's, but it is obvious from Figure D.4 that all three models produced very poor correlation to experimental curves.

Because the kinetic model gave better agreement with the experimental BTC, it was used in subsequent attempts at fitting the laboratory data. This led to model Li BTC #5, which gave values for K_d and k that agreed well with those from the batch studies, and fit the data reasonably well. However, it failed to account for the tailing of the Li pulse.

The tailing effect could be caused by several different processes. A physical process resulting from the existence of dead-end pores or channeling effects could cause the tail on the Li BTC. This appears unlikely because these effects would also cause the Br BTC to exhibit a tail, which was not observed (Figure D.3).

Table D.1. Summary of CXTFIT models and parameters for Br and Li experimental column data.

	Br BTC's		Li BTC's					
Parameter	#1	#2	#1†	#2†	#3	#4†	#5	#6
D	0.05	0.00	0.005	0.005	0.005	0.004	0.005	0.003
R	1.0	1.0	7.0	7.0	1.28	7.0	7.0	1.5
K_d (ml/g)	0	0.002	1.0	1.0	.05	1.0	1.0	.08
F	NA	-3.8	NA	0	NA	NA	0.04	0.5
k (min^{-1})	NA	0.06	$9.5x10^{-5}$	NA	NA	NA	$3x10^{-4}$	$9.5x10^{-3}$
β	NA	0.934	0.143	NA	NA	NA	0.182	0.841
ω	NA	1.729	0.245	NA	NA	NA	0.537	0.947
$R_{apparent}$	NA	0.93	1.00	NA	NA	NA	1.27	1.26
Model	CXTFIT Equilibrium	CXTFIT Kinetic	CXTFIT Kinetic	CXTFIT Equilibrium	CXTFIT Equilibrium	HYDRUS *	CXTFIT Kinetic	CXTFIT Kinetic
Parameters varied	R & D	R, D, F, & k	None	None	R	None	F & k	D, R, F, k & mass of Li in pulse
r^2	0.994	0.998	-	-	0.925	-	0.936	0.992

† Batch values used

*Freundlich coefficient K = 0.55, and exponent, n = 0.376

Chemical processes such as non-linear sorption and/or slow kinetics of sorption/desorption may also explain the tailing of the Li BTC.

The BTC for a solute with non-linear sorption is often characterized by a steep leading edge and a long tail (self-sharpening BTC). The retardation factor for a Freundlich isotherm is written as :

$$R = 1 + \frac{nK\rho_b C^{n-1}}{\theta} \tag{D-4}$$

where all variables are as defined previously.

At the beginning of the column experiment, when the concentration of solute is high, the retardation is less and the solute moves more rapidly than later at stages when the solute concentration is lower and the retardation higher. Therefore, the tail is caused by the slower (more retarded) moving solute. Based on batch studies which show the sorption of Li onto Wedron sand to be described by the Freundlich isotherm, the code HYDRUS should have been able to simulate the Li BTC. While the simulated BTC generated by HYDRUS was similar in shape to the actual Li BTC, the retardation and peak concentration were not. However, HYDRUS assumes instantaneous sorption, so if the sorption reaction were rate-limited, HYDRUS would not be able to accurately simulate the BTC.

If Li sorption is described by a Freundlich isotherm, the effect of different initial Li concentrations on the shape of the BTC should be noticeable. Higher concentrations of the solute in the input pulse should give a BTC with a higher peak and a narrower pulse. At lower concentrations the pulse should broaden as the tail becomes more pronounced and the relative peak concentration drops. A comparison of the 1 ppm Li BTC with a 17.4 ppm Li BTC from a previous experiment (Cheng *et al.*, Figure C.12, in Siegel *et al.*, 1995), shown in Figure D.7, reveals such behavior. The experimental conditions for each experiment were identical, and it is seen that the 1 ppm Li BTC has a lower peak relative concentration, a wider pulse and a more pronounced tail. This supports the batch results of non-linear, Freundlich Li sorption onto Wedron sand.

If the tailing of the Li BTC is a function of slow kinetics of adsorption and insufficient residence time in the column, CXTFIT should have been able to account for it in the kinetic model. Fluid residence time in the column was ~7 hours and previous Li kinetic batch experiments show equilibration times of 24 to 80 hours (Cheng *et al.*, 1995, in Siegel *et al.*, 1995). Model Li BTC #5 gave the best fit to the data but the K_d and k parameters were orders of magnitude different from the values for batch studies. Alternatively, the tailing of the Li BTC could be caused by slow desorption of the Li; this is supported by the observation that the adsorption of Li is irreversible in batch studies (Bryan and Boyle, Appendix C, this report).

Based on the CXTFIT and HYDRUS modeling results, it appears a model capable of incorporating Freundlich type, nonequilibrium sorption into the convective-dispersive equation would best describe the Li BTC. The CXTFIT kinetic model, based on parameters from batch studies, gave the best fit to the actual Li BTC but could not model the tailing effect. HYDRUS simulated the tailing of the Li BTC, but not the actual retardation or peak concentration.

It is apparent that the role of non-equilibrium sorption must be considered when using an equilibrium K_d obtained from batch experiments to predict retardation of a column BTC. Kuhn and Peters (1981) developed a relationship between dimensionless time (T) and the number of theoretical mass transfer units along a column (n). The parameter T is defined by equation D-5, and ranges between 0, for an infinitely slowly sorbing tracer, and 1, for a rapidly sorbing tracer, respectively.

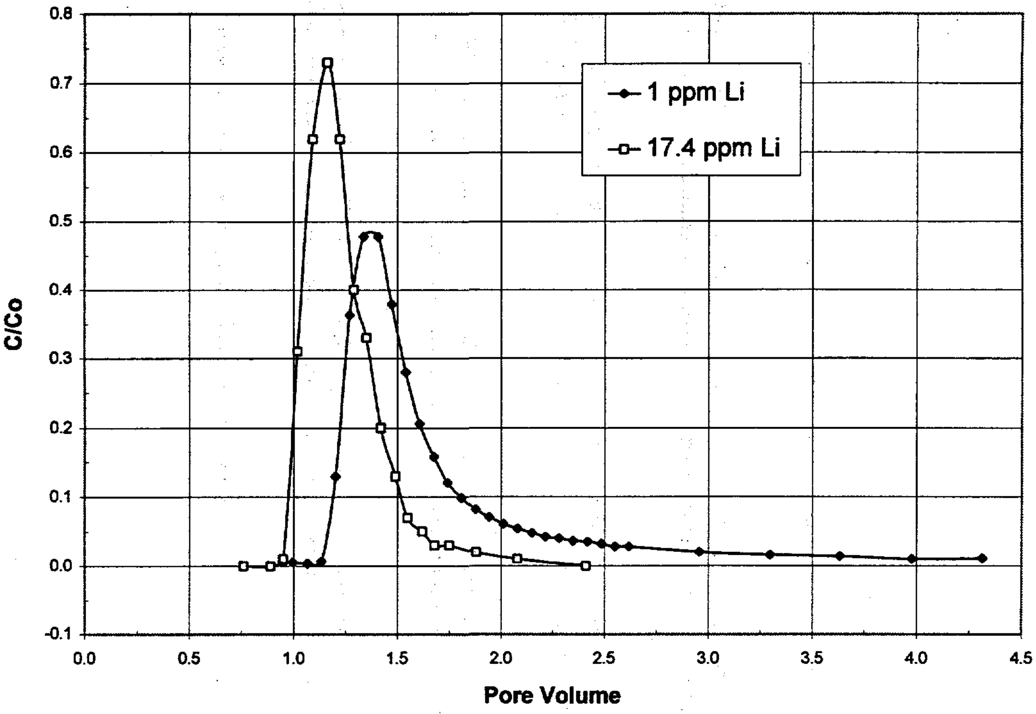

Figure D.7. A comparison of 1 ppm and 17.4 ppm Li BTC's. Both were obtained under identical experimental conditions and illustrate the effect of initial concentration on the shape of the BTC for a sorbing solute described by a Freundlich isotherm.

$$T = \frac{R_{ap} - 1}{R_{eq} - 1} \tag{D-5}$$

The number of mass transfer units is defined by

$$n = \frac{\rho_b K_d L}{\eta V_w} k \tag{D-6}$$

where

V_w = average pore water velocity (cm/min)
R_{ap} = apparent retardation factor of the experimental BTC
$R_{eq} = 1 + (\rho_b K_d / \eta)$, the equilibrium retardation factor
and all other variables are as defined previously.

The analysis of Kuhn and Peters was used by Relyea (1982) as a guide in determining if V_w is too large for equilibrium conditions to exist in a column by comparing tabulated values of n and T (which Relyea (1982) erroneously identifies as R_{ap}/R_{eq}). Using these values of T and n, and assuming the batch equilibrium K_d is 1.0 m*l*/g, R_{ap}/R_{eq} can be plotted as a function of n as shown in Figure D.8 .

Since n=0 corresponds to a non-sorbing tracer, T=0 and R_{ap}/R_{eq} reduces to $1/R_{eq}$. Assuming k is 9.5×10^{-5} min^{-1}, and using values for ρ_b, η, V_w, and L of 1.8 g/cm^3, 0.3, 0.071 cm/min, and 30.5 cm respectively from the column experiment, n is 0.24 and $R_{eq} = 7$. Interpolating between points yields a value for R_{ap}/R_{eq} of 0.176 and therefore R_{ap} is 1.24. This compares well to the apparent R values, shown in Table D.1, obtained from the CXTFIT kinetic models of 1.26 and 1.47, and to the R of 1.28, obtained from the CXTFIT equilibrium model. It should be noted however, that the analysis of Kuhn and Peters (1981) and Relyea (1982) were only applied to values of n greater than two.

A similar analysis was performed for a 17.4 ppm Li column experiment (Cheng *et al.*, 1995, in Siegel *et al.*, 1995). The apparent R values determined from the CXTFIT equilibrium sorption model for the BTC ranged from 1.04 to 1.08 and the apparent R value determined from this analysis was 1.06. Based on the successful application of this analysis to two separate Li column experiments, it would seem that it is a reasonable method for predicting effective retardation factors for Li

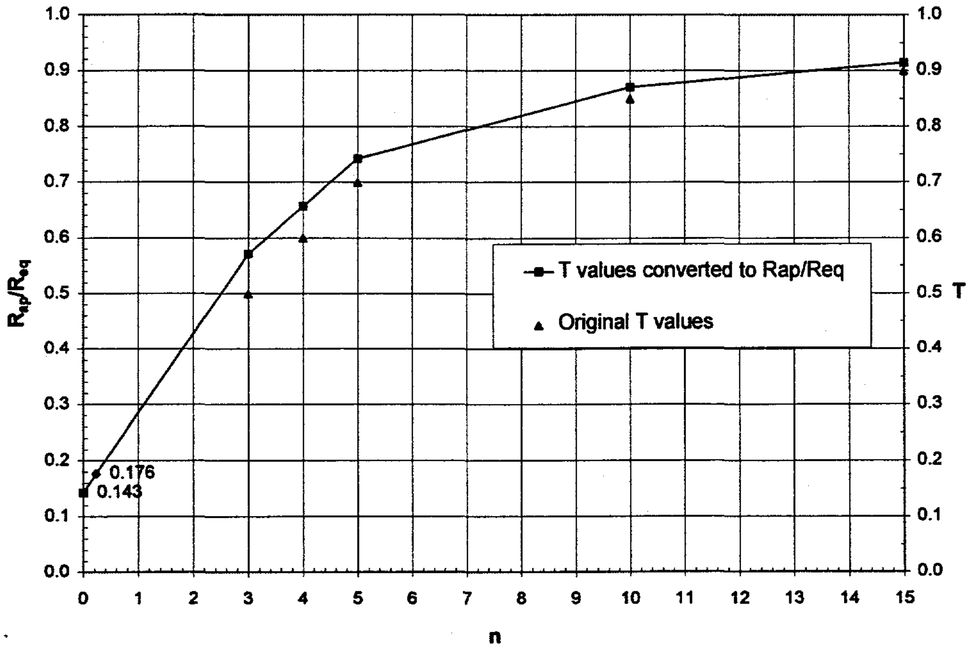

Figure D.8. Retardation factor ratio as a function of number of mass transfer units. At T=0, n was assumed to be equal to 0 and $R_{ap}/R_{eq} = 1/R_{eq} = 1/7$. The values of R_{ap}/R_{eq} are based on tabulated values of T from Relyea (1982).

pulses when adsorption in the column is rate-limited.

D.5. Summary

The computer codes CXTFIT and HYDRUS were used to model laboratory column data based on batch derived sorption constants. The non-sorbing species Br was modeled satisfactorily but the Li data were not. Using values for K_d, k, K, and n obtained in batch studies produced poorly fitting BTC's for both the CXTFIT equilibrium and kinetic models; as well as, the HYDRUS non-linear isotherm model.

CXTFIT models the adsorption process as linear and reversible, which may explain why the code did not adequately model the laboratory data. Recent batch studies have shown that Li adsorption can modeled by a Freundlich isotherm but is dominantly irreversible. The former is confirmed by a comparison of two Li BTC's at different initial input concentrations and the latter by observations that the effluent tracer mass is less than the influent tracer mass from the columns. The differences in shape of the two Li BTC's are consistent with Freundlich sorption. Therefore, a transport model which includes some irreversible sorption sites and allows reversible adsorption to be modeled by the Freundlich isotherm and first-order kinetics, would probably be more appropriate for the modeling of Li adsorption by Wedron sand during transport.

D.6. References Cited

Brusseau, M.L. T. Larsen, and T.H. Christensen, 1991. “Rate-Limited Sorption and Nonequilibrium Transport of Organic Chemicals in Low Organic Carbon Aquifer Materials”, *Water Resources Research*, **27**, 6, 1137-1145.

Bryan, C.R. and C. Boyle, “Li Adsorption by Wedron 510 Sand and Pure Minerals: Reversibility and Kinetic Studies,” in *Batch and Column Studies of Adsorption on Li, Ni, and Br by a Reference Sand for Contaminant Transport Experiments, Appendix C,* Siegel, M.D., D.B. Ward, C.R. Bryan, and C. Boyle, SAND95-0591, Sandia National Laboratories, Albuquerque, NM, 23 pp.

Cheng, W.C., M.D. Siegel, and C.R. Bryan, 1995: “Column Studies in Support of the Caisson Experiments: Design and Preliminary Results for Li and Br,” in *Characterization of Materials for a Reactive Transport Model Validation Experiment, Appendix C,* M.D. Siegel, D.B. Ward, C.R. Bryan, and W.C. Cheng, SAND94-0189, Sandia National Laboratories, Albuquerque, NM, 34 pp.

Kool, J.B., and M. T. van Genuchten, 1992. *HYDRUS, One-Dimensional Variably Saturated Flow and Transport Model, Including Hysteresis and Root Water Uptake.* Research Report No. 124, U. S. Salinity Laboratory, USDA, ARS, Riverside, CA.

Kuhn, W.L., and R.D. Peters, 1981: "WRIT Leaching and Transport Modeling," *Waste/Rock Interactions Technology Program FY-80 Information Meeting,* J.F. Relyea Editor, PNL-3887, Pacific Northwest Laboratory, Richland, Wa., 268-276.

Parker, J.C., and M. T. van Genuchten, 1984: *Determining Transport Parameters from Laboratory and Field Tracer Experiments,* Virginia Agricultural Experiment Station Bulletin 84-3, ISSN 0096-6088, 92 pp.

Relyea, J.F., 1982: "Theoretical and Experimental Considerations for the Use of the Column Method for Determining Retardation Factors," *Radioactive Waste Management and the Nuclear Fuel Cycle,* **3**, 151-166.

Siegel, M.D., D.B. Ward, C.R. Bryan, and W.C. Cheng, 1995: *Characterization of Materials for a Reactive Transport Model Validation Experiment, SAND94-0189,* Sandia National Laboratories, Albuquerque, NM, 271 pp. (in press).

Ward, D.B., C.R. Bryan, W. C. Cheng, and C.R. Boyle, 1995: "Experimental Procedures Used in the Characterization Study", in *Characterization of Materials for a Reactive Transport Model Validation Experiment, Appendix E,* M.D. Siegel, D.B. Ward, C.R. Bryan, and W.C. Cheng, SAND94-0189, Sandia National Laboratories, Albuquerque, NM, 114 pp.

Appendix E.

Transport of Nickel in Saturated Bench-Scale Sand Columns

Connor Boyle and Malcolm Siegel

Table of Contents

E.1 Introduction

Two small (10 cm), saturated, bench-scale column experiments were conducted at two different flow velocities with Ni tracer. The *faster* column experiment was run without provision for monitoring of the effluent pH, and the column had a relatively large dead volume at either end of the column. Because Ni sorption is strongly dependent on pH, the *slower* column was modified to allow monitoring of the effluent pH using in-line pH electrodes. In addition, the effluent dead volume was minimized on the slower column, and the flow rate was almost an order of magnitude lower than that of the faster column. Because of the differences in flow rates, the two columns will be referred to as the *fast* and *slow* columns.

Ni breakthrough curves (BTC's) from both columns were analyzed using the computer code CXTFIT, (Parker and van Genuchten, 1984), to obtain the retardation factor, R, and hydrodynamic dispersion, D, in the one-dimensional convection-dispersion transport equation. Distribution coefficients, K_ds, calculated from the retardation factors of the Ni BTC's, are compared to Ni K_ds determined from batch sorption studies.

E.2 Experimental Methods

Two 10 cm long by 2.5 cm diameter Lexan columns were used (see Figure E.1). The columns were fitted with threaded endcaps at either end. The endcaps were sealed with rubber O-rings and Teflon tape; each contained a porous plate supported by a perforated plastic plate. The dead volume of the column endcaps was 10.5 m*l*. The effluent endcap of the slow column was filled with epoxy, while allowing the effluent to drain through a small tube. This reduced the dead volume to less than 1 m*l*. Inlet and outlet tubing was connected to the endcaps with barbed screw-on fittings.

The bottom endcaps were connected to the columns under water to minimize trapped air bubbles in the assembly. Both columns were filled with Wedron 510 sand through a series of screens which insured homogeneous sand distribution in the column. Electrolyte solution (0.001 M NaCl) was pumped through the columns from the bottom up to allow air in the sand to escape. Saturation of the columns were determined when ponding was visible on the sand surface at the top of each column. After saturation, the pump was turned off and the top (effluent) endcap was screwed on.

The Ni input solution for the fast column experiment was prepared by adding 39.99 g of 10 ppm stock Ni solution to 1960 g of 0.001 M NaCl. All containers were open to the atmosphere during preparation, and the final pH of the solution was

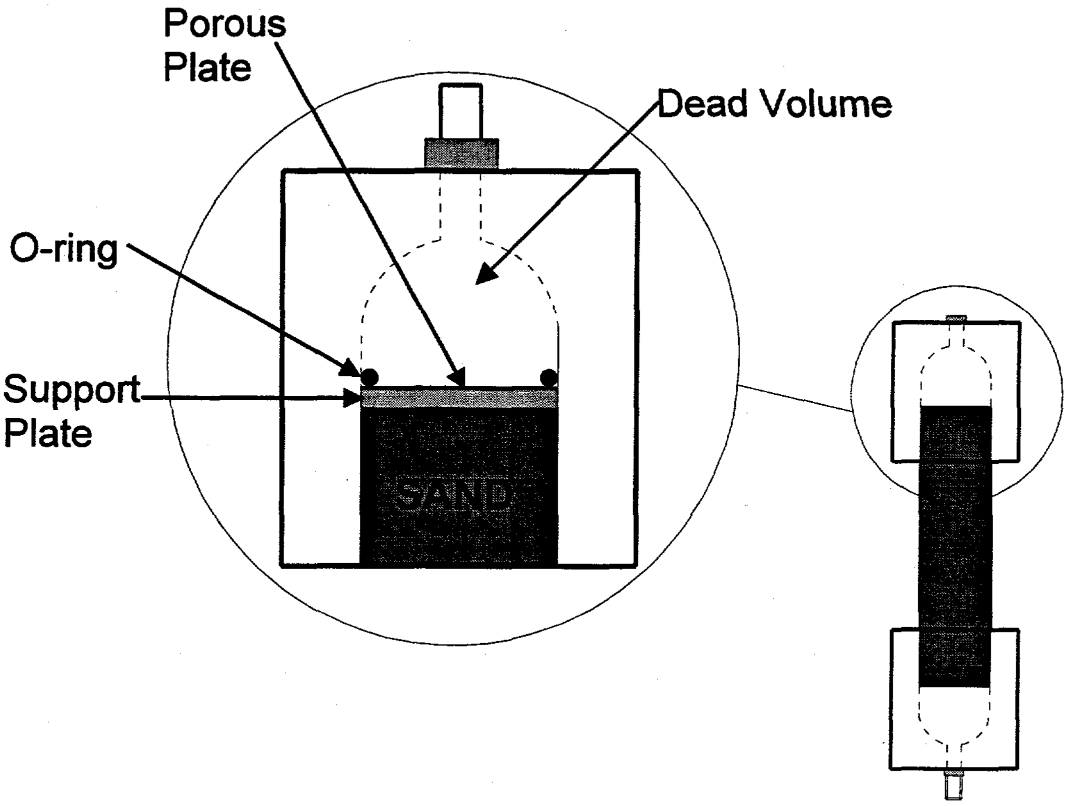

Figure E.1 Diagram of 10 cm column and endcap assemblies.

5.8. The Ni input solution for the slow column consisted of two different solutions. The first of the feed solutions was prepared by adding 20.88 g of the same 10 ppm Ni stock solution used for the fast column Ni feed solution, and then diluting to 1000 g with 0.001 M NaCl. The second of the Ni feed solutions for the slow column experiment was prepared by diluting 19.255 g of a different 10 ppm Ni stock solution to 1000 g with 0.001 M NaCl. Both Ni feed solutions used for the slow Ni column experiment were open to the atmosphere during preparation.

The effluent lines from the top of the columns were connected to automatic fraction collectors, holding 16 mm sample tubes, to collect the column effluent. The mass of the Ni tracer input pulse was 822.3 g for the fast column. The Ni input pulse for the slow column was comprised of two different Ni solutions for a total mass of 1318.6 g. The Ni concentrations for the first and second feed solutions were 198 ppb and 205 ppb (average), respectively. The first Ni feed solution, at an initial pH of 6.85, was changed for the second, also at pH 6.85, after 52 pore volumes had been eluted (refer to Figure E.4). After 76 pore volumes, the Ni pulse was flushed with two 0.001 M NaCl solutions at pH 5.94 and 6.38, respectively. After the flush was switched to the second bottle at 111.5 pore volumes, the pH drifted rapidly to 6.85, were it held steady for the rest of the experiment.

The effluent pH measurements taken, following the procedure in Ward *et al.* (1995) were from samples which had been sitting in the fraction collector for a minimum of 4 hours. These values ranged from 6.2 to 6.8. Only one pH measurement was performed as soon as the sample tube was filled with column effluent, and the reading was significantly higher (7.23) than the other readings. This indicates that although the fraction collector is housed in a sealed chamber, CO_2 diffusion into the open sample tubes is lowering the pH of the effluent solution.

The effluent pH of the slow column was monitored using an in-line pH sensor and reference electrode from Microelectrodes Inc. The electrodes were calibrated against buffer solutions of pH 4, 7, and 10. The corresponding voltage readings were used to obtain a linear regression line, which was then used to calculate pH from the measurement voltage of the electrodes during the experiment. At the conclusion of the experiment, the electrodes were again checked against the buffers; minimal drift was found. The electrodes were connected in-line to the outlet tubing immediately after the column effluent endcap, thus exposure to CO_2 was minimal and degassing should not occur. Readings were recorded every 15 minutes. The pH of the feed solutions was measured with a conventional glass electrode, and the effluent samples were analyzed for Ni by graphite furnace atomic absorption, following the technical procedures in Ward *et al.* (1995). Table E.1 summarizes the parameters for each column.

To determine if the epoxy filler in the effluent endcap of the slow column

Table E.1 Summary of column parameters.

	Fast Column	**Slow Column**
Pore Volume, pv, (m*l*)	16.6	16.9
Mass of sand in column (g)	82.16	82.32
Porosity, η	0.34	0.34
Bulk Density, ρ_b, (g/cm^3)	1.7	1.7
Pore Water Velocity, *v*, (cm/min)	0.24	0.04
Conc. of Ni Tracer (ppb)	182 initial pH=5.8	197.8 (Feed 1) initial pH=5.5 205.4 (Feed 2) initial pH=6.5 201.6 (average)
Amount of Tracer (in pv's)	49.4	78.0
Total Ni input (μg)	149.9	264.1
Total Ni eluted (μg)	112.0	71.8
Ni retained by sand (μg)	37.92	192
Total Ni leached (μg)	2.15	92.1

contributed to Ni sorption, a small batch experiment was performed. About seven grams of epoxy was placed in a 50 ml centrifuge tube and allowed to harden. The exposed surface area of the epoxy was approximately equal to that in the column. After the epoxy hardened, 25 g of 192.5 ppb Ni solution, at pH=6.8, was added and placed on a hematology mixer. After 280 hrs the solution was analyzed for Ni; the results showed that 9% of the Ni was adsorbed by the epoxy (0.4 μg Ni). This amount is inconsequential when compared to the 92 μg of Ni retained in the column, therefore, it is assumed only the sand was responsible for any irreversible Ni sorption.

E.3 Results

E.3.1 Fast Column

The Ni BTC from the fast column is shown in Figure E-2. Breakthrough of the pulse at C/Co = 0.5 occurred at about 17 pore volumes. The high peak value (C/Co ~1.3) was notable, as well as the tailing of the pulse from the peak to a C/Co value of 1. Once the input pulse was stopped, the effluent Ni concentration dropped rapidly. Measured effluent pH values are also plotted on Figure E-2.

Values of the transport parameters R and D of 16.8 and 0.0073 $\mathrm{cm^2/min}$, respectively, were obtained from a CXTFIT model of the BTC. The corresponding K_d, 3.2 m*l*/g, was calculated from the retardation factor equation below, for a linear isotherm, using values of porosity (η) and bulk density (ρ_b) from Table E.1.

$$K_d = \frac{(R-1)\eta}{\rho_b} \qquad \text{(E-1)}$$

The dispersivity, neglecting molecular diffusion, was calculated from D and v, using the following equation

$$\alpha = \frac{0.0073\ \mathrm{cm^2/min}}{0.24\ \mathrm{cm/min}} = 0.035\ \mathrm{cm} \qquad \text{(E-2)}$$

The fitted BTC generated by CXTFIT is shown in Figure E.3 . The input parameters R, D, and the size of pulse were allowed to vary, while the average pore water velocity was held constant. It is obvious that while the model cannot describe the unusually high peak, it does model the leading and trailing edges of the BTC well. A Ni mass balance for the system indicates that 38 μg of Ni was retained by the sand, or about 25% of the influent Ni. Leaching of the column with ~ 2% HNO_3 acid removed 22.15 μg of Ni. If ~35 ng of exchangeable Ni per gram of sand (Bryan

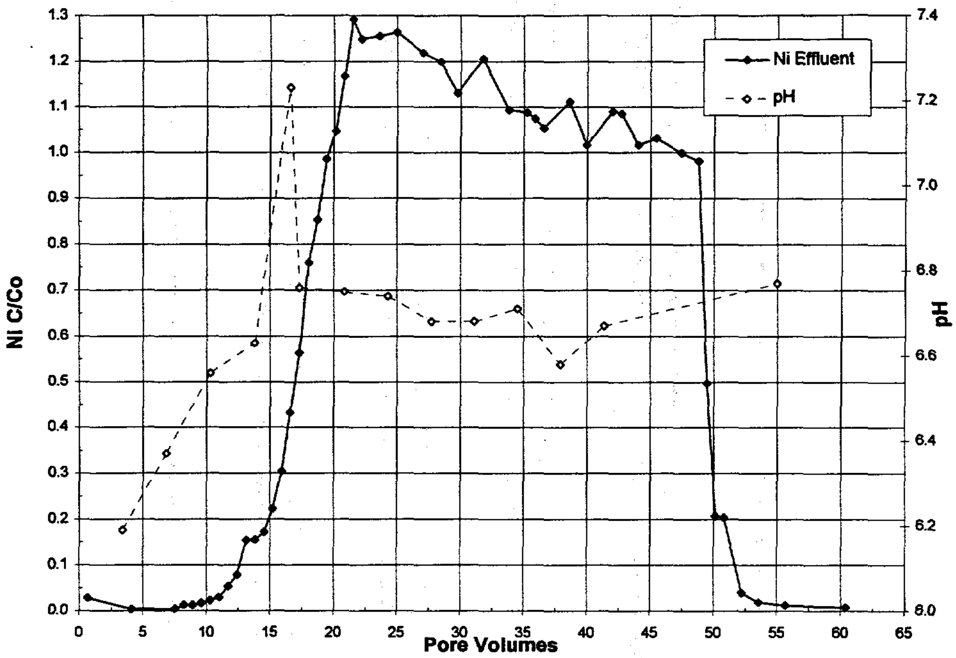

Figure E-2. Ni BTC from the fast Ni column experiment. Input Ni pulse concentration of 182 ppb with average pore water velocity of 0.24 cm/min.

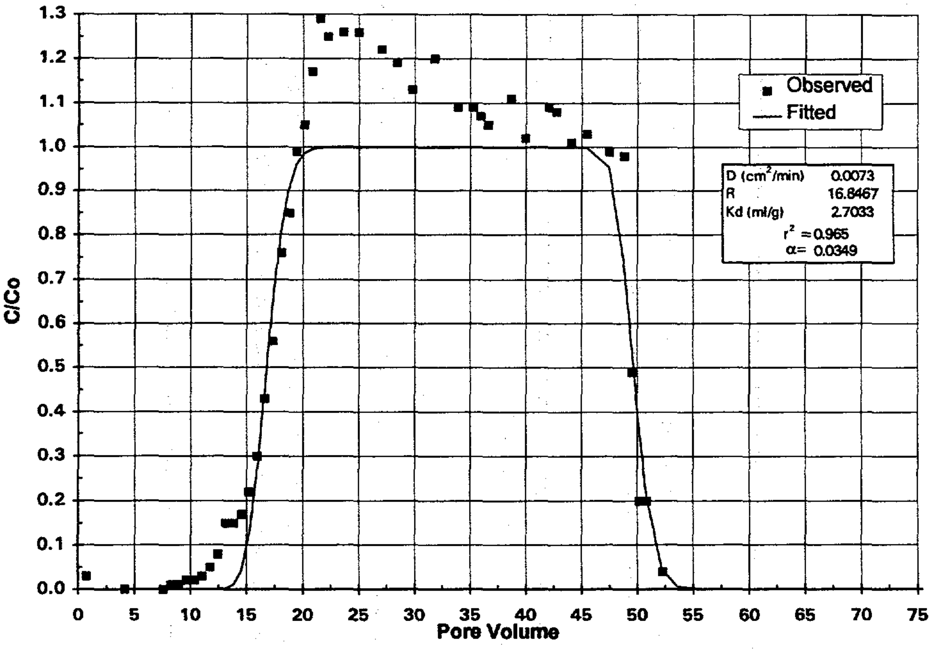

Figure E.3. Fitted Ni BTC using CXTFIT linear equilibrium model. The input parameters R, D, and the size of pulse were allowed to vary, while the average pore water velocity was held constant. Values for K_d and α were calculated from R and D, respectively.

et al., 1995) was also leached from the sand (approximately 3 μg), ~13% of the total input Ni was retained on the sand.

E.3.2. Slow Column

The BTC from the slow column is shown in Figure E.4, along with influent and effluent pH measurements. This BTC is noticeably different from the previous BTC in shape, retardation, and peak concentration. The BTC appears to have two peaks, the first at about $C/C_o = 0.3$, after which the Ni concentration climbs to a second peak of over $C/C_o = 0.7$. The first peak is unusual and may be caused by changing pH conditions in the column, changing flow conditions, or experimental error.

The slow Ni BTC was modeled by CXTFIT in two different ways. The first model used all the data points to estimate the transport parameters, while the second excluded those points which comprised the first peak. The input parameters

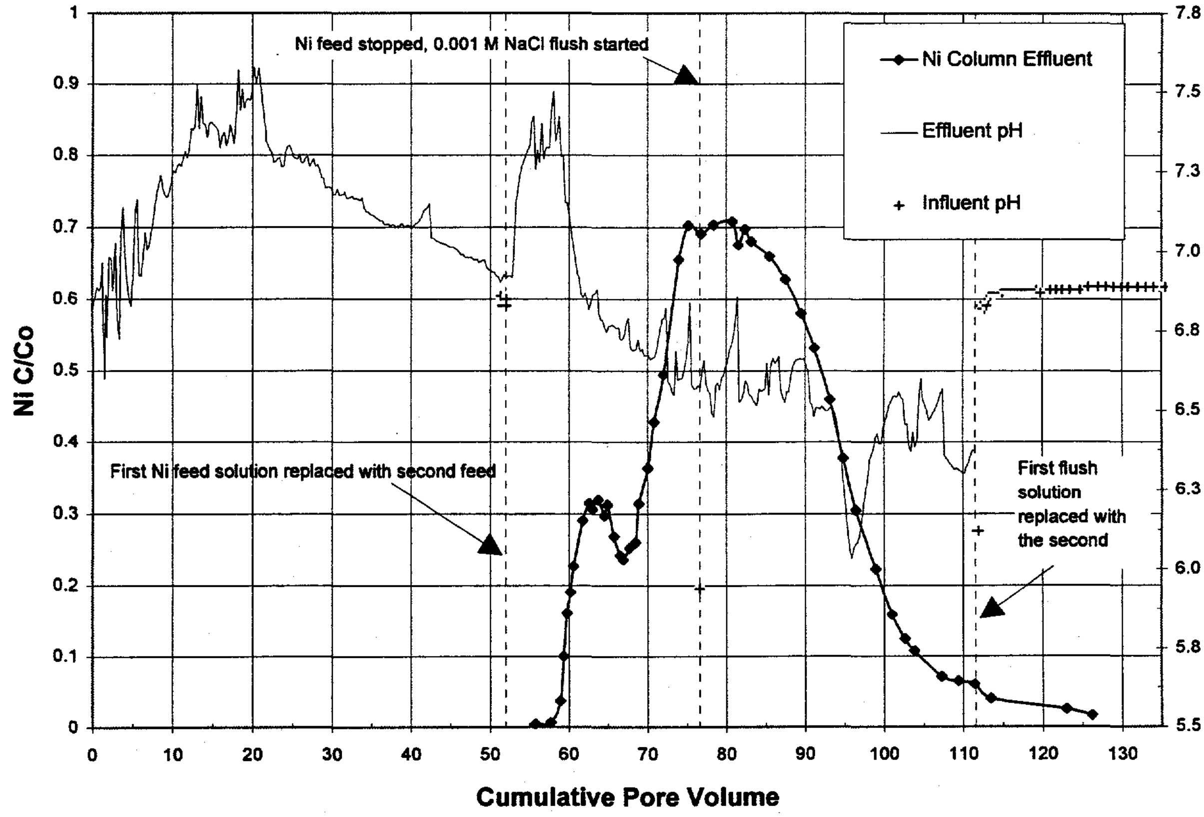

Figure E.4. Ni BTC for the slow column experiment. Average input Ni concentration of 201 ppb and a average pore water velocity of 0.04 cm/min. Effluent pH was measured with in-line (closed to the atmosphere) microelectrodes and influent pH was measured by a glass combination electrode with the feed solution open to the atmosphere.

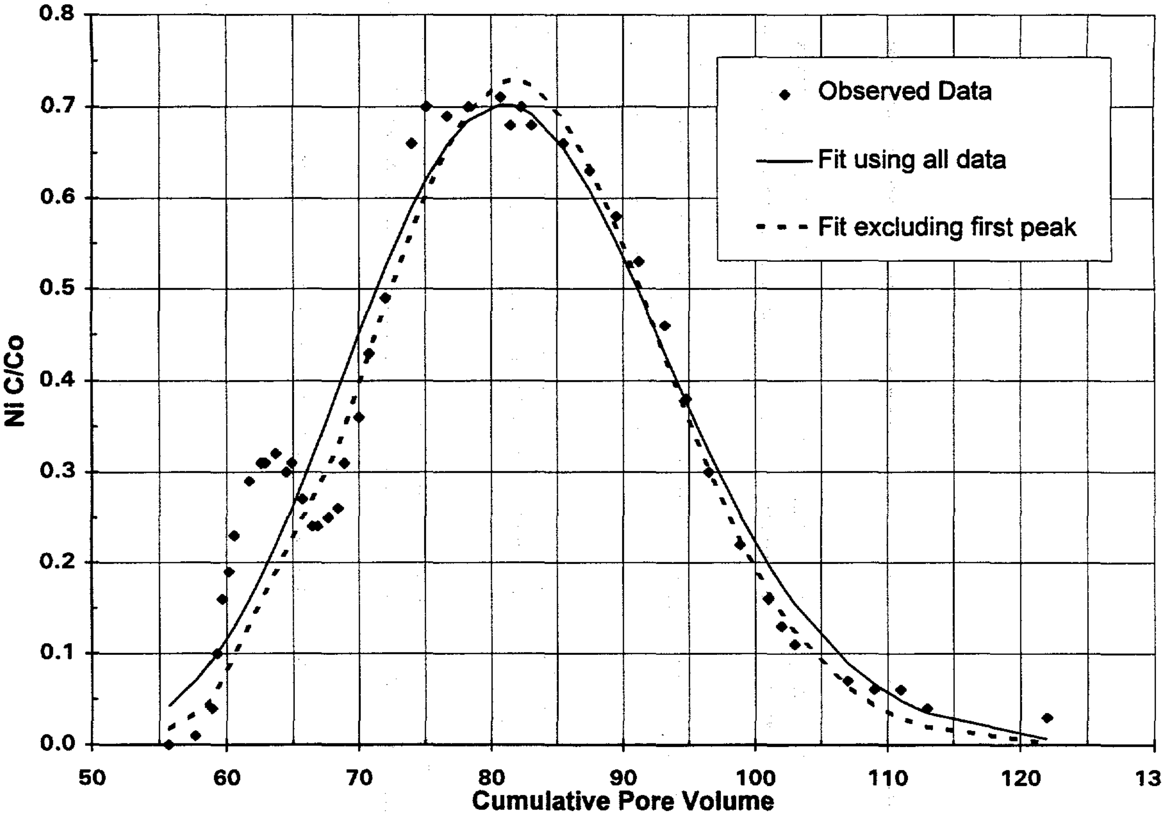

Figure E.5. Slow Ni column effluent data modeled by CXTFIT. The first curve was fitted to all the data while the other used only the data necessary to define the second peak.

R and D were allowed to vary for both models. The resulting curves are shown in Figure E.5, with the corresponding transport parameters presented in Table E.2. The slow BTC is also significantly more retarded than the fast one, with Ni first appearing in the effluent after about 57 pore volumes had been eluted.

A mass balance on the slow column showed that of the 264 μg of Ni contained in the input pulse, 192 μg was retained in the column, or about 73% of the total Ni in the input pulse. Subsequent leaching of the column with ~ 2% HNO_3 acid removed 92 μg of Ni. After correcting for the ~35 ng of exchangeable Ni per gram of sand (Bryan *et al.*, 1995) initially present on the sand, 41% of the total Ni was presumed to be irreversibly sorbed in the column.

Table E.2. Transport parameters obtained from CXTFIT for the curves shown in Figure E.5. Average pore water velocity = 0.04 cm/min.

	D (cm^2/min)	R	K_d (m*l*/g)	α (cm)	r^2
Curve fitted to all data	0.0043	71.9	12.1	0.102	0.925
Curve fitted to only second peak	0.003	73.0	12.3	0.076	0.981

E.4 Discussion

Nickel sorption onto Wedron sand is strongly dependent on solution pH. From previous Ni batch sorption studies (Bryan *et al.* 1995; Figure B.7 and Table B.7,), for a 200 ppb Ni solution, the K_ds ranged from 5 to 50 m*l*/g in the pH range 6.5 to 7.0. The pH-dependent Ni sorption edge flattened out above pH 7 with nearly all of the Ni sorbed from pH 7 to pH 9. In the pH range 6.5 to 7.0 the Ni sorption edge is very steep, so a slight change in pH will result in a large change in K_d. Calculated values of R, using K_ds from batch experiments, in this pH range are 31 to 251. This illustrates that an accurate column pH measurement is critical when trying to compare batch K_ds to the K_ds calculated from the retardation factor of the column Ni BTC.

The measured pH in the effluent fast column ranged from 6.2 to 6.8. At a column pH of ~6.5, the corresponding batch K_d is in the range of 2-5 m*l*/g, which compares well to the K_d of 3.2 m*l*/g calculated from the BTC of the column. However at pH~7 the batch K_d is an order of magnitude larger, which does not match the column K_d.

Although the slow column experiment provided continuous pH measurements of the effluent, determination of a corresponding batch K_d is difficult because of the apparent changing pH conditions within the column (see Figure E.4). At the start of the experiment, the effluent pH gradually rose to about 7.4, possibly due to carbonate dissolution from the sand, and then steadily dropped to about 6.9. After the Ni feed solution was changed the pH rose sharply back up to about 7.4. This was followed by a general decreasing trend to a pH of approximately 6.5.

The effect of changing column pH on retardation of the Ni pulse is unclear. A linear regression, shown in Figure E.6, was performed on the pH-K_d data from Bryan et al. (Table B.7, 1995, in Siegel et al., 1995) for the pH range 6.5 to 7.0. The upper value for K_d, at pH greater than 7.0, was limited to 50 m*l*/g, representing close to 100 % sorption. Values of K_d were then calculated for the effluent pH values measured in the slow column experiment. Next, retardation factors were

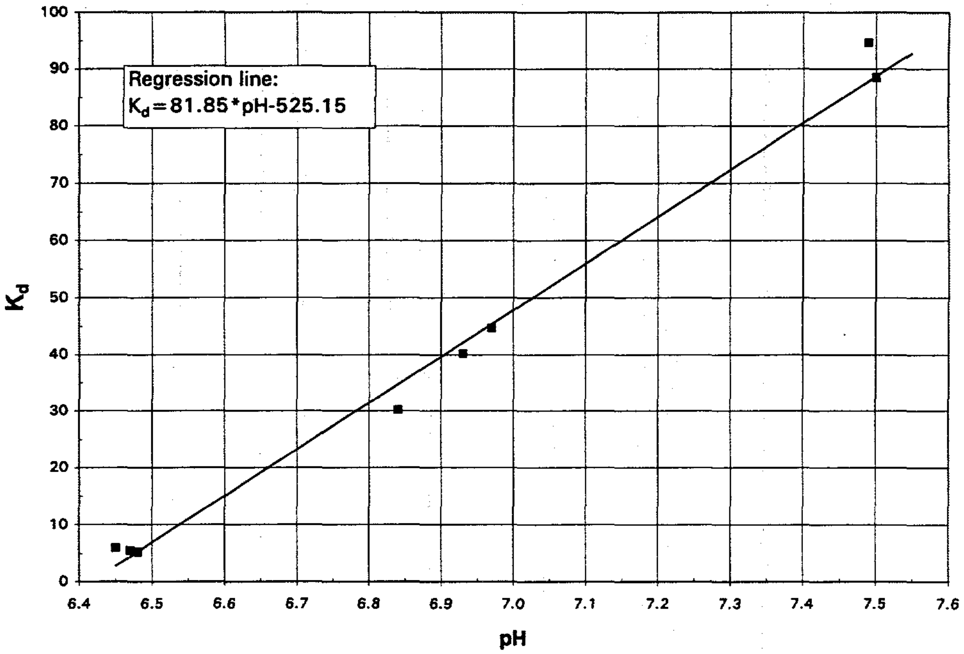

Figure E.6. Regression line calculated from pH-K_d data for Wedron sand obtained from Bryan *et al.*, 1995 (Table B.7).

calculated, using equation E-1, based on the calculated K_ds. Finally, values of % Ni adsorbed by the sand were calculated as 100 x (1 – 1/R). Figure E.7 shows the % Ni adsorbed plotted as a function of eluted pore volume.

The K_d, calculated from the retardation factor obtained from CXTFIT (Table E.2), for the slow column BTC is 14.2 m*l*/g, which corresponds to a calculated pH of about 6.59. This appears to be a reasonable value based on the range of pH conditions in the column. This K_d, however, is probably closer to an average K_d given the fluctuations in pH during the experiment.

If the pH of the column effluent is representative of conditions within the column, then it can be seen from Figure E.7 that there was close to 100 % sorption up to the initial breakthrough of Ni in the effluent. The leading edge of the BTC continued to rise until the Ni input was stopped and the 0.001 M NaCl flush started.

The cause of the unusual shapes of both Ni BTC's is unclear. The high peak concentration of the fast BTC may be due to desorption of the exchangeable Ni initially present in the column sand. A change from high to low pH in the column could have caused near total sorption of the input Ni followed by desorption of both added Ni, and the Ni initially present on the sand. The early peak of the slow column BTC could be the result of changing flow conditions within the column.

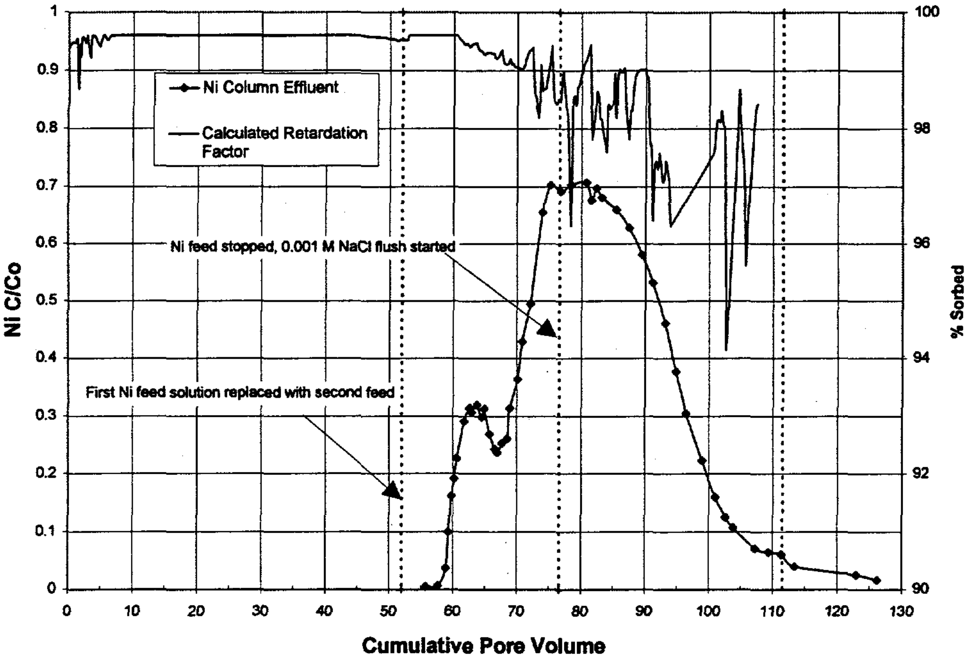

Figure E.7. Calculated retardation factors based on pH dependent K_d values from Bryan et al., 1995 (Table B.7). Equation E-1 was used to calculate a retardation factor based on a Kd value from Figure E.6.

However, due to the uniform size of the sand and the constant input flow rate, this would seem unlikely.

The analysis of Kuhn and Peters (1981) and Relyea (1982) can be applied to predict the apparent retardation, R_{ap}, of the Ni BTC's in a manner similar to that described for Li transport in Appendix D of this report. Because the retardation of Ni is strongly dependent on pH, the analysis was performed for pH's of 6.5 and 7. This is a realistic range for pH in the column, and brackets the range of possible retardation factors.

The parameter T is defined by equation E-3, and ranges from 0, for an infinitely slowly sorbing tracer, and 1, for a rapidly sorbing tracer, respectively.

$$T = \frac{R_{ap} - 1}{R_{eq} - 1} \qquad \text{(E-3)}$$

The number of mass transfer units is defined by:

$$n = \frac{\rho_b K_d L}{\eta V_w} k \qquad \text{(E-4)}$$

where

V_w = average pore water velocity (cm/min)
R_{ap} = apparent retardation factor of the experimental BTC
$R_{eq} = 1 + (\rho_b K_d / \eta)$, the equilibrium retardation factor
and all other variables are as defined previously.

Kinetic adsorption rate constants, k, for Ni at pH 6.4 and 7.7 were found to be 6.6×10^{-4} min^{-1} and 0.0106 min^{-1}, respectively (Appendix A, this report). For this analysis, it was assumed that the rate constant at pH 7.7 was representative of the rate constant at pH 7, and that the rate constant for pH 6.4 was close to that at pH 6.5. Figure E.8 was obtained using equation E-5 , values of n and R_{eq} calculated for values of pH of 6.4 and 7, and tabulated values of n and T from Relyea (1982). Details of the method of analysis are discussed in Appendix D of this report.

$$\frac{R_{ap}}{R_{eq}} = T + \frac{(1-T)}{R_{eq}} \tag{E-5}$$

Interpolation between points on Figure E.8 is required to obtain a corresponding R_{ap}/R_{eq} value when the number of mass transfer units is below 6. If the number of mass transfer units is above 6, the value of T, can be calculated directly from the following equation (Kuhn and Peters, 1981)

$$T = \left(\frac{1}{2} + \sqrt{\frac{1}{4} - \frac{3}{4n}} \right) \tag{E-6}$$

where

T = dimensionless time
n = number of mass transfer units

Table E.3 summarizes the results of the analysis of both column experiments at pH's of 6.5 and 7. The retardation factors obtained from the CXTFIT analysis for the fast and slow columns were 16.8 and 71.9 respectively. Both fall in the range of the calculated apparent retardation factor using this analysis.

Deviations from local adsorption equilibrium within the columns are affected by the fluid residence time and the relationships between pH and Ni adsorption equilibrium and pH and Ni adsorption kinetics. The uncertainties in the column pH prevent discrimination among these effects. Clearly, better control of pH during

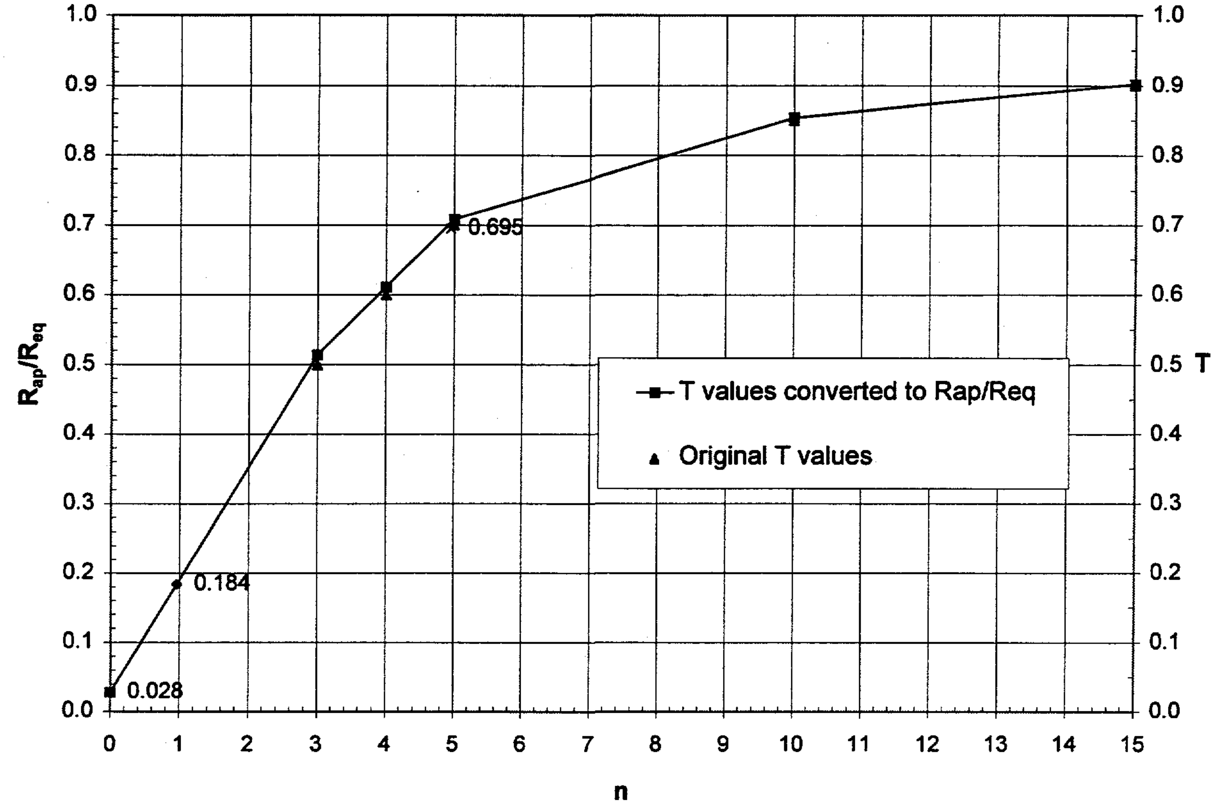

Figure E.8. Retardation factor ratio as a function of number of mass transfer units at pH=6.5. At T=0, n was assumed to be equal to 0 and $R_{ap}/R_{eq} = 1/R_{eq} = 1/36$. The value of R_{ap}/R_{eq} at n=0, and values of T for the fast and slow columns are labeled. The values of R_{ap}/R_{eq} are based on tabulated values of T from Relyea (1982).

Table E.3 Summary of analysis for both columns at pH 6.5 and pH 7

	Fast Column		**Slow Column**	
	pH=6.5	**pH=7**	**pH=6.5**	**pH=7**
k (min^{-1})	6.6×10^{-4}	0.0106	6.6×10^{-4}	0.0106
K_d (ml/g)	7	48	7	48
R_{eq}	36	240	36	240
n	0.962	106	4.95	636
T	0.161	0.986	0.695*	0.998
R_{ap}/R_{eq}	0.184	0.986	0.703	0.998
R_{ap}	6.61	236.6	25.31	239.5
R_{ap} (CXTFIT)	16.8		71.9	

the course of the experiment is needed before meaningful results can be obtained using this analysis.

E.5. Summary

Two saturated laboratory column experiments were conducted at Ni concentrations of about 200 ppb. One was run at a fast flow rate and the other at a slower flow rate. The retardation factors obtained by fitting the BTC's from the fast and slow columns with the CXTFIT code were 16.8 and 72, respectively. Both BTC's were unusually shaped, with the fast BTC displaying a relative peak concentration greater than one, while the BTC from the slower column contained a small initial peak before climbing to the maximum peak concentration.

Comparing the retardation factors obtained from batch adsorption data to those obtained from the BTC's from the columns is difficult because of the sensitivity of adsorption to pH. The pH of the second column effluent was monitored with in-line electrodes, and ranged from about 6.5 to over 7. Batch derived K_d values for this pH range vary from 7 to 48, equivalent to retardation factors of 36 to 240.

Because of this sensitivity to pH, future Ni column experiments should be run using a buffered input solution; as well as, flushing the column prior to introduction of the Ni pulse to remove any leachable carbonate and Ni initially present on the sand. In addition, monitoring of the pH within the columns should be carried out with techniques such as pH-sensitive fiber optic probes that do not require frequent calibration and do not drift appreciably during the course of the column experiments.

E.6 References Cited

Bryan, C.R, D.B. Ward, and M.D. Siegel. 1995: "Ni Sorption and Solubility" in *Characterization of Materials for a Reactive Transport Model Validation Experiment, Appendix C,* Siegel, M.D., D.B. Ward, C.R. Bryan, and W.C. Cheng, SAND94-0189, Sandia National Laboratories, Albuquerque, NM, 32 pp.

Kuhn, W.L., and R.D. Peters, 1981: "WRIT Leaching and Transport Modeling," *Waste/Rock Interactions Technology Program FY-80 Information Meeting*, J.F. Relyea Editor, PNL-3887, Pacific Northwest Laboratory, Richland, Wa., 268-276.

Parker, J.C., and M. T. van Genuchten, 1984: *Determining Transport Parameters from Laboratory and Field Tracer Experiments, Virginia Agricultural Experiment Station Bulletin 84-3*, ISSN 0096-6088, 92 pp.

Relyea, J.F., 1982: "Theoretical and Experimental Considerations for the Use of the Column Method for Determining Retardation Factors," *Radioactive Waste Management and the Nuclear Fuel Cycle*, **3**, 151-166.

Ward, D.B., C.R. Bryan, W.C. Cheng, and C.R. Boyle, 1995: "Experimental Procedures Used in the Characterization Study", in *Characterization of Materials for a Reactive Transport Model Validation Experiment, Appendix E,* M.D. Siegel, D.B. Ward, C.R. Bryan, and W.C. Cheng, SAND94-0189, Sandia National Laboratories, Albuquerque, New Mexico, 114 pp.

Appendix F.

Preliminary results of a 200 ppb Ni pulse through the Sandia/Los Alamos Wedron sand-filled caisson

Charles R. Bryan

Contents

F.1. Introduction

The Sandia/Los Alamos caisson is a 6 m high x 3 m wide culvert, filled with Wedron 510 sand. Details of caisson construction and design are found in Springer *et al.* (1993). The caisson sampling geometry and instrumentation are shown in Figure F.1.

There are 6 sampling levels in the caisson; each containing a centrally-located ceramic cup water sampler and three dialysis tubing (hollow fiber) samplers, spaced symmetrically, halfway between the center and the edge of the caisson. In addition, 4 TDR probes are spaced equally around the edges of each sampling level, and an access tube for a neutron probe extends across the width of the caisson from instrumentation access ports on the side of the caisson. Every other layer contains two thermocouples. Water passing through the caisson drains through a bottom plate covered with 256 ceramic cup samplers. Samples can be drawn from each sampler individually; each upper-layer sampler is equipped with an in-line meter for pH measurements.

During filling and saturation of the caisson, settling and packing of the sand caused several of the water samplers in the sampling layers and in the

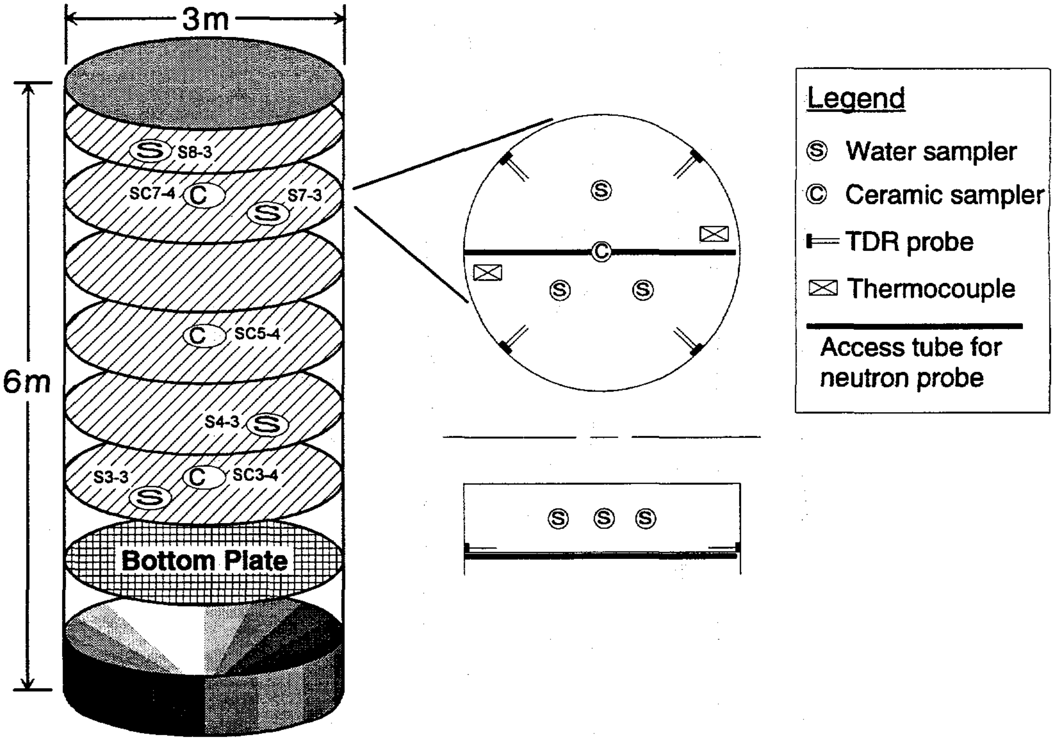

Figure F.1. Caisson geometry and instrumentation. Specifications called for 4 samplers per level, but many failed; working samplers are indicated in the diagram.

bottom plate to malfunction; the working samplers in each layer are illustrated in Figure F.1. About 40% of the samplers in the bottom plate failed as the four sections of the plate settled and shifted with respect to one another.

In addition, it was observed that the water was not distributed uniformly over the top of the sand. The distribution system consisted of a perforated sprinkler bar, rotating about a central shaft. A steady stream of water was observed running off of the shaft and dripping onto the sand, producing a hole 15-20 cm deep. The hose connections were tightened, and the leak reduced, but subsequent examinations revealed it to be a recurring problem. No attempt was made to quantify the volume of water leaking from the central shaft, but there can be little doubt that the center of the sand received a disproportionately large volume of the influent relative to the rest of the caisson.

F.2. Methods

Construction and filling of the caisson was finished in June, 1993. Saturation was commenced from the bottom up to remove air pockets, and a steady-state flow field was achieved by October, 1993. This was maintained until the end of the experiment, in August, 1994. The Darcy flux during this period was 5.78 cm/hr, or 1.39 m/day. Total porosity in the sand is about 0.3; moisture content varied from 0.15 to 0.25, increasing towards the bottom of the caisson. On April 14, 1994, a 10 ppm Li (as LiBr) pulse was added to the caisson; by April 21, effluent Li values had dropped to background levels.

On June 1, 1994, a continuous pulse of 200 ppb Ni in a background electrolyte of Los Alamos tap water was added to the caisson influent. This influent concentration was maintained until July 22 (51 days), and then Ni-free tap water was re-introduced. On August 2 (elapsed time, $t = 62$ days), a LiBr pulse was initiated; the concentration used was ~9 ppm Li (~100 ppm Br). The Li pulse ended August 4; flushing continued until August 18 ($t = 78$ days), at which time the experiment was terminated.

Water samples were collected daily from each working sampler in the 6 upper levels. In many cases, the flow rate into the sampler and sampling line was so slow that it was not possible to purge accumulated water from the line prior to sampling; the accumulated water therefore represents a 24 hour time-averaged sample. For high-flow samplers, both time-averaged and instantaneous samples were collected. For some extremely low-flow samplers, accumulated water was drawn from the sampling line on a weekly basis; these samples proved to be of little use, as transport conditions within the caisson changed much more rapidly than expected.

Two samples of the influent were collected daily, by placing empty sample bottles beneath the rotating sprinkler head which dispersed the water over the surface of the sand. Eight bottom samples, two from each quadrant of the bottom plate, and one composite bottom sample, were collected daily.

The bottom samples were collected with a 40 ml syringe, which generated suction to draw the water from the sample lines. The pH of each bottom sample and each composite sample was measured immediately after collection. It is probable that both types of samples underwent considerable degassing of CO2 prior to pH measurement; the bottom samples would have been degassed rapidly by the suction of the syringe, and there was considerable headspace in the manifold and the drain hose from which the composite samples were collected. Only one of the upper level samplers (S8-3) was flowing freely enough to collect a water sample without pumping, which would cause degassing and CO2-loss; in-line pH measurements were taken twice daily during water sample collection from this sampler. The pH meters were calibrated on a daily basis, and readings on two buffers, pH 7 and 9.3, were recorded before and after sampling to monitor drift. Drift was commonly towards higher pH, and was always less than 0.10 pH units (generally less than 0.05 units).

On August 2, at the start of the Li pulse, the number of bottom cups sampled was increased to 50, and samples were taken several times a day. After August 5, they were only sampled once daily. The total number of samples collected was ~2700; about half of which were taken during and after the Li pulse. Of these, 384 samples have been analyzed for Ni.

F.3. Results and Discussion

F.3.1. pH in the Caisson

Over the course of the Ni pulse, the pH was measured on 609 water samples. Most of these were taken from ceramic samplers on the bottom plate; others were composite samples from the open-ended drain hose through which all water collected by the bottom samplers exits the caisson. The pH of both types of samples was measured immediately after collection.

Interpretation of the pH values obtained in this manner is difficult; degassing of CO_2 occurs very rapidly from the water samples. The pH of samples collected during a test run prior to the Ni pulse rose from ~7 to ~8 within seconds of being exposed to ambient atmosphere (Table F.1). An influent water sample collected under the sprinkler at the top of the caisson, and tap water from a nearby laboratory building, exhibited similar behavior. This suggests that the influent did not lose CO_2 as it was aerated by the sprinkler, and did not degas as it flowed through the unsaturated sand column in the caisson. The probable reason for this is that the headspace of the caisson was enclosed — it was covered with wooden boards and a plastic tarp to exclude rainwater. Given the high influent flow rate (1.8 gal/minute), the air in the headspace probably equilibrated rapidly with the water with respect to CO_2, and degassing stopped.

In addition to the measurements on bottom and composite samples, in-line pH measurements were taken twice daily from a free-flowing hollow fiber sampler (S8-3).

The results of the pH measurements are shown in Figure F.2. The reported pH of the bottom samples showed little variation over the life of the pulse, clustering between 8.0 and 8.4 for most of the run, and dropping to about 8.0 in the last two weeks. It should be remembered, however, that these samples probably degassed CO2 prior to measurement of the pH. The measured pH values from the free-flowing sampler, which presumably reflect

Table F.1. Effect of degassing of CO_2 on measured pH.*

Sampler #	Measured in-line pH	pH after exposure to air
S4-2	6.93	8.15
S4-2	~7.0	8.10
S5-1	7.00 — 6.75**	8.23
SC7-4	7.90 — 7.40**	8.16
SC3-4	7.45 — 6.38**	8.16
S6-1	7.17	8.42
Surface sample (influent)	7.10	8.04
Tap water (nearby bldg)	~7	8.05

* measurements were taken prior to introduction of Li or Ni pulses

** pH drifted downward during sample collection

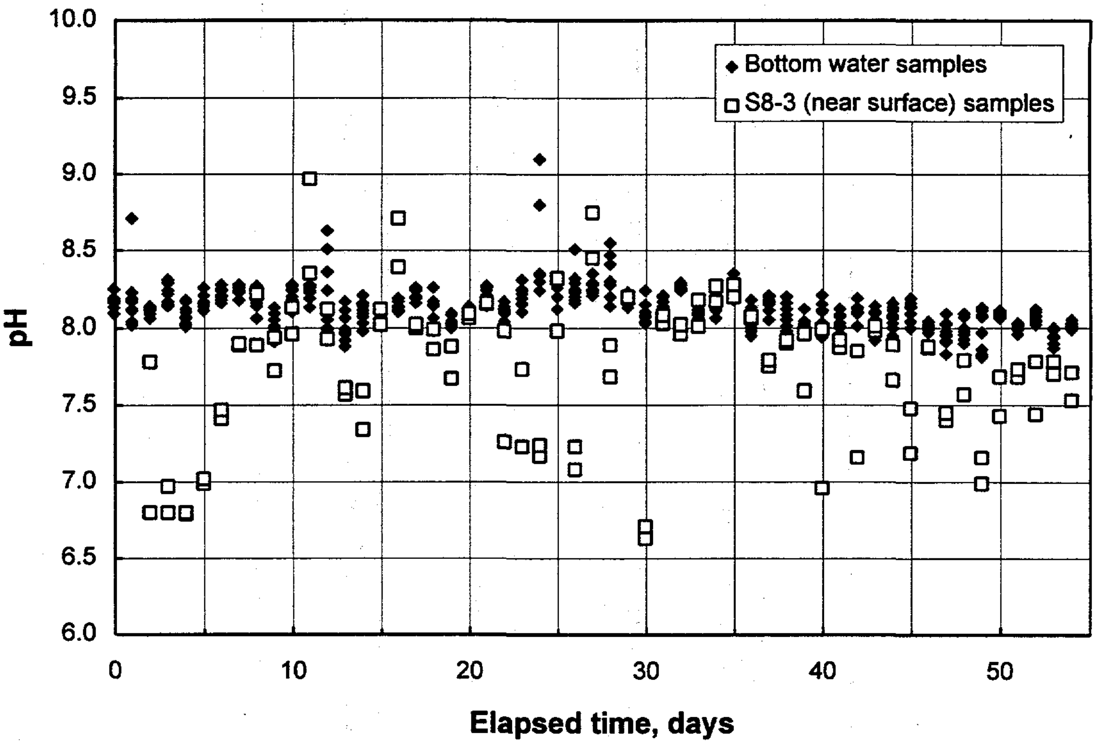

Figure F.2. Measured pH values for caisson bottom and composite bottom water samples, and sampler from a near-surface free-flowing sampler (S8-3).

less degassing, are lower than those from the bottom samplers. There is considerably more scatter, probably reflecting variable amounts of degassing from these samples.

It is difficult to obtain meaningful information about the pH within the caisson from these data. It was almost certainly lower than that indicated by the degassed bottom water samples; the free-flowing sampler measurements suggest that it may have been 7 or less. This is consistent with results from the caisson influent and local tap water, both of which were near pH = 7 prior to equilibrating with the atmosphere. If it is assumed that CO2-loss by the bottom samples was consistent over the course of the experiment, then the lack of variation in these samples suggests that the pH in the caisson (or perhaps the pH profile in the caisson) changed little during the experiment.

F.3.2. Ni breakthrough

The results of the 384 Ni analyses are summarized in Table F.2. The surface water (influent) and composite bottom water breakthrough curve for

Table F.2. Summary of Ni analyses of caisson water samples.

Date	Days Elapsed	Ni concentration, ppb								
		Surf. 1	SC7-4	S7-3	SC5-4	S4-3	SC3-4	Comp. Bottom	C-26	D-58 **D-57**
5/31/94	-1		1.35	2.03				1.21		
6/1/94	0	1.14	2.10	1.31	2.73	2.44	1.84	2.07	1.33	1.46
6/2/94	1	162.38	64.49	33.33	23.36				3.61	0.92
6/3/94	2	209.62	169.77	111.55	56.95	2.90	2.10	1.31	0.87	
6/4/94	3	174.60	166.51	145.89	89.26		115.82	1.18	1.76	2.17
6/5/94	4	183.67	167.69	144.21	111.29	10.56	122.67	1.36	1.00	1.36
6/6/94	5		164.44	159.12	129.25			1.46	0.59	1.10
6/7/94	6		158.84	129.53	114.44	40.29	127.94	2.90	1.70	1.11
6/8/94	7		156.54	154.69	130.20			4.51	0.89	1.17
6/9/94	8	173.59	163.52	148.42	145.60	93.82	136.37	9.49	8.52	1.01
6/10/94	9	180.34	157.41	154.24	141.98		145.02	18.72	17.48	0.98
6/11/94	10		181.87	171.14	147.88	94.93	138.39	33.94	25.29	1.41
6/12/94	11							49.17	30.06	1.18
6/13/94	12	174.44	181.87	169.07	140.75	111.06	158.80	64.97		
6/14/94	13							72.21	35.79	1.62
6/15/94	14	200.83	186.08	157.98	149.95	124.72	150.02	81.20	38.02	2.17
6/16/94	15							85.99	42.17	2.47
6/17/94	16	187.25	163.74	126.94	137.88	114.16		89.89		4.80
6/18/94	17							89.92	57.04	19.52
6/19/94	18		183.74	145.35	135.88	104.05		91.63		
6/20/94	19	207.79	190.31		162.20		133.44	99.62	65.99	29.68
6/21/94	20	188.04	184.79	148.65	150.97	100.71		88.73		
6/22/94	21								73.12	42.01
6/23/94	22				138.92	124.99		90.23		
6/24/94	23		181.44	162.22					76.94	48.46
6/25/94	24	198.39	188.42		159.76	113.93	158.52	94.38		
6/26/94	25								82.53	56.45
6/27/94	26		174.61	136.77	152.72	107.57		94.98		
6/29/94	28	199.81			163.21	89.62		84.89	83.86	62.86
6/30/94	29	198.42	180.66	160.60	181.85		179.08	93.71		
7/1/94	30				170.74	127.73		91.90		
7/2/94	31								85.43	67.63
7/3/94	32	175.16	166.63	160.04	151.22			101.02		
7/4/94	33					124.02				
7/5/94	34	199.27	191.62		161.15		154.36	99.84	92.50	69.33
7/6/94	35		185.74	154.91						
7/7/94	36	179.76			175.00	116.48		99.20		
7/8/94	37								97.86	73.70
7/9/94	38	163.70	121.43	163.20	158.17			104.87		
7/10/94	39	209.09	180.23		161.34		156.33	112.33		
7/11/94	40	175.31	180.00	154.59	148.68	123.49	133.62	112.00	102.88	79.45
7/13/94	42							108.03		
7/14/94	43					113.13				
7/15/94	44	205.19	154.87		150.61			103.11	102.91	83.65
7/17/94	46					100.28		102.17		
7/19/94	48	190.44						105.89		
7/20/94	49		175.63		147.23	108.61			85.93	78.93
7/21/94	50							108.72		
7/22/94	51	192.39	181.03	133.83	141.43	107.08		102.72		
7/23/94	52	9.95	100.44	144.58	144.24	114.76	203.51	103.46	93.23	82.73
7/24/94	53	1.45	26.96	133.98	114.99	121.76		96.40		
7/25/94	54		15.86	143.14	96.59	119.45			97.88	85.21
7/26/94	55		14.97		77.29			99.15	102.64	**91.30**
7/27/94	56		10.82		54.37			102.62	98.12	**87.73**
7/28/94	57		7.14		36.82				102.12	**87.76**
7/29/94	58		5.73		28.12			97.78	101.35	**84.27**
7/30/94	59		5.43		29.33			72.64	93.89	**84.01**
7/31/94	60		6.15		22.85			65.78	88.42	**82.76**
8/1/94	61		8.99		22.30					
8/2/94	62	0.66	3.72	15.13	13.49	25.97		52.10	68.39	**56.61**
8/4/94	64		2.80	10.47	9.85	26.13		54.09	53.36	**65.05**
8/5/94	65	1.21								
8/6/94	66		2.88	7.63	6.83	18.97		35.33	44.61	**51.90**
8/7/94	67							35.36	44.12	
8/8/94	68		2.11	6.71	6.42	13.11				**53.78**
8/10/94	70		3.04	6.34	7.91	14.95		46.44	34.05	**48.21**
8/12/94	72		3.23	16.64	7.10	20.82		26.05	30.59	**43.01**
8/14/94	74		2.66	4.90	6.89	11.94		31.68	27.54	**35.35**
8/16/94	76		2.69	4.44	6.18	9.80		23.40	24.70	**33.75**
8/18/94	78		2.67	4.92	6.74	10.79		31.54	22.45	**28.77**

the Ni pulse are shown in Figure F.3. Also shown are breakthrough curves for 3 individual samplers; C-26 and D-58 are samplers in the bottom plate, located about 50 cm from the center of the plate, and near the edge of the plate, respectively, and SC3-4 is the centrally located (ceramic) sampler in the lowermost sampling level, about 1 m above the bottom plate.

Ni breakthrough (the first appearance of elevated Ni in the collected samples) occurred at different times for each of the three water samplers. Ni showed up at SC3-4, along the central axis of the caisson, in 4 days, and at sampler C-26, 50 cm from the central axis, in 8 days. Breakthrough occurred at D-58, along the edge of the caisson, 8 days after that. After the pulse was terminated, the Ni concentration at C-26 dropped more rapidly than at D-58. It is apparent that flow was channeling through the center of the caisson.

Ni breakthrough occurred at SC3-4, ~4 meters down, in 4 days, but did not appear in the composite water samples, from the bottom plate 1 m below, for an additional 4 days. There are two probable causes for this delay. First, the moisture content (θ) increases from ~0.15 above sampling layer 3 to > 0.25 below it, resulting in a reduction in water velocity, and in Ni transport velocity,

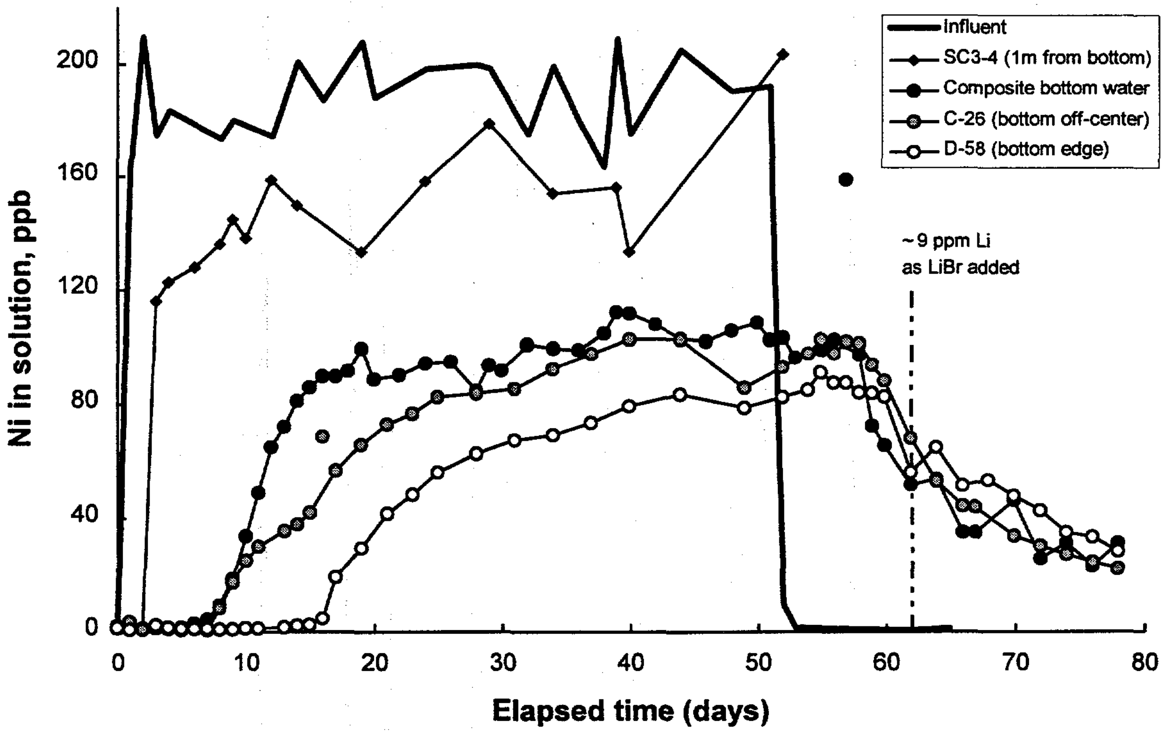

Figure F.3. Breakthrough curves for bottom and near-bottom samplers in the caisson. Two anomalous points (one composite bottom water, one C-26) are shown, but not included in the profiles.

below the layer. Second, the composite bottom water does not represent average effluent from the caisson; instead, it represents some average of the water collected by the *working* samplers in the bottom plate, weighted by flow rate for each sampler. Most of the samplers in the center of the bottom plate are disabled; subsidence of the sand in the center of the caisson may have caused the four quadrants making up the bottom plate to sag in the middle, damaging the ceramic samplers in this area. Thus, Ni contained in water channeling through the center of the caisson will not show up in composite water samples until the width of the central channel grows beyond the area of damaged samplers.

The breakthrough curves for several other samplers are shown in Figure F.4. Examination of these curves confirms that channeling is occurring; breakthough is a function not only of depth, but also of location in the caisson. Breakthough occurs more rapidly and Ni concentration tails off more rapidly at sampler SC7-4, in the center of the caisson, than at sampler S7-3, at the same depth but halfway between the center and the outer edge.

Several of the Ni breakthrough curves in Figures F.3 and F.4 have a steep leading edge, but flatten and level off well below the influent Ni concentration;

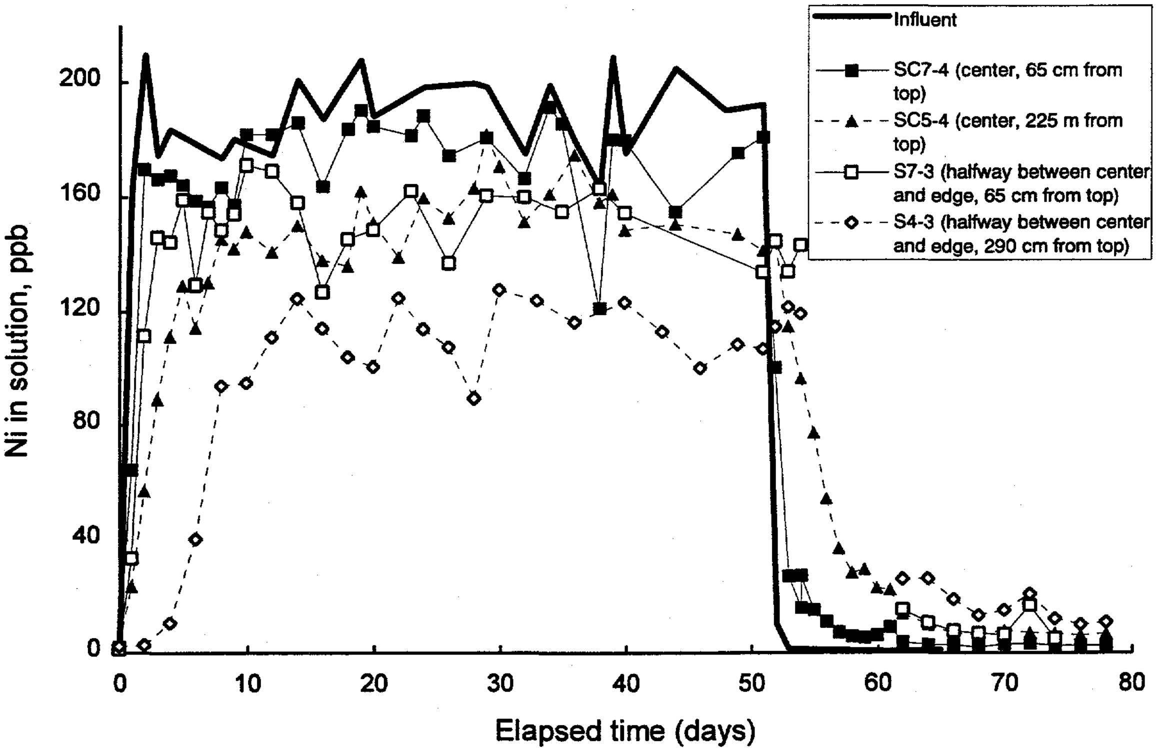

Figure F.4. Breakthrough curves for higher level samplers in the caisson.

this is most pronounced for the bottom samplers and for sampler S4-3. Steady-state or near-steady-state conditions are reached, but, as Ni concentrations are well below influent concentrations, equilibrium conditions with respect to adsorption have not been achieved. For the bottom samplers, this pattern is probably caused by mixing between Ni-rich waters, permeating outward from the more saturated central channel, and slower moving Ni-poor waters percolating downward from the top of the caisson. The increase in water saturation at the bottom of the caisson suggests that ponding and lateral movement of water may have occurred. Mixing may also be the cause of the leveling off below influent concentrations in higher-level samplers.

Alternatively, this pattern might be caused kinetic effects on adsorption. The adsorption kinetics studies described in Appendix B of this report suggest that Ni adsorption is occurring onto two different sites in the sand, with very different reaction rates. In Siegel *et al.* (1995) and in Appendix A of this report, it is shown that goethite is the dominant substrate to which Ni adsorbs in Wedron sand; and it is suggested that adsorption occurs onto two sites in the goethite, a high-energy site comprising about 4% of the total, and a less-favored low-energy site comprising the remainder. If it is assumed that the high-energy site adsorbs very rapidly, and the low-energy site slowly, relative to the electrolyte residence time in the sand, then the timing of initial breakthough will be a function of saturation of the high-energy site. Behind the Ni front, however, the concentration in solution is determined by adsorption onto the low-energy site, which, assuming slow adsorption kinetics, is a function of how long a particular "packet" of water has been in contact with the sand; this in turn is a function of the depth of the sampler and the velocity of the water at that sampler. The Ni concentration will only rise to that of the influent when all of the low-energy sites are also filled.

The Ni velocity and dispersion are listed in Table F.3 for each sampler. Also included is the retardation, calculated relative to the travel time for the conservative tracer Br^-, as determined in the LiBr pulse initiated on day 62 of the experiment. The Br^- data are included for reference.

In Figure F.5, Ni concentration profiles through the caisson are shown as a function of time. Only influent water and samples from the working centrally-located ceramic samplers were used, so these profiles represent the Ni distribution in the high-flow, channelized central axis of the caisson. The profiles can be grouped into four categories; those time slices during which the Ni concentration along the profile is increasing (Figure F.5a); those in which a steady state has been reached (Figure F.5b); those immediately after the Ni pulse was terminated, which show a decrease in the Ni concentration along the

Table F.3 Transport parameters for Ni and Br pulses at individual samplers.

Sampler #	Depth	Velocity (cm/day)	Dispersion (cm^2/day)	Retardation (rel. to Br^-)
Ni transport parameters				
SC7-4	65	93.6	79400	11.2
S7-3	65	17.5	2660	12.2
SC5-4	225	58.4	16000	19.6
S4-3	290	36.7	4600	14.1
SC3-4	387	168.5	6150	*
C-26	487	30.9	1670	*
D-58/D-57	487	23.7	347	*
Composite	487	36.1	3530	13.5
Br transport parameters				
SC7-4	65	1051	370100	-
S7-3	65	214	5472	-
SC5-4	225	1135	109800	-
S4-3	290	523	21130	-
Composite	487	486	8848	-

* Br^- data were not collected

profile with time (Figure F.5c); and those long after the end of the pulse, when a new steady state has been reached (Figure F.5d).

Perhaps the most important feature of the breakthrough curves and the Ni concentration profiles is that breakthrough occurred more rapidly than predicted by laboratory batch adsorption experiments (Siegel *et al.*, 1995). Rather than taking months to break through, Ni showed up in the caisson effluent within days. One reason for this is channeling through the center of the caisson, allowing the Ni to bypass most of the sand, and effectively producing a smaller diameter column with a greatly increased flow rate.

The rapidity of breakthrough might also indicate adsorption reaction rates are slower than expected from batch studies. Batch Ni adsorption experiments described in Siegel *et al.* (1995) and in Appendix B of this paper indicate that both the rate and the degree of Ni adsorption are very pH-sensitive. Adsorption is very rapid and is nearly complete (at these concentrations) above a pH of 7; at lower pH, however, adsorption is orders of magnitude slower, and less complete. As the pH conditions in the caisson are poorly constrained, the importance of kinetic effects is difficult to assess. Even considering the contribution of flow-channeling, it seems unlikely that breakthrough could

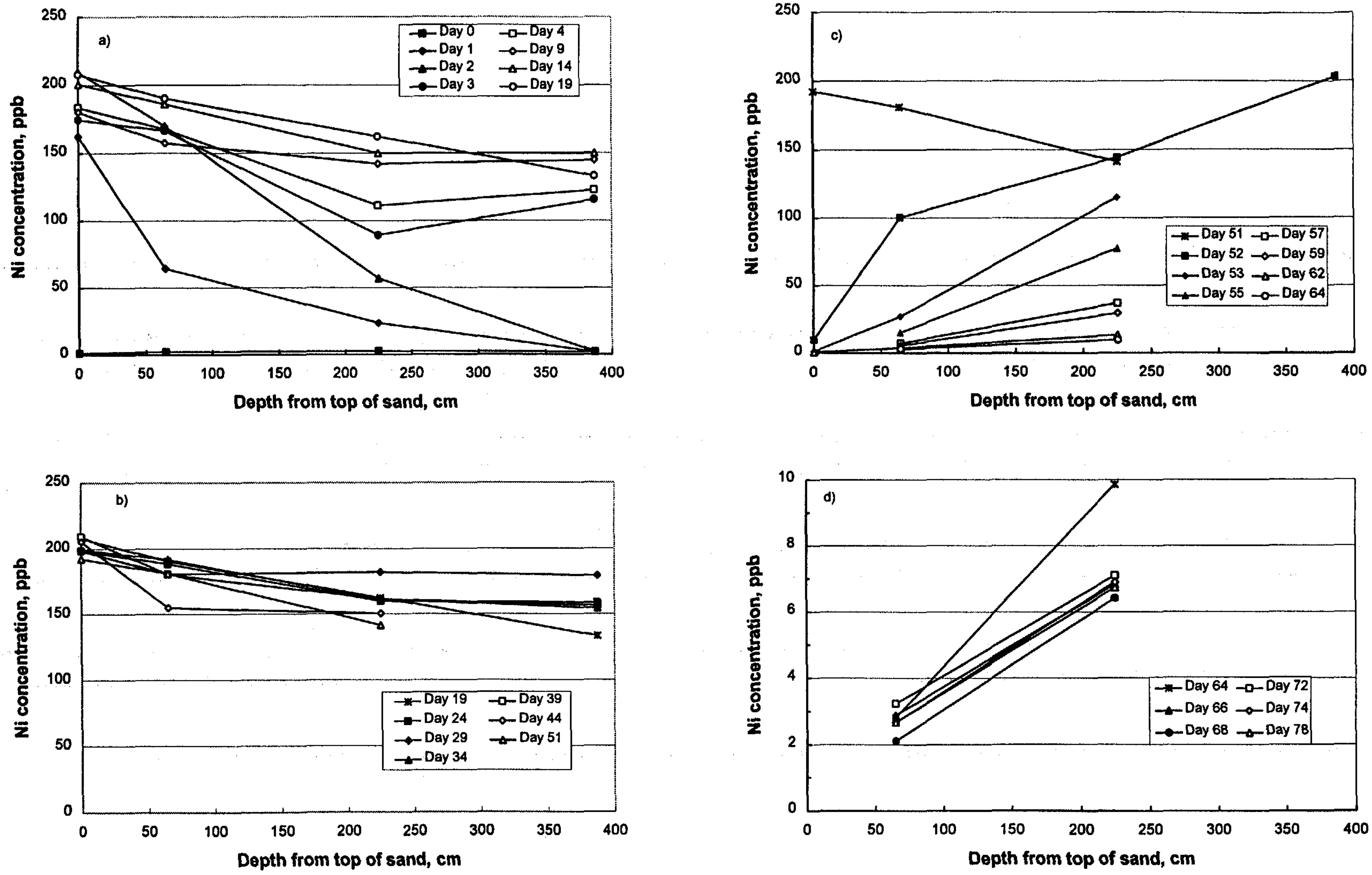

Figure F.5. Change in Ni concentration profiles along the axis of the caisson with time. a) Early profiles – the Ni concentration at any depth increases from day to day; b) Steady state profiles – the Ni concentration at any given depth does not change with time; c) Profiles just after terminating the pulse – the Ni concentration decreases rapidly; d) Profiles long after the end of the pulse – steady state is once again achieved.

have occurred so rapidly if the pH of the water in the caisson was significantly greater than 7.

A schematic cross-section of the possible hydrologic and chemical conditions in the caisson is given in Figure F.6. The contours for Ni concentration are estimated from data collected on 7/11/94, almost 6 weeks after the start of the pulse. The directions of the fluid flow lines are speculative, but there is ample evidence from the tracer study for channeling towards the center of the caisson. TDR data collected during the last few weeks of the experiment indicate that the edges of the caisson were drying out, also suggesting that flow towards the center of the caisson was occurring (E. Springer, pers. comm.).

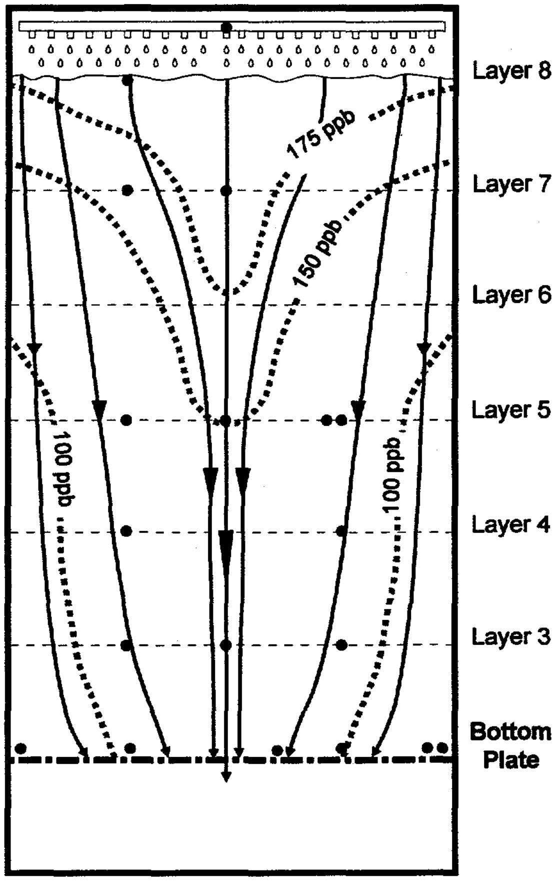

Figure F.6. Schematic cross section of the caisson six weeks (7/11/94) into the experiment. The dashed lines are contours of Ni concentration in solution; the arrows are proposed fluid flow directions. Filled symbols are locations of contoured samples. Radial symmetry is assumed.

F.4. Summary

The usefulness of the results of the 200 ppb Ni pulse through the Sandia/Los Alamos caisson was greatly compromised by the failure of most of the water samplers. The low flow rate of the remaining samplers made pumping necessary, causing degassing of CO_2 from the collected samples, and making in-line pH measurement impossible. The resulting pH data are difficult to interpret. The pH data from the degassed bottom water samples suggests that the pH in the caisson remained relatively constant over the duration of the pulse; however, the actual pH value is not well constrained. In-line pH measurements from the free-flowing sampler indicate that it could have been as low as ~6.7. The difficulties in interpreting the pH data from the caisson emphasize the need for *in-situ* pH probes when running unsaturated column experiments.

The geochemical data strongly indicate that fluid flow within the caisson was channeled in the center. Elevated Ni concentrations appeared earlier in samplers located near the center of the caisson, and, on any given day, center samplers in each layer yielded higher Ni concentration than edge samplers. The reason for the development of a more saturated flow channel through the center of the caisson is not known; it may have been caused by the observed non-uniform distribution of fluid from the sprinkler system due to leakage from the central coupling, or by subsidence of the sand in the center of the caisson associated with shifting and settling of the four quadrants of the bottom plate. The disruption of the bottom plate is inferred from the unexpectedly large volume of sand which washed out of the caisson during and immediately after the initial filling of the caisson, and from the failure of about 1/2 of the attached samplers.

The heterogeneities produced by flow channeling in the center of the caisson make detailed 3-dimensional modeling of the chemical and hydrologic conditions in the caisson virtually impossible, especially considering the paucity of working water samplers.

Ni breakthrough occurred much more rapidly than laboratory batch adsorption experiments had suggested. Flow channeling, allowing the Ni to bypass most of the sand, was probably a major reason for this; however given the poor constraints on the pH conditions in the caisson, the possible effect of adsorption kinetics cannot be ignored. Ni adsorption by Wedron sand is extremely pH-sensitive; both the rate of adsorption (Appendix B, this report) and the amount of adsorption (Siegel et al., 1995, and Appendix A, this report) increase rapidly between pH 6 and 7. The predicted rate of Ni transport was based on the assumption that the pH in the caisson was between 7.2 and 7.8; if it was significantly less than this, a possibility that cannot be ruled out with the available data, then Ni transport through the caisson would be much more rapid than anticipated.

F.5. References

Siegel, M.D., D.B. Ward, C.R. Bryan, and W.C. Cheng, 1995: *Characterization of Materials for a Reactive Transport Model Validation Experiment, SAND94-0189*, Sandia National Laboratories, Albuquerque, NM, 277 pp.

Springer, E.P, M.D. Siegel, P.L. Hopkins, and R.J. Glass, 1993: "Testing Models of Flow and Transport in Unsaturated Porous Media, " in *Proceedings of the Fourth Annual International Conference on High Level Radioactive Waste Management*, 1, Las Vegas, April 26-30, 336-347.

YUCCA MOUNTAIN SITE CHARACTERIZATION PROJECT

UC814 - DISTRIBUTION LIST

1 D. A. Dreyfus (RW-1)
Director
OCRWM
US Department of Energy
1000 Independence Avenue SW
Washington, DC 20585

1 L. H. Barrett (RW-2)
Acting Deputy Director
OCRWM
US Department of Energy
1000 Independence Avenue SW
Washington, DC 20585

1 S. Rousso (RW-40)
Office of Storage and Transportation
OCRWM
US Department of Energy
1000 Independence Avenue SW
Washington, DC 20585

1 R. A. Milner (RW-30)
Office of Program Management
and Integration
OCRWM
US Department of Energy
1000 Independence Avenue SW
Washington, DC 20585

1 D. R. Elle, Director
Environmental Protection Division
DOE Nevada Field Office
US Department of Energy
P.O. Box 98518
Las Vegas, NV 89193-8518

1 T. Wood (RW-14)
Contract Management Division
OCRWM
US Department of Energy
1000 Independence Avenue SW
Washington, DC 20585

4 Victoria F. Reich, Librarian
Nuclear Waste Technical Review Board
1100 Wilson Blvd., Suite 910
Arlington, VA 22209

5 Wesley Barnes, Project Manager
Yucca Mountain Site Characterization
Office
US Department of Energy
P.O. Box 98608--MS 523
Las Vegas, NV 89193-8608

1 Director
Office of Public Affairs
DOE Nevada Operations Office
US Department of Energy
P.O. Box 98518
Las Vegas, NV 89193-8518

8 Technical Information Officer
DOE Nevada Operations Office
US Department of Energy
P.O. Box 98518
Las Vegas, NV 89193-8518

1 P. K. Fitzsimmons, Technical Advisor
Office of Assistant Manager for
Environmental Safety and Health
DOE Nevada Operations Office
US Department of Energy
P.O. Box 98518
Las Vegas, NV 89193-8518

1 J. A. Blink
Deputy Project Leader
Lawrence Livermore National Laboratory
101 Convention Center Drive
Suite 820, MS 527
Las Vegas, NV 89109

2 J. A. Canepa
Technical Project Officer - YMP
N-5, Mail Stop J521
Los Alamos National Laboratory
P.O. Box 1663
Los Alamos, NM 87545

1 Repository Licensing & Quality
Assurance
Project Directorate
Division of Waste Management
US NRC
Washington, DC 20555

1 Senior Project Manager for Yucca
Mountain
Repository Project Branch
Division of Waste Management
US NRC
Washington, DC 20555

1 NRC Document Control Desk
Division of Waste Management
US NRC
Washington, DC 20555

1 Chad Glenn
NRC Site Representative
301 E Stewart Avenue, Room 203
Las Vegas, NV 89101

1 E. P. Binnall
Field Systems Group Leader
Building 50B/4235
Lawrence Berkeley Laboratory
Berkeley, CA 94720

1 Center for Nuclear Waste
Regulatory Analyses
6220 Culebra Road
Drawer 28510
San Antonio, TX 78284

2 W. L. Clarke
Technical Project Officer - YMP
Attn: YMP/LRC
Lawrence Livermore National Laboratory
P.O. Box 5514
Livermore, CA 94551

1 V. R. Schneider
Asst. Chief Hydrologist -- MS 414
Office of Program Coordination
and Technical Support
US Geological Survey
12201 Sunrise Valley Drive
Reston, VA 22092

1 J. S. Stuckless, Chief
Geologic Studies Program
MS 425
Yucca Mountain Project Branch
US Geological Survey
P.O. Box 25046
Denver, CO 80225

1 N. Z. Elkins
Deputy Technical Project Officer
Los Alamos National Laboratory
Mail Stop 527
101 Convention Center Drive, #820
Las Vegas, NV 89109

2 Michaele C. Brady
Technical Project Officer - YMP
Sandia National Laboratories
Organization 6302, MS 1399
101 Convention Center Drive, Suite 880
Las Vegas, NV 89109

1 Ray Wallace
US Geological Survey
106 National Center
12201 Sunrise Valley Drive

1 L. R. Hayes
Technical Project Officer
Yucca Mountain Project Branch
MS 425
US Geological Survey
P.O. Box 25046
Denver, CO 80225

1 A. L. Flint
US Geological Survey
MS 721
P.O. Box 327
Mercury, NV 89023

1 R. E. Lewis
Yucca Mountain Project Branch
MS 425
US Geological Survey
P.O. Box 25046
Denver, CO 80225

1 D. Zesiger
US Geological Survey
101 Convention Center Drive
Suite 860, MS 509
Las Vegas, NV 89109

2 L. D. Foust
Nevada Site Manager
TRW Environmental Safety Systems
101 Convention Center Drive
Suite P-110, MS 423
Las Vegas, NV 89109

1 C. E. Ezra
YMP Support Office Manager
EG&G Energy Measurements Inc.
MS V-02
P.O. Box 1912
Las Vegas, NV 89125

1 E. L. Snow, Program Manager
Roy F. Weston, Inc.
955 L'Enfant Plaza SW
Washington, DC 20024

1 Technical Information Center
Roy F. Weston, Inc.
955 L'Enfant Plaza SW
Washington, DC 20024

1 Technical Project Officer - YMP
US Bureau of Reclamation
Code D-3790
P.O. Box 25007
Denver, CO 80225

1 B. T. Brady
Records Specialist
US Geological Survey
MS 421
P.O. Box 25046
Denver, CO 80225

1 M. D. Voegele
Technical Project Officer - YMP
M&O/SAIC
101 Convention Center Drive
Suite 407
Las Vegas, NV 89109

1 Paul Eslinger, Manager
PASS Program
Pacific Northwest Laboratories
P.O. Box 999
Richland, WA 99352

1 A. T. Tamura
Science and Technology Division
OSTI
US Department of Energy
P.O. Box 62
Oak Ridge, TN 37831

1 P. J. Weeden, Acting Director
Nuclear Radiation Assessment Div.
US EPA
Environmental Monitoring Sys. Lab
P.O. Box 93478
Las Vegas, NV 89193-3478

1 ONWI Library
Battelle Columbus Laboratory
Office of Nuclear Waste Isolation
505 King Avenue
Columbus, OH 43201

1 C. H. Johnson
Technical Program Manager
Agency for Nuclear Projects
State of Nevada
Evergreen Center, Suite 252
1802 N. Carson Street
Carson City, NV 89710

1 John Fordham, Deputy Director
Water Resources Center
Desert Research Institute
P.O. Box 60220
Reno, NV 89506

1 The Honorable Cyril Schank
Chairman
Churchill County Board of
Commissioners
190 W. First Street
Fallon, NV 89406

1 T. Hay, Executive Assistant
Office of the Governor
State of Nevada
Capitol Complex
Carson City, NV 89710

3 R. R. Loux
Executive Director
Agency for Nuclear Projects
State of Nevada
Evergreen Center, Suite 252
1802 N. Carson Street
Carson City, NV 89710

1 Brad R. Mettam
Inyo County Yucca Mountain
Repository Assessment Office
P. O. Drawer L
Independence, CA 93526

1 Lander County Board of Commissioners
315 South Humbolt Street
Battle Mountain, NV 89820

1 Vernon E. Poe
Office of Nuclear Projects
Mineral County
P.O. Box 1600
Hawthorne, NV 89415

1 Les W. Bradshaw
Program Manager
Nye County Nuclear Waste Repository
Project Office
P.O. Box 1767
Tonopah, NV 89049

1 Florindo Mariani
White Pine County Coordinator
P. O. Box 135
Ely, NV 89301

1 Judy Foremaster
City of Caliente Nuclear Waste
Project Office
P.O. Box 158
Caliente, NV 89008

1 Philip A. Niedzielski-Eichner
Nye County Nuclear Waste
Repository Project Office
P.O. Box 221274
Chantilly, VA 22022-1274

1 Dennis Bechtel, Coordinator
Nuclear Waste Division
Clark County Department of
Comprehensive Planning
301 E. Clark Avenue, Suite 570
Las Vegas, NV 89101

1 Juanita D. Hoffman
Nuclear Waste Repository
Oversight Program
Esmeralda County
P.O. Box 490
Goldfield, NV 89013

1 Eureka County Board of Commissioners
Yucca Mountain Information Office
P.O. Box 714
Eureka, NV 89316

1 Economic Development Dept.
City of Las Vegas
400 E. Stewart Avenue
Las Vegas, NV 89101

1 Community Planning & Development
City of North Las Vegas
P.O. Box 4086
North Las Vegas, NV 89030

1 Community Development & Planning
City of Boulder City
P.O. Box 61350
Boulder City, NV 89006

1 Commission of European Communities
200 Rue de la Loi
B-1049 Brussels
BELGIUM

2 Librarian
YMP Research & Study Center
MS 407
P.O. Box 98521
Las Vegas, NV 89193-8521

1 Amy Anderson
Argonne National Laboratory
Building 362
9700 S. Cass Avenue
Argonne, IL 60439

1 Glenn Van Roekel
Director of Community Development
City of Caliente
P.O. Box 158
Caliente, NV 89008

1 G. S. Bodvarsson
Head, Nuclear Waste Department
Lawrence Berkeley Laboratory
1 Cyclotron Road, MS 50E
Berkeley, CA 94720

1 Michael L. Baughman
Intertech Services Corp.
P.O. Box 93537
Las Vegas, NV 89193

1 W. Murphy
Center for Nuclear Waste
Regulatory Analyses
6220 Culebra Road
Drawer 28510
San Antonio, TX 78284

1 R. Pabalon
Center for Nuclear Waste
Regulatory Analyses
6220 Culebra Road
Drawer 28510
San Antonio, TX 78284

1 Dr. James O. Leckie
Environmental Engineering
and Science
Department of Civil Engineering
Stanford University
Stanford, CA 94305

1 Vijay Tripathi
6518 Elnido Drive
McLean, VA 22101

1 Gour-Tsyh Yeh
Professor of Civil Engineering
212 Sacket Bldg.
Penn State University
University Park, PA 16802

1 G. F. Birchard
Office of Nuclear Regulatory Research
MS NL-005
Washington, DC 20555

1 L. A. Kovach
Office of Nuclear Regulatory Research
MS NL-005
Washington, DC 20555

1 G. Jacobs
Oak Ridge National Laboratory
Box 2009
Oak Ridge, TN 37831

2 Dr. Ardyth Simmons
US Department of Energy
YMPO
101 Convention Center Drive
Las Vegas, NV 89109

3 E. Smistad
US Department of Energy
YMPO
101 Convention Center Drive
Las Vegas, NV 89109

1 Dr. Ines Triay
Los Alamos National Lab
INC 9 Mail Stop J514
Los Alamos, NM 87545

1 Dr. Everett Springer
Los Alamos National Lab
ESS 15 Mail Stop J495
Los Alamos, NM 87545

1 Dr. Paul Cloke
SAIC
101 Convention Center Drive
Las Vegas, NV 89109

1 Dr. Stephen Nelson
Woodward Clyde Federal Systems
Yucca Mountain Site
Characterization Project
101 Convention Center Drive
Las Vegas, NV 89109

1 Dr. Abraham Van Luik
INTERA
Yucca Mountain Site
Characterization Project
101 Convention Center Drive
Las Vegas, NV 89109

1 Dr. David Read
RM Consultants Ltd.
Suite 7 Hitching Court
Abingdon Business Park
Abingdon, Oxfordshire, OX14, 1RA
UNITED KINGDOM

1 Joel Chupeau
National Radioactive Waste
Management Agency
Route de Panorama Robert Schuman
B. P. 38
92286 Fontenay-aux-Roses
Cedex
FRANCE

1 Philippe Jamet
ISIGE Institute
Ecole Des Mines De Paris
35 Rue Saint Honore
77305 Fontainbleau Cedex
Paris, FRANCE

1 Benoit Made
Centre d'Informatique Geologique
Ecole Des Mines De Paris
35 Rue Saint Honore
77305 Fontainbleau Cedex
Paris, FRANCE

1 Dr. Henning von Maravic
Programme Radioactive Waste Mgmt.
Rue de la Loi
Wetstraal 200
8-104 Brussels
BELGIUM

1 Robert Fabriol
SGN/UPE/HYDR Department
BRGM
Avenue de Concyr
B. P. 6009-45060
Orleans Cedex 2
FRANCE

1 Dr. David Sevougian
INTERA
101 Convention Center Drive, Suite P-110
Las Vegas, NV 89109

	MS	
2	1330	C. B. Michaels, 6352 100/12546/SAND95-0591/QA
20	1330	WMT Library, 6352
1	1324	P. B. Davies, 6115
1	1375	D. A. Dahlgren, 4400
10	1320	M. D. Siegel, 6748
1	1320	B. Thomson, 6119
1	0750	H. Westrich, 6118
1	0750	P. Brady, 6118
1	0750	H. Stockman, 6118
1	0827	P. Hopkins, 1511
3	0750	D. B. Ward, 6118
3	1320	C. R. Bryan, 6748
1	0719	D. Marozus, 6621
1	1325	L. S. Costin, 6302
1	1399	M. Brady, 6314
1	9018	Central Technical Files, 8523-2
5	0899	Technical Library, 13414
1	0619	Print Media, 12615
2	0100	Document Processing, 7613-2 for DOE/OSTI